520467

Sandia National Laboratories
Technical Baseline Reports

WBS 1.3.5.3
Compliance Monitoring
WBS 1.3.5.4
Repository Investigations
Milestone RI110

January 31, 2002

Prepared for the United States Department of Energy
Carlsbad Field Office

Sandia National Laboratories

© 2002 Sandia Corporation

WIPP:1.3.5.4:PLN:NO:Milestone RI-110

Information Only

Sandia National Laboratories
Technical Baseline Reports

WBS 1.3.5.3
Compliance Monitoring
WBS 1.3.5.4
Repository Investigations
Milestone RI110

January 31, 2002

Prepared for the United States Department of Energy
Carlsbad Field Office

Sandia National Laboratories

© 2002 Sandia Corporation

Information Only

Sandia National Laboratories
Technical Baseline Reports

WBS 1.3.5.3
Compliance Monitoring
WBS 1.3.5.4
Repository Investigations

F.D. Hansen, Acting Manager 6822 1/31/2002 Date

The contents of this report follow the WBS structure for Sandia's FY2002 program. Subject matter includes compliance monitoring and repository investigations and follows the WBS numerically. The section on 191/194 Compliance Monitoring (1.3.5.3) includes discussion of both monitoring activities and analysis. The sections comprising Repository Investigations (1.3.5.4) are subdivided into fifth and sixth level WBS Elements. The intent of this organization is to facilitate direct comparison between the BOE's and progress, thereby providing the CBFO with current technical status and program tracking information.

Information Only

Table of Contents

Information Only

Table of Contents

Information Only

Information Only

Executive Summary Abstract

1.0 Compliance Monitoring

Change in regional groundwater flow within the Culebra Member of the Rustler Formation has been identified by the U. S. Department of Energy (DOE) as one of ten compliance monitoring parameters (COMPs) considered important in the evaluation of the long-term performance of the Waste Isolation Pilot Plant (WIPP). A monitoring program has been designed and implemented to acquire data for this COMP as well as the other nine COMPs identified by the EPA. These acquired data are evaluated annually against performance expectations for the disposal system.

The transmissivities used to predict regional groundwater flow in the Culebra were estimated by calibrating the flow model used for the DOE Compliance Certification Application (CCA) to the steady-state heads in 32 WIPP wells taking into account the inherent uncertainty or range in the observed steady-state heads. An implication of this approach is that if the heads in the wells exceed the range used in the CCA, then flow velocity and/or flow direction could change from model predictions. Recent data acquired from the Culebra monitoring program indicate some water levels fall outside the range used in the CCA prompting the need for additional investigations. Relevant investigations include:

- Monitoring of injection well flows and site meteorological conditions
- Use of continuous water level monitoring equipment in selected wells
- Recompletion of monitoring wells to nearby geologic members within the Rustler Formation (e.g., the Magenta Member) as well as the development of hydrological models for these members
- Collection of field and drill-hole evidence to evaluate water level change scenarios
- Assessment of the impact of the changes in water levels using hydrological modeling/analyses.

Data acquired in the investigation will necessarily consider well integrity because well integrity influences data quality. This report presents the status of these investigations as well as plans for future activities.

2.0 Geochemistry

2.1 Microbial Degradation: Brookhaven Abstract

Gas generation from the microbial degradation of the organic constituents of transuranic waste under conditions expected at the WIPP repository is being investigated at Brookhaven National Laboratory. This report summarizes progress from the period July 14, 2001 – January 31, 2002. During this period, we analyzed the total gas, carbon dioxide, and methane production; microbial degradation products of cellulose; and the diversity of microbial community in samples incubated under inundated conditions for 9.5 years (3464 days). The total volume of gas produced has leveled-off or diminished in anaerobic inundated cellulose samples with and without bentonite since the last analysis at 2718 days. Carbon dioxide production generally followed the same trend except in amended inoculated samples (2.10 μmol g^{-1} cellulose produced over 2 years (0.0028 μmol g^{-1} cellulose day^{-1})). There was a large variation in CO_2 produced between triplicate samples in the anaerobic amended inoculated samples containing excess nitrate, indicating that certain treatments may be showing further activity at 3464 days. The enhanced CO_2 production due to the addition of bentonite remains evident at 3464 days even

Information Only

though there was no increase in production since 2718 days. Almost all of the initially aerobic samples showed slight increases in total gas produced at 3464 days; CO_2 increased slightly in amended inoculated samples (0.0066 μmol g^{-1} cellulose day^{-1}). In general, CO_2 production in initially aerobic samples continued to remain at the same level. Up to 5.9 nmol methane g^{-1} cellulose was detected in anaerobic unamended inoculated samples, and for the first time, methane was detected in samples that were treated with excess nitrate. The rate of methane production in anaerobic samples was 2.5 pmol CH_4 g^{-1} cellulose d^{-1} in both unamended inoculated and amended treatments, and 3.45 pmol CH_4 g^{-1} cellulose d^{-1} in samples containing excess nitrate. Methane was also detected for the first time in initially aerobic inundated samples. In general, unamended samples showed the greatest quantities of methane. Acetic and butyric acids accumulated to a significant extent in anaerobic samples amended with nutrients (6.99 and 6.38 mM respectively); the accumulation of these acids was stimulated by the presence of bentonite (38.6 and 49.8 mM respectively). The overall organic acid content was lowest in anaerobic samples containing excess nitrate and in samples incubated under initially aerobic conditions. These results are consistent with oxidative processes being dominant in these samples. Microbial characterization of anaerobic inundated samples showed *Halobacter utahensis* as the predominant species in unamended samples with the nutrient amended samples dominated by *Halobacterium*, *Halobacter*, *Halococcus*, and the haloalkalophiles *Natranobacterium* and *Natranomonas*. Work in progress includes analysis of data from studies of methane produced in humid samples and samples containing plastic and rubber materials, and initiation of studies designed to quantify microbial gas production under conditions of MgO-constrained water activity.

2.2 Geochemistry Studies

This section consists of five parts:

- Complexation of Metal Ions With Hypochlorite
- The Test Plan titled: Complexation of Metal Ions with Hypochlorite, TP02-01
- Abstract titled: Effect of Actinide Complexation by Organic Ligands on WIPP Performance Assessment
- Abstract titled: The Use of Th, U, Np, Am as Oxidation State Analogs for Pu in the WIPP Actinide Chemistry Program
- Abstract titled: Interactions of Actinides with the Polyoxometalates $[NaP_5W_{30}O_{110}]^{14-}$ $[As_2W_{21}O_{69}]^{6-}$, $[P_2W_{18}O_{62}]^{6-}$ and $[P_2W_{17}O_{61}]^{10-}$

The section "Complexation of Metal Ions with Hypochlorite" describes experimental work and some results from the aforementioned study. The test plan documenting the work is provided under the same title. The three abstracts in the above list have been submitted and accepted for presentation to the Nuclear Chemistry and Technology Division of the American Chemical Society (ACS) at the National Meeting of the ACS during April, 2002.

The submittal titled "Effect of Actinide Complexation by Organic Ligands on WIPP Performance Assessment" will describe the influence of acetate, citrate, oxalate, and EDTA on actinide solubility in WIPP brines. Author is D. E. Wall, Sandia National Laboratories.

The submittal titled "The Use of Th, U, Np, Am as Oxidation State Analogs for Pu in the WIPP Actinide Chemistry Program" will describe the validity of the oxidation state analogy in modeling chemical behavior of plutonium. The co-authors of the abstract are N. A. Wall and L. H. Brush of Sandia National Laboratories.

Information Only

7

The submittal titled Interactions of Actinides with the Polyoxometalates $[NaP_5W_{30}O_{110}]^{14-}$ $[As_2W_{21}O_{69}]^{6-}$, $[P_2W_{18}O_{62}]^{6-}$ and $[P_2W_{17}O_{61}]^{10-}$ will describe the use of soluble metal oxides as thermodynamic models for the interactions of actinide ions with colloids. The authors of the abstract are D. Wall and G. R Choppin.

3.0 Engineered Barriers

3.1 MgO Studies Abstract Experimental Work Conducted at SNL/Carlsbad

The Carlsbad Programs Group of Sandia National Laboratories is currently investigating several issues with respect to the efficacy of MgO under expected repository conditions. Previous work was described in the January and July 2001 Status Reports to the DOE (Milestones RI010 & RI020). Characterization of Premier Chemicals MgO, with respect to both mineralogy and composition, and its ability to absorb water (H_2O) and carbon dioxide (CO_2) under repository conditions continues. Sandia is currently carrying out a series of experiments to measure hydration rates for Premier MgO under both inundated and humid conditions. Results to date suggest that, in general, the hydration rate can be a modeled as a diffusion-limited reaction, although interpretation of the hydration results in GWB is complicated by the formation of a second hydrated phase, a magnesium chloride hydroxide hydrate (hereafter referred to as sorel cement).

In addition, MgO carbonation rates are being measured at CO_2 partial pressure (P_{CO2}) of about $10^{-3.5}$ atm, the P_{CO2}. characteristic of ambient atmospheric conditions. At atmospheric P_{CO2}, as expected, carbonation has been slow. Sandia is also working to obtain further information on the MgO hydration-carbonation pathway relevant to repository conditions. Of particular importance is the metastable magnesium hydroxycarbonate mineral that forms initially, as this mineral (along with brucite, $Mg(OH)_2$) will control the P_{CO2} and pH in the repository. These are important parameters for predicting actinide solubilities. Sandia is also carrying out experiments to evaluate the generation of isosaccharinic acid (ISA), a potentially strong complexant for the actinides, in the presence of MgO.

3.2 MgO Studies Test Plan: Colloids

The results of this study will be used to determine whether the WIPP backfill "Premier Chemicals MgO", which is being used in the WIPP to mitigate the effect of microbial CO_2 generation on actinide mobility in a post-closure repository environment, will generate colloids, whether these colloids will be stable in WIPP conditions and whether these colloids will affect the WIPP compliance.

3.3 Cementitious Materials Abstract

Sandia National Laboratories/Carlsbad is currently performing research to develop a model for cement/brine interactions to be used in performance assessment (PA) of the Waste Isolation Pilot Plant (WIPP). Modeling cement degradation in WIPP-relevant brines is critical for predicting the long-term integrity of cement borehole plugs, an area of uncertainty in conceptual models used for WIPP PA. Assumed degradation rates have a first order influence on PA conceptual models by controlling brine flow into and out of the repository in human intrusion scenarios, directly affecting such PA parameters as the source term for the Culebra Dolomite, gas generation rates, and spallings releases. In addition, cementitious waste forms are a significant fraction of the waste inventory, and cement-brine reactions may affect repository chemistry and

Information Only

actinide solubility. Dissolution of cement components could result in high-pH microenvironments, while calcium released during cement degradation will serve as an additional sink (with MgO) for carbon dioxide.

Information for developing a model for cement/brine reactions and borehole plug failure rates is being gathered from two sources. The first consists of laboratory experiments with cement and brine, being run to develop an equilibrium thermodynamic model. They include gibbsite ($Al(OH)_3$) solubility experiments to determine Pitzer parameters for Al under conditions relevant to the WIPP, and batch experiments with crushed, hydrated cement to determine the equilibrium mineral assemblages that form at varying cement/brine ratios. Applying this model to borehole plug degradation rates requires obtaining additional data on the effects of non-equilibrium processes (diffusion, mineral precipitation, etc.). Batch experiments with cement wafers and cement core-column (flow-through) experiments are being run for this purpose.

The second source of information on borehole plug degradation is sampling of downhole cement samples and casing corrosion products during borehole plugging and abandonment (P&A), borehole recompletion, and general borehole maintenance at the WIPP site. Casing corrosion is of importance because it represents a second, possibly much faster, mode of borehole plug failure. This opportunistic sampling allows recovery of samples that have been exposed to WIPP brines for up to 20 years—a much longer time scale than that available for laboratory experiments. Several wells were sampled in FY00 and FY01, but only casing corrosion products were collected and analyzed—no opportunity for cement retrieval occurred.

3.4 Panel Closures

Physical Barriers Studies involving the panel closure system (PCS) are reported in this section. This work addresses WBS element 1.3.5.4.3.2, which comprises both the re-evaluation of the PCS and studies of cementitious materials. The term "Engineered Barriers" in the context of repository investigations includes MgO hydration, carbonation and colloids, cementitious materials research, and panel closure systems. In order of maturity of investigations, the MgO work in Carlsbad is now well underway, cementitious materials laboratory studies in Carlsbad are initiating and panel closure evaluations have been re-directed as recently as January 7, 2002.

The CBFO has identified new panel closure considerations to be evaluated by Sandia. A summary of the expected path forward will be given. Over this recent reporting period, effort was lent to address an array of issues pertaining to Panel Closure Systems (PCS). A short review of the PCS issues and material delivered to the CBFO this reporting period is given here.

4.0 Rock Mechanics

4.1 Disturbed Rock Zone (DRZ) Repository Studies Abstract

This report briefly describes the Disturbed Rock Zone (DRZ) repository studies conducted in the Waste Isolation Pilot Plant (WIPP) repository during the current reporting period. Tests associated with these studies were performed in accordance with the Sandia National Laboratories (SNL) National Waste Management Program (NWMP) Test Plan TP 99-04, *Disturbed Rock Zone Characterization Test Plan* (DRZ Test Plan. DRZ repository studies have been limited to activities associated with ultrasonic velocity tests in the Air Intake Shaft (AIS) and near the Q Room.

Information Only

4.2 Disturbed Rock Zone NARMS Paper

This section provides an abstract submitted to the North American Rock Mechanics conference. An alcove constructed about 12 years ago provides an opportunity to conduct geophysical investigations of the damage that has developed in the salt for a complex three-dimensional configuration. Specifically, an interior room corner is used to study the damage caused by stress fields unique to the corners of rectangular openings in salt formations. The mature DRZ is the macroscopic manifestation of grain-scale and larger cracks that form as a result of the shear stress around the newly created opening, and as a result of creep-related deformation over a period of years. As part of a suite of measurements designed to study the hydrological and mechanical properties of the salt in the alcove corner, twelve, 10-cm diameter ultrasonic transducer emplacement holes were drilled in the alcove corner rib to a depth of about 7.5 m. Elastic wave velocity and attenuation in the salt are a function of the density of cracks, as is the permeability. The design of the borehole array and the transducer assemblies allows the measurement of elastic wave velocities and amplitudes (for attenuation studies) along vertical and horizontal paths tangential to the alcove corner and, within the same hole, at a 45° angle to the rib. Orthogonal paths are necessary to detect the anisotropy of the cracking in the DRZ.

4.3 Disturbed Rock Zone Memo

This deliverable to CBFO describes ultrasonic wave assessment of the DRZ at WIPP. As part of a suite of measurements designed to study the hydrological and mechanical properties of the salt in the alcove corner, twelve, 10-cm diameter ultrasonic transducer emplacement holes were drilled in the alcove corner rib to a depth of about 6 meters. The design of the borehole array and the transducer assemblies allows the measurement of elastic wave velocities along vertical and horizontal paths parallel to the walls intersecting at the alcove corner and, within the same hole, at a 45° angle to the rib. Orthogonal paths are necessary to detect the anisotropy of the cracking in the DRZ.

It is expected that the current results will be useful to other studies of the long-term deformation characteristics of salt. The data delineate the DRZ as a function of depth from the alcove corner and as a function of the varying stress-state around a rectangular alcove corner cross-section. The significance of the results lies in the length of time the DRZ has had to develop (approximately 12 years), the geometrical complexity of the alcove corner, which will allow a more rigorous test of models than is possible in simpler geometries, and the hydrological measurements to be made in conjunction with the velocity and attenuation measurements. Understanding the time-dependent changes in damage, and thus permeability, as the DRZ develops is important because these changes strongly affect the sealing of underground openings at the WIPP.

4.4 DRZ Core Studies

A snap-shot of the DRZ core studies is summarized in Table 4.4.1. Our observational work in the Carlsbad laboratory includes quantifying fracture porosity, free dislocation density, mineralogy and moisture. In addition to WIPP cores, we are evaluating similar properties of DRZ cores from sites in Germany. The German information will be compared to WIPP data and discussed with researchers involved in the BAMBUS II consortium research.

Information Only

1.0 Compliance Monitoring

Information Only

1.0 Compliance Monitoring

Status of the Far Field Rustler Formation Hydrological Studies[1]

T. W. Pfeifle, 6822
R. M. Roberts, 6822
Sandia National Laboratories, MS 1395
4100 National Parks Highway
Carlsbad, NM USA 88220

Abstract

Change in regional groundwater flow within the Culebra Member of the Rustler Formation has been identified by the U. S. Department of Energy (DOE) as one of ten compliance monitoring parameters (COMPs) considered important in the evaluation of the long-term performance of the Waste Isolation Pilot Plant (WIPP). A monitoring program has been designed and implemented to acquire data for this COMP as well as the other nine COMPs identified by the DOE. These acquired data are evaluated annually against performance expectations for the disposal system.

The transmissivities used to predict regional groundwater flow in the Culebra were estimated by calibrating the flow model used for the DOE Compliance Certification Application (CCA) to the steady-state heads in 32 WIPP wells taking into account the inherent uncertainty or range in the observed steady-state heads. An implication of this approach is that if the heads in the wells exceed the range used in the CCA, then flow velocity and/or flow direction could change from model predictions. Recent data acquired from the Culebra monitoring program indicate some water levels fall outside the range used in the CCA prompting the need for additional investigations. Relevant investigations include:

- Monitoring of injection well flows and site meteorological conditions
- Use of continuous water level monitoring equipment in selected wells
- Recompletion of monitoring wells to nearby geologic members within the Rustler Formation (e.g., the Magenta Member) as well as the development of hydrological models for these members
- Collection of field and drill-hole evidence to evaluate water level change scenarios
- Assessment of the impact of the changes in water levels using hydrological modeling/analyses.

Data acquired in the investigation will necessarily consider well integrity because well integrity influences data quality. This report presents the status of these investigations as well as plans for future activities.

[1] This work is covered by BOE #1.3.5.3.1 and WBS #1.3.5.3.1.1 and 1.3.5.3.1.2

Information Only

Introduction

Several individual monitoring programs have been implemented at the Waste Isolation Pilot Plant (WIPP) to ensure environmental protection, public and worker health and safety, proper characterization of the disposal system, and continued compliance with applicable regulations. Each of these programs has one or more drivers based on the applicable governing requirements. The monitoring programs were initiated before the first waste was received to establish baseline conditions, are continuing during the operational period of the repository, and in some cases will be maintained for established periods of time following closure of the facility as specified by the applicable regulations.

One monitoring program implemented by the U. S. Department of Energy (DOE) is the Compliance Monitoring Program (CMP) developed to meet requirements described in the DOE's application to the U. S. Environmental Protection Agency (EPA) that demonstrated the compliance of the WIPP with radioactive waste disposal regulations 40 Code of Federal Regulation Parts 191 (40 CFR 191) Subparts B and C and 40 CFR 194. Monitoring activities described in the WIPP Compliance Certification Application (CCA) are performed as assurance measures to ensure that any deviations from the expected long-term performance of the repository are identified at the earliest possible time. The long-term performance expectations for the disposal system are derived from conceptual models, scenarios, and assumptions developed for the WIPP Performance Assessment (PA) used to predict performance of the disposal system over a 10,000-year period.

The DOE Carlsbad Field Office, Office of Regulatory Compliance (CBFO/ORC), has responsibility for the CMP and developed an implementation plan [DOE, 1999] that

(1) Identified activities and organizations required to comply with 40 CFR Parts 191 and 194
(2) Established the compliance monitoring schedule
(3) Defined the process for ensuring monitoring results were assessed for importance and integrated into the continuing compliance and re-certification process
(4) Defined the process for reporting results
(5) Defined the process for assessing the usefulness of the monitored parameters with respect to PA and for modifying the sampling and monitoring program, as appropriate.

In response to the requirements put forth by EPA in 40 CFR 194.42(a), DOE performed an analysis of potential monitoring parameters in the CCA and developed the monitoring program using these parameters. The EPA documented their approval of the parameter analysis and the CMP in their certification decision [EPA, 1998a] and the Certification Application Review Document Number 42 [EPA, 1998b]. Ten compliance monitoring parameters (COMPs) were identified as important in the DOE analysis and were grouped into four categories including:

- Regional Hydrology (2 COMPs)
- Human Intrusion (2 COMPs)
- Geotechnical Performance (5 COMPs)
- Waste Activity (1 COMP).

Information Only

Data collection and data reporting for the ten COMPS are the responsibility of the WIPP Management and Operating Contractor (Westinghouse TRU Solutions (WTS)), while data analysis and evaluation of the COMPs data against performance expectations of the disposal system are the responsibility of the Scientific Advisor (Sandia National Laboratories). The COMPs are evaluated annually against performance expectations for the disposal system, and significant deviations from the performance expectations are flagged as potential problems requiring further investigation.

In the 1999 annual COMPs assessment, the data for one of the regional hydrological COMPs, *Change in Culebra Groundwater Flow*, indicated conditions outside of expected limits [Sandia, 2000]. An assessment was performed to determine the effects of the condition relative to PA assumptions. Because the freshwater heads measured at some of the Culebra wells exceeded those used for the CCA, investigations into the causes for the changes in water level were recommended. The DOE CBFO authorized the Scientific Advisor (SA) to conduct these more detailed investigations. Specific investigations initiated by the SA included:

1. Monitoring of injection well inflows into the Bell Canyon Formation near the H-9 hydropad [Jepsen, 2000]
2. Meteorological monitoring at the H-7 and H-9 hydropads [Jepsen, 2000]
3. Continuous water level monitoring in selected wells completed to the Culebra Member of the Rustler Formation and the Bell Canyon Formation [Jepsen, 2000]
4. Development of a Magenta hydrological flow model including the recompletion of wells to the Magenta Formation [Beauheim, 2000]
5. Collection of field and drillhole evidence to support or refute events/processes that may affect Culebra water levels [Powers, 2001]
6. Impact assessment of changes in Culebra water levels using hydrological modeling/analyses [Powers, 2001].

This report presents a brief review of the need for the investigations and discusses the current status of the individual investigations as well as planned activities to be conducted during the next reporting period. As indicated above, Activities 1 through 3 are controlled by Sandia Test Plan TP 99-10 [Jepsen, 2000], Activity 4 is controlled by Sandia Test Plan TP 00-03 [Beauheim, 2000], and Activities 5 and 6 are controlled by Sandia Test Plan TP 01-01 [Powers, 2001].

Monitoring of Injection Well Inflows into the Bell Canyon Formation Near the H-9 Hydropad

Private resource exploration companies are currently involved in deep-well injection activities (specifically, injection of produced oil-field brines into the Bell Canyon Formation) that are being conducted outside, but near, the WIPP site boundary area. WIPP stakeholders have suggested that a hydrological connection may exist between these injection activities and the changes in water levels measured in some of the Culebra monitoring wells. The premise for such a hydrological connection is vertical flow from the Bell Canyon to the Culebra induced by a change in hydraulic gradient between the two formations during brine injection. Possible vertical flow paths include:

Information Only

(1) Poorly cemented and/or leaking injection wells
(2) Old abandoned wells that extend through the Culebra to the Bell Canyon or deeper
(3) Porous media flow from the Bell Canyon up through the Castile and Salado Formations (a highly unlikely scenario given the low hydraulic conductivity of the Castile and Salado and the relatively long flow path - a distance of more than 1,100 meters).

To investigate the various hydrological connection scenarios, inflow data for six injection wells located near the H-9 hydropad are being collected for comparison with the water levels measured at the H-9 hydropad (H-9 water levels are discussed later in this chapter). The location of the H-9 hydropad is approximately 6.5 miles south of the WIPP site boundary as shown in Figure 1.

The six injection wells monitored in this investigation are Cal Mon #5, Sand Dunes 28F#1, Pure Gold B F#20, Todd 26F#2, Todd 26F#3, and Todd 27F#16. These wells are located from 1.5 to 3 miles northeast of (and up-gradient from) the H-9 hydropad (Figure 2). The injection zones for all six wells are shown in Table 1. With the exception of Pure Gold B F#20, the injection zones are located in the Bell Canyon Formation at depths typically between 4,500 to 5,500 feet (below ground surface, bgs). The injection zone for Pure Gold B F#20 is in the Brushy Canyon member of the Bell Canyon Formation at a depth of 7,740 to 7,774 feet (bgs). Injection data for the wells are being collected daily by WTS during non-weekend and non-holiday periods (except during August 23, 2001 through October 8, 2001 when no data were collected). The data collected include total cumulative injection volume as read on the injection meter for each well, well injection pressure, and the date and time each meter was read.

As part of the current investigations, an average daily injection rate for each well was calculated by dividing the difference in injection volumes for consecutive meter readings by the elapsed time (in days) between readings. With the exception of the Pure Gold B F#20, the average daily injection rates for each of the six wells are shown in Figure 3 for the entire monitoring period beginning in July 1999. Pure Gold B F#20 was recently added to the injection well cluster so the data for this well are shown only for the period from June 1, 2001 through December 31, 2001.

Information Only

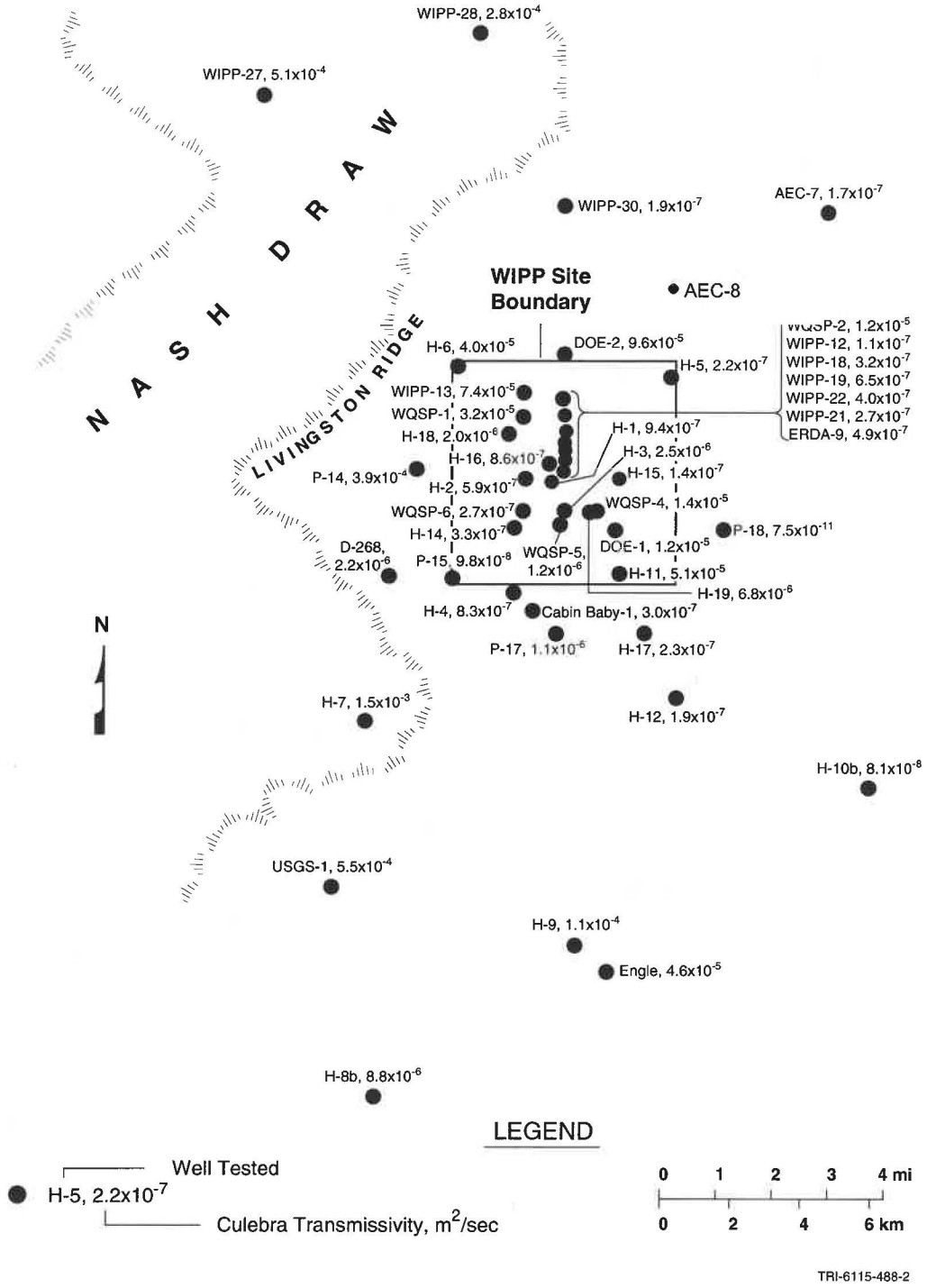

Figure 1. Location of WIPP Monitoring Wells.

Information Only

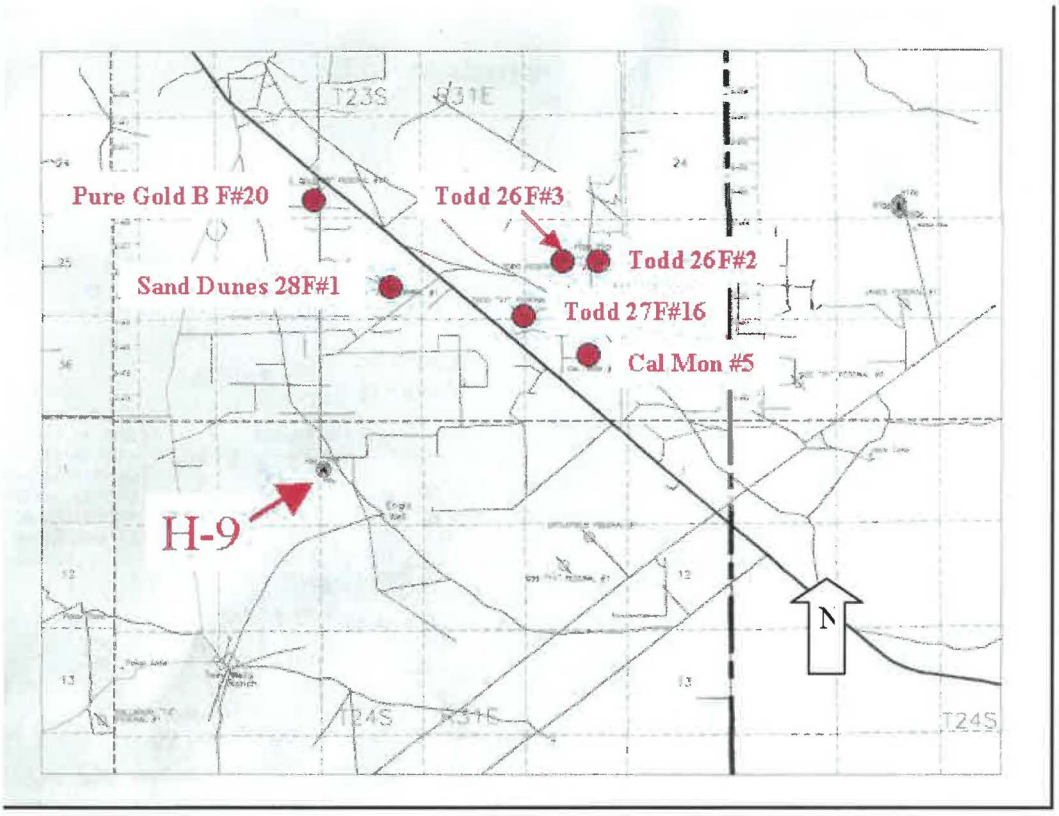

Figure 2. Location of Injection Wells Relative to the H-9 Hydropad.

Information Only

17

Table 1. Injection Zone Depth Intervals for the Injection Wells Located Near the H-9 Hydropad

Well No.	Injection Zone Depth, feet[(a)]
Cal Mon #5	4484 – 5780
Sand Dunes 28F#1	4295 – 5570
Pure Gold B F#20	7740 – 7774
Todd 26F#2	4460 – 5134
Todd 26F#3	4390 – 6048
Todd 27F#16	4694 – 5284

(a) below ground surface, bgs

The current average daily injection rate for Todd 26F#2 is approximately 700 barrels/day or about one-half the rate reported in July 2001. The average daily injection rate for Todd 26F#3 is approximately 650 barrels/day, also about one-half the rate reported in July 2001. The average daily injection rate for Todd 27F#16 is currently about 1,700 barrels/day and has steadily decreased from a high of 2,800 barrels/day recorded in April and May 2000. With the exception of a few short time-intervals, the average daily injection rate for Cal Mon #5 ranges from 500 to 1,000 barrels/day. The injection rates for Sand Dunes 28F#1 are highly variable, but have typically ranged between 1,000 and 1,500 barrels/day. At the beginning of June 2001, Pure Gold B F#20 was added to the Sand Dunes 28F#1 brine manifold. As a result, the injection rate at Sand Dunes 28F#1 dropped to zero and the initial injection rates for Pure Gold B F#20 ranged between 1,000 and 1,500 barrels/day. The injection rates at Sand Dunes 28F#1 remained zero until October 2001 when they increased to 500 to 1,000 barrels/day. During this same time, the injection rates at Pure Gold B F#20 were highly variable with rates as high as 2,500 barrels/day and as low as 500 barrels/day; however over the last two months the rates have stabilized at about 750 barrels/day. The sum of the injection rates for Sand Dunes 28F#1 and Pure Gold B F#20 are currently equivalent to the rates for Sand Dunes 28F#1 immediately before Pure Gold B F#20 was added to the brine manifold.

As shown previously in Table 1, the injection zones for five of the six wells cover approximately the same depth interval (between 4,500 and 5,500 feet, bgs). In addition, because the wells are located near one another (1 to 3 miles) in a horizontal plane, the injection can be approximated as a point source on the regional scale. Using this assumption, the total injection rate at the point source is simply the cumulative total of the injection rates of the five individual wells. Figure 4 gives the total cumulative injection rate as a function of time for all six wells. Because of the large variability in the cumulative rates, two running average injection rates were calculated. One running average included the data from all six wells, while the second included data only from the five wells injecting at the same depth interval. Both of these running average injection rates are plotted in Figure 4 for comparison with the measured cumulative rate. Each running average rate is calculated as the average total injection rate for all of the data falling inside a sliding "time window." Subsequent rates are determined by simultaneously adding and dropping a data point from either end of the time window until all of the data have eventually been included in one of the time windows. The

Information Only

average rates are then plotted at the midpoints of their respective time windows. As shown in Figure 4, this technique "smooths" the measured data so that local trends and/or peaks and valleys become obvious. Peak rates of about 6,500 barrels/day occur in the fall and spring, while valley rates of about 5,000 barrels/day generally occur near major holidays (i.e., Christmas and Independence Day). The running average injection rates for the six wells parallel the rates for the five wells, but are offset in magnitude as expected.

Injection rate monitoring will continue at least through the next reporting period.

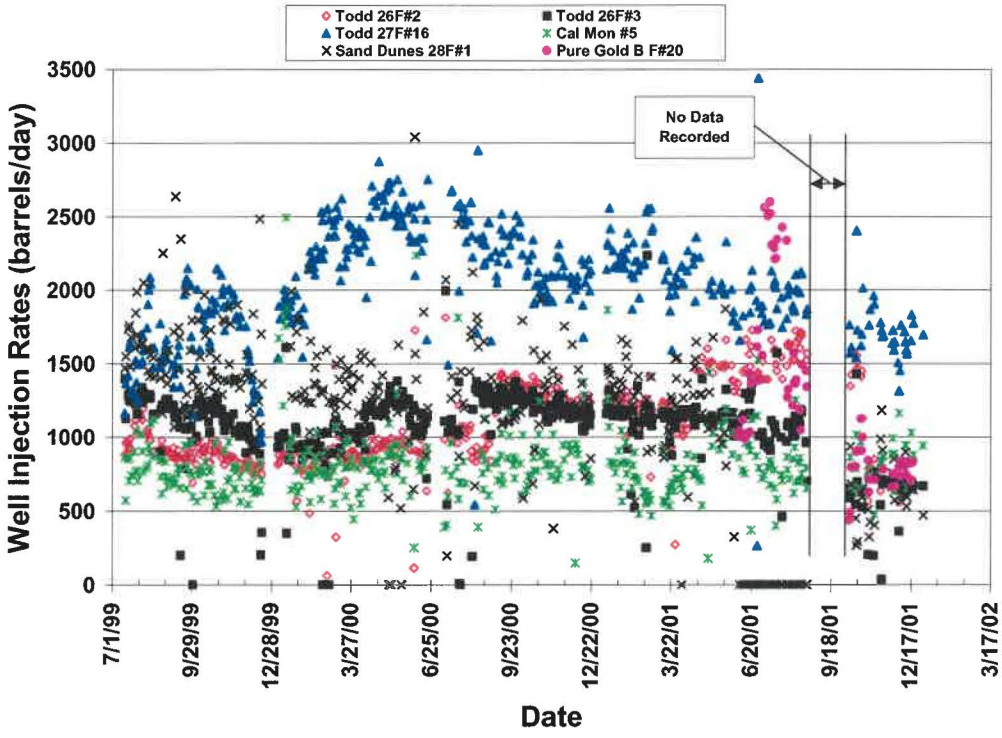

Figure 3. History of Daily Injection Rates for Six Wells Located Near the H-9 Hydropad.

Information Only

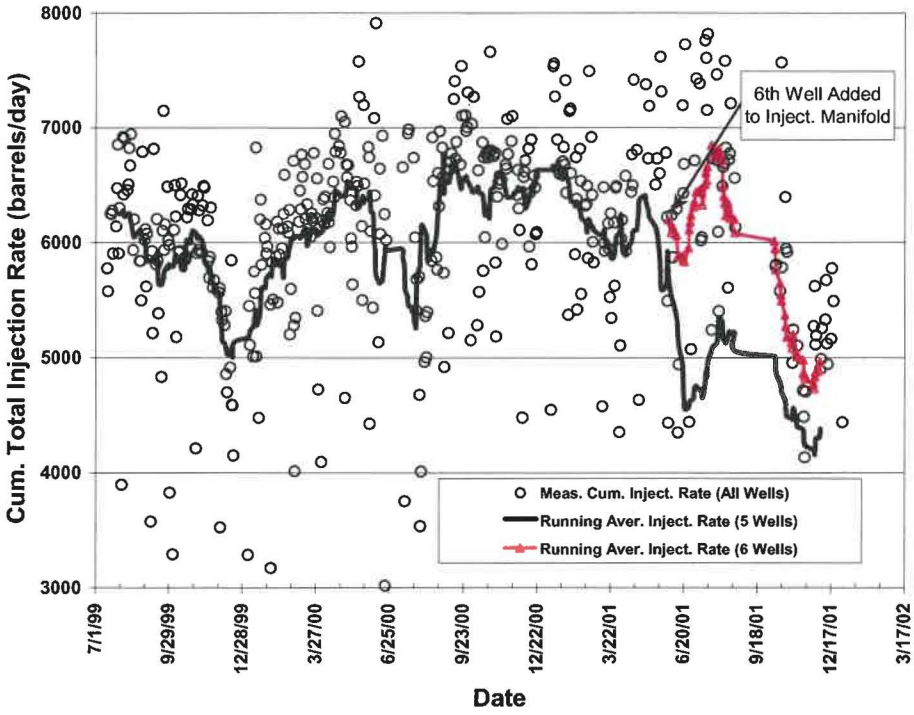

Figure 4. History of Cumulative Daily Injection Rates for Injection Wells Located Near the H-9 Hydropad

Meteorological Monitoring at the H-7 and H-9 Hydropads

Although the WIPP site boundary comprises only 16 square miles, the WIPP well monitoring network encompasses an area of approximately 250 square miles. Weather patterns within this relatively large area can produce significant variability in precipitation on a local scale. Precipitation recharge has been postulated as a possible mechanism to explain changes in Culebra water levels so measurement of precipitation at or near individual monitoring wells is necessary to determine if such a mechanism is important. The H-7 and H-9 hydropads are two monitoring locations considered to be good candidates for testing the precipitation recharge postulate; however, the nearest meteorological station to the H-7 and H-9 hydropads is located at the WIPP site, approximately 5 miles and 8 miles from the H-7 and H-9 hydropads, respectively. Therefore, both the H-7 and H-9 hydropads have been instrumented with stand-alone, remote tip-bucket rain gauges and data loggers to record precipitation directly at the hydropads. The H-9 hydropad was instrumented in late February 2000, while the H-7 hydropad was instrumented in mid-May 2001.

Monthly precipitation totals measured at the H-9 hydropad from March 2000 through December 2001 are shown in Figure 5. Precipitation at this site is highly variable ranging from 0 to more than 5 inches/month. Monthly precipitation totals measured at the H-7 hydropad from June 2001 through December 2001 are shown in Figure 6 and range from near 0 to approximately 2.2 inches/month. For comparison, the differences in monthly precipitation totals at the two sites range from approximately 5 to 50 percent.

Information Only

Precipitation measurements will be continued at least through the next reporting period.

Continuous Water Level Monitoring in Selected Wells Completed to the Culebra Member of the Rustler Formation and the Bell Canyon Formation

At present, WTS measures the water levels in the WIPP monitoring wells on a monthly basis using manually-operated water level sounder tapes. Although this frequency is adequate for assessing the long-term regional changes in water levels, it does not necessarily give the resolution required to evaluate the effects of short-term transients (e.g., injection, precipitation, etc) on water levels in specific wells. Therefore, submersible trolls[2] have been placed in some monitoring wells to record, on a more or less continuous basis, the water levels in the Bell Canyon Formation and the Culebra Member of the Rustler Formation. Rather than measuring freshwater head, each troll actually measures the pressure induced by the column of water in the well that rises above the sensing element of the instrument. Head is then inferred from the measured pressure using appropriate values for water density as described by Jepsen [2000]. The data-logging interval for the trolls is currently 45 minutes; however, the database developed to hold the measurements imports the raw troll data using a six-hour interval so that each record is more manageable and can hold a 30-year history in a single file.

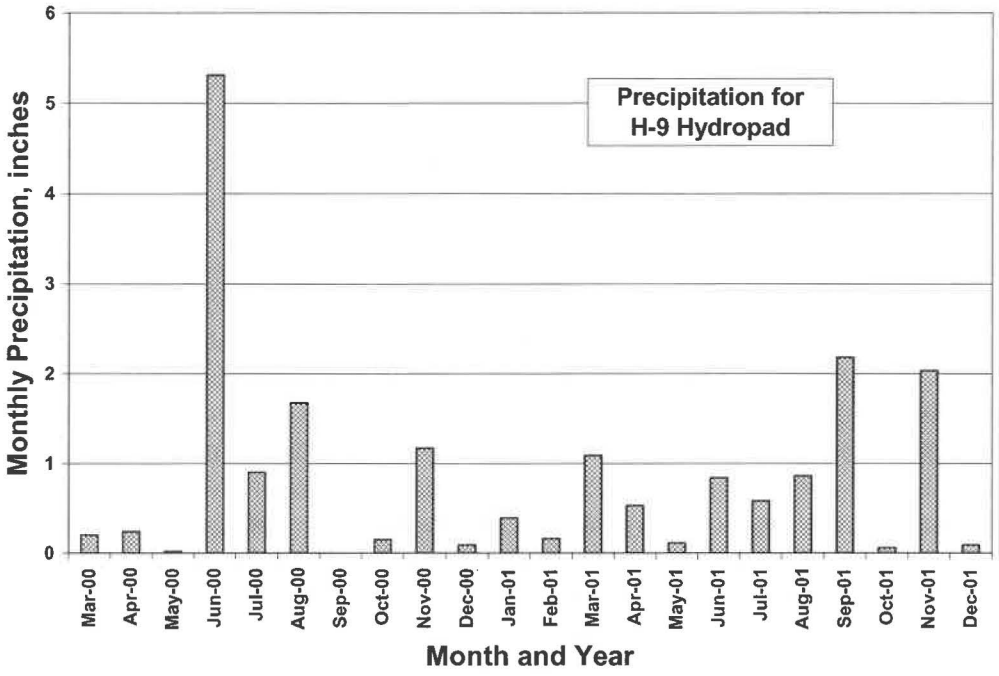

Figure 5. Monthly Precipitation Totals for the H-9 Hydropad.

[2] A troll is an electronic transducer that is positioned below the water level in a well and measures the fluid pressure of the column of water standing above the transducer.

Information Only

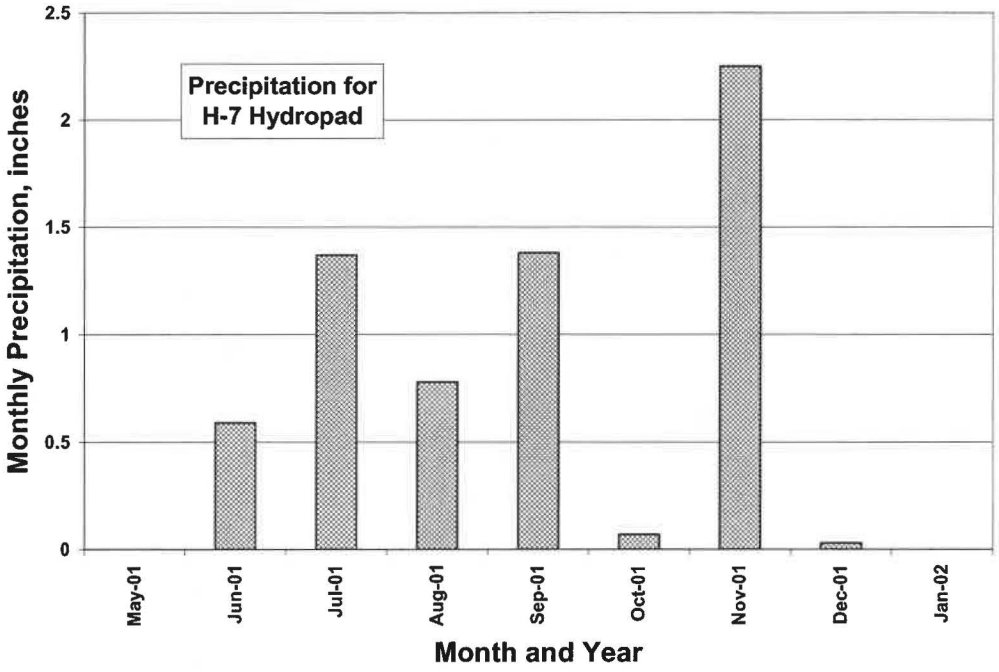

Figure 6. Monthly Precipitation Totals for the H-7 Hydropad.

In 1999, trolls were placed in six wells including four wells completed to the Culebra, i.e., H-9, P-17, WIPP-13, and WIPP-30, and two wells completed to the Bell Canyon, i.e., AEC-8 and Cabin Baby-1. In March 2001, the troll used to monitor the Culebra water levels in WIPP-13 was moved to monitor Culebra water levels in Well H-7b1. Troll measurements for these seven wells are shown in Figures 7 through 13.

The troll measurements are expressed as head above the current position of the troll. Head for each well is calculated from the measured troll pressure and a constant water density of 1.0 gram per cubic centimeter rather than the actual density of the water in each well. In future calculations, freshwater heads will be determined using well-specific water densities based on values determined from ongoing pressure-density (P-D) surveys being conducted by WTS. The gaps in time and the vertical offsets in heads shown in some of the troll data of Figures 7 through 13 occur, respectively, either when a troll is removed for calibration or some specific well activity (e.g., P-D surveys) or when a troll is re-positioned to ensure that a positive hydraulic pressure is maintained on the troll throughout the monitoring period.

In addition to the troll data described above, water level elevations (above mean sea level, amsl) determined by WTS from monthly surveys are also shown in Figures 7 through 13. The water levels shown for the Culebra wells have been adjusted to freshwater elevation heads by WTS using historical values for water density. In contrast, the water level elevations shown for the Bell Canyon wells have not been corrected for water density because historical density data are not available for these wells.

Information Only

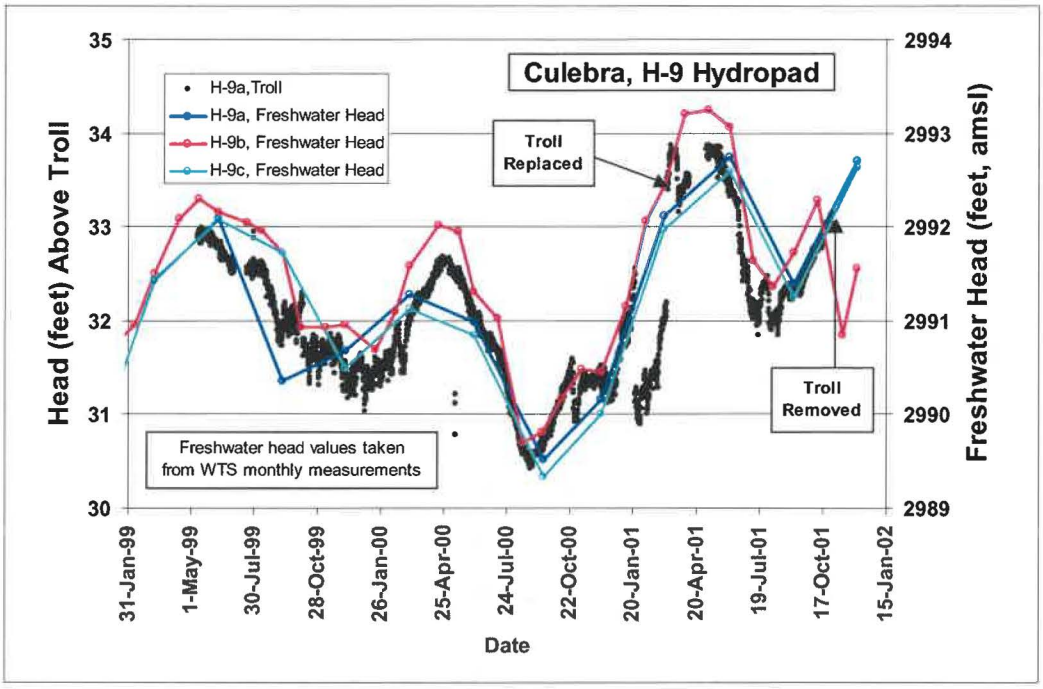

Figure 7. Culebra Head Levels Measured at the H-9 Hydropad.

The H-9 hydropad comprises three wells (H-9a, H-9b, and H-9c) that are configured in a pattern that approximates an equilateral triangle. The wells are located at the vertices of the triangle with a nominal horizontal spacing between wells of 100 feet. The Culebra head levels shown in Figure 7 are measured quarterly in H-9a and H-9c using a sounder tape, monthly in H-9b also using a sounder tape, and continuously in H-9a using trolls. The water levels in the three wells appear to be somewhat cyclical with a peak-to-valley difference of 3 to 4 feet. In general, the troll measurements are in good agreement with the WTS manual water level measurements, particularly for the higher frequency monthly readings. The gap in troll data in early July 1999 was caused by the temporary removal of the troll during well clean-out and Colloidal Borescope work.

The Culebra water levels measured in P-17 (Figure 8) show a one-foot linear rise over the period May 1999 through December 2001. The troll measurements and the WTS manual measurements compared well during this monitoring period with two exceptions. During December 1999 to January 2000, the troll recorded a drop of six feet in the Culebra water level of P-17 in comparison to the constant water levels measured by WTS during this same time. The difference in measurements was attributed to a malfunction in the troll, which was subsequently replaced in March 2000. During October 2000 to January 2001, the WTS measurements showed a two-foot perturbation, while the troll measurements indicated no change in water levels. No explanation for this difference is currently available. The troll was replaced again in April 2001 as indicated by the small offset in the troll data on this date.

Information Only

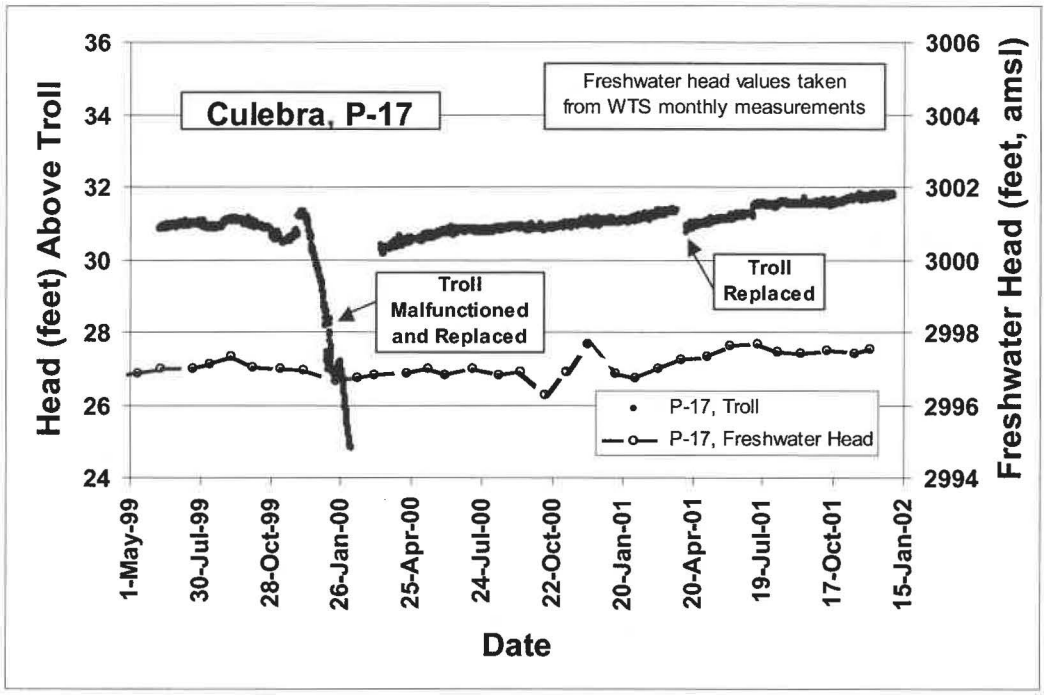

Figure 8. Culebra Heal Levels Measured at Well P-17.

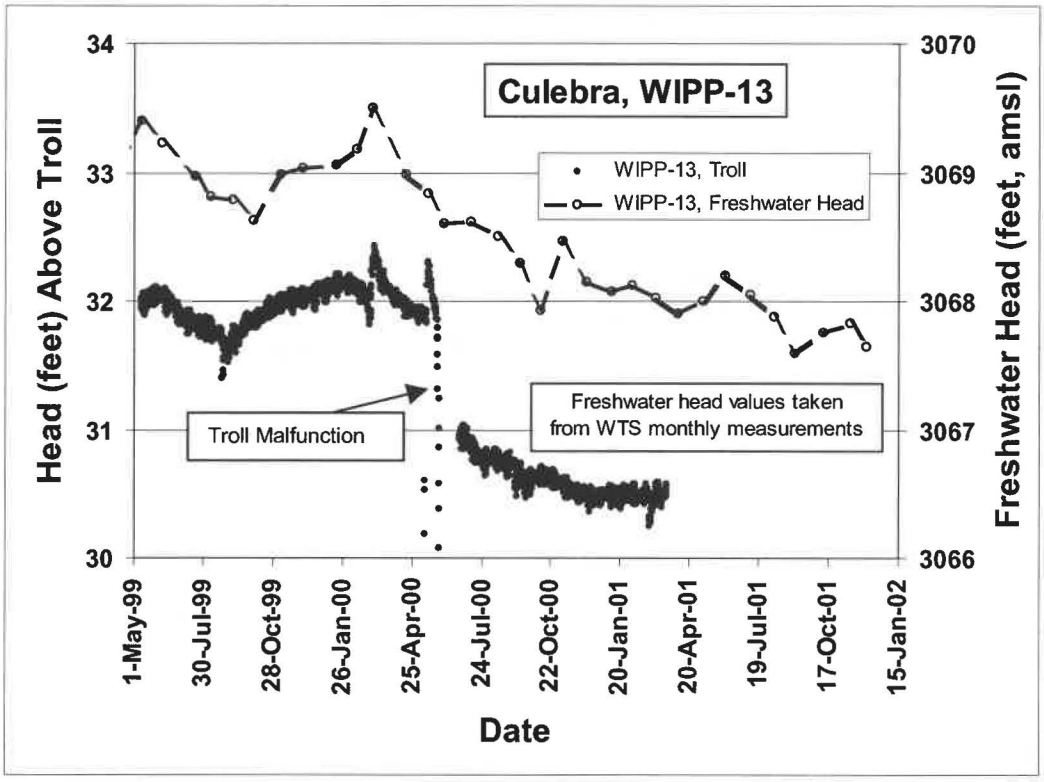

Figure 9. Culebra Head Levels Measured at Well WIPP-13.

Information Only

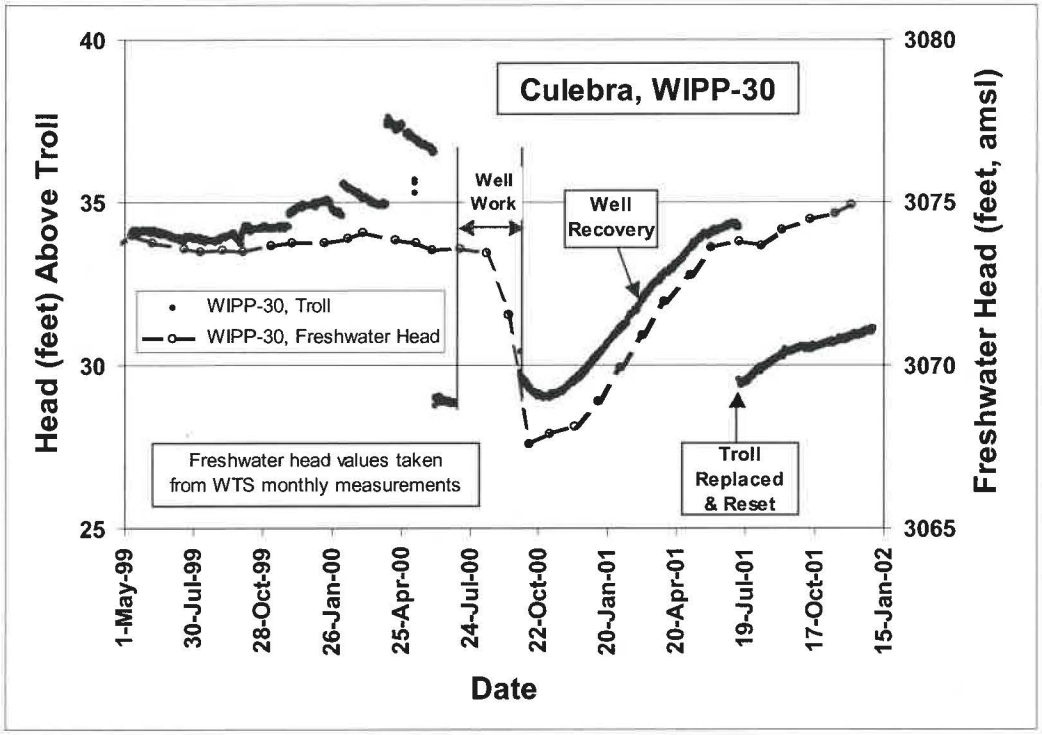

Figure 10. Culebra Head Levels Measured at Well WIPP-30.

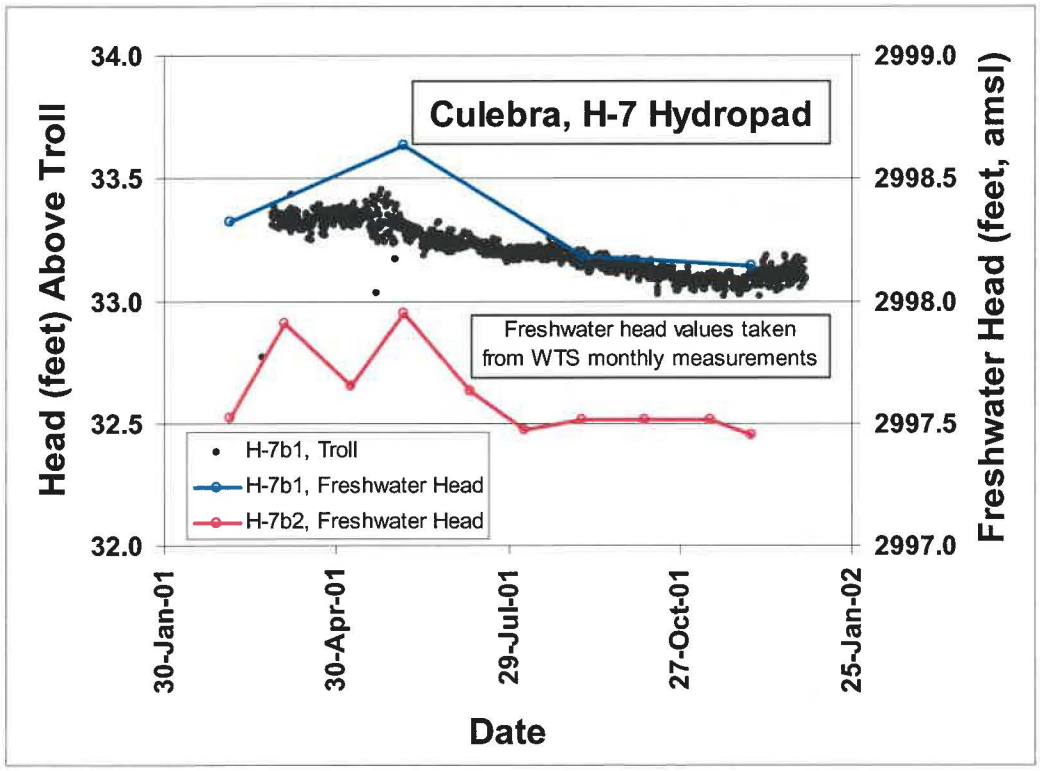

Figure 11. Culebra Head Levels Measured at the H-7 Hydropad.

Information Only

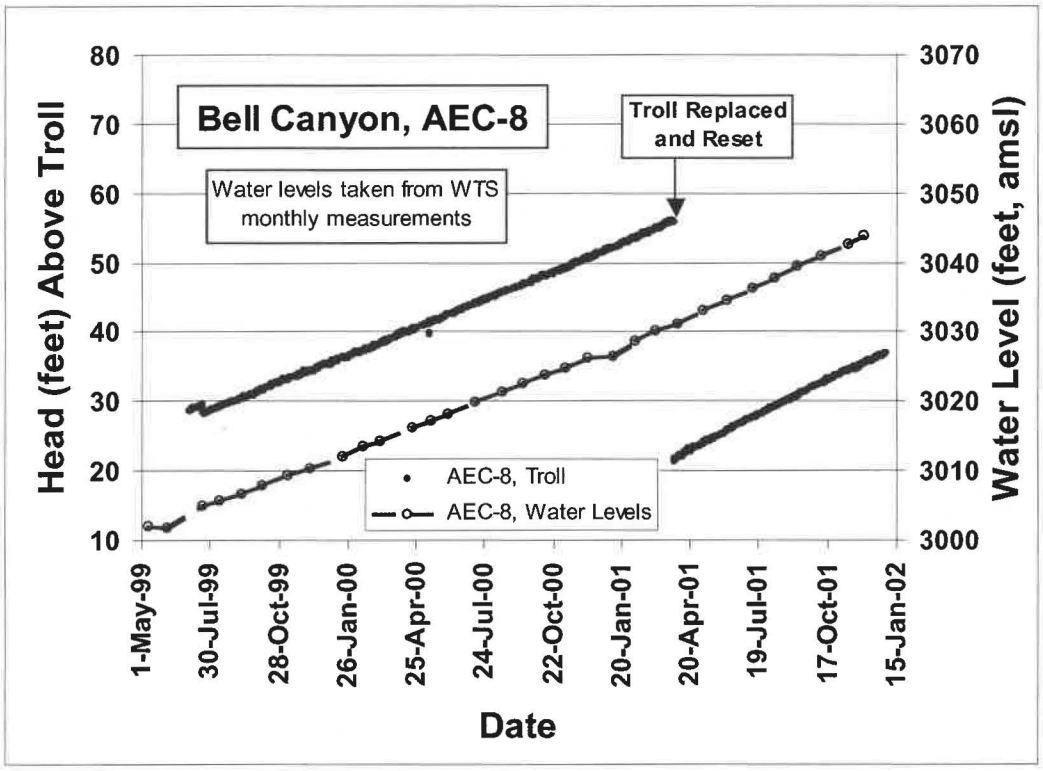

Figure 12. Bell Canyon Head Levels Measured at Well AEC-8.

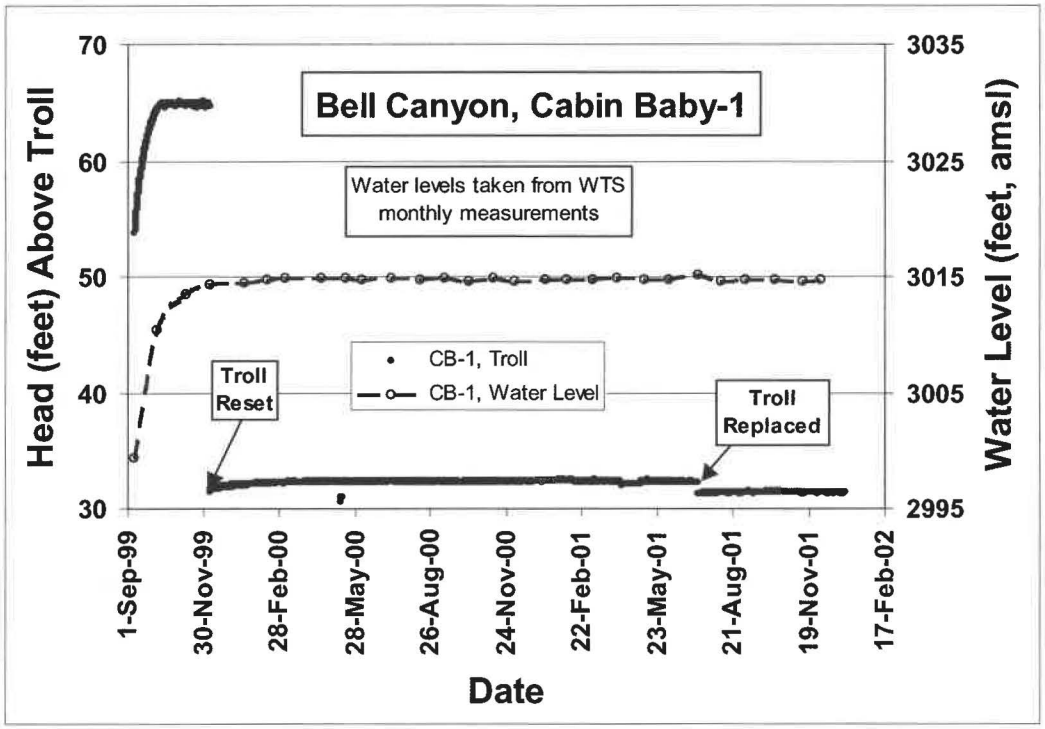

Figure 13. Bell Canyon Head Levels Measured at Well Cabin Baby-1.

Information Only

The Culebra water levels measured in WIPP-13 (Figure 9) show a 1- to 1.5-foot linear drop over the period May 1999 through December 2001. The troll measurements and the WTS manual measurements compared well during this monitoring period except in May 2000 when the troll indicated a 2-ft drop in water levels, while the manual measurements indicated constant water levels. The drop in the troll water levels was attributed to a malfunction in the troll. Given the limited number of trolls available for monitoring, troll measurements of Culebra water levels in WIPP-13 were discontinued in March 2001 so that the troll could be moved to H-7b1. H-7b1 is thought to be a better site for investigating the possible hydrological connection between water levels and rainfall because of its location in Nash Draw.

The troll measurements of Culebra water levels in WIPP-30 (Figure 10) were generally constant from May 1999 through January 2000. In early 2000, the troll was repositioned several times accounting for the offsets in the data. The troll was removed completely in July 2000 to allow for well work by WTS. Therefore, no troll data were acquired during July and August 2000. When the troll was returned to the well in September 2000, water levels rose rapidly in response to recovery from the well work and continue to rise at a rate of about 0.25 feet/month. The troll measurements and the WTS manual measurements compare well throughout the monitoring period. The WTS manual measurements indicate the Culebra water level in WIPP-30 is currently about 1-ft higher than the water levels measured immediately before the well work was initiated.

The troll measurements of Culebra water levels in H-7b1 were initiated in May 2001 using the troll removed from WIPP-13. These troll measurements, together with manual water level measurements made by WTS in H-7b1 and H-7b2, are shown in Figure 11. H-7b1 and H-7b2 are two of the four wells located at the H-7 hydropad and are separated horizontally by approximately 100 feet. The four wells are configured in a diamond pattern with wells located at the corners. The other wells at the H-7 hydropad are H-7a and H-7c. Neither of these wells is currently used for monitoring water levels. Since May 2001, the Culebra head levels have dropped steadily by about 0.5 feet. The WTS manual water level measurements made in H-7b1 and H-7b2 are more variable than the troll measurements, but do indicate the same downward trend exhibited by the troll data.

The Bell Canyon water levels measured in Cabin Baby-1 (Figure 12) and AEC-8 (Figure 13) show contrasting trends over the May 1999 through December 2001 monitoring period. Although the Bell Canyon water level in Cabin Baby-1 rose initially in response to recovery from previous well work, it has been stable for more than 2 years at a level of 3015 feet, amsl. At AEC-8, the Bell Canyon water level has risen steadily at a rate of about 1.6 feet/month or more than a 40-foot rise since the monitoring was initiated. At the end of December 2001, the Bell Canyon water level in AEC-8 was approximately, 3044 feet, amsl. The water levels measured using the trolls are in good agreement with the manual water level measurements made in both wells except for the large offsets in head attributable to re-positioning of the troll.

The continuous monitoring of water levels in the Culebra and Bell Canyon using trolls will be maintained at least through the next reporting period. Troll data will be compared with direct measurements of water levels to evaluate the long-term performance of the trolls and will be converted to true freshwater elevation heads when well specific-density data become available.

Information Only

Development of a Magenta Hydrological Flow Model

Previous hydrological and transport calculations for the CCA have shown that the consequences of a release of radionuclides to the Magenta are less severe than the consequences of a release to the Culebra. Therefore, most early studies concentrated on hydrological characterization and groundwater monitoring of the Culebra. Recently however, some of the focus has returned to the Magenta and activities are planned and currently under way to develop a groundwater flow model for the Magenta to understand better the hydrology in the region. An added benefit of the development of a Magenta flow model is that the flow model can be used to analyze the effects of potential leakage from the Magenta to the Culebra, an occurrence that may account for some of the change in the water levels of the Culebra.

The development of the Magenta flow model requires a variety of spatial and temporal hydrological data for the Magenta including depth and thickness, transmissivity, storativity, hydraulic head, and fluid density. Depth and thickness have been well characterized through the drilling of approximately 100 wells and exploratory holes under previous studies; however, the other properties are not well established. Therefore, a plan for collecting additional hydrological data has been developed and implemented [Beauheim, 2000]. The plan calls for the following activities:

- Recompletion of up to eleven wells to the Magenta
- Water quality/density measurements
- Selective slug tests and/or drill stem tests
- Selective pump tests
- Long-term water level monitoring

In addition to these activities, water level data from wells already completed to the Magenta are being assembled to supplement the data expected from the recompleted wells. To date, the Magenta well recompletion activity has been initiated and historical water level data from nine existing Magenta wells have been assembled.

The development of a Magenta flow model requires, among other activities, the recompletion of wells to the Magenta Member of the Rustler Formation so that water levels can be monitored and hydrological tests can be performed. Recompletion is being considered for 11 wells selected because they are in locations where Magenta data are currently lacking. For some of these wells, data on hydraulic head are particularly important (e.g., DOE-2, H-11b2, H-15, P-15), while in other wells (e.g., H-18 and WIPP-18), data on transmissivity are of primary importance. For completeness however, hydraulic-head, transmissivity, and fluid-density data are likely to be collected from all locations. The 11 wells considered for recompletion are shown in Figure 1.

Recompletion of the 11 wells is scheduled to occur in 2 phases. In the first phase, the six wells considered most important for the model development (i.e., DOE-2, H-18, H-15, H-11b2, P-15, and WIPP-18) will be recompleted and instrumented to collect pertinent data. These data will be evaluated to determine whether the database is adequate for construction of a reliable Magenta model, or whether additional data are needed from some or all of the remaining five wells (i.e., WIPP-13, H-14, DOE-1, ERDA-9, and H-

Information Only

17). If additional data are required, recompletion of the remaining five wells will occur during the second phase of the effort. The Magenta model will then be developed and used to assess water leakage from the Magenta to the Culebra.

Early in 2001, six wells were recompleted to the Magenta during the first phase of this activity including Wells DOE-2, H-11b2, H-14, H-15, H-18, and WIPP-18. Recompletion of Well P-15 rather than Well H-14 was scheduled for the first phase of the activity; however, while attempting to set the bridge plug in Well P-15, scale build-up in the casing was so extensive that the plug could not be positioned properly. The well casing was subsequently scraped to remove the scale, but the scraping revealed a hole in the casing near the ground surface. As a result, recompletion activities for Well P-15 were abandoned in favor of Well H-14.

Following the bailing of the recompleted wells under Phase I, water level recovery in each of the six wells was measured using both a sounder tape referenced to the top of casing and a submersible troll. The water levels measured using the tape are plotted in Figure 14, which shows the recovery responses for all six wells. Sounder tape and troll data for individual wells are presented in Figures 15 through 20.

The water level in DOE-2 (Figure 15) has shown a steady rise of 1.2 feet/month since October 2001 and is currently at 3,060 feet, amsl. The Magenta wells nearest to DOE-2 are H-5c and H-6c (Figure 1). The current water levels in these wells are 3,157 feet (amsl) and 3,065 feet (amsl), respectively so, by interpolation, the steady-state water levels at DOE-2 are expected to be about 3,110 feet (amsl). Therefore, the water level in DOE-2 is not currently at its steady-state value and will likely continue to rise over time.

Following the bailing of WIPP-18, the water level in the well (Figure 16) recovered to a steady value of 3,140 feet (amsl). In July 2001, the water level began to drop at a steady rate of approximately 6 feet/month and is currently 3,112 feet (amsl). The bridge plug placed between the Magenta and Culebra is presumed to be leaking allowing water from the Magenta to enter the Culebra. If water from the Magenta is entering the Culebra at this location, water levels in Culebra wells near WIPP-18 should be rising. To confirm this hypothesis, the water level history for Culebra well WIPP-19 (nearest to WIPP-18) was examined and showed that the Culebra water level has risen approximately 1 foot during the period when the water level in WIPP-18 was falling. Sandia has recommended to WTS that Well WIPP-18 be added to the well logging priority list. During logging, the bridge plug will be removed and eventually re-seated and well casing integrity will be examined.

Information Only

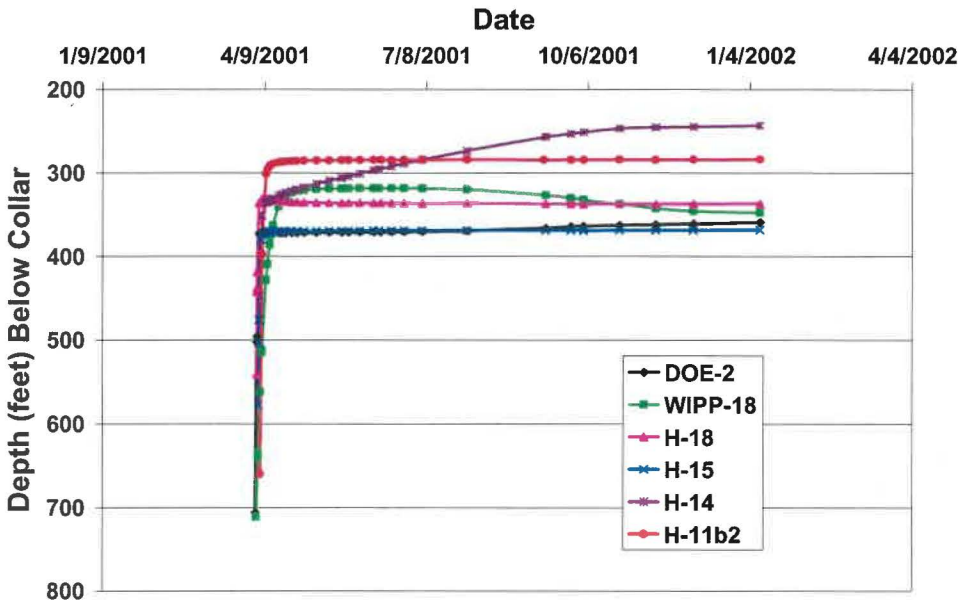

Figure 14. Water Level Recovery for Bailed Wells Recompleted to the Magenta.

The Magenta water level in Well H-18 (Figure 17) reached a peak shortly after the well was bailed, then monotonically decreased to a constant value of 3,077 feet (amsl). The current Magenta water level in H-18 is comparable to the water level in the Culebra at this location even though the Magenta water level was expected to be approximately 100 feet higher. Because of this deviation from expected conditions, Sandia has recommended to WTS that H-18 be added to the well logging list so that the integrity of the well can be determined.

The Magenta water level in Well H-15 (Figure 18) has stabilized at approximately 3,113 feet (amsl). The current water level is consistent with other wells completed to the Magenta in this location (e.g., H-2, H-3, and H-5) and is approximately 100 feet higher than the water levels at adjacent Culebra wells consistent with previous knowledge about the hydraulic gradient between the Magenta and Culebra. Because data collected to date indicate the Magenta water levels in H-15 are representative of the site conditions, Sandia has recommended to WTS that the final development of the well be completed so that Sandia can initiate its well testing activities.

From April 2001 through October 2001, the Magenta water levels in Well H-14 rose steadily at a rate of approximately 15 feet/month (Figure 19). Since November 1, 2001, the water level rise has slowed considerably (1 foot/month) indicating well recovery is nearly complete. The stabilized water level is expected to be between 3,100 and 3,120 feet (amsl), a range consistent with previous hydrological knowledge. Because data collected to date indicate the Magenta water levels in H-14 are representative of the site conditions, Sandia has recommended to WTS that the final development of the well be completed so that Sandia can initiate its well testing activities.

Information Only

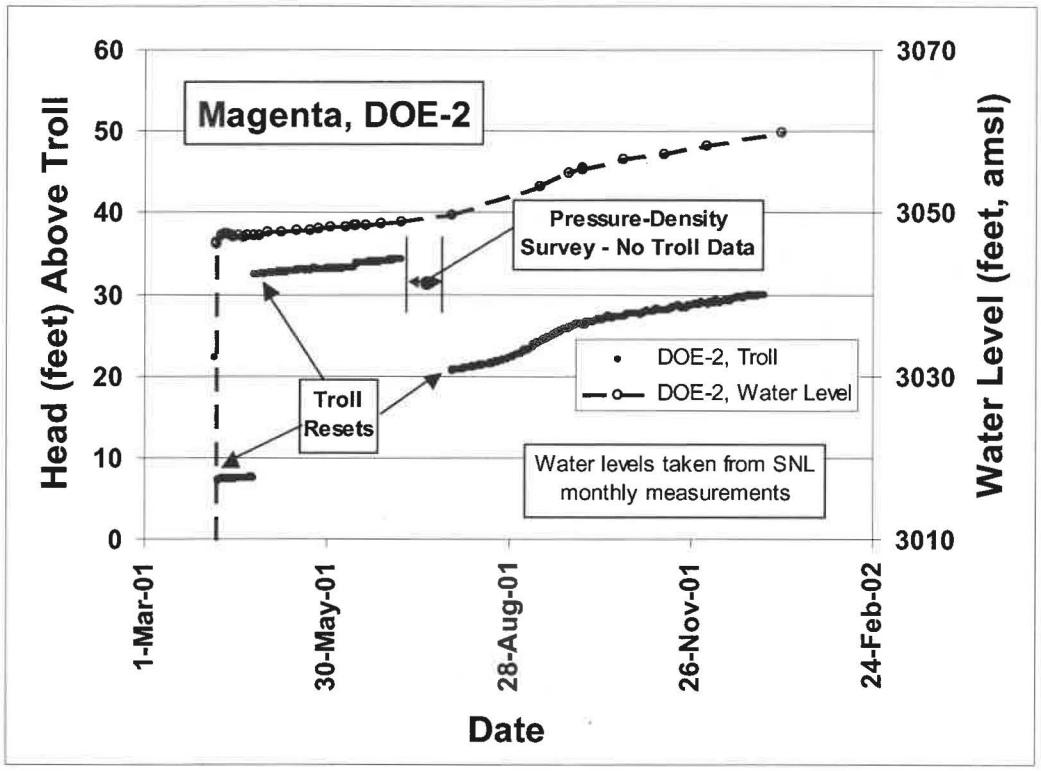

Figure 15. Magenta Head Levels Measured at DOE-2.

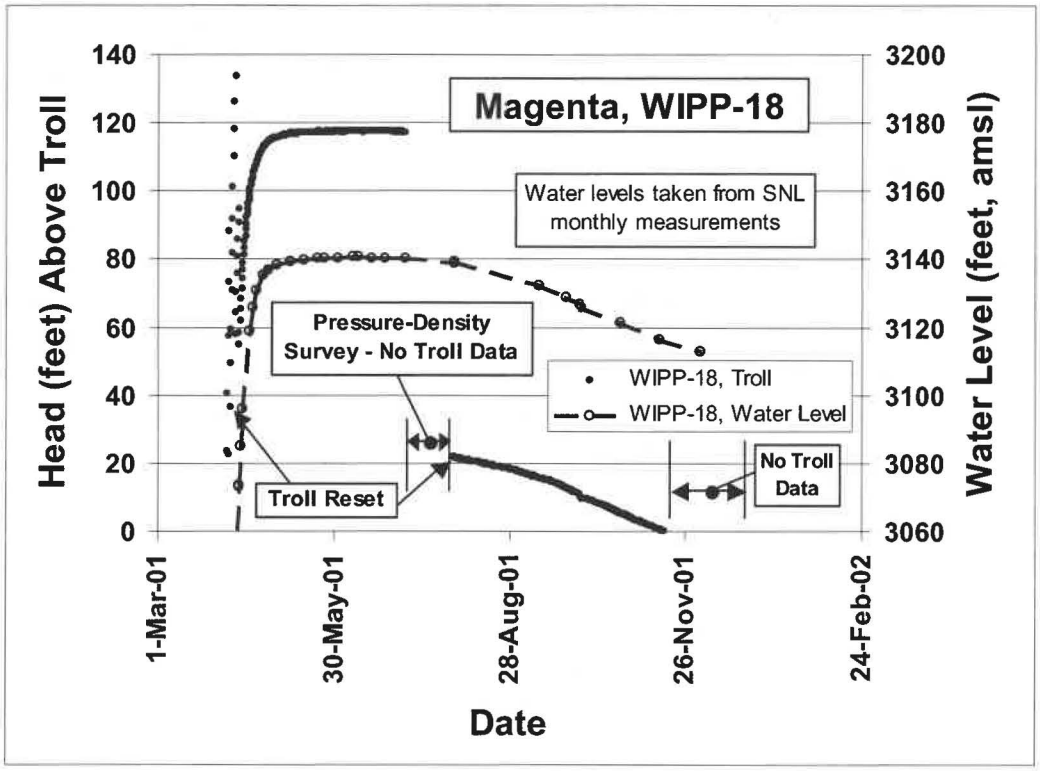

Figure 16. Magenta Head Levels Measured at WIPP-18.

Information Only

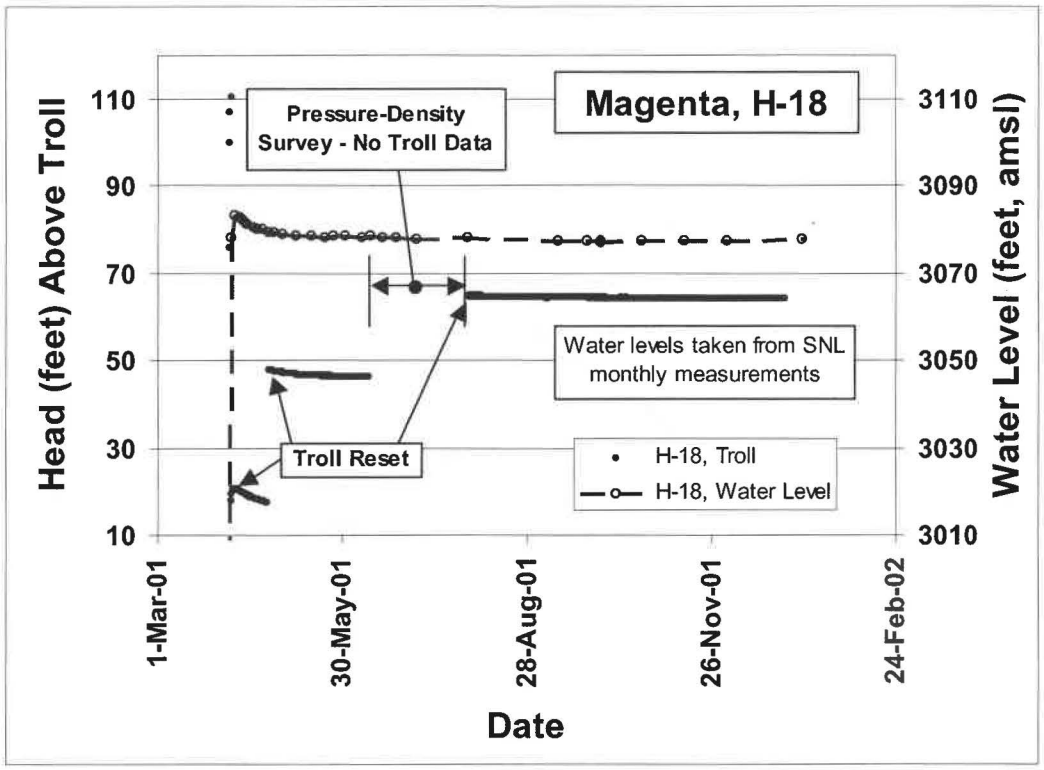

Figure 17. Magenta Head Levels Measured at H-18.

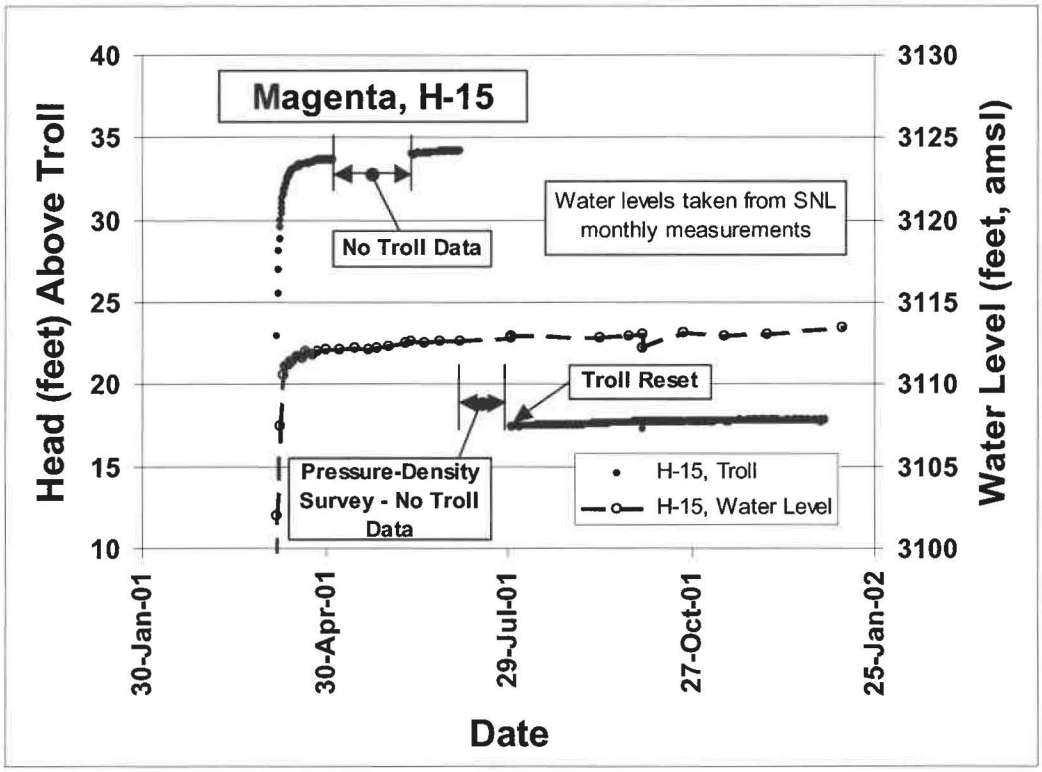

Figure 18. Magenta Head Levels Measured at H-15.

Information Only

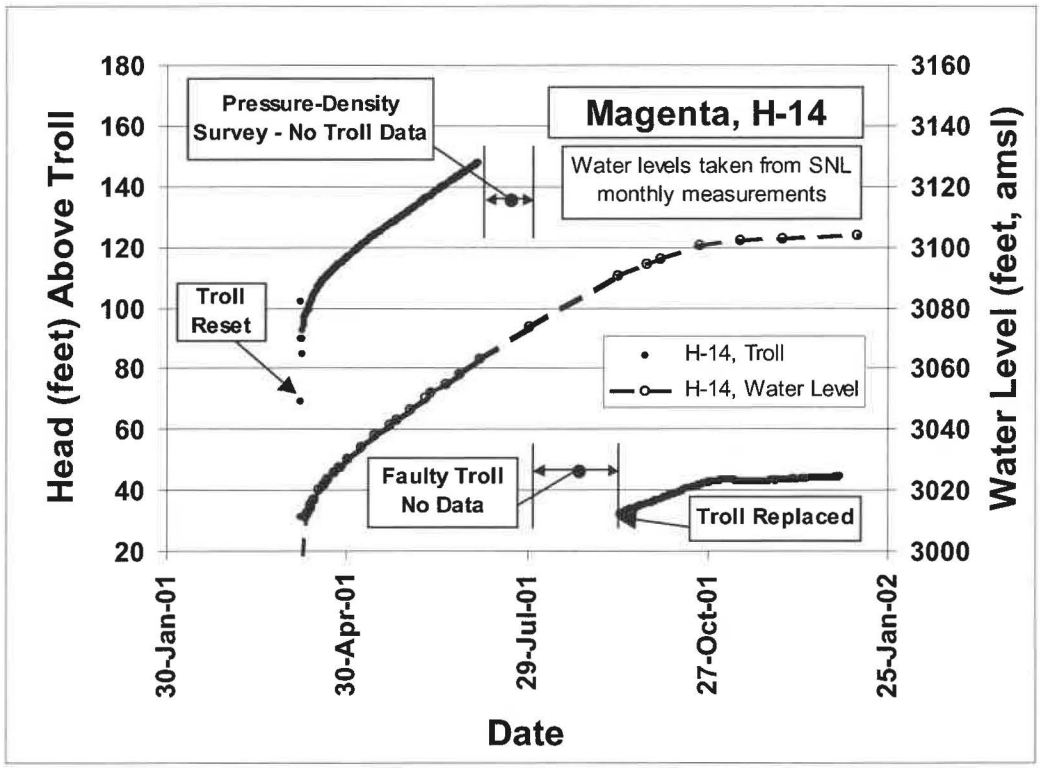

Figure 19. Magenta Head Levels Measured at H-14.

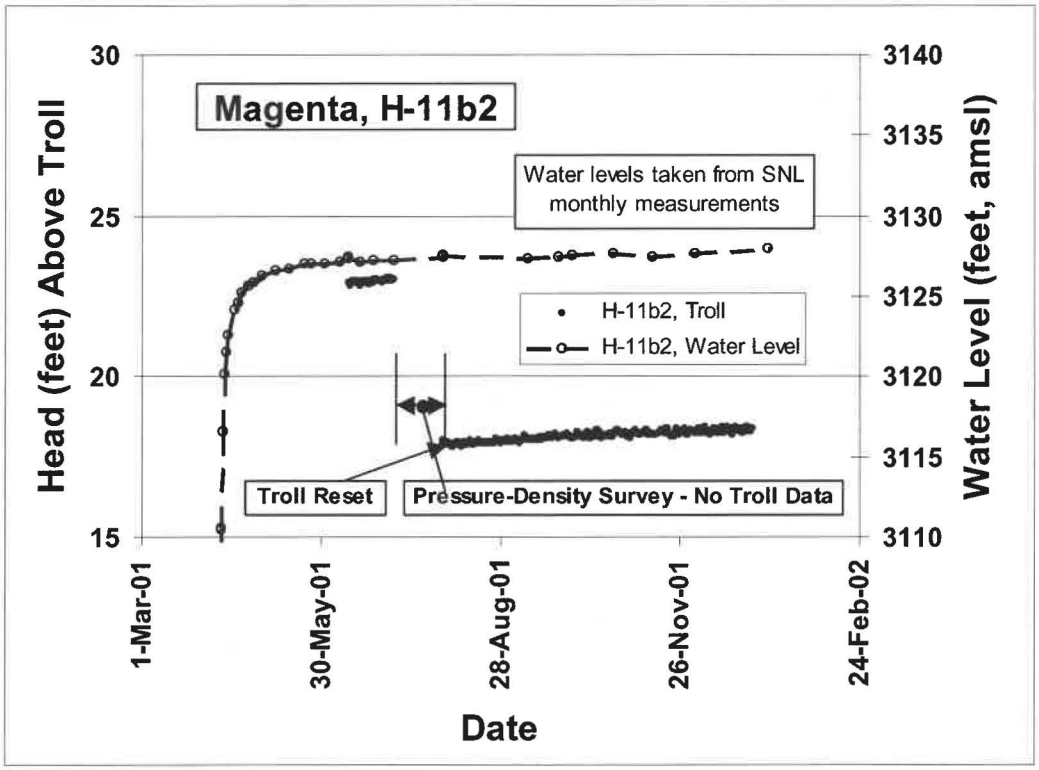

Figure 20. Magenta Head Levels Measured at H-11b2.

Information Only

Magenta water levels in Well H-11b2 recovered quickly after the bailing activity and have increased less than 1 foot from July 2001 to December 2001 (Figure 20). The current water level is 3,128 feet (amsl), a value consistent with previous hydrological knowledge at this location. Because data collected to date indicate the Magenta water levels in H-11b2 are representative of the site conditions, Sandia has recommended to WTS that the final development of the well be completed so that Sandia can initiate its well testing activities.

Collection of Field and Drill Hole Information

Field and drill hole information is being collected to aid in the interpretation of the hydrological data collected to date or to be collected under this investigation. Specific information includes:

- Compilation of events that could affect water levels in the Rustler Formation monitoring wells
- Surface geological studies
- Aerial photographic records.

Compilation of events includes logging the types of events (e.g., well tests, shaft sinkings), physical locations of each event, type of data available for each event (e.g., pumping rates, water volume estimates), and begin and end dates for each event. More than 900 events that could affect Culebra water levels have been identified and will eventually be compared to hydrographs for individual wells. Events that could affect Magenta water levels have yet to be identified.

Karst, natural subsidence, and mining-induce subsidence may affect recharge/discharge into and out of the Rustler formation. Surface geological studies are being conducted to collect evidence for these types of phenomena. The studies include the review of information available from highway alignment projects near the WIPP site, ground-truth field surveillances in and near the WIPP site boundary, and previous WIPP surface geological investigations.

Historical changes in site topography are also being investigated through a review of existing aerial photography and limited new aerial photography to be acquired under this investigation. The primary use of these records is to identify changes both in drainage and in drainage patterns caused by karst and subsidence phenomena. Photographic coverage of the site is not fully complete, but photographs of portions of the site are available from 1957, 1976-1977, 1983, and 1996. The 1957 coverage contains black and white photographs with a scale of 1:40,000 and includes portions of Nash Draw and the WIPP site. The 1976-1977 coverage contains color photographs taken along diagonal (NW to SE) tracks over the WIPP site. Black and white photographs and false color images of the Nash Draw/WIPP site area are also available for 1983. The 1996 coverage includes 1:40,000 scale, overlapping black and white photographs of the Nash Draw/WIPP site that can be viewed with a stereoscope. Only limited low-angle aerial photographic information is available, but is being used to supplement the vertical images.

Information Only

Assessment of Changes in Culebra Water Levels Using Hydrological Models/Analyses

Water-level data from Culebra monitoring wells have been used to produce maps of water-level changes. Net changes in water levels are shown below for 20-, 15-, 10-, and 5-year intervals (Figures 21, 22, 23, and 24, respectively). With few exceptions, water levels have consistently increased over the monitoring period. The increment ranges shown in the legends of each of the figures are currently being discussed to determine what ranges would best convey the varying rates of water-level changes observed around the WIPP site. The results of these discussions will determine the increment ranges displayed in the final versions of these figures. Final versions will also include information about the underlying geology and location of any groundwater divides.

As well-logging activities to determine potential leaks in well casings continue, wells may be removed from the figures if it is believed that the water-level changes do not reflect actual changes in the Culebra water levels.

The large changes in water levels near the center of the land withdrawal area result from shaft construction activities (Figures 22 and 23). Shaft construction activities began in 1981 and ended in 1988. Water levels recover rapidly immediately following construction activities and then decrease exponentially with time. Figure 24 (Net 5-year change) shows that the rates of change near the shafts have decreased relative to the prior 10-year period and are now similar to the rates of change further from the shaft construction activities.

Discussion of Results

Effects of Well Injection on Observed Water Levels at the H-9 Hydropad. A persistent hypothesis for rising water levels in the Culebra is the hydraulic connection between the Culebra and the injection activities conducted by private resource exploration companies. Six injection wells are located in close proximity to the H-9 hydropad. Five of these wells have comparable injection intervals in the Bell Canyon, while the sixth (Pure Gold B F#20) has an injection interval in the Bell Canyon that is approximately 3000 feet deeper. Assuming the five wells with comparable injection intervals can be treated as a point source, the average daily injection rates for all five wells can be summed to yield a cumulative injection rate. The temporal cumulative injection rate can then be compared to the H-9 well heads as shown in Figure 25. During early time (July 1999 through December 2000), the H-9 well heads track the total injection rates reasonably well. However during the last year, the correlation between injection rates and Culebra water levels at H-9 is not nearly as good. The cumulative average daily injection rate for all six wells is also shown in Figure 25 for comparison with the H-9 water levels. As with the five-well data, the correlation with Culebra water levels is not particularly strong. Additional analyses need to be performed and longer-term data need to be acquired to examine better the hydraulic connection.

Information Only

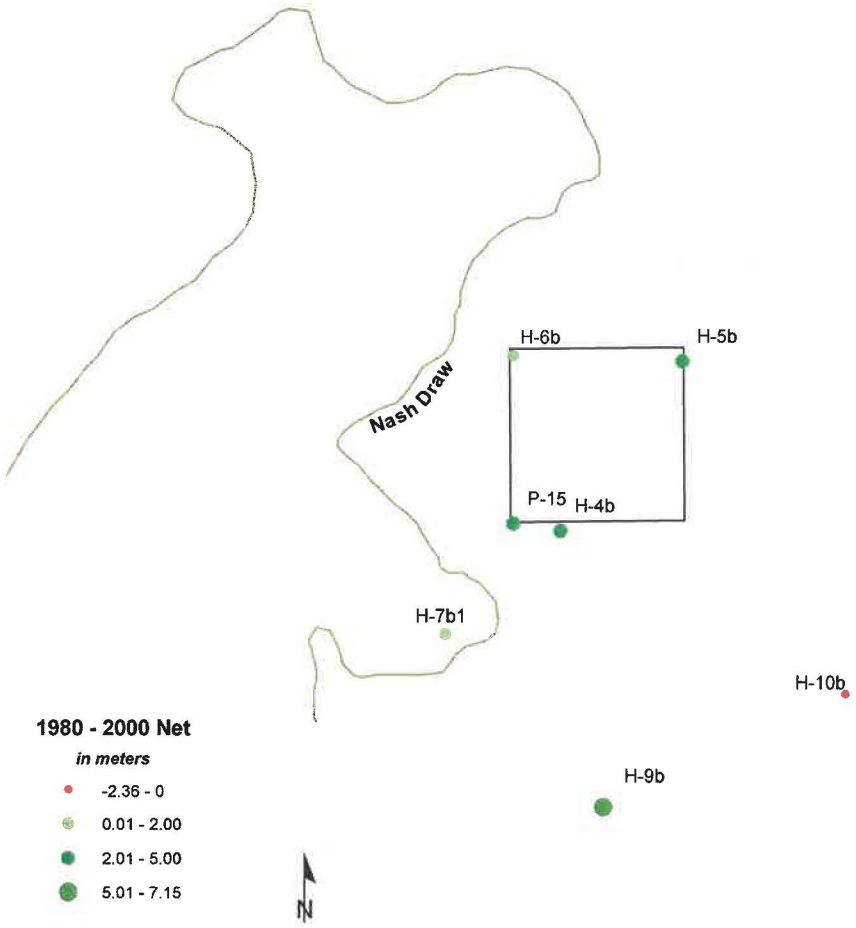

Figure 21. Net 20-Year Changes in Culebra Water Levels.

Information Only

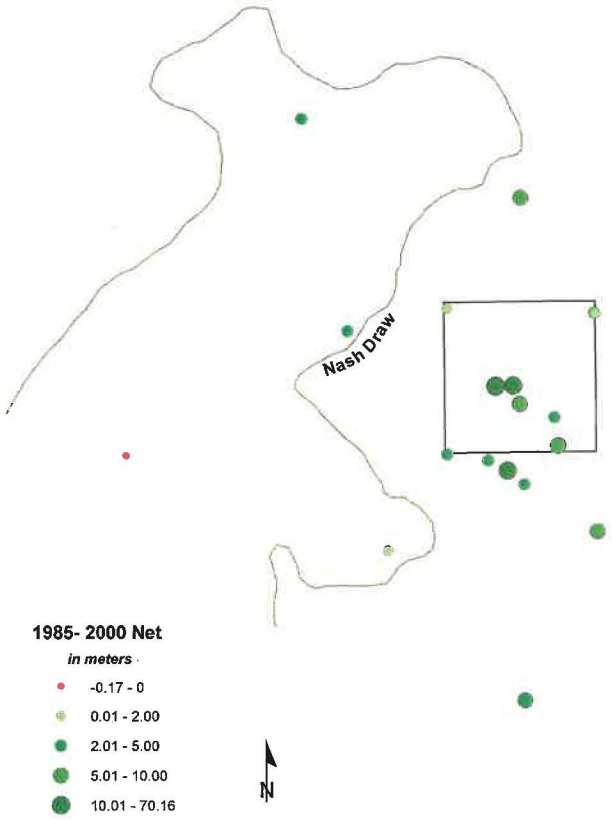

Figure 22. Net 15-Year Changes in Culebra Water Levels.

Information Only

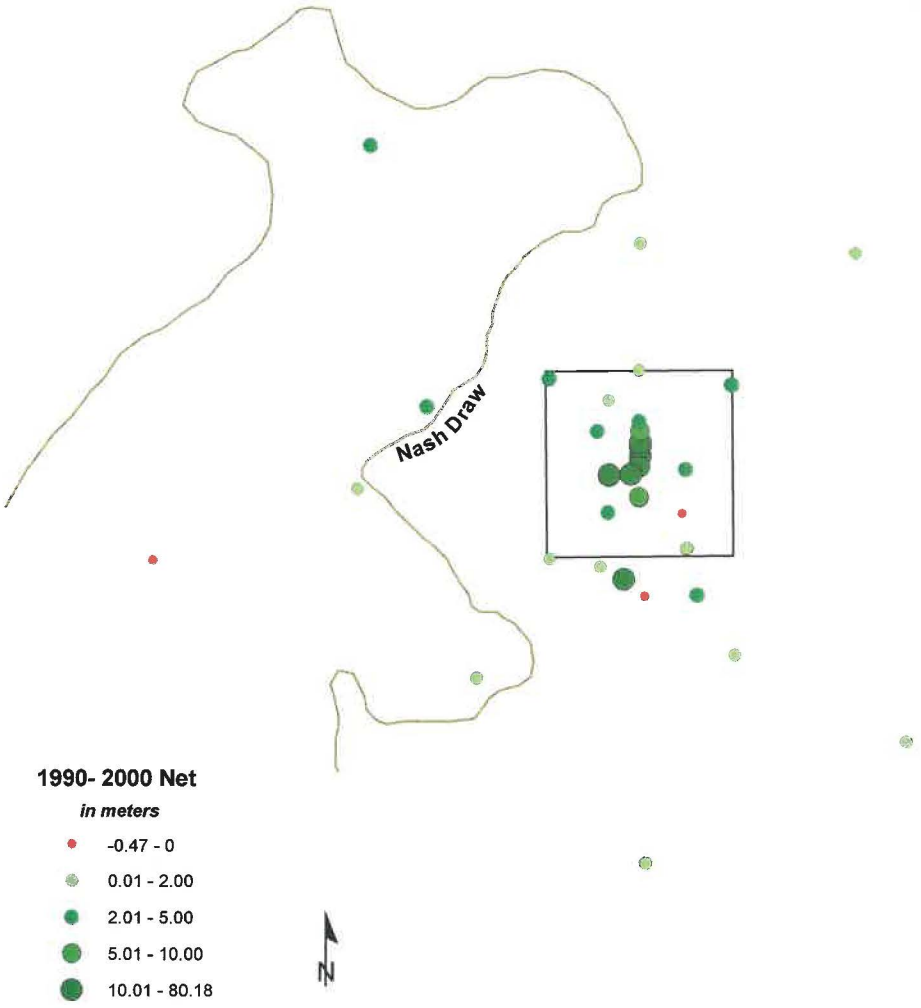

Figure 23. Net 10-Year Changes in Culebra Water Levels.

Information Only

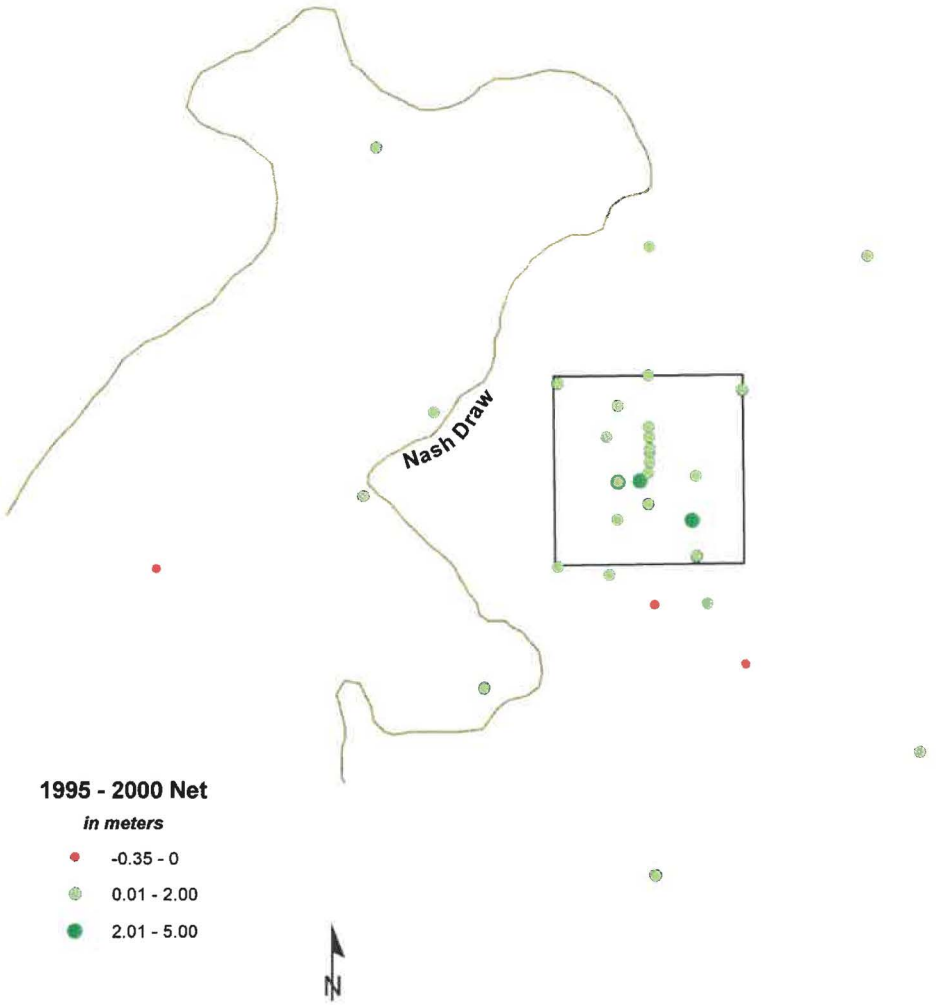

Figure 24. Net 5-Year Changes in Culebra Water Levels.

Information Only

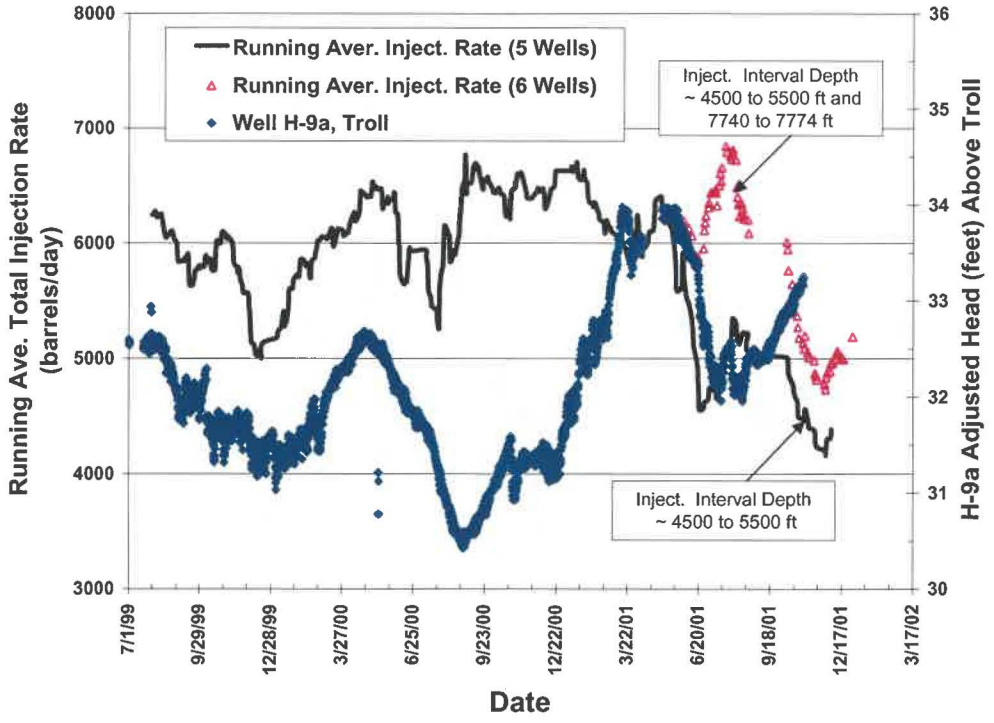

Figure 25. Temporal Comparison of Injection Rates and Culebra Water Levels in Well H-9a.

Effect of Precipitation on Observed Water Levels in H-9. Precipitation may affect the water levels in a nearby well if a hydraulic connection exists between the well and the area where a rainfall event has occurred. Figure 26 plots rainfall events at the H-9 hydropad from January 2000 through December 2001 and head levels at Well H-9a from May 1999 through October 2001. During the time interval the two data sets overlap, no clear correlation exists between rainfall events and head levels. For example, during the relatively high rainfall activity shown in June 2000, the Culebra water levels in Well H-9a are actually decreasing, while during the low rainfall activity shown in November 2000 through February 2001, the water levels in Well H-9 are increasing. Figure 27 plots rainfall events at the H-7 hydropad from May 2001 through December 2001 and head levels at Well H-7b1 from March 2001 through December 2001. Again, there appears to be no clear correlation between rainfall and head levels at H-7b1. The lack of obvious correlation could also mean head levels in the Culebra lag behind the rainfall events. As with the injection data, additional analyses need to be performed and longer-term data need to be acquired to examine better any hydraulic connection that might exist.

Information Only

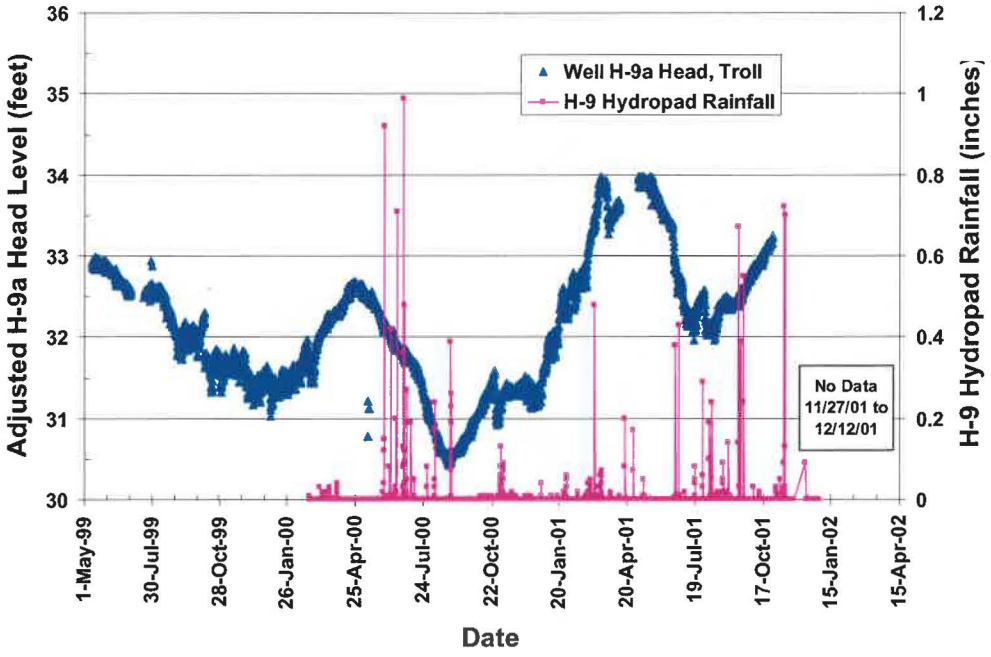

Figure 26. Temporal Comparison of Rainfall Events and Culebra Water Levels at the H-9 Hydropad.

Continuous Water Level Monitoring Measurements. The continuous water level measurements made in various Culebra and Bell Canyon wells using trolls agree well with the manual measurements made using sounder tapes. Therefore, troll use should be continued, particularly at the H-7 and H-9 hydropads, because the higher frequency data obtained with trolls are useful in assessing the effects of localized rainfall and brine injection on water levels.

As discussed during the last reporting period, the water level data for the two Bell Canyon wells (i.e., AEC-8 and Cabin Baby-1) show significantly different trends. The water level in AEC-8 continues to show a steady rise of about 1.7 feet/month, while the water level in Cabin Baby-1 remains relatively constant. Because of the relative positions of these wells around the site (AEC-8 and Cabin Baby-1 are on the north and south sides, respectively), continuous monitoring with trolls should continue here as well.

Information Only

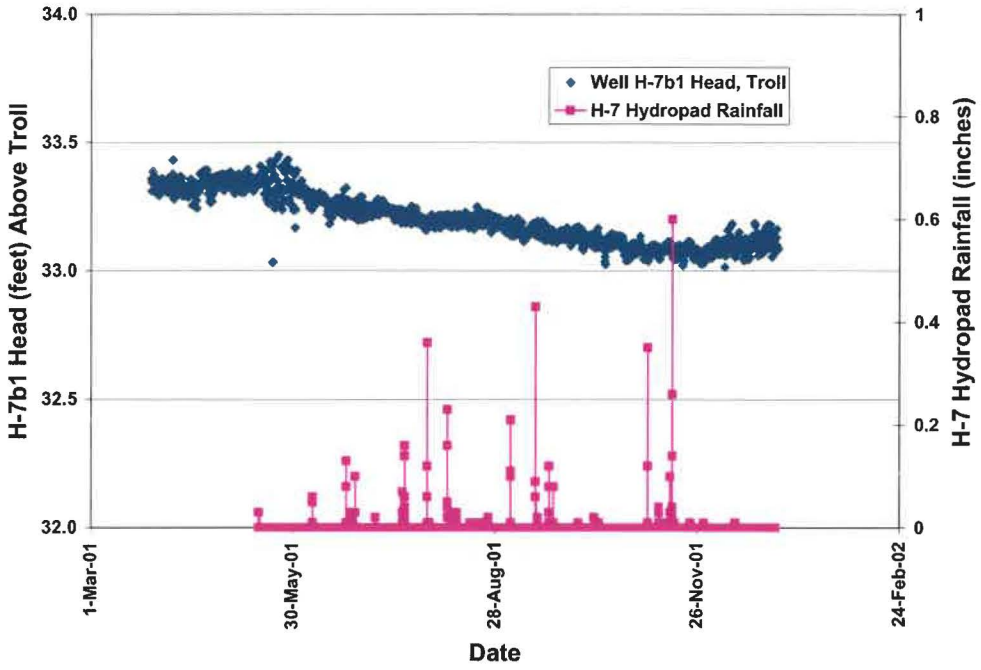

Figure 27. Temporal Comparison of Rainfall Events and Culebra Water Levels at the H-7 Hydropad.

Development of a Magenta Hydrological Flow Model. To date, the only activity performed under this task includes the recompletion of six wells to the Magenta and the subsequent bailing of the wells and monitoring of the water levels to evaluate recovery behavior following bailing. No attempt has been made to estimate hydrological parameters such as transmissivity or storativity because data are not yet available for the specific gravity of the water in each well, a quantity needed to correct water level measurements to fresh-water heads. Following the completion of water quality/density evaluations and subsequent slug and drill stem testing, activities will be initiated to determine hydrological properties for the Magenta.

Monitoring of water levels in the six wells previously recompleted to the Magenta will continue, as appropriate. Well logging and integrity testing of Wells WIPP-18 and H-18 has been recommended to WTS because of questions concerning the data being acquired at these sites. Initiation of well testing in Wells H-15, H-14, and H-11b2 is now possible because these wells have recovered from previous bailing activities. However, well testing cannot begin until the wells are fully developed. Sandia has recommended to WTS that this development be scheduled during the next reporting period. The water levels in DOE-2 are still recovering from the bailing activity so no additional activities other than water level measurements are recommended for this well.

Information Only

Summary and Conclusions

Changes in the Culebra water levels in some WIPP monitoring wells fall outside the range of water levels used in the CCA. Relevant investigations have been initiated to study the changes in observed water levels. Particular investigations initiated include:

- Monitoring of injection well flows and site meteorological conditions
- Use of continuous water level monitoring equipment
- Recompletion of monitoring wells to the Magenta Member of the Rustler Formation as well as the development of a hydrological model for the Magenta
- Collection of field and drill hole evidence relevant to water level changes in the Culebra and Magenta
- Assessment of impacts of various recharge and anthropogenic effects using hydrological modeling/analysis.

Culebra water levels in Well H-9a have been continuously monitored using a troll and have been compared to both injection well data acquired for wells located near the H-9 hydropad and meteorological (rainfall) data acquired with a remote, stand-alone rain gauge and automatic data logger installed near the hydropad. Preliminary analyses suggest the water levels in H-9a are not correlated either to injection rate or rainfall events; however, the current data set is limited because injection and rainfall data have been collected for two years or less. All current monitoring at the H-9 hydropad should be continued to develop a larger database for continued evaluation. Culebra water levels in Well H-7b1 have also been continuously monitored using a troll and have been compared to rainfall data acquired directly at the H-7 hydropad. As with the H-9a data, no correlation between rainfall and water levels at H-7b1 is apparent.

Six wells have been recompleted to the Magenta and have been bailed and instrumented to observe well recovery behavior. To date, three wells (H-15, H-14, and H-11b2) have fully recovered, one well (DOE-2) is still recovering, and two wells (WIPP-18 and H-18) appear to be yielding anomalous water level information. Well testing is recommended for the fully recovered wells, while continued water level monitoring is recommended for the well still recovering. The wells yielding anomalous information should be logged to determine if well integrity is the cause of the anomalous data.

The collection of field and drill hole information has included compilation of events that could affect water levels in the Rustler Formation monitoring wells, surface geological studies, and gathering of historical aerial photographs. More than 900 events have already been identified for the Culebra wells alone. Surface geological studies are being conducted to obtain evidence for karst features and natural and mining-induced subsidence. Partial aerial coverage of the WIPP site and Nash Draw is available for the years 1957, 1976-1977, 1983, and 1996. Additional data will be collected during the next reporting period.

Water level data from Culebra monitoring wells have been used to produce maps of the water level changes. Maps of net changes in water levels are now available for 20-, 15-, 10-, and 5-year intervals. Large net water level changes near the center of the WIPP land withdrawal area are a result of shaft construction activities. Current changes are smaller and are now similar to the changes that are occurring further from the shaft construction activities.

Information Only

References

Beauheim, R. L. 2000. *Compliance Monitoring Program: Recompletion and Testing of Wells for Evaluation of Monitoring Data from the Magenta Member of the Rustler Formation on the WIPP Site*, Sandia National Laboratories Test Plan, TP-00-03.

Jepsen, R. A. 2000. *Groundwater Monitoring Activities: Troll Measurements, Bell Canyon Injection Well Monitoring Near H-9, and Meteorological Monitoring at H-9*, Sandia National Laboratories Test Plan, TP 99-10.

Powers, D.W., 2001. *Examining Culebra Water Levels, Sandia National Laboratories Test Plan TP01-01*, draft.

Sandia National Laboratories, 2000. "Sandia National Laboratories Annual Compliance Monitoring Parameter Assessment," WBS 1.3.5.2.1.1, Pkg. No. 510062, October.

U. S. Department of Energy (DOE), 1999. *40 CFR Parts 191 and 194 Compliance Monitoring Implementation Plan,* Carlsbad Area Office, Carlsbad, NM, April.

U.S. Environmental Protection Agency (EPA), 1998a. *40 CFR Part 194 Criteria for the Certification and Recertification of the Waste Isolation Pilot Plant's Compliance with the Disposal Regulations: Certification Decision; Finale Rule,* Federal Register, Vol. 63, No. 95, p. 27354, May 18, 1998, Washington, D. C.

U.S. Environmental Protection Agency (EPA), 1998b. *Compliance Application Review Documents for the Criteria for the Certification and Recertification of the Waste Isolation Pilot Plant's Compliance with 40 CFR 191 Disposal Regulations: Final Decision,* EPA 402-R-97-013, May 1998, Washington, D. C.

Information Only

Information Only

2.0 Geochemistry

2.1 Microbial Degradation

Re-evaluation of Microbial Gas Generation Under Expected Waste Isolation Pilot Plant Conditions[1]

Data Summary and Progress Report (July 14, 2001 – January 31, 2002)
January 22, 2002

J.B. Gillow and A.J. Francis
Environmental Sciences Department, Brookhaven National Laboratory
Upton, NY 11973

Abstract

Gas generation from the microbial degradation of the organic constituents of transuranic waste under conditions expected at the WIPP repository is being investigated at Brookhaven National Laboratory. This report summarizes progress from the period July 14, 2001 – January 31, 2002. During this period, we analyzed the total gas, carbon dioxide, and methane production; microbial degradation products of cellulose; and the diversity of microbial community in samples incubated under inundated conditions for 9.5 years (3464 days). The total volume of gas produced has leveled-off or diminished in anaerobic inundated cellulose samples with and without bentonite since the last analysis at 2718 days. Carbon dioxide production generally followed the same trend except in amended inoculated samples (2.10 μmol g^{-1} cellulose produced over 2 years (0.0028 μmol g^{-1} cellulose day^{-1})). There was a large variation in CO_2 produced between triplicate samples in the anaerobic amended inoculated samples containing excess nitrate, indicating that certain treatments may be showing further activity at 3464 days. The enhanced CO_2 production due to the addition of bentonite remains evident at 3464 days even though there was no increase in production since 2718 days. Almost all of the initially aerobic samples showed slight increases in total gas produced at 3464 days; CO_2 increased slightly in amended inoculated samples (0.0066 μmol g^{-1} cellulose day^{-1}). In general, CO_2 production in initially aerobic samples continued to remain at the same level. Up to 5.9 nmol methane g^{-1} cellulose was detected in anaerobic unamended inoculated samples, and for the first time, methane was detected in samples that were treated with excess nitrate. The rate of methane production in anaerobic samples was 2.5 pmol CH_4 g^{-1} cellulose d^{-1} in both unamended inoculated and amended treatments, and 3.45 pmol CH_4 g^{-1} cellulose d^{-1} in samples containing excess nitrate. Methane was also detected for the first time in initially aerobic inundated samples. In general, unamended samples showed the greatest quantities of methane. Acetic and butyric acids accumulated to a significant extent in anaerobic samples amended with nutrients (6.99 and 6.38 mM respectively); the accumulation of these acids was stimulated by the presence of bentonite (38.6 and 49.8 mM respectively). The overall organic acid content was lowest in anaerobic samples containing excess nitrate and in samples incubated under initially aerobic conditions. These results are consistent with oxidative processes being dominant in these samples.

[1] This work is covered by BOE #1.3.5.4.1 and WBS #1.3.5.4.1.1

Information Only

Microbial characterization of anaerobic inundated samples showed *Halobacter utahensis* as the predominant species in unamended samples with the nutrient amended samples dominated by *Halobacterium*, *Halobacter*, *Halococcus*, and the haloalkalophiles *Natranobacterium* and *Natranomonas*. Work in progress includes analysis of data from studies of methane produced in humid samples and samples containing plastic and rubber materials.

Information Only

BNL Project Objectives

1. Re-evaluate the existing microbial gas data and develop appropriate technical approaches to reducing the conservatism in the current gas generation model.

2. Re-examination and improvement of the experiment for cellulose degradation under humid conditions to derive a more realistic rate for humid microbial degradation.

3. Determine the effect of MgO on the rate and extent of gas generation under humid conditions.

4. Scoping experiments to clarify the factors that caused a diminishing microbial gas generation rate with time in the ongoing experiments, including testing the effect of crystallinity on cellulose degradation under hypersaline conditions.

5. Determine the rate and extent of methanogenesis by halophilic microorganisms. Due to the fact that methanogenesis is the terminal electron-accepting process in any system it is important to understand the occurrence and rate of this process.

Progress Report

Long-term experiments designed to examine gas generation due to biodegradation of the organic fraction of transuranic wastes under WIPP repository-relevant conditions have been ongoing at Brookhaven National Laboratory (BNL). Table 1 provides information about the status of these studies as of January 31, 2002.

Table 1. Status of Microbial Gas Generation Experiments at BNL.

Experiment	Start Date	Most Recent Analyses (Days/Years)*	Data Reported (this report) (Days/Years)
Long-Term Inundated Cellulose	1/29/92	*(3462 / 9.5) (CH_4 partial data set)* (2718 / 7.4) (CO_2)	(3462 / 9.5) (CH_4 complete data set) (3464 / 9.5) (CO_2) aqueous metabolite analysis (3561 / 9.9)
Initially Aerobic Humid Cellulose	4/7/93	*(3009 / 8.2)*	(methane completed, CO_2 planned for FY02)
Anaerobic Humid Cellulose	5/4/94	*(2616 / 7.2)*	(methane completed, CO_2 planned for FY02)
Inundated PE, PVC, and Neoprene	3/9/93	(2612 / 7.2)	(methane completed)
Inundated Hypalon	8/3/93	(2464 / 6.8)	(methane completed)

* Data from incubation times in italics were reported in the July 13, 2001 progress report.

Information Only

Research performed during this reporting period was conducted according to Sandia National Laboratories (SNL) Waste Isolation Pilot Plant Test Plan TP-99-01, effective 3/21/01, under contract AT-8739. Note that the Sandia-approved BNL QA Program remained in effect during this reporting period, and is effectively implemented to date. During this period (July 14, 2001 – January 31, 2002) the following tasks were completed:

1. Total gas, carbon dioxide (CO_2), and methane (CH_4) analysis for samples from the long-term inundated cellulose biodegradation experiment.
2. Aqueous metabolites (organic acids and alcohols) produced due to biodegradation of cellulose in inundated samples analyzed by high-performance liquid chromatography.
3. Microbiological characterization, based upon molecular (ribosomal DNA) analyses for select samples from the long-term inundated experiment and initiated for additional samples and those from the humid experiments.
4. A protocol for the examination of gas production under conditions of MgO-constrained water activity was prepared and new experiments initiated.

More complete details of the progress made during this reporting period are provided below.

1. Quality Assurance Program: The program was approved by the SNL QA Team Lead on February 23, 2001. An audit was performed on June 6-7, 2001 to verify effective implementation, and no deficiencies that needed remedy after audit close-out were identified. This program remains in effect to date.

2. Gas Analysis of Inundated Samples: Tables 1-2 provide data for total gas and CO_2 produced in inundated cellulose samples incubated for 3462 days (the data for 1228 and 2718 days are included for comparison). Data have been corrected for gas produced in the absence of cellulose; data, reported as gas produced g^{-1} cellulose, are the mean ± SEM of analysis of triplicate samples.

Information Only

Table 1. Total gas and carbon dioxide produced in anaerobic inundated cellulose samples over the three latest time periods of analysis.

Sample	Total Gas (ml g^{-1} cellulose)			Carbon Dioxide (μmol g^{-1} cellulose)		
	1228 Days	2718 Days	3464 Days	1228 Days	2718 Days	3464 Days
Anaerobic						
Unamended/ Uninoculated	-0.24 ± 0.05	-0.30 ± 0.08	-0.97 ± 0.23	3.13 ± 0.02	8.29 ± 3.77	4.56 ± 0.26
Unamended/ Inoculated	2.23 ± 12	2.45 ± 0.27	1.56 ± 0.26	13.9 ± 1.0	24.0 ± 1.7	26.1 ± 2.2
Amended/ Inoculated	3.78 ± 0.09	4.21 ± 0.04	2.72 ± 0.11	49.2 ± 0.8	66.9 ± 1.1	55.4 ± 2.6
Amended/Inoc. + Exc. Nitrate	12.12 ± 0.44	11.03 ± 0.43	9.98 ± 0.52	194 ± 4	251 ± 5	236 ± 42
Anaerobic + Bentonite						
Unamended/ Uninoculated	0.00 ± 0.04	0.26 ± 0.06	0.23 ± 0.05	4.70 ± 4.90	8.72 ± 0.55	8.05 ± 4.49
Unamended/ Inoculated	2.39 ± 0.20	2.48 ± 0.31	2.08 ± 0.68	55.2 ± 1.4	59.0 ± 7.1	58.6 ± 3.2
Amended/ Inoculated	3.62 ± 0.56	3.72 ± 0.63	2.72 ± 0.11	99.4 ± 4.4	83.6 ± 8.2	76.7 ± 3.0
Amended/Inoc. + Exc. Nitrate	14.9 ± 0.6	12.0 ± 0.4	11.1 ± 0.35	370 ± 14	350 ± 36	325 ± 14

Information Only

Table 2. Total gas and carbon dioxide produced in initially aerobic inundated cellulose samples over the three latest time periods of analysis.

Sample	Total Gas (ml g^{-1} cellulose)			Carbon Dioxide (μmol g^{-1} cellulose)		
	1228 Days	2718 Days	3464 Days	1228 Days	2718 Days	3464 Days
Initially Aerobic						
Unamended/ Uninoculated	-0.04 ± 0.08	-0.02 ± 0.00	0.064 ± 0.01	4.43 ± 0.06	4.61 ± 0.14	4.70 ± 0.16
Unamended/ Inoculated	0.30 ± 0.07	0.64 ± 0.04	0.71 ± 0.04	14.4 ± 0.1	16.2 ± 0.1	12.9 ± 0.5
Amended/ Inoculated	1.42 ± 0.28	1.33 ± 0.56	1.71 ± 1.03	22.0 ± 2.9	21.9 ± 2.1	26.8 ± 3.5
Amended/Inoc. + Exc. Nitrate	10.3 ± 1.5	8.42 ± 1.40	7.15	186 ± 8	165 ± 44	150 ± 44
Initially Aerobic + Bentonite						
Unamended/ Uninoculated	0.33 ± 0.13	-0.97 ± 0.26	1.94 ± 0.21	11.0 ± 0.2	11.7 ± 0.8	5.23 ± 0.19
Unamended/ Inoculated	1.47 ± 0.22	-0.09 ± 0.04	2.72 ± 1.43	69.6 ± 4.8	73.9 ± 14.7	77.9 ± 13.1
Amended/ Inoculated	6.09 ± 0.04	4.02	2.00 ± 0.50	169 ± 11	120 ± 6	101 ± 11
Amended/Inoc. + Exc. Nitrate	8.10 ± 0.75	7.76 ± 2.34	9.08 ± 1.37	154 ± 7	233 ± 5	226 ± 56

Information Only

A summary of these data is provided in the following figures: i) Figures 1 and 2 present total gas and CO_2, respectively, produced in anaerobic inundated cellulose samples over the course of the experiment, and ii) Figures 3 and 4 present the same data for initially aerobic samples. Figure 1 and Table 1 show that the total volume of gas produced has leveled-off or diminished in anaerobic samples with and without bentonite since the last analysis at 2718 days (it has been 746 days, or 2 years, between the latest and last gas analysis of these samples). Carbon dioxide production generally follows the same trend except in unamended inoculated samples (2.10 μmol g^{-1} cellulose produced over 2 years (0.0028 μmol g^{-1} cellulose day^{-1})(Table 1). There was a large variation in CO_2 produced in anaerobic amended inoculated samples containing excess nitrate (234 ± 42 μmol g^{-1} cellulose) shown in Figure 2 (error bar for open-diamond) indicating that certain treatments may be showing further activity at 3464 days (Table 1). The enhanced CO_2 production due to the addition of bentonite remains evident at 3464 days even though there was no increase in production since 2718 days. Almost all of the initially aerobic samples showed slight increases in total gas produced at 3464 days (Table 2); most significant was the unamended uninoculated samples with bentonite (0.004 ml g^{-1} cellulose day^{-1}) and amended inoculated samples (0.0005 ml g^{-1} cellulose day^{-1}). In initially aerobic samples, excess nitrate plus bentonite resulted in the production of 0.0018 ml g $cellulose^{-1}$ day^{-1} over the 2-year period since the last analysis (Figure 3). Finally, CO_2 increased slightly in initially aerobic amended inoculated samples (0.0066 μmol g^{-1} cellulose day^{-1}) and in unamended inoculated samples plus bentonite (0.005 μmol g^{-1} cellulose day^{-1}). Notwithstanding these samples, CO_2 production in initially aerobic samples has, in general, leveled off (Figure 4).

Information Only

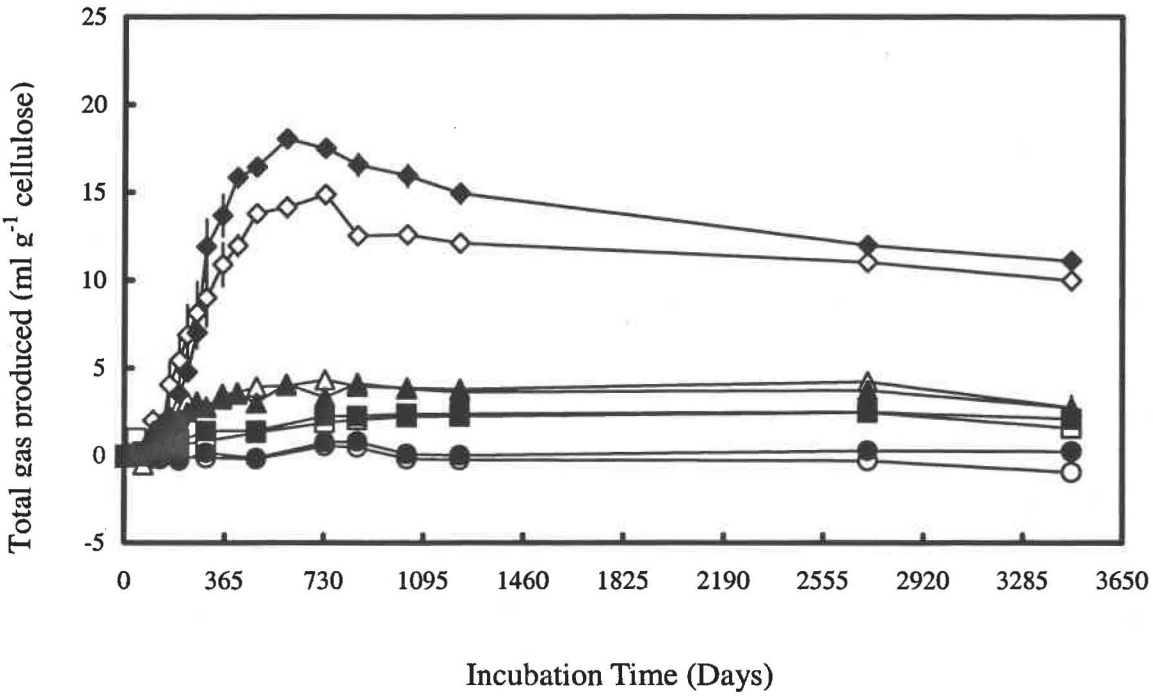

Figure 1. Total volume of gas produced in anaerobic samples inundated with brine: unamended (○); unamended and inoculated (□); amended and inoculated (△); amended, inoculated, plus excess nitrate (◊). Closed symbols are samples with bentonite.

Information Only

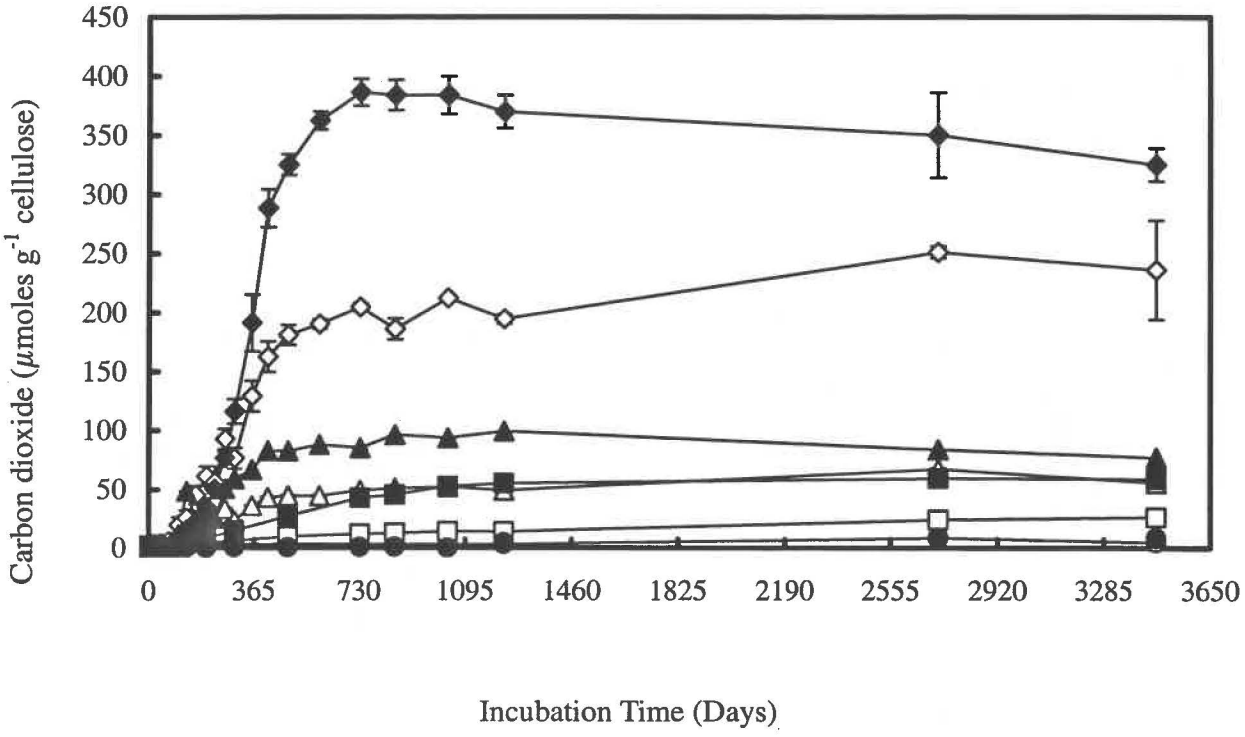

Figure 2. Carbon dioxide produced anaerobic samples inundated with brine: unamended (○); unamended and inoculated (□); amended and inoculated (△); amended, inoculated, plus excess nitrate (◊). Closed symbols are samples with bentonite.

Information Only

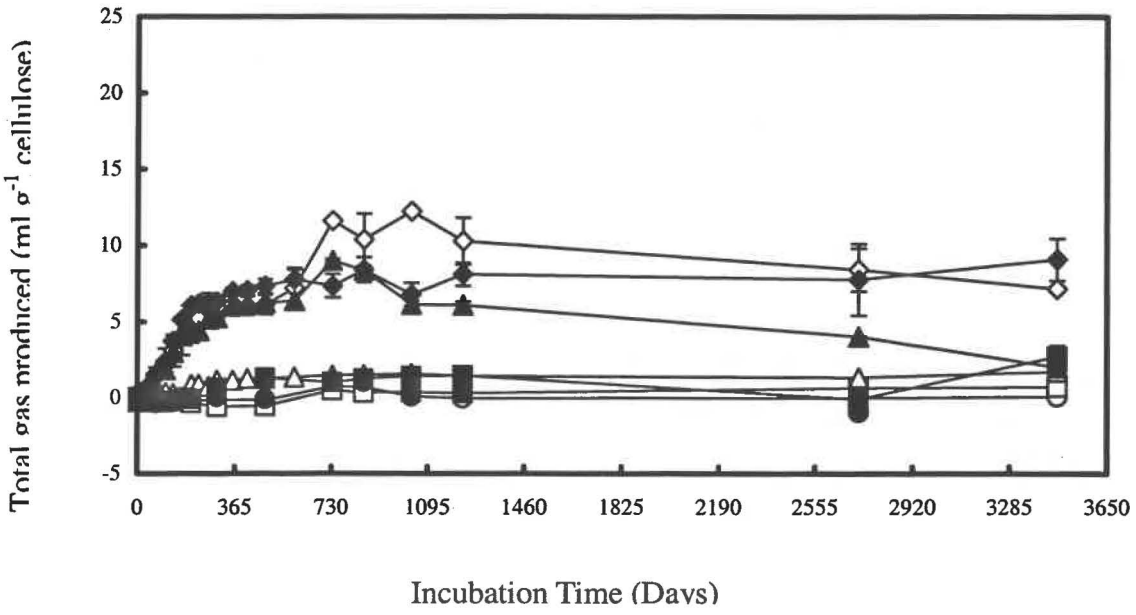

Figure 3. Total gas produced in initially aerobic samples inundated with brine: unamended (○); unamended and inoculated (□); amended and inoculated (△); amended, inoculated, plus excess nitrate (◊). Closed symbols are samples with bentonite.

Information Only

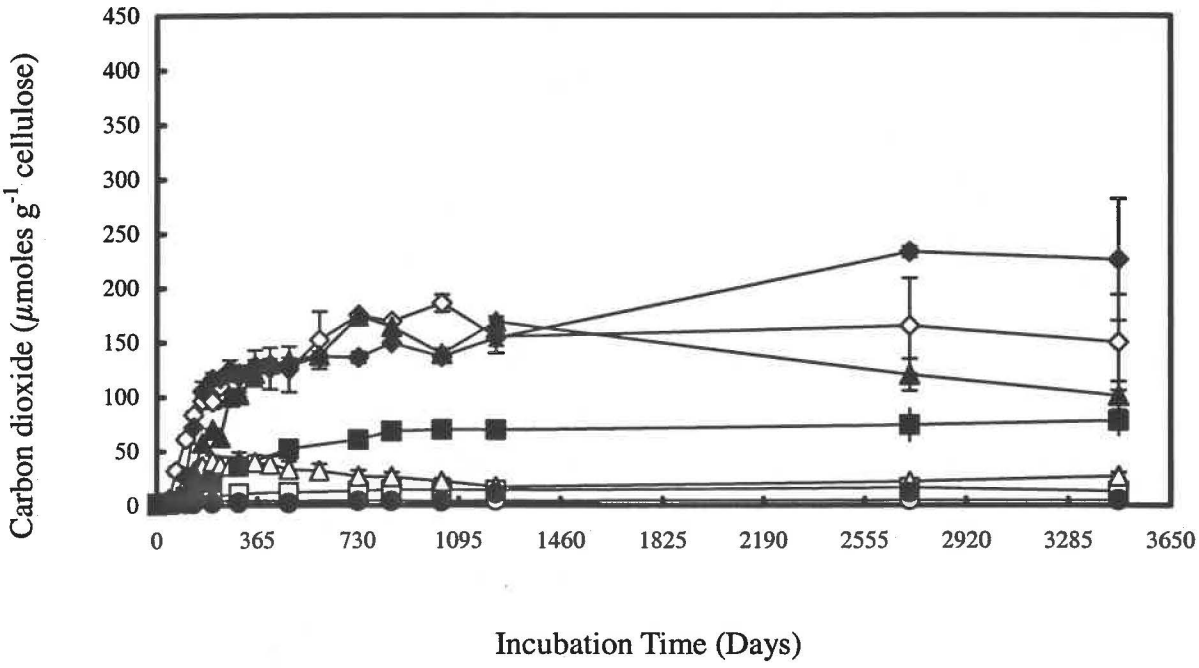

Figure 4. Carbon dioxide produced in initially aerobic samples inundated with brine: unamended (○); unamended and inoculated (□); amended and inoculated (△); amended, inoculated, plus excess nitrate (◊). Closed symbols are samples with bentonite.

Information Only

3. Methane Analysis. Tables 3-4 provide data for methane analysis of inundated cellulose samples up to 3462 days incubation. Methane was analyzed by gas chromatography using flame ionization detection. The minimum detectable quantity is 0.2 nmol CH_4 g^{-1} cellulose dry wt. Methane was first detected in small quantities in most anaerobic samples except those with excess nitrate (Table 3, 2718 days). At 3462 days (9.5 years) methane was still detected in greatest quantity in samples that were not amended with any nitrogen-containing compounds (NH_4NO_3, KNO_3) specifically the unamended/inoculated samples. However, for the first time, methane has been detected in samples that initially contained excess nitrate (2.57 ± 0.79 nmol CH_4 g^{-1} cellulose (w/o bentonite) and 2.81 ± 0.16 nmol CH_4 g^{-1} cellulose (w/ bentonite). Although the time to initial production was lengthy, these samples are now accumulating methane at a relatively rapid rate: the rate of methane production was 2.5 pmol CH_4 g^{-1} cellulose d^{-1} in unamended and amended inoculated samples and 3.45 pmol CH_4 g^{-1} cellulose d^{-1} in samples containing excess nitrate (over 744 days between time 2718 and 3462). Overall, the slow rate of CH_4 accumulation, relative to CO_2, may be due to the extreme difficulty methanogens have in metabolizing the substrates such as acetate, CO_2, and H_2 (the presence of H_2 was reported in SAND96-2582, CO_2 concentrations are given in Section 2.0 of this report, and acetate concentrations are reported in the next section) under hypersaline conditions due to bioenergetic constraints (Oren, 1999). The preferred substrate is methylated amine, such as trimethylamine, commonly found in saline surface waters. Methane was detected in initially aerobic samples at 3462 days, with those samples that were not amended producing the largest initial quantities. Production rates range from 0.7 to 1.7 CH_4 pmol g^{-1} cellulose d^{-1}. Due to its importance as the terminal electron-accepting microbial process, and the need to understand production in hypersaline WIPP-relevant conditions, additional analyses of CH_4 will be performed in FY2002. Other analyses will include an attempt at subculturing the methanogens in these samples and molecular biological detection of methanogens.

Information Only

Table 3. Methane analysis of anaerobic inundated cellulose samples.

Sample	Incubation Time (d) 1228	2718	3462
	---------- (nmol g^{-1} cellulose) ----------		
Anaerobic			
Unamended	nd	3.92 ± 0.27	4.40 ± 0.28
Unamended/Inoculated	nd	4.03 ± 1.38	5.89 ± 1.30
Amended/Inoculated	nd	0.85 ± 0.7	2.74 ± 0.90
Amended/Inoc. + Exc. Nitrate	nd	nd	2.57 ± 0.79
Anaerobic + Bentonite			
Unamended	nd	3.84 ± 0.40	4.51 ± 0.06
Unamended/Inoculated	nd	3.52 ± 0.20	4.06 ± 0.15
Amended/Inoculated	nd	1.12 ± 0.03	3.41 ± 0.13
Amended/Inoc. + Exc. Nitrate*	nd	nd	2.81 ± 0.16

nd = not detected

Information Only

Table 4. Methane analysis of initially aerobic inundated cellulose samples.

Sample	Incubation Time (d) 1228	2718	3462
	---------- (nmol g^{-1} cellulose) ----------		
Initially Aerobic			
Unamended	nd	1.25 ± 0.29	1.82 ± 0.05
Unamended/Inoculated	nd	1.10 ± 0.13	1.34 ± 0.03
Amended/Inoculated	nd	nd	0.84 ± 0.05
Amended/Inoc. + Exc. Nitrate	nd	nd	1.27 ± 0.37
Initially Aerobic + Bentonite			
Unamended	nd	nd	1.59 ± 0.47
Unamended/Inoculated	nd	nd	2.16 ± 0.07
Amended/Inoculated	nd	nd	0.64 ± 0.06
Amended/Inoc. + Exc. Nitrate*	nd	nd	1.45 ± 0.26

nd = not detected

Information Only

4. Aqueous Metabolite Analysis. Samples from the inundated experiments reserved at t=0 for aqueous chemical analysis were analyzed for organic acids and alcohols by high-performance liquid chromatography (HPLC). The presence of these aqueous metabolites, produced by bacterial metabolism of cellulose, provides insight into the effect of various nutrient treatments on the succession of microbial processes. These metabolites may accumulate and disappear depending upon microbial activity (they accumulate as a result of fermentation of glucose and they are consumed as electron-donor substrates for iron-reduction, sulfate-reduction, and methanogenesis). Finally, quantification of these metabolites provides important information relative to the carbon-balance in the samples, since cellulose hydrolysis and subsequent metabolism results in both aqueous and gaseous intermediates and end-products. A 0.25 ml sample was withdrawn from select samples and diluted to 1.0 ml with deionized water. Analytes were separated by HPLC using ion-exclusion chromatography where 1) strong and weak electrolytes (NaCl, KNO_3) are eluted unseparated at the beginning of the elution and 2) the retention times of the organic acids and alcohols are proportional to their dissociation constant values. A sulfonated macroporous styrene HPLC-column was used where analytes with higher pKa values are retained longer on the column. Acids with larger pKa values and molecular weights than butyric (pKa=4.85, MW=88.11) are separated by a secondary mechanism, hydrophobic adsorption, which is a size-exclusion phenomenon. Low-molecular weight carboxylic acids of the form $CH_3(CH_2)_nCOOH$ were principally quantified using UV detection at 210 nm; alcohols (ethanol, propanol, butanol) and glucose were quantified by refractive index detection. Retention times using both detection methods were compared to commercially-prepared standard mixtures, and both detection methods were used for positive identification of analytes. The standards included the following: 1. volatile acids (formic, acetic, propionic, butyric, isobutyric, valeric, isocaproic, isovaleric, hexanoic, heptanoic), 2. non-volatile acids (pyruvic, lactic, oxalacetic, oxalic, methyl malonic, malonic, fumaric, succinic), 3. alcohols (butanol, pentanol, propanol, ethanol), and 4. glucose. Results of HPLC of anaerobic and initially aerobic inundated samples are presented in Tables 5-8 (data are the mean of duplicate analyses; relative standard error was generally <0.5%). Previous data reported in

Information Only

SAND96-2582 are included for comparison. Most of the formic and lactic acids that were produced in the early stage were consumed by 3561 days (see Table 5, unamended and amended samples). Acetic and butyric acids accumulated to a significant extent in anaerobic samples with nutrients (6.99 and 6.38 mM respectively, Table 5); the accumulation of these acids was stimulated by the presence of bentonite (38.6 and 49.8 mM respectively, Table 6). The presence of excess nitrate decreased the overall acetic and butyric acid content in anaerobic samples but formic, fumaric, and lactic acids were produced in significant quantities by 3561 days (3.26, 2.94, and 3.03 mM respectively). The accumulation of these acids at 3561 days and may indicate a shift in microbial metabolic processes which appears correlated with an increase in CO_2 production as evidenced by the large error in the data from these samples (see Figure 2 and 4, open-diamond). Bentonite, a source of iron-oxyhydroxides, stimulated the production of oxalic and oxalacetic acids (Table 6 and 8) as well as formic and fumaric acids in anaerobic samples. The organic acid content of initially aerobic samples was generally lower than anaerobic samples (Tables 7,8); this is consistent with less mature fermentative processes in these samples due to the intial bias toward aerobic respiration. Acetic acid accumulation was on par with anaerobic samples (6.91 mM, initially aerobic amended inoculated vs. 6.99 mM produced in the same anaerobic treatment and 11.0 mM initially aerobic amended inoculated plus excess nitrate vs. 5.21 mM produced in the same anaerobic treatment). The addition of bentonite resulted in decreased production of carboxylic acids in most initially aerobic samples. The production of malonic acid was unique to the initially aerobic samples. The extremely transitory nature of glucose was proven by its absence in all but one treatment (Table 6, amended inoculated samples + bentonite); the carbohydrate is consumed as fast as it is produced. Alcohols were not detected in any samples. The addition of nutrients, which stimulated microbial activity, resulted in the production of organic acids that could not be identified in certain samples; additional analyses will be performed in order to positively identify and quantify these compounds.

Information Only

Table 5. Organic acids detected in anaerobic inundated cellulose samples (latest data is in bold (3561 days incubation)).

Anaerobic Treatment & Incubation Time (days)	Organic Acid (mM)								
	Acetic	Butyric	Formic	Fumaric	Lactic	Oxalic	Oxalacetic	Propionic	Succinic
Unamended									
885	0.28	nd	0.23	nd	0.05	nd	nd	nd	nd
1228	1.38	nd	1.74	nd	0.14	nd	nd	nd	nd
3561	**0.20**	**nd**	**0.13**	**0.01**	**nd**	**nd**	**nd**	**nd**	**nd**
Unamended/Inoculated									
885	1.06	nd	nd	nd	0.29	nd	nd	nd	nd
1228	3.48	nd	nd	nd	0.26	nd	nd	nd	nd
3561	**6.17**	**nd**	**nd**	**0.17**	**0.50**	**nd**	**nd**	**0.02**	**nd**
Amended/Inoculated									
885	3.73	0.16	0.48	nd	0.67	nd	nd	0.10	nd
1228	3.90	nd	1.02	nd	0.44	nd	nd	nd	nd
3561	**6.99**	**6.38**	**0.03**	**0.35**	**0.02**	**nd**	**nd**	**0.20**	**nd**
Amended/Inoculated + Excess Nitrate*									
885	nd	nd	nd	nd	nd	nd	nd	0.18	nd
1228	1.90	nd	5.95	nd	1.41	nd	nd	nd	nd
3561	**5.21**	**5.49**	**3.26**	**2.94**	**3.03**	**0.163**	**nd**	**0.43**	**nd**

*Isocaproic acid and two unknown acids with pKa, MW > butyric were detected at significant quantities at 3561 days.

Information Only

Table 6. Organic acids detected in anaerobic inundated cellulose samples w/ bentonite (latest data is in bold (3561 days incubation)).

Anaerobic + Bentonite Treatment & Incubation Time (days)	Organic Acid (mM)								
	Acetic	Butyric	Formic	Fumaric	Lactic	Oxalic	Oxalacetic	Propionic	Succinic
Unamended									
885	0.20	nd	0.13	nd	0.10	nd	nd	nd	nd
1228	0.40	0.25	0.52	nd	0.06	nd	nd	nd	nd
3561	**nd**	**nd**	**0.54**	**nd**	**nd**	**nd**	**nd**	**nd**	**nd**
Unamended/Inoculated									
885	7.78	0.07	0.54	nd	2.42	nd	nd	0.17	0.30
1228	2.41	nd	0.65	nd	0.26	nd	nd	nd	nd
3561	**4.55**	**nd**	**nd**	**nd**	**nd**	**nd**	**nd**	**nd**	**nd**
Amended/Inoculated*									
885	6.41	0.59	0.98	nd	2.03	nd	nd	0.32	nd
1228	2.54	nd	1.80	nd	nd	nd	nd	nd	0.02
3561	**38.6**	**49.8**	**9.05**	**5.35**	**nd**	**4.04**	**0.38**	**nd**	**nd**
Amended/Inoculated + Excess Nitrate									
885	12.6	0.97	3.50	nd	20.64	nd	nd	4.52	nd
1228	8.36	1.20	15.5	nd	4.90	nd	nd	0.13	nd
3561	**8.22**	**nd**	**9.05**	**5.35**	**nd**	**nd**	**0.06**	**nd**	**nd**

*Isobutyric acid (50 mM), valeric (39 mM), glucose, and three unknown acids with pKa, MW > butyric were detected at significant quantities at 3561 days.

Information Only

Table 7. Organic acids detected in initially aerobic inundated cellulose samples (latest data is in bold (3561 days incubation)).

Initially Aerobic Treatment & Incubation Time (days)	Organic Acid (mM)								
	Acetic	Butyric	Formic	Fumaric	Lactic	Oxalic	Oxalacetic	Propionic	Succinic
Unamended									
885	0.18	nd	0.39	nd	0.10	nd	nd	0.12	0.01
1228	1.30	nd	1.85	nd	0.36	nd	nd	nd	nd
3561	**0.10**	**nd**	**0.72**	**nd**	**nd**	**nd**	**nd**	**nd**	**0.01**
Unamended/Inoculated									
885	0.07	nd	0.04	nd	0.52	nd	nd	0.08	nd
1228	2.01	nd	0.87	nd	0.09	nd	nd	nd	nd
3561	**0.36**	**nd**	**0.26**	**nd**	**nd**	**nd**	**nd**	**nd**	**nd**
Amended/Inoculated*									
885	1.72	0.05	0.26	nd	1.00	nd	nd	0.30	0.52
1228	4.45	nd	2.52	nd	0.69	nd	nd	0.20	nd
3561	**6.91**	**nd**	**nd**	**1.99**	**nd**	**nd**	**0.18**	**nd**	**nd**
Amended/Inoculated + Excess Nitrate**									
885	1.23	0.09	0.33	nd	0.30	nd	nd	0.82	nd
1228	4.43	nd	3.41	nd	1.57	nd	nd	0.12	nd
3561	**11.0**	**nd**	**nd**	**nd**	**nd**	**nd**	**0.32**	**nd**	**nd**

*Malonic acid was detected at 3561 days (1.13 mM) and a significant acid (unknown) with pKa, MW>butyric.
**Malonic acid was detected at 3561 days (4.72 mM) and valeric acid (8.82 mM) as well as two acids of unknown identity (pKa > butyric).

Information Only

Table 8. Organic acids detected in initially aerobic inundated cellulose samples w/ bentonite (latest data is in bold (3561 days incubation)).

Initially Aerobic + Bentonite Treatment & Incubation Time (days)	Organic Acid (mM)								
	Acetic	Butyric	Formic	Fumaric	Lactic	Oxalic	Oxalacetic	Propionic	Succinic
Unamended									
885	0.09	nd	0.16	nd	0.04	nd	nd	nd	nd
1228	1.08	nd	2.00	nd	0.10	nd	nd	nd	nd
3561	**0.13**	**0.21**	**0.63**	**nd**	**nd**	**nd**	**nd**	**nd**	**nd**
Unamended/Inoculated*									
885	3.95	nd	0.23	nd	0.86	nd	nd	nd	nd
1228	3.16	nd	2.02	nd	0.47	nd	nd	nd	nd
3561	**5.91**	**0.11**	**nd**	**nd**	**0.13**	**nd**	**nd**	**nd**	**nd**
Amended/Inoculated**									
885	4.61	0.20	0.24	nd	0.66	nd	nd	nd	nd
1228	3.66	nd	2.56	nd	1.85	nd	nd	nd	nd
3561	**7.70**	**nd**	**nd**	**nd**	**nd**	**nd**	**0.17**	**nd**	**nd**
Amended/Inoculated + Excess Nitrate***									
885	0.31	nd	nd	nd	nd	nd	nd	nd	nd
1228	1.30	nd	0.39	nd	0.06	nd	nd	nd	nd
3561	**5.00**	**nd**	**nd**	**nd**	**nd**	**nd**	**0.13**	**nd**	**nd**

*Malonic acid was detected at 3561 days (0.45 mM); ** 3561 days - malonic acid, 2.56 mM; *** 3561 days - malonic acid, 0.33 mM.

Information Only

5. Microbiological Characterization: In order to completely address Objectives 1, 4, and 5, we need to understand the composition (identity and microbial community structure) of microorganisms in samples that show CO_2 and methane production. Understanding differences in community structure may help to explain difference in gas generation rates. In an anaerobic gloved box, a 10 ml sample was withdrawn from one of the triplicate reserve samples (not used for periodic gas analysis) of each of the following anaerobic inundated treatments: i) unamended, uninoculated, ii) unamended, inoculated, iii) nutrient amended and inoculated, iv) nutrient amended, inoculated, plus excess nitrate. A fifth sample, consisting of three "known" halophiles (*Halobacterium salinarium*, *Haloanaerobium praevalens*, and *Halomonas* sp.) was analyzed to verify and validate the method. Culture-independent methods were used to quantify and identify microorganisms, phospholipid fatty acid (PLFA) and denaturing gradient gel electrophoresis (DGGE) analysis, described below.

PLFA Analysis: Microbial membrane lipids, specifically phospholipid fatty acids (PLFA), were recovered from the samples according to White, et al. (1979). PLFA were analyzed by gas chromatography with peak confirmation performed by electron impact mass spectrometry (GC/MS). The individual fatty acids differ in chemical composition depending on the organism and environmental conditions. PLFA analysis provides quantitative insight into three important attributes of microbial communities: viable biomass, community structure, and metabolic activity.

DGGE: Nucleic acid extraction was performed using a bead-beating method. Polymerase chain reaction (PCR) amplification of 16S rDNA gene fragments was performed as described in Muyzer et al. (1993) with modifications. The primers targeted eubacterial 16S rDNA regions corresponding to *E. coli* positions 341-534. Purified DNA was sequenced with an ABI-Prism automatic sequencer model 377 with dye terminators. Sequence identifications were performed using the BLASTN facility of the National Center for Biotechnology Information (http://ncbi.nlm.nih.gov/Blast) and the "Sequence Match" facility of the Ribosomal Database Project. (http://www.cme.msu.edu/RDP/analyses.html).

Information Only

Results: PLFA analysis results are currently being examined and will be reported shortly, DGGE results are presented in Figure 5. Each lettered band in the figure corresponds to a unique bacterial species; the greater the number of bands the greater number of bacterial species in the samples. Higher diversity, as determined by a greater number of microbial species, was correlated with nutrient amendment and concomitant gas production. One gram-positive microorganism (genus *Clostridium,* band A, Figure 5) was detected in the anaerobic unamended uninoculated treatment; this is of interest given that almost all halophiles are gram-negative. This treatment is characterized by a low starting biomass and continual stress induced by lack of abundant electron acceptors. Introduction of mixed inoculum, but not nutrients, also resulted in dominance by one species, *Halobacter utahensis* (bands B, M, N, and O, Figure 5). In general, abundant nutrient availability lowers microbial diversity, as has been found in non-saline, low-carbon environments. Samples from the inundated cellulose experiment are analagous to environments loaded with highly complex-carbohydrates. Cellulolytic microbial populations associated with the animal rumen, a very high carbon-loading environment, have been shown to be diverse (Cho and Kim, 2000). Besides organic carbon availability, Roling et al. (2001) showed that microbial community structure in a benzene-impacted groundwater environment was determined by available electron acceptor. *Halobacterium, Haloarcula, Halobacter, and Natranobacterium* were found in the nutrient amended, inoculated treatment ((Four genera) bands C, D, E, P, Q, R, Figure 5); a fairly high diversity and unique due to the presence of *Natranobacterium*. This genus consists of species adapted to life under hypersaline, extremely alkaline conditions (pH 9-10 such as soda lakes). Excess nitrate resulted in the establishment of *Halobacterium*, *Halobacter*, *Halococcus*, *Natranobacterium*, *Natranomonas* ((Seven genera) bands F, G, H, S, T, U, and V, Figure 5), and unidentified archaea (bands S and V). The known sample resulted in the identification of three genera, thus verifying the applicability of this technique to halophilic bacteria: bands I, J (*Halomonas* sp.); K, L (*H. praevalens*); and the archaea, *H. salinarium* (band W). An obvious limitation of the technique, however, is the size of the bacterial databases; these are generally less populated with environmentally-relevant isolates, especially extremophiles, and in some instances a positive identification is not possible (eg. bands S and V, Figure 5).

Information Only

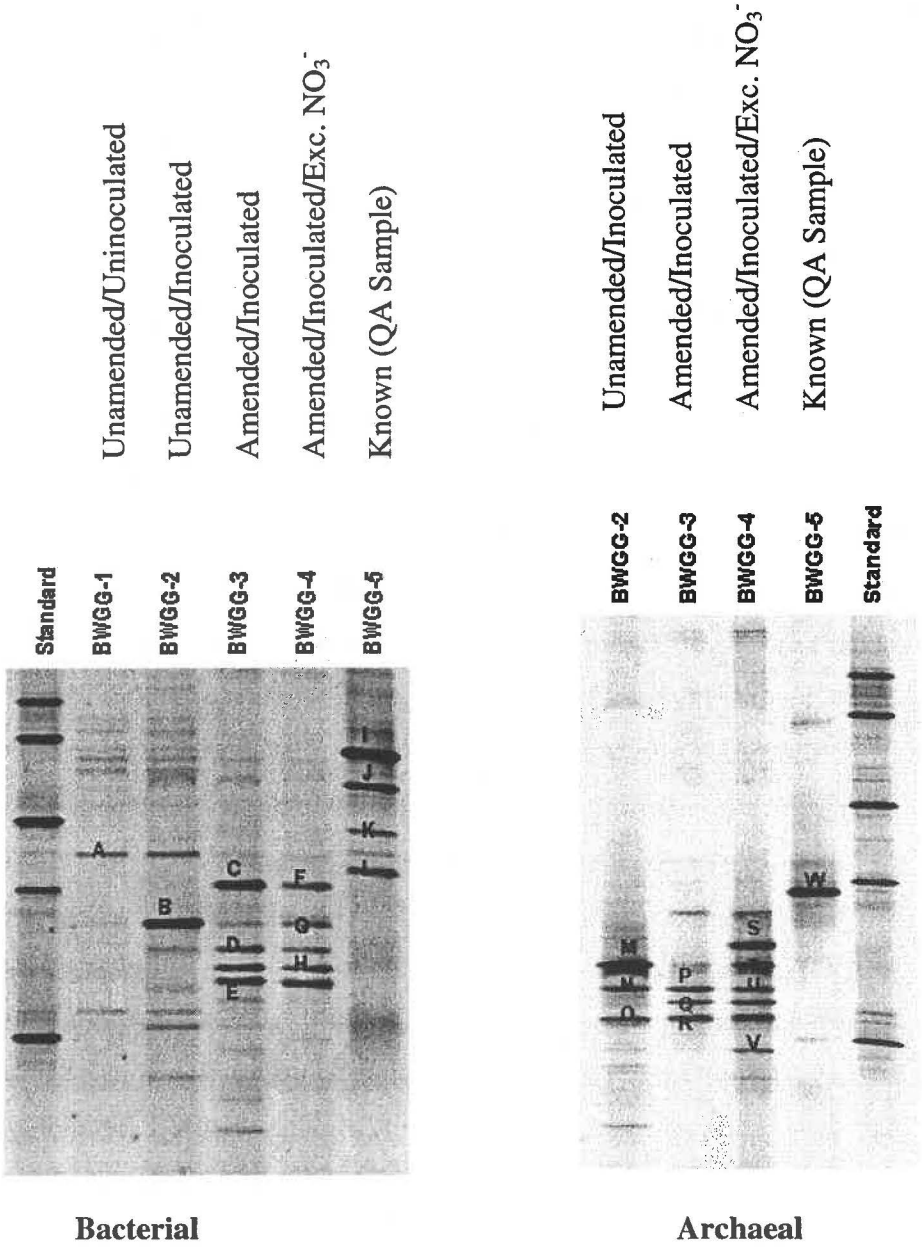

Figure 4. DGGE gel image of amplified primers from a conserved region of bacterial and archaeal 16S rDNA. Banding patterns and relative intensities of the recovered bands provide a measure of differences among the communities. Dominant species must constitute at least 1-2% of the total bacterial community to form a visible band. Labeled bands were excised and sequenced.

Information Only

6. Microbial Gas Generation Under Conditions of MgO-Constrained Water Activity: The two experiments in-progress at BNL are to examine gas generation due to cellulose biodegradation under humid conditions. Samples were prepared to maintain a 70% relative humidity environment. Most of the samples in these experiments received 2.0 to 2.5 ml of liquid (2.0 ml of liquid inoculum or 2.0 ml of liquid inoculum and 0.5 ml of a nutrient solution). Experiments performed at an RH of 70% may no longer appropriately simulate WIPP disposal rooms post-closure due to the fact that MgO is being emplaced. Microbial gas generation rates under MgO-constrained humid conditions may be much lower due to sequestering of water, which is necessary for microbial activity. An experiment procedure has been prepared that tests microbial activity under more relevant MgO-constrained water activity conditions (with activity bounded at the high end by the absence of MgO and at the low-end by its presence). In order to obtain relevant gas generation data rapidly and accurately, the following will be used: i) a "dry" inoculum, ii) ^{14}C-labeled substrate (for metabolism and growth) and, iii) extremely sensitive techniques for capturing and quantifying microbially produced CO_2 (alkaline trapping and $^{14}CO_2$ liquid scintillation counting).

Progress to date: A dry inoculum was prepared by growing a *Halomonas* sp. (isolated from the WIPP environment) and its viability was confirmed. Radiolabeled substrates were obtained (^{14}C-acetate, ^{14}C-succinate, ^{14}C-cellulose) and were proven useful for providing gas-generation rates under inundated hypersaline conditions. Samples with MgO-constrained water activity were prepared and their moisture content is currently being determined by gravimetric techniques in order to standardize the treatments. A series of experiments is planned to start in early 2002.

Information Only

7.0 Ongoing Work

- Select samples from the humid experiment to examine biodegradation of plastic and rubber materials have been analyzed for methane production. This data is being prepared for presentation.
- A draft manuscript, planned for submittal to a peer-reviewed journal, has been prepared that details gas production due to cellulose biodegradation under hypersaline conditions; this is currently undergoing review.
- Results of PLFA analysis of microbial populations in the anaerobic inundated cellulose samples are being examined and prepared for presentation.
- Additional samples have been taken for microbial characterization from the humid and inundated experiments; characterization work is underway.
- The experiment to examine microbial growth and gas production under conditions of MgO-constrained water activity will be started early in FY2002.

8.0 Future Work

- Aqueous chemistry data will be coupled with weight-loss determinations to provide a more complete analysis of carbon and substrate mass-balance in the samples.
- Additional aqueous chemical analyses will be performed, including i) pH, ii) further analysis of soluble carbohydrates and organic acids, iii) electron acceptors (Fe^{3+}, NO_3^-, sulfate), and iv) nitrogen/phosphorus content.
- Material characterization techniques including infrared and x-ray spectroscopy will be used to assess the extent of biopolymer degradation due to microbial activity in samples containing cellulose and plastic and rubber materials thus providing an assessment of polymer crystallinity and its relation to the extent and rate of gas generation
- A manuscript concerned with methanogenesis under hypersaline conditions will be prepared for submittal to a peer-reviewed journal.

Information Only

References

Cho, J-C, and Kim, S-J. 2000. Increase in bacterial community diversity in subsurface aquifers receiving livestock wastewater input. Applied Environ. Microbiol. 66(3): 956-965.

Muyzer, G., De Waal, E.C., and Uitterlinden, A.G. 1993. Profiling of complex microbial population by denaturing gradient gel electrophoresis analysis of polymerase chain reaction-amplified genes coding for 16S rRNA. Applied Environ. Microbiol 59(3): 695-700.

Oren, A. (1999). "Bioenergetic aspects of halophilism." Microbiology and Molecular Biology Reviews 63(2): 334-348.

Roling, W.F.M., Van Breukelen, B.M., Braster, M., Lin, B., and Van Verseveld, H.W. 2001. Relationship between microbial community structure and hydrochemistry in a landfill leachate-polluted aquifer. Applied Environ. Microbiol. 67(10): 4619-4629.

White, D.C., Davis, W.M., Nickels, J.S., King, J.D., and Bobbie, R.J. 1979. Determination of the sedimentary microbial biomass by extractable lipid phosphate. Oecologia 40: 51-62.

Information Only

Information Only

2.2 Geochemistry Studies[1]

2.2.1 Complexation of Metal Ions with Hypochlorite

Donald Wall
Sandia National Laboratories, MS 1395
4100 National Parks Highway
Carlsbad, NM USA 88220

Abstract

Studies of the chemical behavior of hypochlorite in high ionic strength solutions have commenced. The test plan describing these studies is: TP 02-01, Complexation Behavior of Hypochlorite with Metal Ions. The thermodynamic and stoichiometric acid dissociation constants of hypochlorous acid have been measured. It was found that hypochlorous acid is unstable in acidic brines, probably decomposing to diatomic chlorine. Experiments have been devised to measure the kinetics of the decomposition reactions. Additional experiments are planned to determine the efficacy of hypochlorite as a complexing agent for metal ions.

Introduction

The production of hypochlorite (OCl^-) by α-particle induced radiolysis of NaCl brines has been previously reported (Pashalidis et al., 1993). The presence of OCl^- and hydrogen peroxide (H_2O_2) has been invoked as being responsible for the production of oxidized Pu (i.e. PuO_2^+ and PuO_2^{2+}) in the Source Term Test Program (STTP) (Villareal, 2002). Studies are planned at Los Alamos National Laboratory (LANL) to take a look at the role of hypochlorite on the redox speciation of Pu in brine solutions. There have been very few reports of complexation of metal ions by the hypochlorite anion; as a result there are insufficient data to determine whether complexation of actinides by hypochlorite is a potentially significant process in actinide solubilization. The objective of this work is to determine whether hypochlorite can serve as a complexing agent for metal ions, including the actinides, and consequently act to solubilize actinide metal ions. A full description of the experimental objectives of this study is presented in the Test Plan TP02-01 "Complexation Behavior of Hypochlorite with Metal Ions." The trivalent lanthanide ion, neodymium, (Nd), will be used as an analog for the trivalent oxidation state of plutonium, in the present complexation studies.

In order to accurately calculate the concentration of hypochlorite under solution conditions where it may be partially protonated, it is necessary to measure the stoichiometric acid dissociation constant of hypochlorous acid before performing experimental determination of stability constants of hypochlorite with metal ions.

Spectrophotometry

The molar absorptivity of hypochlorite at 292 nanometers ($\varepsilon_{292}^{OCl^-}$) has been reported to be 350 $M^{-1}cm^{-1}$, although the complete spectrum was not provided (Gray et al., 1977).

[1] This work is covered by BOE #1.3.5.4.1 and WBS #1.3.5.4.1.2

Information Only

The electronic configuration of hypochlorite is similar to that of diatomic chlorine; however, in OCl^- the negative charge of the anion is primarily centered on the oxygen atom. A molecular orbital diagram of diatomic molecules bound by a single sigma-type bond formed by overlap of sp^3 hybridized atomic orbitals indicates that the electronic transition responsible for the absorbance band at 292 nm is probably due to a $\sigma^* \leftarrow \sigma$ electronic transition. A hypsochromic (blue) shift in the absorbance spectrum would indicate either an increase in energy of the σ^* orbital, or a stabilization of the σ orbital, conversely, a bathochromic (red) shift of the spectrum would indicate stabilization of the σ^* orbital or destabilization of the σ orbital. Therefore, assessment of the wavelength shift associated with formation of metal complexes with hypochlorite may give insight into the nature of the bonding between the metal and ligand.

In order to investigate the utility of spectrophotometry in measurement of metal complexation by OCl^-, it was undertaken to perform a series of spectrophotometric titrations with various solution compositions and ionic strengths. The titrations were performed to assess the impact of solution composition upon the molar absorptivity, as well as to determine whether the composition caused hypsochromic or bathochromic shifts in the absorbance peaks. Analysis of spectrophotometric data may be particularly useful in the investigation of stability constants with lanthanides because the spectrophotometric method exhibits greater sensitivity than the potentiometric method. Increased sensitivity allows analysis of complexes in the near-neutral or basic pcH region where the metal ions exhibit lower solubility due to the pronounced hydrolysis.

Potentiometry

It is necessary to determine the acid dissociation constant of HOCl before it is possible to determine complexation constants of OCl^- with most metal ions, including Nd. Acid dissociation constants may be described as either stoichiometric or thermodynamic. In the following discussion brackets, [ ] indicate concentrations, and braces { } indicate thermodynamic activities. The symbol γ is used to indicate the thermodynamic activity coefficient. The equilibrium condition for dissociation of a weak acid, HA, may be written as

$$[HA] \leftrightarrow [H+] + [A-] \qquad (1)$$

or

$$\{HA\} \leftrightarrow \{H+\} + \{A-\} \qquad (2)$$

where equation (1) is the stoichiometric equilibrium expression and equation (2) is the thermodynamic equilibrium expression. Equation (2) may also be rewritten as

$$[HA]\gamma_{HA} \leftrightarrow [H^+]\gamma_{H^+} + [A^-]\gamma_{A^-} \qquad (3)$$

The stoichiometric equilibrium constant for equation (1) is given by

Information Only

$$Q_a = \frac{[H^+][A^-]}{[HA]} \tag{4}$$

The thermodynamic equilibrium constant for equation (3) is given by

$$K_a = \frac{[H^+]\gamma_{H^+}[A^-]\gamma_{A^-}}{[HA]\gamma_{HA}} \tag{5}$$

Discernment between the two equilibrium constants and use of the appropriate equilibrium constant is absolutely critical for proper experimental design and data interpretation. For example, experimental methods that measure thermodynamic activity, such as potentiometric electrode measurement of acidity, must not be coupled with methods that directly measure concentration, such as spectrophotometry, unless specific allowances are made for the effect of the activity coefficients. Allowance for the difference between stoichiometric and thermodynamic quantities is particularly critical for experimental work in high ionic strength solutions. Failure to consider the effect of mixing thermodynamic and stoichiometric quantities would constitute critical failures in experimental design and data analysis. Comparison of the stoichiometric and thermodynamic forms of the Henderson-Hasselbalch equation for the weak acid HA illustrates the need for consistency in use of thermodynamic and stoichiometric quantities:

$$pcH = pQ_a + \log\frac{[A^-]}{[HA]} \tag{6}$$

where pcH is the negative logarithm of the hydrogen ion concentration, and pQ_a is the negative logarithm of the stoichiometric acid dissociation constant. The thermodynamic form of the Henderson-Hasselbalch equation is provided as equation (7)

$$pH = pK_a + \log\frac{[A^-]\gamma_{A^-}}{[HA]\gamma_{HA}} \tag{7}$$

where pH is the negative logarithm of the hydrogen ion activity and pK_a is the negative logarithm of the thermodynamic acid dissociation constant. Potentiometric measurement of the hydrogen ion activity, pH, coupled with a direct measurement of the protonated and deprotonated acid concentration, such as by spectrophotometry, would necessarily result in a mixed acid dissociation constant, combining both thermodynamic and stoichiometric terms, as illustrated in equation (8)

$$K_{a,mixed} = \frac{[H^+]\gamma_{H^+}[A^-]}{[HA]} \tag{8}$$

Information Only

Such a mixed constant would be useful only for the exact solution composition in which the constant were determined.

In practice, concentrations of metal ions and other analytes are often experimentally easier to determine than the respective thermodynamic activities. Commercially available standard calibration buffer solutions are not available for high ionic strengths; therefore, it is necessary to calibrate potentiometric systems by strong acid/strong base titration at the ionic strength of interest. The calibration may be done by accurately measuring a known amount of standardized NaOH solution into a titration vessel, adding known volumes of standardized HCl solution, and recording the electrode potential in millivolts (mV) at each step. The pcH of the solution at each step is readily calculated, and a calibration curve of electrode response in mV as a function of pcH may be prepared. The performance of such a system may be evaluated by comparison with the Nernst equation:

$$E = E^{o} + \frac{RT}{nF}\ln([H^{+}]\gamma_{H^{+}}) \qquad (9)$$

where E is the measured cell potential in volts, E^{o} is the standard reduction potential in volts, R is the ideal gas constant, (8.314 $Jmol^{-1}K^{-1}$), T is the temperature in Kelvin, n is the number of equivalents of analyte involved in the reaction of interest, and F is the Faraday constant, 96,485 $Cmol^{-1}$. Combining the constants for n=1 at 25° C and converting from Naperian to base 10 logarithms gives

$$E = E^{o} + 0.059 \log[H^{+}] + 0.059 \log \gamma_{H^{+}} \qquad (10)$$

When the concentration of the predominant electrolyte(s) are much greater than the hydrogen ion concentration, the ionic activity coefficient, $\gamma_{H^{+}}$, exhibits little dependence on the hydrogen ion concentration and may be regarded as constant. Glass electrodes for pH measurement are usually constructed to provide a response of about 0 mV at pH = 7 in low ionic strength solutions, where the value of the ionic activity coefficient for H^{+} is close to 1. In other words, in low ionic strength solutions, a typical glass electrode responds to acidity with a value of: $E - E^{o} \cong 0$. Since the value of $\gamma_{H^{+}}$ is dependent on the concentration of the bulk electrolyte, and independent of the hydrogen ion concentration, the value of the last term in equation (10), $0.059 \log \gamma_{H^{+}}$, is a function of ionic strength, rather than concentration of the hydrogen ion. Therefore, a plot of E as a function of pcH should yield a straight line with a slope of -0.059, with an x-intercept that describes the magnitude of the H^{+} ionic activity coefficient. Refer to Figure 1 as an example.

Information Only

Experimental

Equipment

Spectrophotometry
Spectrophotometric analysis was performed with a Cary 300 UV/VIS spectrophotometer, which is controlled by a Dell Optiplex GX1 personal computer. Absorbance calibration was performed by setting the 0% and 100% transmittance with solutions of the same electrolyte composition as the analytical samples, but without presence of the chromophores.

Potentiometry
Potentiometric titrations were performed with a Mettler DL25 Automatic Buret, interfaced with an HP Laserjet II P printer, which generates columns of data during the course of the titration, providing the electrode potential in mV and volume of titrant delivered. The columns of data are entered into Microsoft Excel to generate figures and perform calculations. The potentiometric measurement system performs automated titrations, featuring a nitrogen purge to maintain a CO_2 free atmosphere, and a constant temperature water bath controlled at 25.0 + 0.1 degrees C. The N_2 gas is bubbled through a 50 mM $Ba(OH)_2$ solution to remove CO_2, then through deionized water to humidify the gas stream, and remove any residual hydroxide.

Methods

Calibration of the potentiometric titration system
The electrode response is calibrated by HCl/NaOH titration at the ionic strength of interest, and a plot of electrode potential in millivolts as a function of solution pcH is made to determine a function that describes the electrode response over the pcH range of approximately 2.5 to 12. Refer to the discussion in the Introduction section, particularly of equation (10), for an explanation of the theory.

Stoichiometric acid dissociation constant of hypochlorous acid
In a typical experiment the titration vessel is filled with 49.00 ml of NaCl solution, and 1.00 ml of stock OCl^- solution is added. The titration vessel is fitted to the automatic titration system, purged with N_2, and allowed to reach thermal equilibrium with the controlled temperature water bath. Standardized HCl, adjusted to the same ionic strength as the solution in the titration vessel, is added with the automatic buret titration system, and the electrode potential in mV is recorded after each addition of titrant.

Spectrophotometric titration
A typical spectrophotometric titration was performed as follows: 49.50 ml of NaCl solution was measured into a titration vessel, to which was added 0.500 ml of stock OCl^- solution. The titration vessel was fitted to the programmable automatic buret system,

Information Only

purged with N_2 gas, and allowed to reach thermal equilibrium with a 25.0 $\pm$ 0.1° C water bath. The solution potential was measured with a pH electrode that was calibrated by HCl/NaOH titration. A 4.00 ml aliquot was withdrawn for measurement of the UV-VIS spectrum. Small amounts, usually 0.200 ml, of standardized HCl were then delivered by buret to the titration vessel, the solution was allowed to re-equilibrate, then a subsequent sample withdrawn for spectrophotometric measurement.

Results

Examples of plots of calibration data in 1, 1.9, and 5 molal NaCl are given in Figure 1. Examples of potentiometric titration of hypochlorite with HCl at 1, 1.9, and 5 molal NaCl are given in Figure 2 and Table I. Figures 3 and 4 present spectrophotometric titrations of hypochlorous acid at 1 and 5 molal NaCl.

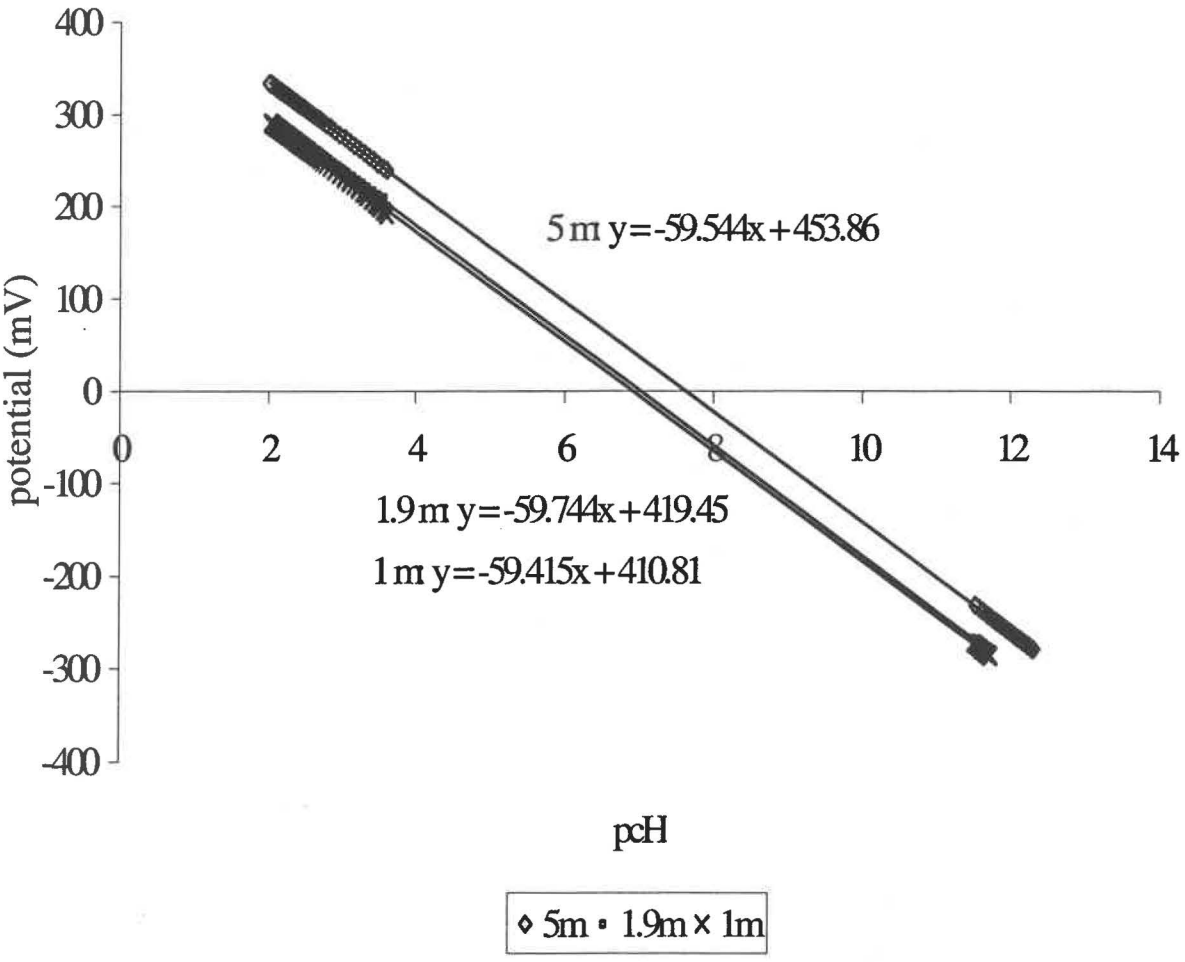

Figure 1. Electrode calibration at different ionic strengths (NaCl)

Information Only

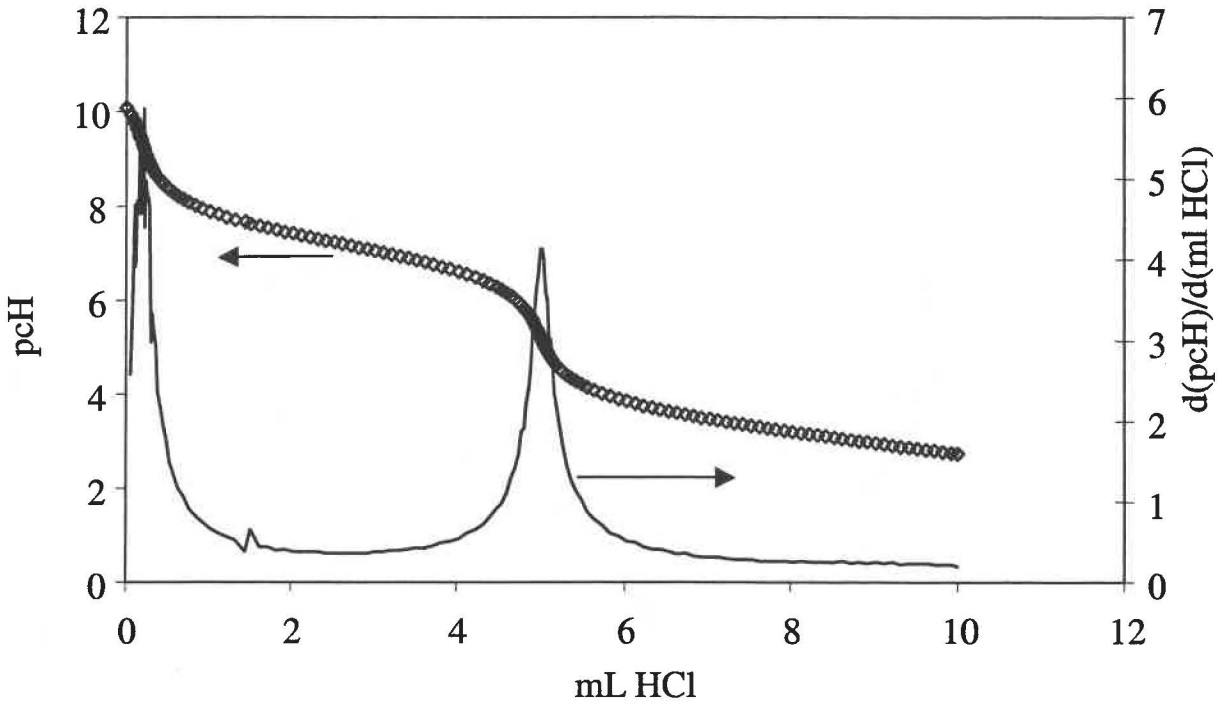

Figure 2. Example of titration of hypochlorite, in medium 1 m NaCl. Solid line = 1st derivative, diamonds = titration data points. Arrows indicate y-axis scale for the titration data and 1st derivative curve.

Table 1. Stoichiometric acid dissociation constants of HOCl in 1, 1.9, and 5 molal NaCl

molality	pKa1	pKa2
1	9.92	7.27
1	9.88	7.28
1	9.95	7.3
1.9	10.017	7.35
1.9	9.938	7.317
1.9	9.98	7.316
5	10.595	7.860
5	10.560	7.860
5	10.444	7.860

Information Only

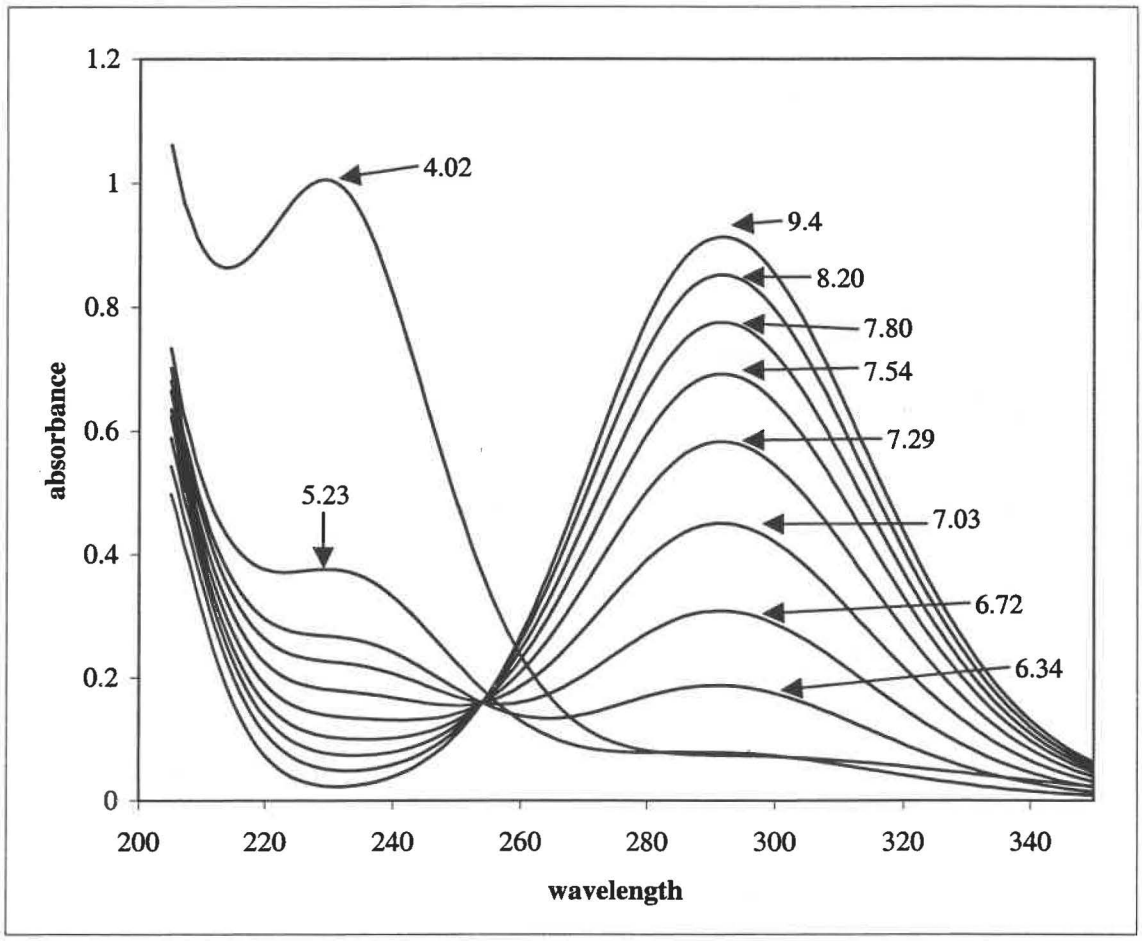

Figure 3. Spectrophotometric titration of HOCl in 1.0 molal NaCl solution. The pcH value for each spectrum is indicated. The deviation from the isosbestic point for pcH 5.23 and 4.02 indicate formation of a third species.

Information Only

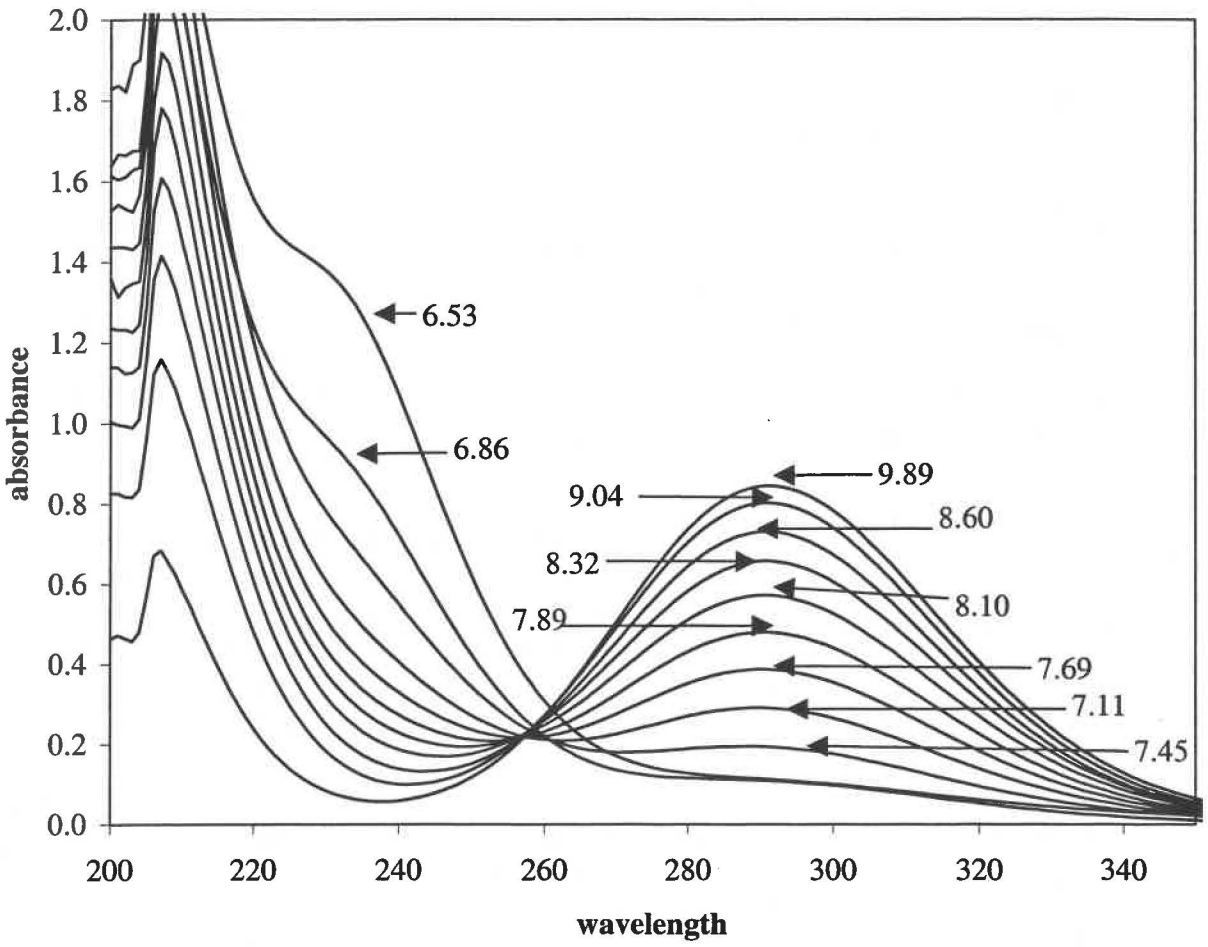

Figure 4. Spectrophotometric titration of HOCl in 5.0 molal NaCl solution. The pcH value for each spectrum is indicated. The deviation from the isosbestic point for pcH 6.53 and 6.86 indicate formation of a third species.

Information Only

Discussion

Data treatment

Calibration and HOCl potentiometric titration data are entered into Microsoft Excel for preliminary examination, which includes examination of the titration curves for identifiable titration endpoint(s) and first derivative analysis of inflection points. Refer to Figure 2 for an example. Approximate calculations of the stoichiometric acid dissociation constants may be made by using the first derivative curve of a titration curve to find the pcH at the half-equivalence point (after correction for the initial concentration of hydroxide). Further refinement of the value will be done with the off-the-shelf program "BEST" which has previously been described (Martell, 1988). Data analysis is currently in progress.

Spectrophotometric titrations

An isosbestic point is formed at the wavelength where two chromophores have identical molar absorptivities when multiple spectra are overlain and the total concentration of the chromophores are held constant. Formation of a sharp isosbestic point in titrations with constant analytical concentrations of chromophores usually indicates the presence of only two species. Conversely, a poor or non-existent isosbestic point often indicates either multiple species or poor experimental control. The isosbestic point shown in Figure 3 for the pcH range 9.4 to 6.34 in the 1 molal NaCl titration indicates that the two species are HOCl and OCl^- with the absorbance maximum at 230 nm due to HOCl and at 292 nm due to OCl^-. Deviation from the sharpness of the isosbestic point at pcH values of 5.23 and 4.02 indicate formation of an additional species. The time elapsed between generation of each spectrum was approximately 5 minutes. It was noted that, upon acidification, the sample container emitted a gas with a pungent odor, which was probably Cl_2. Additionally, it was found that raising the pcH by addition of OH^- to the solution regenerates a solution with a lowered concentration of hypochlorite due to loss of gaseous Cl_2. This observation leads to the conclusion that the protonation of hypochlorite is not a reversible process under these experimental conditions. The decomposition of hypochlorous acid in 5 molal NaCl becomes rapid when the solution pcH is about 1 unit greater than occurs in 1 molal NaCl, as shown in Figure 4. This is readily explained by the fact that the ionic activity coefficient of the hydrogen ion is about 1 log unit greater in 5 m NaCl than in 1 m NaCl. Therefore, it appears that the decomposition of hypochlorous acid, with production of Cl_2 is more facile in the neutral pcH region in high ionic strength solution.

Presence of hypochlorous acid has been invoked as responsible for maintenance of oxidized Pu in acidic conditions. Preliminary results of the present study indicate that hypochlorous acid rapidly decomposes in acidic high ionic strength solutions. When one of the reaction products is a gas, the thermodynamic reversibility of the process is dependent upon sample storage conditions. For example, purging or ventilation of the sample leads to loss of the volatile product with a concomitant change in the redox potential associated with the half-cell reaction of HOCl and the volatile product,

Information Only

presumably Cl_2. Cl_2 is sufficiently soluble in aqueous solutions to maintain an oxidizing environment, although its solubility is dependent upon its activity coefficient in a given electrolyte. The "salting out effect" usually leads to an increase of activity coefficients of non-ionic solutes as a function of ionic strength, as opposed to the approximately parabolic dependence of activity coefficients of ionic solutes on ionic strength. Therefore, it may be expected that the solubility of Cl_2 would decrease with increasing ionic strength, in solutions of indifferent electrolytes. However, chloride brines may not be indifferent with respect to Cl_2. For example, I_2 is much more soluble in solutions containing the I^- anion due to formation of I_3^- (Vogel, 1989). Nevertheless, it is unlikely that HOCl is responsible for maintenance of oxidizing conditions under acidic conditions, while Cl_2 seems a more probable candidate. As such, it also seems likely that maintenance of oxidizing conditions in acidic solutions of HOCl over periods of time longer than hours to days is due to the presence of Cl_2, which is in turn dependent on storage conditions.

Experiments are currently underway to measure decomposition rate constants for hypochlorous acid/hypochlorite as functions of pcH and electrolyte composition. The kinetic data are important for accurate, quantitative thermodynamic modeling of the long-term effects of hypochlorite generation. Decomposition rate constants can be used with radiolytic production rate constants to quantitatively determine steady state concentrations of hypochlorite, and consequently to make a quantitative determination of the effect on metal complexation or the redox potential associated with hypochlorite production.

References

Gray, E.T., Taylor, R.W., Margerum, D.W., Kinetics and Mechanisms of the Copper-Catalyzed Decomposition of Hypochlorite and Hypobromite. Properties of a Dimeric Copper (III) Hydroxide Intermediate, Inorg. Chem. 16 (12) 3047 (1977)

Martell, A. E., Motekaitis, R.J., *The Determination and Use of Stability Constants*, VCH Publishers, New York, 1988

Vogel, A.I., Vogel's Textbook of Quantitative Chemical Analysis, 5th Ed. Revised by Jeffery, G.H., Bassett, J., Mendham, J., Denney, R.C., Longman Scientific & Technical. N.Y., 1989

Pashalidis, I., Kim, J.I., Lierse, Ch., Sullivan, J.C., The Chemistry of Pu in Concentrated Aqueous NaCl Solution: Effects of Alpha Self-Radiolysis and the Interaction between Hypochlorite and Dioxoplutonium (VI), Radiochim. Acta 60, 99, 1993

Villareal, R. Presentation at Carlsbad Environmental Monitoring & Research Center, January 16, 2002

Information Only

This page intentionally left blank

Information Only

IMPORTANT NOTICE: The current official version of this document is available via the Sandia National Laboratories NWMP On-line Documents web site. A printed copy of this document may not be the version currently in effect.

SANDIA NATIONAL LABORATORIES
WASTE ISOLATION PILOT PLANT
TEST PLAN, TP 02-01

Complexation Behavior of Hypochlorite with Metal Ions

Revision 0

Task 1.3.5.4.1.2

Effective Date: 12/05/01

Prepared by:

Donald Wall (6822)

Sandia National Laboratories
Carlsbad, NM

WIPP:1.3.5.4.1.2:TD:QA:DPRP1:NF:Test Plan for Complexation Behavior of Hypochlorite with Metal Ions, TP 02-01

© 2001 Sandia Corporation

Information Only

85

1.0 Approval Page

Author:	*Original signed by Donald Wall* Donald Wall (6822)	*11/15/01* Date
Technical Reviewer:	*Original signed by L.H. Brush* Larry Brush (6822)	*11/16/01* Date
Management Reviewer	*Original signed by M.K. Knowles* M. Kathryn Knowles (6821)	*11/16/01* Date
QA Reviewer	*Original signed by Greg Miller* Greg Miller (6820)	*11/16/01* Date

Information Only

86

2.0 Table of Contents

Information Only

3.0 List of Acronyms

$\mathcal{A}_n$	Thermodynamic activity
An	Actinide
An(III)	Actinide in the +III oxidation state
An(IV)	Actinide in the +IV oxidation state
An(V)	Actinide in the +V oxidation state
An(VI)	Actinide in the +VI oxidation state
C	Coulomb
CCA	Compliance Certification Application
Ce	Cerium
$Cl^{\bullet}$	Atomic chlorine free radical
$Cl_2^{\bullet-}$	Molecular chlorine free radical
ClO_3^-	Chlorate
DBR	Direct Brine Release
E^0	Standard reduction potential
EDTA	Ethylenediaminetetraacetic acid
ERDA-6	Descriptive label applied to a Castile brine composition
F	The faraday constant, (96,487 coulombs)
Fe	Iron
GWB	Generic weep brine
H^+	Hydrogen ion
$H^{\bullet}$	Atomic hydrogen free radical
HCl	Hydrochloric acid
HOCl	Hypochlorous acid
$HOCl^{\bullet-}$	Hypochlorous acid, anionic free radical
ICP-OES	Inductively coupled plasma optical emission spectroscopy
J	Joule
Ln	Lanthanide
NaOH	Sodium hydroxide
Nd	Neodymium
NIST	National Institute of Standards and Technology
$OH^{\bullet}$	Hydroxyl free radical
OCl^-	Hypochlorite
OH^-	Hydroxide
pK_a	Negative base 10 logarithm of an acid dissociation constant
R	Ideal gas constant, 8.314 J/molK
T	temperature, in degrees Celsius or kelvins
UV-VIS	Ultraviolet-Visible (spectroscopy)
WIPP	Waste Isolation Pilot Plant
ΔG	Gibbs free energy of reaction
α-particle	High energy particle expelled from a nucleus during an α-decay process
β-particle	A positron or negatron expelled from a nucleus during a β-decay process
β_{pqr}	Stability constant for a metal/ligand complex
γ	Activity coefficient (not related to γ-ray)

Information Only

γ-rays	High-energy photons emanating from a nucleus due to a nuclear decay process
μ	ionic strength

4.0 Revision History

This is the first version of this test plan. Subsequent revisions will be done in accordance with the Sandia National Laboratories Nuclear Waste Management Program Procedures: NP 20-1 Test Plans, NP 6-1 Document Review Process and NP 6-2 Document Control Process.

5.0 Purpose & Scope

Complexation of actinide ions with organic ligands solubilizes the metal ions, and must be quantified to make meaningful predictions of dissolved actinide concentrations. Well defined values for complexation constants (commonly called stability constants) as well as solubility product constants are necessary to calculate actinide solubilities. Accurate solubility values are critical parameters for evaluation of releases of radioactivity from a permanent transuranic waste disposal site. Any repository component that causes an increase in actinide solubilities also causes an increase in the magnitude of overall releases, with concomitant adverse effects on repository performance. Much research has been done to determine the stability constants of metal complexes with numerous organic ligands in high ionic strength solutions.[1-10] The four ligands of greatest concern are acetate, citrate, oxalate, and ethylenediaminetetraacetate (EDTA), due to the large amounts destined to be emplaced within the repository, and their high stability constants with actinide ions. The quantities of these ligands that are in the projected WIPP inventory and their expected concentrations in WIPP brines, are summarized in Table I.

Table I. Projected Quantities and Concentrations of Organic Ligands in the WIPP

Ligand	Inventory Amount (grams)	Concentration (mol/l) (a)
acetate	1.3×10^{6}	5.2×10^{-4}
citrate	1.4×10^{8}	3.6×10^{-3}
oxalate	1.6×10^{6}	2.3×10^{-4}
EDTA	2.3×10^{4}	2.0×10^{-6}

(a) based on an inundated repository volume of 29,841 m^3. Data taken from Table SOTERM-4 in the CCA[11]

Stability constants of the actinides with these ligands have been measured by both solvent extraction and potentiometric titration, and are summarized in Table II.[12] The data in Tables I and II suggest that the organic ligand of greatest concern is citrate.

It has been shown that hypochlorite (OCl^-) is a principal product of α-radiolysis in brine solutions, and that the concentration of OCl^- is dependent upon brine composition and the

Information Only

rate of bombardment of α-particles upon the brine.[13] The complexing ability of OCl^- with actinide ions has not been systematically studied, although Kim has reported formation of OCl^- complexes with PuO_2^{2+}.[14] Experimentally observed OCl^- concentrations, and a brief summary of likely complexation properties are discussed within this document. Previous reports suggest that OCl^- may be present in millimolar concentrations in the immediate vicinity of α-emitting radioactive material.[13,14]

Table II. Stability Constants of Actinide Ions with Organic Ligands (a)

Ligand	Actinide ion	NaCl conc. (m)	log β (b)
Acetate	Th^{4+}	0.3 to 5	3.68 - 4.18
	UO_2^{2+}	0.3 to 4	2.23 - 3.09
	NpO_2^+	0.3 to 4	1.05 - 1.8
	Am^{3+}	0.3 to 4	1.44 - 2.2
Citrate	Th^{4+}	0.1 to 5	9.31 - 10.18
	UO_2^{2+}	0.3 to 4	7.07 - 7.32
	NpO_2^+	0.1 to 5	2.39 - 2.56
	Am^{3+}	0.3 to 4	4.84 - 5.9
Oxalate	Th^{4+}	0.3 to 4	7.04 - 7.47
	UO_2^{2+}	0.3 to 4	5.82 - 6.7
	NpO_2^+	1 to 5	3.62 - 4.63
	Am^{3+}	0.3 to 4	4.17 - 4.63
EDTA	Th^{4+}	0.3 to 4	15.56 – 16.94
	UO_2^{2+}	0.3 to 4	10.75 – 12.16
	NpO_2^+	0.3 to 4	5.45 - 6.7
	Am^{3+}	0.3 to 4	13.76 - 15.1

(a) Data taken from Table SOTERM-5 in the CCA.[12]
(b) The range is due to variations in solution composition and experimental uncertainty

Information Only

90

The objectives of the studies proposed in this test plan are to:

- Determine the stability constants for complex formation of OCl^- with metal ions
- Determine and measure solution conditions that have an impact on complex formation of metal ions with OCl^-

Intended use of the data:
Actinide solubility affects the magnitude of the contribution of the direct brine release to the generation of a Complementary Cumulative Distribution Function (CCDF) which is used as an EPA mandated evaluation of regulatory compliance.
The results of this study will be used to determine whether complexation by radiolysis products, such as OCl^-, will contribute to increased actinide solubility in the WIPP, which may, in turn affect compliance.

5.1 Radiolysis

The effect of radioactive decay on aqueous solutions is markedly dependent upon the type and energy of radiation involved. For example, beta particles, with a charge of $\pm$ 1.602×10^{-19} C and a mass of 9.11×10^{-31} kg, have much larger rates of energy transfer to target material than high energy photons, such as γ-rays, which have neither charge nor mass. The α-particles, with charges of $+3.204 \times 10^{-19}$ C and masses of 6.647×10^{-27} kg, exhibit much larger rates of linear energy transfer than β particles, leaving intense tracks of ionized target material, including many atomic and molecular species in highly excited states. In general, α-particles have ranges of 30-70 μm in water.[15] The ionization tracks of α-particles in aqueous solutions include numerous hydrogen, oxygen, and hydroxyl free radicals. Ordinarily, free radicals have very short lifetimes in solution due to rapid reaction with solute and solvent molecules. Combination processes become increasingly important in the diffusive control-limited environment surrounding particle tracks of high linear energy transfer species. H_2 and O_2 are two well-known gas generation products due to radiolysis of water and recombination of the hydrogen free radicals, $H^\bullet$, or the oxygen free radical, $O^\bullet$. The superscript dot indicates a free radical species. Recombination processes may also yield hydrogen peroxide (H_2O_2) as a product of the reaction of two hydroxyl radicals. Also significant, but dependent upon the solution composition are generation of molecular chlorine (Cl_2), hypochlorous acid (HOCl) and OCl^-. Specific mechanisms for generation of radiolysis products are described in the following section.

In the following discussion, the symbol "$\rightarrow$" denotes a thermodynamically irreversible process, while the symbol "$\rightleftharpoons$" indicates a thermodynamically reversible process. Water radiolysis in the tracks of α-particles leads to generation of numerous species, such as:

$$H_2O \xrightarrow{\alpha} e^-_{aq}, OH^\bullet, H^\bullet\ H_2O_2, H_2, O_2, H^+, OH^- \qquad (1)$$

Information Only

91

Aquated electrons and free radical species are very reactive, combining with many other dissolved species. Additional reactions take place in the presence of significant concentrations of other solute species, such as Cl^-. Participation of Cl^- in radiolytically initiated reactions leads to generation of additional chemical species due to subsequent oxidation-reduction reactions. For example, the hydroxyl radical can oxidize chloride, yielding the hypochlorous acid anion $HOCl^{\bullet-}$

$$OH^\bullet + Cl^- \rightarrow HOCl^{\bullet-} \quad (2)$$

The hypochlorous acid anion is also a radical species that equilibrates rapidly with H^+ to give the chlorine radical

$$HOCl^{\bullet-} + H^+ \rightleftharpoons Cl^\bullet + H_2O \quad (3)$$

The likelihood of the chlorine radical combining with chloride is greater in solutions with high chloride content:

$$Cl^\bullet + Cl^- \rightleftharpoons Cl_2^{\bullet-} \quad (4)$$

$Cl_2^{\bullet-}$ reacts rapidly to produce the Cl_3^-, which is more stable than $Cl_2^{\bullet-}$,[16]

$$Cl_2^{\bullet-} + Cl_2^{\bullet-} \rightarrow Cl_3^- + Cl^- \quad (5)$$

The Cl_3^- species is in equilibrium with other chlorine species, ultimately producing hypochlorite:

$$Cl_3^- \rightleftharpoons Cl_2 + Cl^- \quad (6)$$

$$Cl_2 + H_2O \rightleftharpoons HOCl + Cl^- + H^+ \quad (7)$$

$$HOCl \rightleftharpoons H^+ + OCl^- \quad (8)$$

It has been reported that the production of HOCl and OCl^- depends on the Cl^- concentration.[13] The dependence of OCl^- concentration on NaCl concentration is illustrated in Figure 1.

Information Only

92

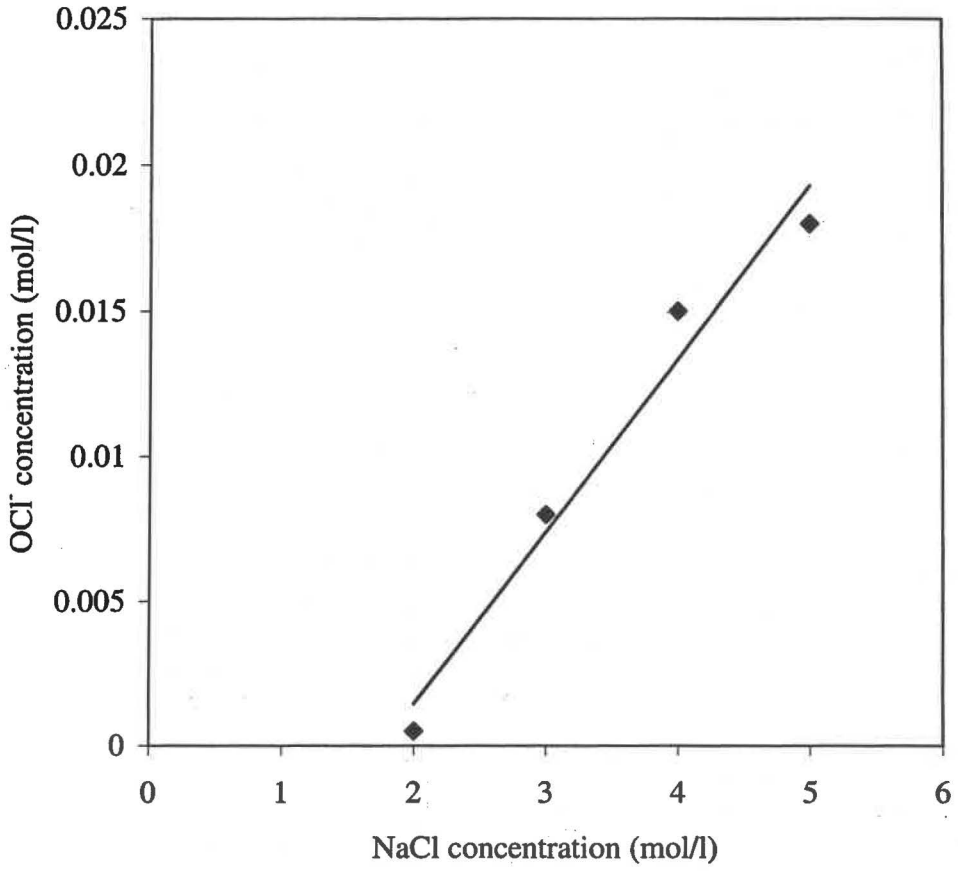

Figure 1. Generation of hypochlorite as a function of aqueous NaCl concentration. Data used to generate this figure were taken from reference 17. Each sample contained 1 Ci/L of ^{238}Pu introduced as finely divided precipitate of Pu(VI)hydroxide. The solutions were adjusted to a pH of ca. 12. No error bars are included because the literature reference includes insufficient data to estimate or evaluate the uncertainty. The equation for the linear best fit line is $y = 0.0059x - 0.0105$.

Hypochlorite production is not a significant process for chloride concentrations less than ca. 1.8 molar at radioactivity levels of 1 Ci/L. The minimum concentration of Cl^- required for hypochlorite generation most likely reflects the decreased probability of reactions (4) and (5) taking place. Conversely, the data indicate that the reactions leading to HOCl production in 5 M NaCl solution produce significant quantities of OCl^-, (nearly 20 mM), in the presence of 1Ci/L of α-emitting radionuclides.

The pK_a value of HOCl is 7.43 (μ=1.0 $NaClO_4$, T= 25° C), indicating that at pH relevant to WIPP conditions (pH≈9-10) the conjugate base (OCl^-) will be the predominant form.[18] The symbol "μ" indicates ionic strength.

Information Only

5.2 Hypochlorite as a Ligand

Hypochlorite can act as a ligand, and has been reported to form complexes with PuO_2^{2+}, which are illustrated in equations (9) and (10):

$$PuO_2^{2+} + OH^- + OCl^- \rightleftharpoons PuO_2(OH)(OCl) \quad (9)$$

$$PuO_2^{2+} + 2OCl^- \rightleftharpoons PuO_2(OCl)_2 \quad (10)$$

Stability constants for reaction (9) have been reported as log $\beta_{1\text{-}11}$ = 14.0 at pH=6.7 and log $\beta_{1\text{-}11}$ = 14.5 at pH= 8.4 (μ=0.55 M, T=22° C). The stability constant for reaction (10) is log β_{102} = 10.3 (μ=0.55, T=22° C), respectively.[14]

The short range of α-particles in solution can cause chemical environments that feature greater concentrations of radiolysis products in the immediate vicinity of radioactive sources than in the bulk solution, i.e. the actinides and ligands will occur together in close proximity. In fact it is likely that dissolution processes in localized heterogeneous microenvironments in a steady-state, non-equilibrium condition will be governed not by average solution concentrations of complexing ligands, but by concentration gradients that increase in magnitude as a function of proximity to the surface of the radiation-emitting solid. Figure 1 demonstrates that significant amounts of hypochlorite may be generated in NaCl solutions, especially brines. It is not necessary for multiple curie levels to be dispersed in brine to generate high local concentrations of hypochlorite because localized solution conditions will be established in the environs of the α-emitting radioactive source.

Figure 2 illustrates the steady state concentration of OCl^- generated as a function of radioactivity in 5 molar NaCl solution. The data points at ca. 6 and 12 Ci/L had not reached their respective steady state concentrations, therefore, there is not enough data to determine the type of function that correctly defines hypochlorite generation. However, the high-radioactivity solutions are not generally representative of conditions expected to persist within the WIPP.

Information Only

94

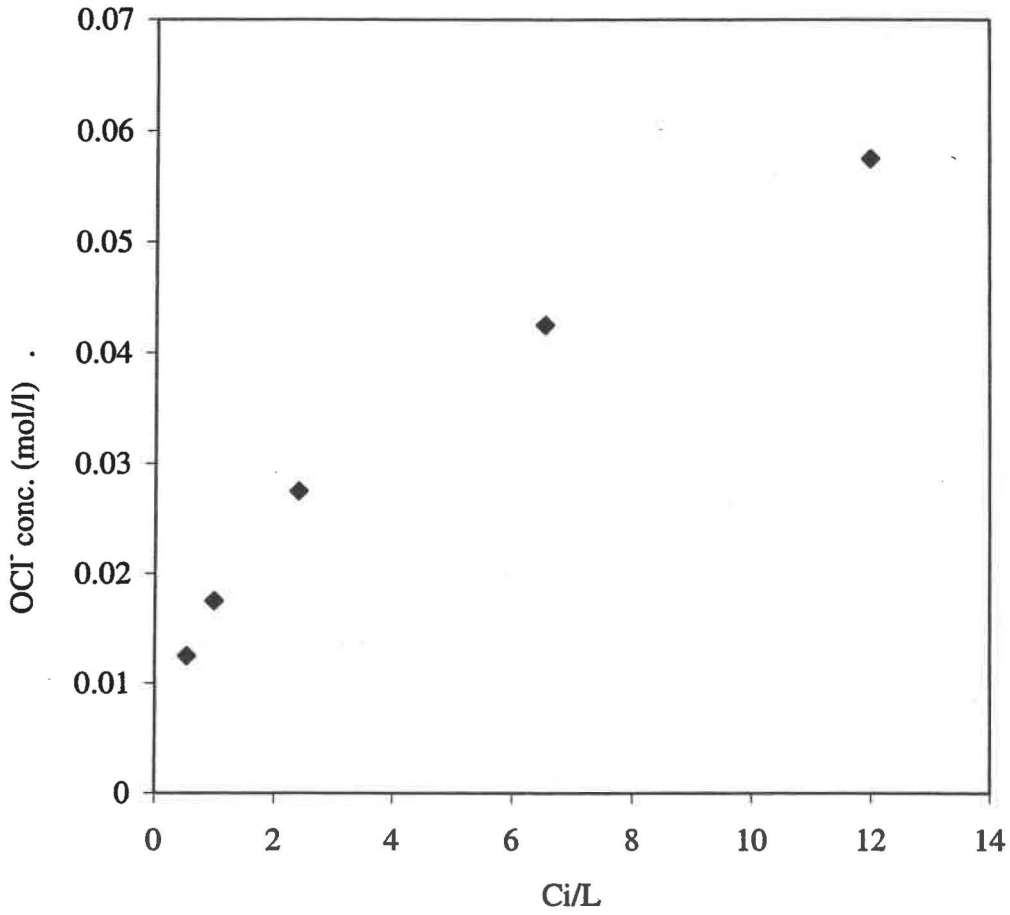

Figure 2. Generation of a hypochlorite as a function of radioactivity in 5 mol/L NaCl at pH ca. 12. The data used to generate the data points in this figure were taken from reference 17.

5.3 Prediction of log β

The An(III,IV,V,VI) ions, which behave as hard acids due to their relatively low polarizability and high ionization potentials, interact with ligands primarily by electrostatic interaction.[19] As a result, an extended form of the Born equation, which relates electrostatic attraction to the Gibbs free energy of formation, may be used to make an approximate prediction of the magnitude of the stability constant for trivalent actinides or lanthanide analogs when the stability constant for another actinide/ligand pair is known.[20] The relationship is illustrated by equation (11)

$$\Delta G = \frac{-N_A e^2 Z_1 Z_2}{418.7 D_e d_{12}} - \nu RT 55.5 + \sum \ln f(I) \qquad (11)$$

Information Only

where ΔG is the Gibbs free energy of complex formation, N_A is Avogadro's number, e is the fundamental unit of charge, Z_1 is the charge on the metal ion, Z_2 is the charge on the ligand, D_e is the effective dielectric constant (57 for An^{3+} or Ln^{3+}, 40 for An^{4+}, 65 for AnO_2^+, 55 for AnO_2^{2+})[21], d_{12} is the distance between the metal and ligand, m is the change in number of the reacting species, and is $\Sigma \ln f(I)$ the activity coefficient term to correct for effect of ionic strength. The relationship between the Gibbs free energy and the stability constant, β, is illustrated by the relationship in equation (12)

$$\Delta G = -RT\ln\beta \qquad (12)$$

where R is the ideal gas constant, 8.314 J/molK and T is the absolute temperature in kelvins. Substituting equation (12) into equation (11) gives:

$$\ln\beta = \frac{N_A e^2 Z_1 Z_2}{RT418.7 D_e d_{12}} - \nu RT55.5 + \sum \ln f(I) \qquad (13)$$

Equation (13) may be simplified for reactions involving the same number of reacting species and at constant ionic strength:

$$\log\beta = \frac{AZ_1Z_2}{D_e d_{12}} + B \qquad (14)$$

Equation 14 indicates that a plot of the logarithm of the stability constants vs. charge on the metal ion for complexes of actinides with a given ligand should be linear when corrected for variations in the effective dielectric constant and the metal-ligand distance. A useful modification of equation (14) is given by equation (15)[21]

$$\log\beta_n(A) = \log \beta_n(B) \times (Z_A/Z_B) \times (D_B/D_A)(d_{B/A}) \qquad (15)$$

The effective charge on the metal ion for the four common actinide oxidation states may be summarized as:[22]

$$\begin{array}{ccccccc} Pu^{4+} & > & PuO_2^{2+} & > & Pu^{3+} & > & PuO_2^+ \\ Th^{4+} & > & UO_2^{2+} & > & Am^{3+} & > & NpO_2^+ \\ 4 & > & 3.3 & > & 3 & > & 2.3 \end{array}$$

Plutonium follows the same pattern for effective charges in the corresponding oxidation states. The larger effective charge on the AnO_2^{2+} ion relative to the An^{3+} ion often causes the magnitude of the logarithm of the stability constants for AnO_2L^{2-n+} complexes to be about 10-30% greater than the respective complexes with An^{3+} when steric effects to not

Information Only

96

interfere. Therefore, the magnitude of β_{102} for the Am^{3+} (and Nd^{3+}) complexes with OCl^- should be about 8-9 log units.

5.4 Comparable ligands

A survey of the National Institute of Standards and Technology (NIST) stability constant database reveals a paucity of data for complexes of metals with hypochlorite. Cyanate (OCN^-) may be expected to exhibit similar complexion behavior to hypochlorite since the pseudohalogen cyanide group replaces the chlorine atom. Cyanate exhibits linkage isomerism, therefore, this comparison would be valid only for coordination through the oxygen atom of the cyanate group. HOCN has pKa = 3.48 (μ=0 M, T=25° C), making it a weaker conjugate base than OCl^-. Therefore OCN^- complexes formed through the oxygen atom should be weaker than corresponding complexes with OCl^-. Unfortunately, the database for complexation with cyanate is limited to Co^{2+} and Ag^+, both of which may coordinate through the nitrogen atom of cyanate, and neither of the metal ions are suitable analogs for lanthanides or actinides.

The halite anion ClO_3^- may also be generated as a result of α-radiolysis in chloride brine. Ligands with higher pK_a values form stronger conjugate bases, with attendant greater affinity for metal cations. In general, the stabilities of complexes are proportional to the pK_a values of the protonated form of a ligand. The pK_a value for $HClO_3$ is –2.7 (μ=0.10 M $NaClO_4$, T=298 K), making ClO_3^- a rather weak base. Most ligands, with $pK_a<2$ (including ClO_3^-) form only outer sphere complexes with actinides, and it has been shown that $LnClO_3^{2+}$ and $UO_2ClO_3^+$ conform to this behavioral model.[23] In contrast, OCl^- most likely forms inner-sphere complexes with actinides; with the accompanying differences in the nature of the enthalpy and entropy driving forces of the complexation reaction. As a result, halates do not make useful analogs for hypohalite anions.

5.5 Effect of Complexing Agents on Actinide Solubility

The effect of ligand complexation upon actinides under WIPP conditions causes an increase of actinide solubility and mobility. Actinide solubility is controlled by the extent of complexation and by the solubility product constant of actinide precipitates, or actinide bearing solids in which actinides are co-precipitated as members in a non-actinide host phase. The dissolution of actinide precipitates may be generally described by the equation:

$$(An_p^{n+}B_q^{t-})_s \rightleftharpoons pAn^{n+} + sB^{t-} \qquad (16)$$

where np = st, An represents an actinide cation with overall charge of n+, and B is a counter-ion that participates in formation of a precipitate.

The solubility product constant is generally expressed as

$$K_{sp} = \{An^{n+}\}^p\{B^{t-}\}^s \qquad (17)$$

Information Only

where the braces indicate thermodynamic activities.

Complexation of the actinide ion in solution will cause further dissolution of the solid phase to compensate for perturbation of the equilibrium expressed in equation (16). Formation of actinide/ligand complexes is described by equation (18), where charges on the metal and ligand are omitted for simplicity:

$$pAn + H_qL_r \rightleftharpoons An_pH_qL_r \tag{18}$$

The thermodynamic stability constant for such a complex is defined as

$$\beta_{pqr} = \frac{\{An_pH_qL_r\}}{\{An\}^p\{L\}^r} \tag{19}$$

The relationship between the solubility product constant of an actinide bearing solid and the solubilizing effect of complexation is illustrated by substituting equation (19) into equation (17):

$$\frac{K_{sp}}{\{B^{t-}\}^s} = \frac{\{An_pH_qL_r\}}{\beta_{pqr}\{L\}^r} \tag{20}$$

The total solubility of an actinide ion is the sum of the free metal ion concentration and the concentrations of all other soluble species. Equation (19) indicates that a complexing ligand has the capacity to increase solubility (and mobility) of actinides.

5.6 Liquid/Liquid Extraction Method for Determination of Stability Constants

Liquid/liquid extraction is a well-developed method and has been extensively used in support of the WIPP actinide science program to determine the stability constants of actinide metal ions and other metal cations with numerous different ligands.[1-3,5-8,10] The distribution of a metal ion between two immiscible phases in the presence of an organophilic extractant is described by a distribution coefficient:

$$D = \frac{\sum[M_{org}]}{\sum[M_{aq}]} \tag{21}$$

where $\Sigma[M_{org}]$ is the sum of the concentrations of all metal species in the organic phase and $\Sigma[M_{aq}]$ is the sum of the concentrations of all metal species in the aqueous phase. An aquophilic complexing agent may exert a competitive influence on the metal distribution,

Information Only

98

that is described by equation (22):

$$\frac{D_0}{D} - 1 = \sum_{1}^{n} \beta'_{10n}[L]^n \qquad (22)$$

where D_0 is the distribution coefficient in the absence of the complexing ligand, β_{10n} are the successive apparent stability constants, and [L] is the ligand concentration. The apparent stability constant is related to the true stability constant as expressed by equation (23):

$$\beta'_{101} = \beta_{101} / (1 + \sum_{1}^{n} \beta_n^{OH^-} ([OH^-])^n + \sum_{1}^{n} \beta_n^{B^-} ([B^-])^n) \qquad (23)$$

where $\beta_n^{OH^-}$ is the n^{th} hydrolysis constant, $\beta_n^{B^-}$ is the n^{th} stability constant of the metal with the buffer, [OH^-] is the hydroxide concentration and [B^-] is the free buffer concentration.

In solvent extraction determination of stability constants, it is necessary that the complexing ligand and the metal/ligand complex are much more soluble in the aqueous phase than in the organic phase. This condition is often fulfilled when the metal ligand complex is charged, solvated with water molecules, or has ligands that exhibit aquophilicity through hydrogen bonding. Metal/hypochlorite complexes are expected to satisfy these conditions.

The Gibbs free energy of complex formation may be determined from stability constants by using equation (24):

$$\Delta G = -RT \ln \beta \qquad (24)$$

where R is the ideal gas constant, 8.314 J/molK, and T is the absolute temperature on the Kelvin scale.

5.7 Reduction Potentials

The oxidizing potential of a metastable system is not necessarily accurately measured by electrode potentiometric determination. Accurate potentiometric measurements require the redox reactions to be at equilibrium at the electrode surface and to be thermodynamically reversible, which is often not the case, especially when free radicals are intermediates. Electron transfer reactions that are not pH dependent (i.e. no metal/oxygen bonds are formed or broken) are very rapid. The equilibrium that is established between two oxidation states of a redox active metal, such as Fe, may serve

Information Only

99

as a useful indicator of the half-cell reduction potential under equilibrium but non-standard state conditions. The equilibrium concentrations may be ascribed to reaction of the metal to redox conditions established by other solution components.

If possible, an internal redox potential indicator will be used. For example, the standard reduction potential of the Fe^{2+}/Fe^{3+} couple is given in equation (25)

$$Fe^{3+} + e^- \rightarrow Fe^{2+} \qquad E^0 = 0.771 \text{ volts} \qquad (25)$$

The magnitude of the standard reduction potential indicates that Fe^{3+} can only exist to a significant extent in oxidizing solutions. It will be necessary to determine the value for the Fe^0/Fe^{2+} and Fe^{2+}/Fe^{3+}redox potentials under the conditions used in the proposed experiments. The standard reduction potential for the reaction of hypochlorite with water is given in equation (26), and is sufficiently oxidizing to drive equation (25) in the reverse direction

$$ClO^- + H_2O + 2e^- \rightleftharpoons Cl^- + 2OH^- \qquad E^0 = 0.81 \text{ V} \qquad (26)$$

The potential for the reaction in equation (26) can be calculated for non-standard state conditions using the Nernst equation:

$$E = E^o - \frac{RT}{nF} \ln \frac{[Cl^-][OH^-]^2}{[ClO^-]} \qquad (27)$$

where E is the half-cell potential for non-standard conditions, E^0 is the standard reduction potential, R is the ideal gas constant, T is the temperature on the Kelvin scale, n is the number of electrons in the half-reaction, and F is the faraday constant. Equation (27) can be simplified for T = 298 K and converting to base 10 logarithms:

$$E = E^o - \frac{0.059}{n} \log \frac{[Cl^-][OH^-]^2}{[ClO^-]} \qquad (28)$$

Therefore, the half-cell potential for equation (28) in 5 molar NaCl at pH = 9, and for 10 mM OCl^- is:

$$E = 0.81 - \frac{0.059}{2} \log \frac{[5][1x10^{-5}]^2}{[0.010]} = 1.025 \text{ v} \qquad (29)$$

Information Only

100

Determination of the standard reduction potentials of the Fe^{2+}/Fe^{3+} and/or Ce^{3+}/Ce^{4+}couples under the chemical conditions of the experiments proposed in this document may be performed and subsequently used as internal redox potential indicators. The pH dependent redox reactions that involve making or breaking of covalent metal/oxygen bonds may be very slow, particularly at high pH. Such an example is given as:

$$PuO_2^+ + 4H^+ + 1e^- \rightleftharpoons Pu^{4+} + 2\,H_2O \quad (30)$$

Reaction (30) is not a simple one-electron transfer reaction, and may take many hours to respond to changes in the oxidizing conditions of the solution. As a result, the equilibrium between the plutonium oxidation states depends not only upon solution conditions, but also the history of the solution., indicating that the redox state of the solution may not be uniquely defined.

5.8 Use of Analogs

The trivalent lanthanide Nd(III) will be used for stability constant determinations due to its redox stability and to its similarity in charge density to Am(III) and Pu(III). The use of lanthanide cations as analogs for the trivalent actinides is a widely accepted practice, and has been documented elsewhere.[21]

5.9 Brine Compositions

Compositions of WIPP Brine A and ERDA-6 and GWB are given in Table IV. The ionic strengths were calculated from data in Table IV with the equation

$$\mu = 1/2 \sum c_i z^2 \quad (31)$$

where μ represents the ionic strength, c_i is the concentration of component "i", and z is the charge on the ion. In this case, ionic strength is given in concentration units, rather than activities. The higher ionic strength of Brine A is predominantly due to the higher Mg^{2+} content.

Other metal cations such as Fe, Co, Ni, and Mn will be present in the WIPP in significant quantities as a result of corrosion of waste containers. The concentrations of these metals will be treated as controlled variables by systematically adding known amounts to samples in order to evaluate the effect upon solution behavior.

Information Only

101

Table IV. Chemical Components of WIPP Brines

Ion or Chemical Property	Brine A (a)	ERDA-6 (a)	GWB (b)
B^{3+} (mM)	63	20	156
Br^- (mM)	11	10	27
Ca^{2+} (mM)	12	20	14
Cl^- (mM)	4800	5350	5610
K^+ (mM)	97	770	467
Mg^{2+} (mM)	19	1440	1020
Na^+ (mM)	4870	1830	3570
SO_4^{2-}	170	40	178
ionic strength (M)	5.57	7.07	6.0

(a) data taken from Table SOTERM-1, Appendix SOTERM, Compliance Certification Application
(b) data taken from Reference 24

5.10 Activity Coefficients

The thermodynamic activity of solute components depends upon the ionic strength of the solution and is expressed by the following relationship:

$$\mathcal{A}_n = \gamma_n[N] \qquad (32)$$

where $\mathcal{A}_n$ is the thermodynamic activity of component N, γ_n is the activity coefficient which is dependent on ionic strength and solute composition, and [N] is the concentration.

Generality of the mathematical expressions that describe thermodynamic relationships is needed to develop predictive capability for solution equilibrium conditions. For example, thermodynamic parameters, such as stability constants, must be determined at a variety of ionic strengths to satisfactorily evaluate the activity coefficients in equation (32). This is a necessary part of WIPP related solution chemistry, largely due to the fact that the Salado and Castile brines are considerably different in composition, both of which differ from Culebra solutions.

5.11 Specific Tasks and Critical Variables to be Controlled and Measured

The acid dissociation constant of HOCl (pKa = 7.47, μ=1.0 M $NaClO_4$, T=25° C) has not been reported for concentrated electrolyte solutions. It will be necessary to determine the acid dissociation constant of HOCl at a variety of ionic strengths and with different

Information Only

solution components, i.e. in Brine A and ERDA-6 and GWB, in order to accurately calculate free OCl^- concentrations. It may be necessary to perform other experiments that are not delineated here in order to complete the defined tasks.

The goals described within this test plan may be divided into the following tasks:
Task 1: Determine the acid dissociation constant for HOCl as a function of ionic strength and electrolyte identity.
Task 2: Determine stability constants of Nd^{3+} with OCl^- as functions of ionic strength and electrolyte identity.

6.0 Experimental Process Description

6.1 Sample and Data Control

6.1.1 Critical variables to be measured and controlled

Variables that must be controlled in the types of experiments described within this document include:
- ionic strength
- pH
- temperature
- sample volume
- sample composition

Ionic strength will be controlled during sample preparation processes by preparing samples of known compositions. Solution pH will be controlled by adding small amounts of non-interfering acid or base, such as HCl or NaOH solution, and measured with a standard, calibrated pH meter equipped with a combination glass electrode. The temperature will be controlled, if necessary, by performing the experiments in sample containers designed for constant temperature, such as water jacketed cells connected to a controlled temperature circulator. Sample volumes will be measured with standardized volumetric glassware and calibrated Class A pipets, or calibrated autopipets. Sample composition will be determined by solution preparation using standard laboratory techniques with calibrated equipment. Deviations from these standards, such as allowing sample temperature to equilibrate with ambient temperature rather than remaining under controlled conditions, will be noted in the laboratory notebook, along with descriptions of the acceptability of such deviations and the impact upon the experiment.

6.1.2 Identification of special environmental conditions

Environmental conditions, including temperature regulation and occlusion of airborne contaminants, will be controlled by appropriate management of sample preparation, treatment and storage conditions. Relevant conditions will be recorded in the laboratory notebooks.

Information Only

6.1.3 Known sources of error and uncertainty

Sources of error include:

- pH measurement
- volume measurement
- weighing error
- impure reagent
- instrumental response error
- data transcription error

Errors of pH measurement will be minimized by calibration of measuring equipment with standard buffer solutions and by titration with standardized acid and base solutions. Standard procedures for instrumental pH measurement are widely practiced and published in peer reviewed literature. Procedures will be described in the laboratory notebook and relevant procedural references provided. Volume and weighing measurement error will be minimized by calibration of all volumetric and weighing equipment with accompanying documentation in the laboratory notebooks. All reagents will be A.C.S. reagent grade or better. If necessary, reagents will be purified by standard, documented procedures. Using manufacturer recommended calibration techniques with standardized samples will minimize instrumental response error. When possible, hardcopies of instrumental data output will be attached within the laboratory notebook.

6.1.4 Data Processing and Mathematical Models

Data processing may be done by hand calculation with the aid of an electronic calculator, or with a standard spreadsheet program, such as Microsoft Excel.

6.1.5 Sample Handling and Control Requirements

Standard procedures for sample identification, handling, storage, shipping, archiving and disposition have been described in Sandia National Laboratories Nuclear Waste Management Program Procedure NP 13-1. Sample handling will be performed under the guidance of NP 13-1.

Samples will be labeled with unique identification numbers, date, and a reference to specific laboratory notebook page(s).

Solutions, such as standardized stock metal solutions, will be handled and stored in accordance with documented procedures. Chemical stability of OCl^- in high ionic strength solutions is unknown. Appropriate preparation, treatment, and storage conditions must be experimentally determined. Stock solutions will be re-standardized as necessary.

6.1.6 Sample Disposal

Aqueous and organic solutions will be disposed of in accordance with standard operating procedures in place at the Sandia National Laboratories Carlsbad laboratory.

Information Only

6.1.7 Experimental Controls

Each experimental determination of the metal/ligand stability constant will be performed at least three times, with no less than two nominally identical samples used to determine values for each data point. Known quantities of reagents will be introduced into each sample, so mass balances may be calculated from the amount recovered from each phase, making internal and surrogate standard spikes generally unnecessary. It should be noted that experimental procedures may be altered such that spikes are included in experimental procedures if it is necessary to account for variations in instrumental response.

6.1.8 Data Identification and Use

Data that is amenable to written recording will be inscribed by hand in appropriate laboratory notebooks. Such information includes, but is not limited to:

- reagent and solution preparation and purification procedures and results
- sample preparation procedures
- sample composition and conditions e.g. pH, reagent volume, reagent concentration, temperature
- sample handling
- sample analysis procedures and results

6.1.9 Data Transfer and Reduction Controls

Typical data transfer is from instrumental output to laboratory notebook and from laboratory notebook to a spreadsheet program. Printed copies of spreadsheets with full explanations of spreadsheet calculations will be permanently attached to the laboratory notebook within the section dedicated to the pertinent experiment.

6.1.10 Identification, Segregation, Disposal of Erroneous Data

Data that is suspected to be erroneous will be tested by comparison to replicate samples or replicate experiments. Statistical justification for rejection of erroneous data will be provided within the laboratory notebook.

6.1.11 Measuring and test equipment

Measuring and test equipment, including but not limited to, the Sandia National Laboratories Carlsbad laboratory ICP-OES, balance, pipets, pH meter, UV-VIS spectrophotometer will be used in accordance with the Sandia National Laboratories Nuclear Waste Management Program Procedure NP 12-1, Control of Measuring and Test Equipment.

6.2 Reagents and Procedures

6.2.1 Reagents

Distilled deionized water will be used to prepare all aqueous solutions.

All aqueous and organic solutions will be filtered through 0.20 or 0.45 mm pore size

Information Only

membrane filters.

High purity OCl^- will be synthesized by one of several methods documented in peer-reviewed literature, or obtained from documented commercial sources. Possible methods include bubbling Cl_2 gas through carbonate free 0.6 M aqueous NaOH or passing Cl_2 gas through an HgO slurry with subsequent reduced pressure distillation into aqueous NaOH.[25,26]

Concentration of OCl^- may be determined spectrophotometrically (ε = 350 M^{-1} cm^{-1} at 292 nm) [25,27], by potentiometric titration, or by other appropriate, documented methods.

6.2.2 Metal Solutions

Lanthanide solutions will be standardized by published procedures, such as complexometric titration with volumetric standard EDTA solution and xylenol orange indicator.[27]

6.2.3 Electrolyte Solution Compositions

The proposed work will be conducted in solutions of four different general composition types:

1. NaCl at the following ionic strengths 0.01, 0.1, 0.2, 0.3, 0.5 1, 2, 3, 4, 5 molal
2. Modified WIPP Brine A
3. Modified WIPP ERDA-6
4. Modified GWB

Brine A, ERDA-6 and GWB are saturated solutions, so loss of small amounts of water, (e.g. by evaporation), causes precipitation, and possible formation of lanthanide-bearing solids, either as co-precipitates, or as adsorbates onto the crystal surfaces of solids. Using a diluted form of the brine in order to remain below saturation most easily mitigates the potential for manifestation of such an uncontrolled variable. Consequently, modified forms of Brine A, ERDA-6, and GWB will be prepared that are diluted by 5% on the molar scale.

6.2.4 Experimental Procedures

Sample preparation and analysis procedures, (weighing, pipetting, etc.) are parts of standard laboratory analytical procedures. Instrumental analyses will be performed in accordance with written procedures that have been supplied by the instrument manufacturer, or other documented procedures that have been demonstrated to be appropriate.

A general description of the experimental process is supplied here, but it will be necessary to experimentally determine specific parameters, such as appropriate reagent concentrations. In a typical experiment, a series of glass liquid scintillation vials (or other appropriate sample vessels), (≈20 ml) will be filled with 5 ml of the aqueous phase and 5 ml of the organic phase. The aqueous phases will contain varying concentrations of the complexing ligand. Other variables, such as pH, ionic strength, temperature,

Information Only

extractant concentration and volumes of the phases, will be monitored. The vials will be mechanically shaken long enough to ensure equilibration of complex formation and interphase transfer reactions. The length of equilibration time must be experimentally determined, but it usually ranges between 15 minutes and several hours. After equilibrium has been reached, the sample containers may be centrifuged to assist in phase separation, then an aliquot removed from each phase for measurement of distribution ratios of the metal ion.
Metal ion concentrations in the sample aliquots may be measured by a variety of techniques, such as UV-VIS spectroscopy, or ICP-OES. ICP-OES or another documented technique will be employed to measure phase distribution of Nd, and other metals that will be systematically added to the solutions, such as Fe, Co, and Ni.

7.0 Training and Other Standard Procedures

All personnel participating in the work described in this Test Plan will be trained and qualified for the assigned tasks. This requirement will be implemented in accordance with NWMP procedure NP 2-1, "Qualification and Training." Evidence of qualification and training will be documented with Form NP 2-1-1 *Qualification and Training*. Additionally, the following NWMP Procedures and Project Specific Procedures are applicable:

SOP-C001: "Standard Operating Procedure for Activities in the SNL/Carlsbad Laboratory Facility."
SP 13-1 "Chain of Custody
NP 6-1 "Document Review Process"
NP 13-1 "Sample Control"
NP 12-1 "Control of Measuring and Test Equipment"
NP 20-1 "Scientific Notebooks"
NP 2-1 "Qualification and Training
NP 17-1 "Records"

8.0 Health & Safety

The health and safety requirements relevant to the tasks for work in this test plan are described in SOP-C001

9.0 Permitting/Licensing

There are no special licenses or permitting requirements for the work described in this test plan.

10.0 References

1. Complexation and Ion Interactions in Am(III) ETDA/NaCl Ternary System; J. Chen, G.R. Choppin, R. Moore, Actinide Speciation in High Ionic Strength Media, D. Reed Ed., Kluwer Academic/Plenum Publishers, N.Y., USA, p. 187, (1999)

2. UO_2^{2+} and NpO_2^{+} Complexation with Citrate in Brine Solutions; M. Bronikowski,

Information Only

O. Pokrovsky, M Borkowski, G.R. Choppin, , Actinide Speciation in High Ionic Strength Media D. Reed Ed., Kluwer Academic/Plenum Publishers, N.Y., USA, p. 177, (1999)

3. Neptunium (V) Complexation by Acetate, Oxalate, and Citrate in $NaClO_4$ Media at 25° C; G.R. Choppin, O. Pokrovsky, Radiochim. Acta, 79 167 (1997)

4. Stability of Plutonium(VI) in Selected WIPP Brines; D. Reed, S. Okajima, M. Richmann, Radiochim. Acta 66/67, 105 (1994)

5. Interaction of Neptunyl(V) and Uranyl(VI) with EDTA in NaCl Media: Experimental Study and Pitzer Modeling; M. Bronikowski, G.R. Choppin, R. Moore, O. Pokrovsky, Radiochim. Acta, 80 23 (1998)

6. Thermodynamic Modeling of Actinide Complexation with Acetate and Lactate at High Ionic Strength; M. Borkowski, M. Bronikowski, J. Chen, G.R. Choppin, R. Moore, O. Pokrovsky, Y. Xia, J. Solution Chem. 28(5), 521 (1999)

7. Complexation Study of NpO_2^+ and UO_2^{2+} Ions with Several Organic Ligands and Aqueous Solutions of High Ionic Strength; M. Borkowski, G.R. Choppin, S. Lis, Radiochim. Acta, 74, 117, (1996)

8. Thermodynamic Modeling of Actinide Complexation with Oxalate at High Ionic Strength; J. Radioanalytical and Nuclear Chem., 248(2), 467 (2001)

9. Neptunium(V) Hydrolysis and Carbonate Complexation: Experimental and Predicted Neptunyl Solubility in Concentrated NaCl Using the Pitzer Approach; D. Clark, W. Runde, M. Neu, Geochimica et Cosmochimica Acta, 60(12) 2065 (1996)

10. Thermodynamic Modeling of Metal-Ligand Interactions in High Ionic Strength NaCl Solutions: the Co^{2+}-Oxalate System; M. Borkowski, G.R. Choppin, R. Moore, Radiochim Acta, 88 599 (2000)

11. Appendix SOTERM, Table SOTERM-4, Title 40 CFR 191 Compliance Certification Application, DOE/CAO-1996-2184, U.S. Department of Energy, Carlsbad, NM (1996)

12. Appendix SOTERM, Table SOTERM-5, Title 40 CFR 191 Compliance Certification Application, DOE/CAO-1996-2184, U.S. Department of Energy, Carlsbad, NM (1996)

13. Radiolytically Induced Oxidation Reactions of Actinide Ions in Concentrated Salt Solutions; J.I. Kim, Ch. Lierse, K. Buppelmann, S. Magirius, Mat. Res Soc. Symp. Proc. (1987) Vol. 84, 603-612

Information Only

14. The Chemistry of Pu in Concentrated NaCl Solution: Effects of Alpha Self-Radiolysis and the Interaction between Hypochlorite and Dioxoplutonium(VI); I. Pashalidis, J.I. Kim, Ch. Lierse, J.C. Sullivan, Radiochim. Acta, 60 99 (1993)

15. Theory of Radiation Chemistry. III. Radical Reaction Mechanism in the Tracks of Ionizing Radiations; A.K. Ganguly, J.L. Magee, J. Chem. Phys., 25(1), 129 (1956)

16. The Redox-Behaviour of Plutonium in Saline Solutions under Radiolysis Effects; K Büppelmann, J.I. Kim, Ch. Lierse, Radiochim. Acta, 44/45, 65, (1988)

17. Spectroscopic Investigation on the Formation of Hypochlorite by Alpha-Radiolysis in Concentrated NaCl Solutions; M. Kelm, I. Pashalidis, J.I. Kim, Applied Radiation and Isotopes, 51 637 (1999)

18. Critically Selected Stability Constants of Metal Complexes Database Version 5.0, A.E. Martell, R.M. Smith, R.J. Motekaitis Texas A&M University, College Station, TX, USA, 1998

19. Hard and Soft Acids and Bases; R. Pearson, J. Am. Chem. Soc., 85(22), 3533 (1963)

20. Solution Chemistry of the Lanthanides and Actinides; G.R. Choppin, E.N. Rizkalla, Handbook on the Physics and Chemistry of the Rare Earths, Vol. 18, Ch. 128, K.A. Gschneidner, L. Eyring, G.R. Choppin, G.H. Lander, Eds. Elsevier Science, (1994)

21. Utility of Oxidation State Analogs in the Study of Plutonium Behavior; G.R. Choppin, Radiochim. Acta 85, 89 (1999)

22. Complexation of Pentavalent and Hexavalent Actinides by Fluoride; G.R. Choppin, L. Rao, Radiochim. Acta, 37, 143, (1984)

23. The Nature of U(VI) Complexation by Halates and Chloroacetates; G.R. Choppin, F. Khalili, E. Rizkalla, Inorg. Chem. 143 131 (1988)

24. Kinetics and Mechanisms of Formation of Magnesite from Hydromagnesite in Brine; P. Zhang, H. Anderson, J. Kelly, J. Krumhansl, H. Papenguth, SAND99-1946J, Sandia National Laboratories, Carlsbad, NM (1999)

25. M. Anbar, I. Dostrovsky, J. Chem. Soc. 1105 (1954)

26. L. C. Adam, G. Gordon, Inorg. Chem. 38, 1299, (1999)

Information Only

27. A. I. Vogel, Vogel's Textbook of Quantitative Chemical Analysis, 5th ed. p 309-322 John Wiley & Sons, NY (1989)

Information Only

110

NOTICE: This document was prepared as an account of work sponsored by an agency of the United States Government. Neither the United States Government nor any agency thereof, nor any of their employees, nor any of their contractors, subcontractors, or their employees, makes any warranty, express or implied, or assumes any legal liability or responsibility for the accuracy, completeness, or usefulness or any information, apparatus, product or process disclosed, or represents that its use would not infringe privately owned rights. Reference herein to any specific commercial product, process or service by trade name, trademark, manufacturer, or otherwise, does not necessarily constitute or imply its endorsement, recommendation, or favoring by the United States Government, any agency thereof or any of their contractors or subcontractors. The views and opinions expressed herein do not necessarily state or reflect those of the United States Government, any agency thereof or any of their contractors.

This document was authored by Sandia Corporation under Contract No. DE-AC04-94AL85000 with the United States Department of Energy. Parties are allowed to download copies at no cost for internal use within your organization only provided that any copies made are true and accurate. Copies must include a statement acknowledging Sandia Corporation's authorship of the subject matter.

Information Only

This page intentionally left blank

Information Only

2.2.3 Effect of Actinide Complexation by Organic Ligands on WIPP Performance Assessment

D.E. Wall
Sandia National Laboratories – Carlsbad Programs Group
4100 National Parks Highway - Carlsbad, NM 88220 – USA

The Waste Isolation Pilot Plant (WIPP) is located 42 kilometers east of Carlsbad, New Mexico, at a subsurface depth of 655 meters. A probabilistic approach is used to evaluate alternative isolation scenarios and the uncertainty in physical processes to construct a Complementary Cumulative Distribution Function for radionuclide releases. The most likely scenario for release of radioactivity to the environment is human intrusion, with brine released from the repository acting as a transport medium. Solubilities calculated with the FMT computer code for An(III), An(IV), An(V) are: 1.2×10^{-7} M, 1.3×10^{-8} M, 2.4×10^{-7} M , respectively, in Salado brine, and 1.4×10^{-8} M, 4.1×10^{-8} M, and 4.8×10^{-7} M, respectively, in Castile brine. The role of acetate, citrate, oxalate, and EDTA on actinide solubilization at high ionic strength, high pH, reducing E_h, and the effect on performance assessment is described.

2.2.4 The Use of Th, U, Np, Am as Oxidation-State Analogs for Pu in the WIPP Actinide Chemistry Program

Nathalie A. Wall, Laurence H. Brush and Donald E. Wall

Sandia National Laboratories – Carlsbad Programs Group
4100 National Parks Highway - Carlsbad, NM 88220 - USA

The Waste Isolation Pilot Plant, located in southeastern New Mexico, is the first deep geological disposal facility for transuranic waste. Performance assessment calculations show that, in the absence of human intrusion, vertical migration of radionuclides through the Salado Formation or through the shaft seal system will not occur, however, borehole intrusions resulting from exploratory drilling may release radioactive materials to the surface and subsurface environments. Knowledge of Pu chemistry is important to model repository behavior in response to intrusion scenarios, but the factors influencing Pu solubility (e.g. complexation with organic ligands) are difficult to measure due to redox lability of Pu.
Am(III), Th(IV), Np(V) and U(VI) were used as analogs for Pu(III), Pu(IV), Pu(V) and Pu(VI) in complexation studies with acetate, citrate, oxalate and EDTA. WIPP reviewers have questioned the validity of the analogy. The utility of the oxidation state analogy in high ionic strength solutions is discussed.

Information Only

2.2.5 Interaction of Actinide Ions with the Polyoxometalates $[NaP_5W_{30}O_{110}]^{14-}$, $[As_2W_{21}O_{69}]^{6-}$, $[P_2W_{18}O_{62}]^{6-}$, and $[P_2W_{17}O_{61}]^{10-}$

D.E. Wall*, G.R. Choppin
Department of Chemistry, The Florida State University, Tallahassee, FL, 32306, USA

* Present Address: Sandia National Laboratories – Carlsbad Programs Group
4100 National Parks Highway - Carlsbad, NM 88220 – USA

The thermodynamics of complex formation of Th^{4+}, UO_2^{2+}, NpO_2^{+} and Am^{3+} with $[NaP_5W_{30}O_{110}]^{14-}$, $[As_2W_{21}O_{69}]^{6-}$, $[P_2W_{18}O_{62}]^{6-}$ and $[P_2W_{17}O_{61}]^{10-}$ were examined in 0.1 molar NaCl solution at 25°C. The respective stability constants with $[NaP_5W_{30}O_{110}]^{14-}$ are log β_{101} = 6.10 ± 0.05, 3.80 ± 0.06, 2.98 ± 0.04, 5.85 ± 0.05; and with $[As_2W_{21}O_{69}]^{6-}$ are 9.9 ± 0.1, 6.32 ± 0.04, 4.39 ± 0.03, 10.1 ± 0.1. The log β_{101} of NpO_2^{+} with $[P_2W_{18}O_{62}]^{6-}$ is < 2 , and with $[P_2W_{17}O_{61}]^{10-}$ is 4.81 ± 0.03. The order of the stability constants are: $Th^{4+} > UO_2^{2+} > Am^{3+} > NpO_2^{+}$ when the primary binding sites are tetragonal. The stability constants follow the order: $Th^{4+} > Am^{3+} > UO_2^{2+} > NpO_2^{+}$ when trigonal or pentagonal binding sites are predominant due to steric effects. Entropy values correlate with the magnitude of dehydration of the metal ion, which depends on the geometry of the binding site.

Information Only

Information Only

3.0 Engineered Barriers

3.1 MgO Studies Experimental Work Conducted at SNL/Carlsbad[1]

Efficacy of Premier Chemicals MgO as an Engineered Barrier

Anna C. Snider
Sandia National Laboratories, MS 1395
4100 National Parks Highway
Carlsbad, NM USA 88220

Abstract

The Carlsbad Programs Group of Sandia National Laboratories is currently investigating several issues with respect to the efficacy of MgO under expected repository conditions. Previous work was described in the January and July 2001 Status Reports to the DOE (Milestones RI010 & RI020). Characterization of Premier Chemicals MgO, with respect to both mineralogy and composition, and its ability to absorb water (H_2O) and carbon dioxide (CO_2) under repository conditions continues. Sandia is currently carrying out a series of experiments to measure hydration rates for Premier MgO under both inundated and humid conditions. Results to date suggest that, in general, the hydration rate can be a modeled as a diffusion-limited reaction, although interpretation of the hydration results in GWB is complicated by the formation of a second hydrated phase, a magnesium chloride hydroxide hydrate (hereafter referred to as sorel cement).

In addition, MgO carbonation rates are being measured at CO_2 partial pressure (P_{CO2}) of about $10^{-3.5}$ atm, the P_{CO2}. characteristic of ambient atmospheric conditions. At atmospheric P_{CO2}, as expected, carbonation has been slow. Sandia is also working to obtain further information on the MgO hydration-carbonation pathway relevant to repository conditions. Of particular importance is the metastable magnesium hydroxycarbonate mineral that forms initially, as this mineral (along with brucite, $Mg(OH)_2$) will control the P_{CO2} and pH in the repository. These are important parameters for predicting actinide solubilities. Sandia is also carrying out experiments to evaluate the generation of isosaccharinic acid (ISA), a potentially strong complexant for the actinides, in the presence of MgO.

Introduction and Objectives

In the Compliance Certification Application (CCA), the DOE asserted that MgO, along with panel closures, shaft seals, and borehole plugs, would help meet the requirement for multiple natural and engineered barriers, one of the assurance requirements in the

[1] This work is covered by BOE #1.3.5.4.3 and WBS #1.3.5.4.3.1

Information Only

regulations for the radioactive waste constituents of transuranic waste. In May 1998, the EPA certified that the WIPP complies with these regulations. In its certification, the EPA recognized MgO as the only engineered barrier in the WIPP disposal system, and that MgO will prevent or delay the movement of radionuclides toward the accessible environment. MgO will sequester CO_2 generated by possible microbial degradation of organic materials in the waste, in addition to reducing the amount of free liquid in the repository by hydration. Thus, it maintains the pH and CO_2 fugacity ($\approx P_{CO2}$) in the repository within optimal ranges, in which actinide solubilities in brine are at a minimum.

Experimental work carried out previously at Sandia has shown that MgO is effective at absorbing H_2O and CO_2 (Papenguth et al., 1997, 1999). Currently, more MgO will be emplaced in the WIPP than gas generation calculations suggest would actually be necessary to absorb CO_2 generated through microbial degradation of organic materials. In total, about 66,000 tons of MgO will be placed in the WIPP repository.

Although the work done to date on MgO is sufficient to show that it is effective as an engineered barrier by buffering repository conditions and limiting actinide solubilities, Sandia is currently examining several additional issues, as discussed in the January, 2001 Status Report (Milestone RI010). Experimental programs are evaluating the ability of the new material to sequester H_2O and CO_2, and are determining the hydration and carbonation pathways that Premier MgO will follow under WIPP-relevant conditions. The P_{CO2} predicted from performance-assessment calculations for the CCA is based upon the assumption of equilibrium with brucite and magnesite ($MgCO_3$). However, metastable hydromagnesite phases commonly form upon initial carbonation of MgO and/or brucite, and these phases have higher solubilities than magnesite. Thus, they might buffer the P_{CO2} at values higher than those used in the CCA. Previous work with MgO has been criticized for failing to consider the potential effect of metastable hydroxycarbonates such as hydromagnesite on repository chemistry. Sandia is currently working to identify the hydroxycarbonate phase(s) that might form.

Sandia is also evaluating the production of ISA under repository conditions. ISA is known to be a degradation product of cellulosic materials under strongly basic conditions (Glaus et al., 1999), and is a strong complexant for the actinides (Greenfield et al., 1992). Cellulosic materials are a significant part of the waste inventory, and the production of ISA could significantly affect the solubilities of the actinides in the repository. However, it has never been demonstrated that ISA forms under the mildly basic conditions expected in MgO-dominated systems. Sandia's experiments are assessing this by using a variety of WIPP-relevant brines and cellulosic materials.

The objectives of these experiments are multifold: (1) continued characterization of a new batch of Premier Chemicals MgO; (2) determination of hydration rates and pathways; (3) quantification of carbonation rates and identification of the metastable mineral(s) produced; (4) quantification of the effect(s) of possible lithification on hydration and carbonation rates and pathways; (5) evaluation of the production of ISA under repository conditions; (6) investigation of MgO colloid formation (see next section, TP 02-02). These experiments are governed by test plan TP 00-07 (Wang et al., 2001) All of these experiments are being run using MgO from Premier Chemicals, the new vendor supplying the repository.

Information Only

Characterization of Premier Chemicals MgO

The new material being supplied is manufactured using a different process than the old, is dissimilar texturally, and contains higher levels of potentially reactive impurities, especially CaO. CaO hydrates more rapidly than MgO, causing a transient, initial rise in the pH of the brine. Sandia is characterizing the new material chemically and physically, and is performing experiments to evaluate its ability to sequester H_2O and CO_2 relative to the material used in previous experiments.

As stated in the January 2001 Status Report (Milestone RI010), a quantity of the reported MgO and CaO in Premier MgO is present as magnesium and calcium silicates. Two batches of Premier MgO have been analyzed to date. Details of the chemical analysis are given in Milestone RI010. This could affect the capacity of the Premier MgO to sequester H_2O and CO_2. Both of these samples were obtained from Premier Chemicals before they began shipping material to the WIPP. However, when shipments began, the purity of the MgO was increased slightly. This new material will be examined by XRD during FY02.

Hydration Rate Experiments

A large experimental matrix has been initiated to investigate both inundated and humid hydration rates of the Premier material, and to identify the hydration pathway in WIPP brines.

Inundated hydration experiments

Inundated hydration experiments are currently being run to evaluate several factors affecting the MgO hydration rate. A complete description of the experiments, results, and interpretation as of July 2001 are found in the July 2001 Status Report (Milestone RI020). Experimental conditions for these are summarized in Table 1.

Information Only

Table 1. Experimental Matrix for Inundated Hydration Experiments

Experiment	T, °C	Premier MgO, g	Electrolyte
Inundated hydration, samples agitated frequently	25° 50° 70° 90°	5 g	DI water, 100 ml 4.0 M NaCl, 100 ml ERDA-6 (Castile) brine, 100 ml GWB (Salado), 100 ml
Experiment to evaluate the effects of GWB/ MgO ratio	70°	5 g	GWB (60, 90, 120,160, 200, 240 ml)

The initial inundated hydration experiment has come to completion. Figures 1, 2, and 3 show the current data plotted as: hydration (mole percent brucite) vs. time, hydration vs. the square root of time, and the rate constants obtained from Figure 2 vs. the reciprocal of temperature in Kelvin (Arrhenius plots). Interpretation of the data is presented in the July 2001 Status Report (Milestone RI020). In summary, x-ray diffraction (XRD) analysis indicates that brucite is the only hydration phase present in the samples from deionized (DI) water, 4.0 M NaCl, and in ERDA-6 (a synthetic solution representative of brines in the Castile Formation). In GWB (a synthetic solution representing brines from the Salado Formation), a different hydration phase, sorel cement, precipitates rapidly and early; brucite becomes the stable hydration phase only at higher degrees of hydration. Figure 1 shows that, to date, hydration has proceeded to completion only in the samples from the DI water at 90° C. In Figures 2 and 3, data that produce a straight line when

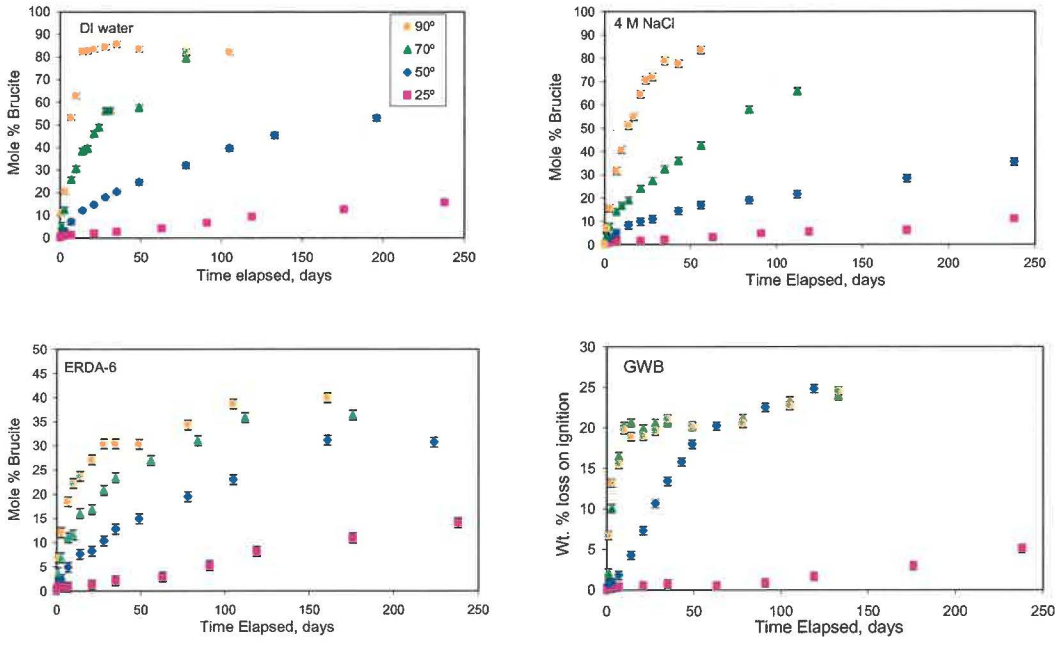

Figure 1. Results from inundated hydration experiments.

Information Only

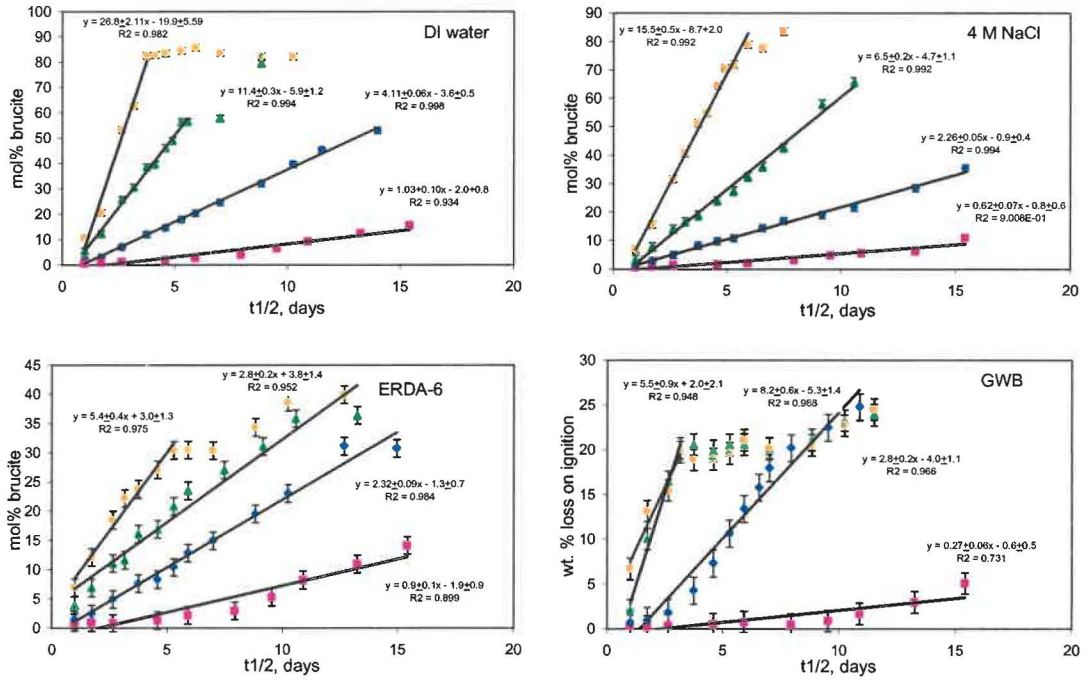

Figure 2. Inundated hydration data plotted as a function $t^{1/2}$. Symbols are as shown in Figure 1.

plotted against the square root of time imply that hydration can be modeled as a diffusion-limited reaction. This is true in all of the solutions except GWB.

Much of the difficulty in interpreting the GWB results is caused by the presence of two hydration phases (Sorel cement and brucite), rather than just brucite. Because the degree of hydration in the sample is determined by weight loss upon ignition, the presence of a second hydration phase containing a different amount of stochiometric water complicates interpretation of the results. Sorel cement has not been identified by XRD. The hydration phase has been identified under the scanning electron microscope (SEM; Figure 4); however, the only samples analyzed to date are from the cemented cake and carbonation experiments (both described in detail below). The cemented samples were run under the same conditions as the inundated hydration experiment, except the former samples were not agitated. It appears that sorel cement is also forming in the inundated hydration samples. The exact mineral phase must be identified in order to quantify the amount of MgO hydration that occurs with time.

On November 14, 2001, a new set of experiments was initiated to extend the hydration curves for ERDA-6 and GWB. Most of the samples will not be analyzed for many more months. However, some samples will be collected before then to confirm reproducibility of previous results from the initial experiment.

Information Only

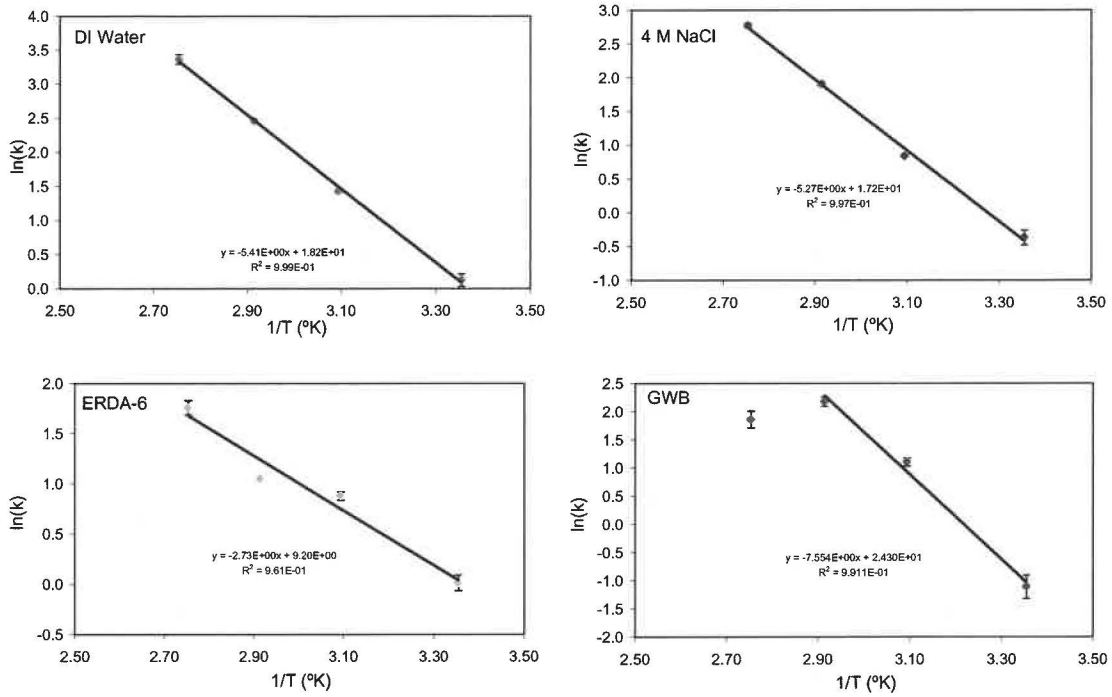

Figure 3. Arrhenius plots of the inundated hydration data.

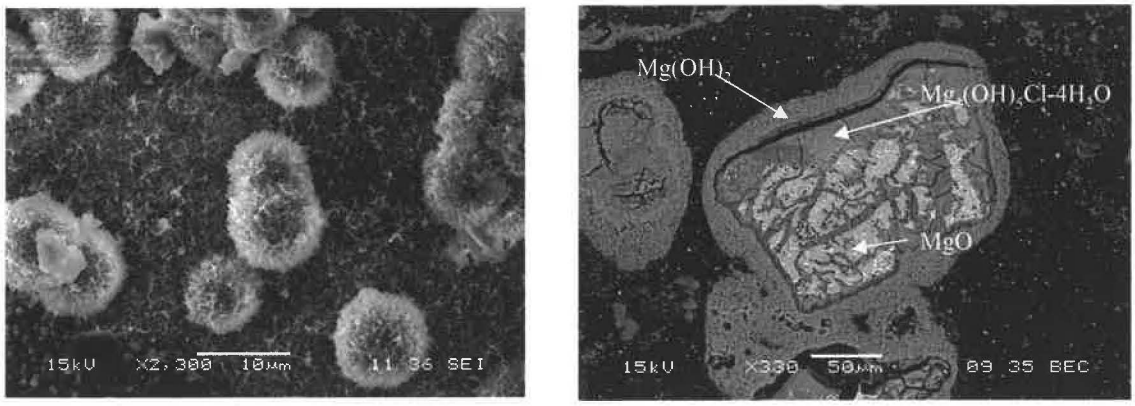

Figure 4. SEM images of magnesium chloride hyroxide hydrate, $Mg_3(OH)_5Cl{\cdot}4H_2O$. Note $Mg(OH)_2$ is brucite.

Information Only

A second experiment evaluated the effect of the brine volume present in GWB/MgO systems. The greater the volume of brine in the sample, the greater the fraction of sorel cement in the hydration products. The bottles contained five grams of MgO in GWB volumes ranging from 60-250 ml, and were run for 28 days. The experiment has concluded. An in depth report on this work is presented in the July 2001 Status Report (Milestone RI020).

An additional brine volume/MgO experiment was conducted in a similar manner to a previous inundated hydration experiment, except 2.5 times as much GWB was used. The aim was to compare the resulting hydration curves to previous inundated ones. The comparison would define what effect the greater amount of brine had on the system. Samples were placed in the 70°C oven and sampled at the same interval as the inundated samples at 70°C. Figure 5 compares data from the two experiments. The two sets of data follow each other closely initially, then diverge after the rate of hydration decreases. The plot suggests that the samples containing 250 ml brine did not exhaust the excess Mg in the brine by the end of the experiment. This is determined by a higher weight loss on ignition (sorel cement loses more weight when it hydrates than brucite) and smaller brucite peaks seen in the XRD patterns.

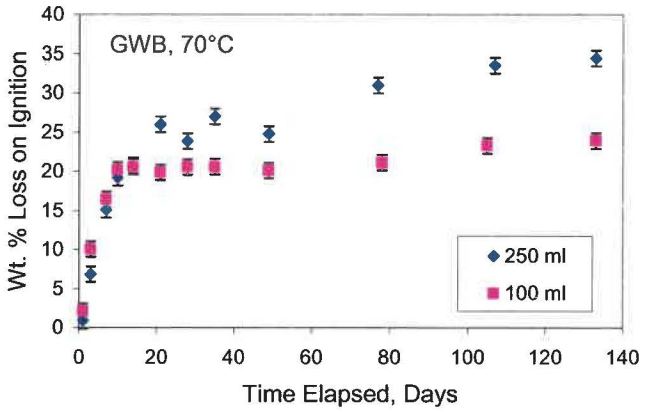

Figure 5. Plot comparing data from inundated hydration experiments containing 100 and 200 ml of GWB.

Humid Hydration experiments

Humid hydration experiments were started June 6, 2001. (Refer to the July 2001 Status Report, Milestone RI020, for a detailed description of the experimental setup.) In summary, 384 samples, each consisting of three grams of uncrushed Premier Chemicals MgO, are being run at temperatures of 25°, 40°, 60°, and 80°C and relative humidities of 35%, 50%, 75%, and 95% (Table 2).

Information Only

Table 2. Saturated Salt Solutions and the Relative Humidity Values They Produce.

Salt	RH Value, %*
K_2SO_4	95
NaCl	75
$NaBr \cdot 2H_2O$	50
$MgCl_2 \cdot 6H_2O$	35

* RH values vary a few % with temperature

Samples are being analyzed over a period of months to years. Each sample is dried and analyzed by weight loss on ignition and XRD. Brucite concentration will be determined by weight loss at 500°C. This technique assumes that brucite formation is the only reaction that occurs; a few samples will be analyzed by XRD to verify that carbonate formation is not significant under humid conditions.

Humid hydration results since July 2001 are shown in Figure 6. Hydration is relatively slow at lower temperatures and humidities, but appears to occur readily at elevated temperatures. After four weeks, the degree of hydration reached over 80% in higher humidity samples at 80°C. XRD analysis indicates that no periclase (MgO) remains. After 200 days at 60°C, the higher humidities are reaching 70 % mole conversion.

Hydration versus the square root of time has been plotted for the higher humidities, shown in Figure 7. The rate constant at each temperature can be determined if the data

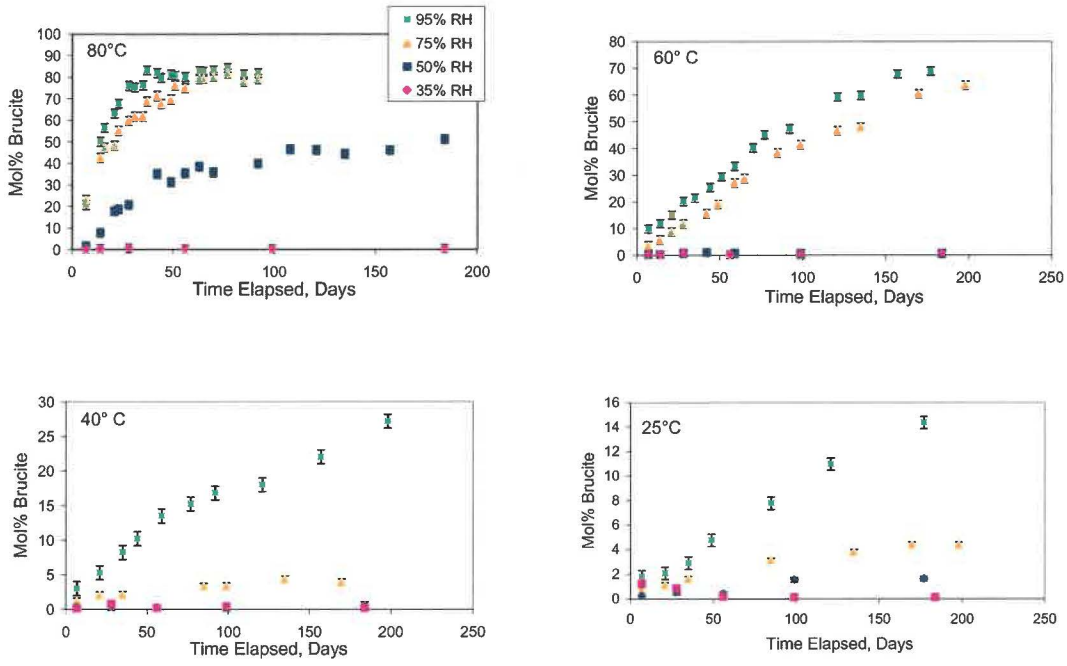

Figure 6. Results from humid hydration experiments.

Information Only

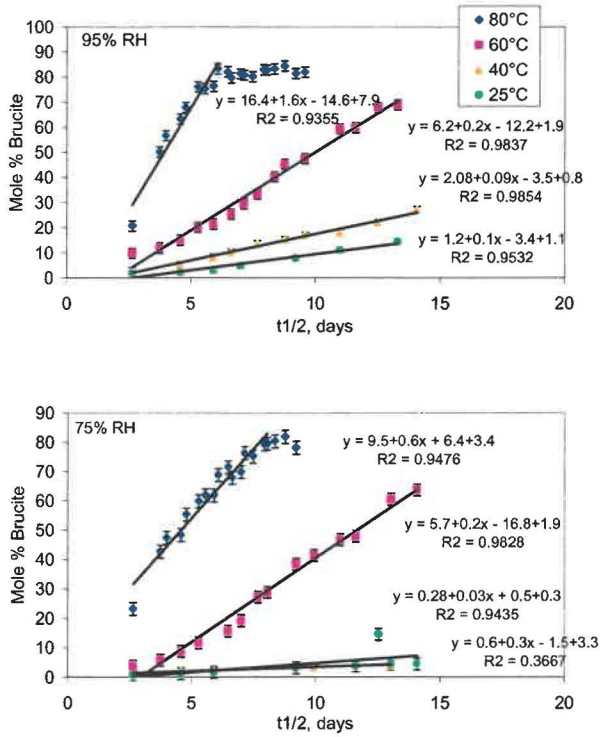

Figure 7. Humid hydration data plotted as a function $t^{1/2}$

plotted results in a straight line. The data points in the two plots below (95 % and 75 % RH; Figure 7) follow straight lines and can be modeled as a diffusion-limited reaction.

Below the rate constants are plotted against 1/T (°K), at 95 % relative humidity, producing an Arrhenius plot (Figure 8). The four rate constants fall on a straight line. Therefore, the data can be modeled as a simple, diffusion–limited reaction at the higher humidity.

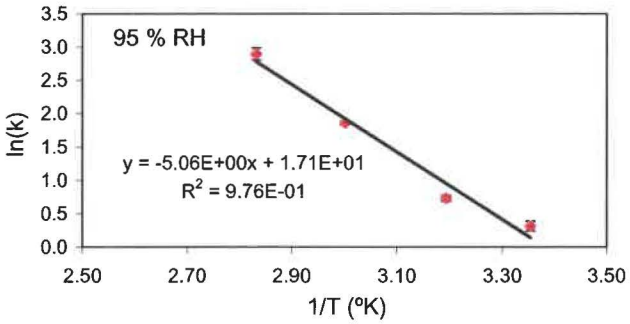

Figure 8. Arrhenius plot of 95% humid hydration data.

Information Only

Carbonation Rate Experiments

Sandia is attempting to examine carbonation under conditions similar to those expected in the repository. The carbonation experiments described in the July 2001 Status Report (Milestone RI020), are continuing. These experiments are using four different solutions: DI water, 4 M NaCl, GWB, and ERDA-6. Each sample bottle includes five grams Premier Chemicals MgO and 100 ml of solution. Room air is bubbled continuously through the samples using a gas manifold. Each manifold holds 24 samples. To minimize evaporation, the air is humidified by bubbling through water prior to entering the manifold.

As of June 14, 2001, 64 carbonation rate samples (four brines, sixteen samples) were running on the bench top under atmospheric P_{CO2} ($\approx 10^{-3.5}$ atm) conditions. Thirty-two samples have been analyzed; on January 9, 2002, 32 additional samples were added to the manifold to extend the life of the experiment.

Samples from atmospheric P_{CO2} conditions were collected at weekly intervals and are now collected on a monthly to bimonthly interval. Samples are measured for pH, filtered, dried, and crushed. Carbonate conversion rates are ascertained by using a carbon coulometer and XRD. The carbon coulometer determines the percent carbon in the solid, whereas the XRD identifies the carbonate phase present.

Carbon coulometer results from atmospheric P_{CO2} conditions are displayed in Figure 9 below. These results show that carbonation is proceeding slowly in both of the WIPP brines (GWB and ERDA-6). Analysis of samples from ERDA-6 indicate over 1 % carbon in the solid, whereas samples with GWB have < 1% carbon present. However, these results are not surprising in view of the fact that this experiment is being run at a low P_{CO2} in order to simulate the very slow rates at which microbial activity will produce CO_2 in the repository. (Experiments carried out at high CO_2 pressures result in faster carbonation rates, but could produce metastable Mg-hydroxycarbonates different from those that will form in the repository. These phases could in turn buffer the P_{CO2} and pH at values different from those in the repository.) In view of the uncertainties associated with these

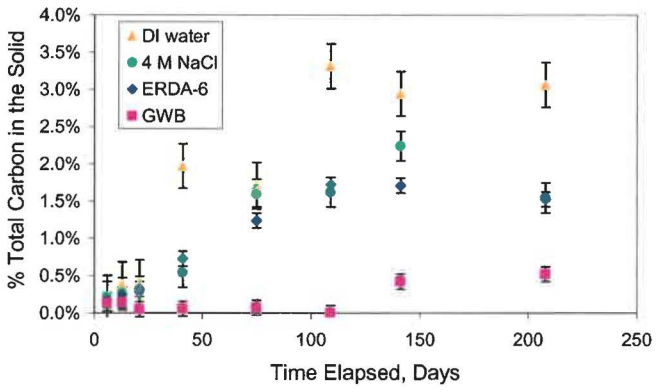

Figure 9. Results of the atmospheric P_{CO2} experiment.

Information Only

data (see error bars in Figure 9), it is not believed that the decrease in the C content of the ERDA-6 samples from 141 to 208 days represents de-carbonation, or even a cessation of carbonation, of these samples. Rather, it is likely that the overall upward trend exhibited by the ERDA-6 samples - and the samples from the other three solutions - will continue, albeit slowly.

Samples taken at 141 days were additionally analyzed using XRD and SEM to determine what carbonate phase might be present. Carbonates were not detected by XRD analysis. The XRD has a detection limit of several percent. If carbonates were present, they would constitute only a few percent of the total sample. The SEM did show evidence of carbonates. Calcium-rich carbonates, determined using energy-dispersive x-ray spectrometry (EDS), were seen in both samples that had reacted in DI water and ERDA-6 (Figure 10).

An SEM phase identification program was used to identify the carbonate phase(s) present. To identify a mineral, it must have a flat crystal surface that faces towards the detector. A pattern can then be produced as seen in Figure 11. The pattern produced did not have an exact phase ID match. The pattern most closely corresponded to a monoclinic calcium carbonate and, to a lesser degree, a calcium-magnesium carbonate.

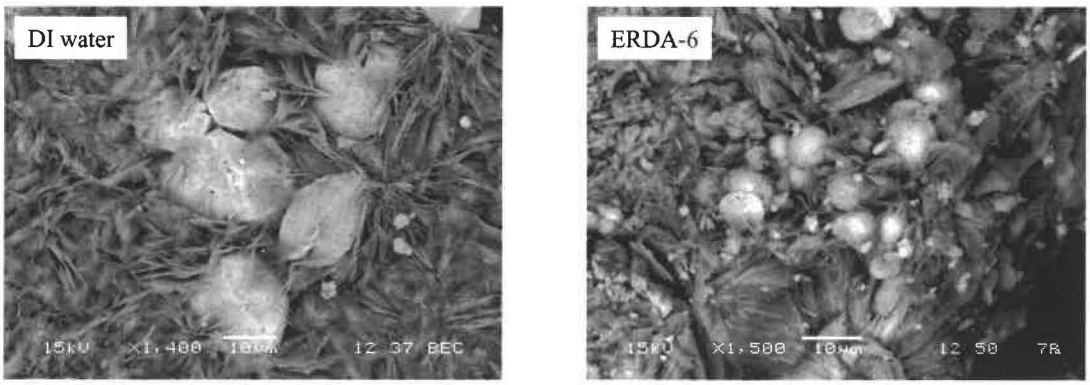

Figure 10. SEM images of calcium-bearing carbonates (white) surrounded by brucite (gray).

Information Only

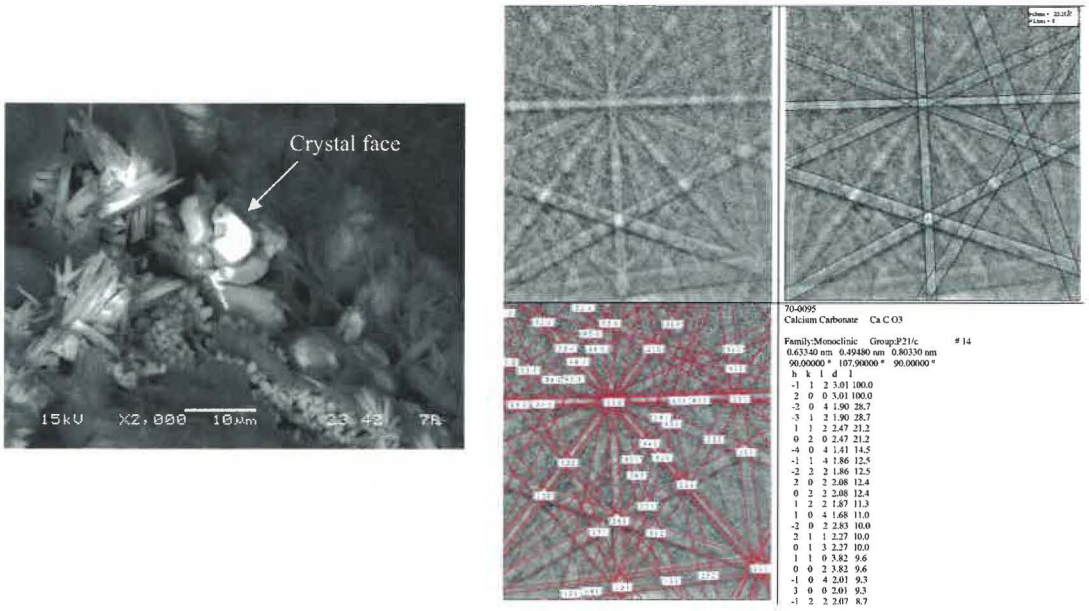

Figure 11. SEM image showing the crystal face (from a DI water sample) that was analyzed to find the accompanying pattern (right) using a SEM Phase ID program. The red lines superimposed on the pattern are a match that the computer found, identifying the mineral as a monoclinic calcium carbonate.

Despite the lack of direct evidence for the conversion of brucite to a magnesium bearing carbonate, there is indirect evidence for carbonation of brucite. Calculations imply that 1.7 % conversion of the total solid (ERDA-6 at 141 days) is equivalent to the conversion of ~ 5.7 % moles of Mg or ~7.9 % moles of Ca. However, as stated in the January 2001 Status Report (Milestone RI020), Premier Chemicals MgO contains < 1 % CaO. Therefore, there is not enough CaO in this material to have reacted with all of the CO_2.consumed by 141 days in ERDA-6. Assuming that there were 1 % CaO in the Premier Chemicals MgO, there would only be enough CaO to react with 12.7 % of the CO_2 in the ERDA-6 sample after 141 days. This calculation suggests that other carbonate-bearing minerals must be present, most likely Mg-bearing carbonate minerals.

These other (Mg?) carbonates have not been identified using the SEM. When the SEM is operated in backscatter-electron mode, the images produced reflect elemental atomic number. The higher the atomic number, the lighter and whiter the mineral appears. MgO, brucite, and magnesium carbonates are hard to differentiate from one another due to the similarity in atomic number. However, a calcium-bearing carbonate is much easier to find due to the relatively high atomic number of Ca, which makes Ca-bearing minerals appear white.

Information Only

Carbonation at room temperature is dependent on MgO hydration and is a slow process. This is not unexpected and in future months it is thought that the samples will contain enough carbonate to properly identify the phase on the XRD.

Carbonation-rate experiments will be started as soon as possible at a CO_2 concentration of 5% and (perhaps) in the future at $^1/_{10}$ atmospheric ($\approx 10^{-4.5}$ atm CO_2 — room air will be diluted by a factor of 10 with nitrogen). These experiments will be conducted in a manner similar to that of the experiments under atmospheric P_{CO2}, except the samples and manifolds will be inside glove boxes. A purchased mixture of 5% CO_2 in nitrogen gas and room air diluted to 1/10 of its original concentration with inert N_2 will be pumped into the glove boxes and bubbled through the samples.

The 5% CO_2 experiment will quantify carbonation in two brines, GWB and ERDA-6. The matrix differs from the experiment under atmospheric P_{CO2}. There are 64 samples (two brines, four solids, eight samples). Each bottle contains five grams of one of the following solids: Premier Chemicals MgO, Fisher Scientific MgO, pre-hydrated, crushed Premier Chemicals MgO, and pre-hydrated Fisher MgO. Hydrated samples were prepared by adding five grams of either crushed Premier Chemicals MgO, or Fisher MgO to 100 ml of brine. The bottles were placed in a 90°C oven for approximately three weeks. Before the pre-hydrated samples were added to the manifold, a small portion was sampled and will be analyzed for brucite. The experiment with 5% CO_2 will be sampled at a higher frequency due to the anticipated accelerated reactions.

Cemented "Cake" Experiments

The effects of possible formation of a cemented cake of hydration products are being examined. This experiment was started in June 2001. In this experiment, five-, ten-, and 15-mm-thick layers of Premier MgO were placed in containers with GWB or ERDA-6, and are being run in ovens at 25°–90° C. The samples are not agitated.

Sampling is being carried out over weeks to months. Samples are taken from the oven, cooled, and pH is measured. They are filtered, dried, and crushed, then analyzed by weight loss on ignition and XRD. SEM analysis is conducted on selected samples before they are crushed.

Figure 12 shows four plots representing data with three different MgO thicknesses inundated in ERDA-6 at four different temperatures, whereas Figure 13 shows data from GWB. Although it was anticipated that the thicker layers would hydrate at a slower rate, MgO thickness has not affected the hydration rate under inundated conditions in ERDA-6 (Figure 12). Data collected at 50° and 70°C indicate that hydration was rapid at first and has now decreased. At 25°C and 90°C, hydration proceeds at a more-or-less constant rate. However, there are data gaps in the 70°C and 90°C plots (both in ERDA-6 and GWB) due to sampling schedule. A new set of experiments has been initiated (September 2001) in order to fill these gaps and to extend the curves.

Information Only

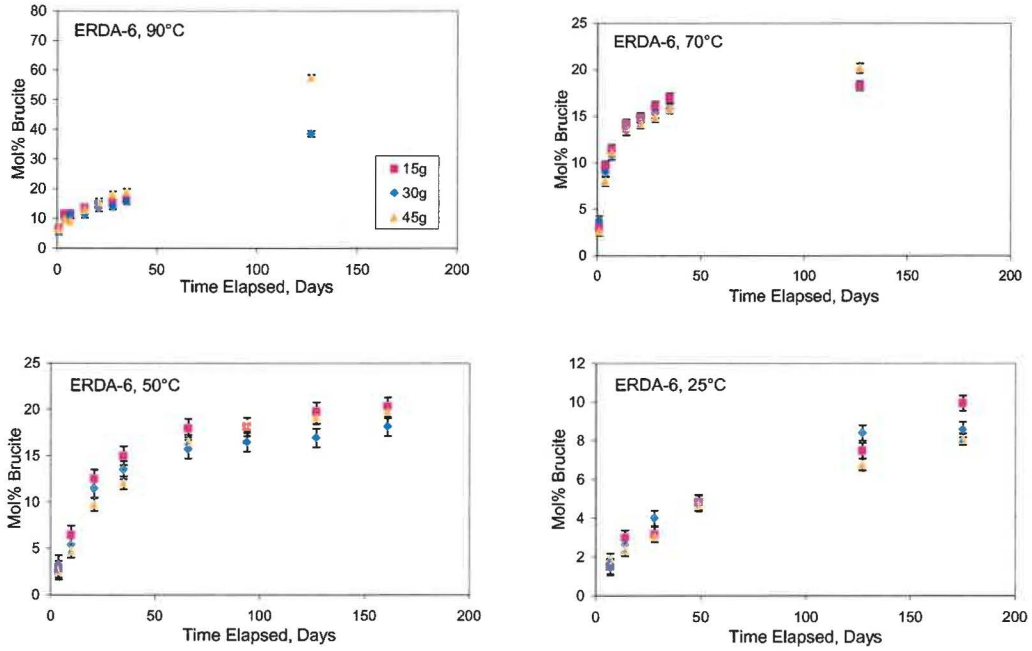

Figure 12. ERDA-6 results of cemented cake experiment.

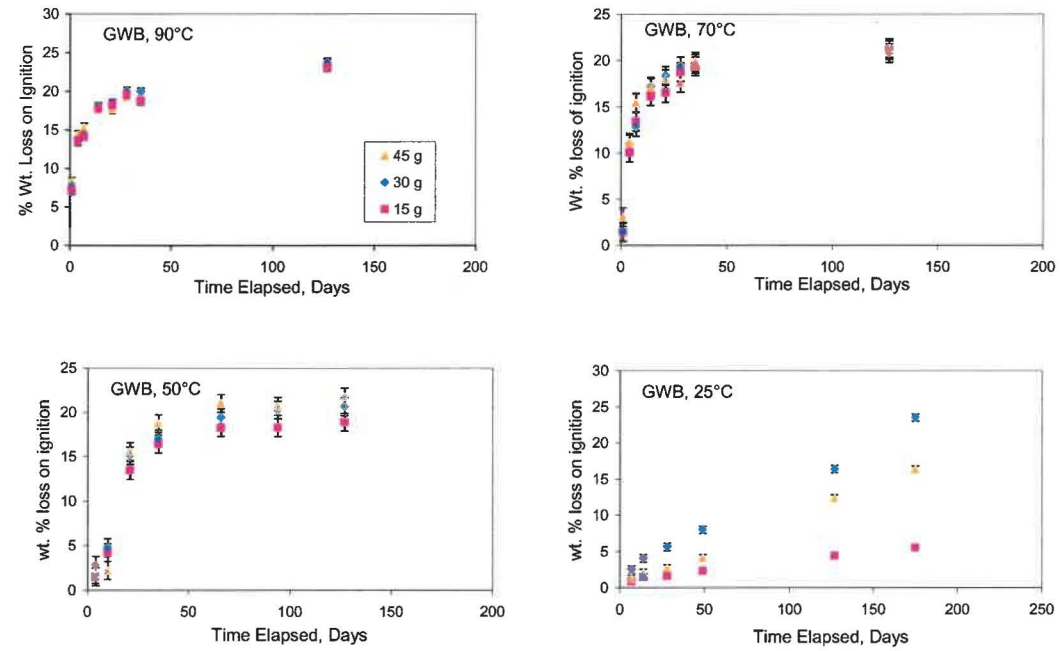

Figure 13. Results of the GWB cemented-cake experiment.

Information Only

In GWB at 50°, 70°, and 90°C (Figure 13) thickness does not affect hydration. Hydration, as seen in the samples from ERDA-6, proceeded rapidly and then decreased over time. Remember, however that these plots represent the result of two hydration phases: brucite and sorel cement. At 25°C the rates for all three thicknesses are nearly constant, but the rates for all three thicknesses are significantly different. Little hydration has occurred at 25°C and data may appear to be more scattered compared to the other higher temperatures.

Figure 14 compares the extent of hydration in the (unagitated) cemented cake samples to the (agitated) inundated hydration samples at 70° and 90°C in ERDA-6 and GWB. At both 70° and 90°C in ERDA-6, the agitated samples contain more than 35 mol % brucite, whereas the cemented cake never contains more than 25 mol % brucite. These results might seem to indicate that lithification is occurring in ERDA-6 at the two higher temperatures, but visual observation of the solids in these 70° and 90°C samples demonstrated that they were very friable. On the other hand, the solids from the 70° and 90°C GWB cemented-cake samples were well indurated, but hydrated at rates very similar to those of the agitated GWB samples at the same temperatures (see Figure 14). Therefore, it is not clear what is responsible for the differences between hydration rates of the 70° and 90°C, agitated and unagitated ERDA-6 samples.

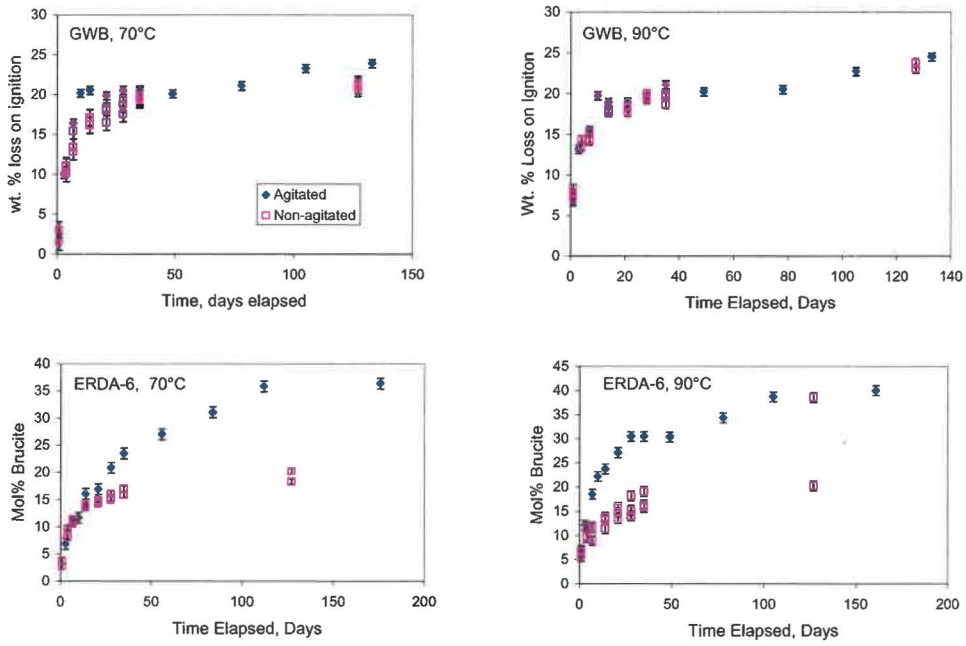

Figure 14. Plots comparing (agitated) inundated ERDA-6 and GWB hydration rates to the (non-agitated) cemented cake hydration rates.

Information Only

ISA Generation

Sandia is continuing to evaluate the production of ISA under repository conditions. In August 2000, cellulosic materials and MgO were placed in bottles containing three different solutions: DI water, GWB, ERDA-6. The samples were placed in ovens ranging from 25°C to 90°C. A detailed description, recounting the importance of the experiment and the experimental method used, are found in the January 2001 Status Report (Milestone RI010). At this time, the experiment is no longer being sampled. No samples have been analyzed to date, because a gas chromatograph-mass spectrometer (GC-MS) has not been available. However, at each sampling, pH has been monitored.

MgO Colloids

A study of the possible formation of MgO colloids will be initiated in the near future. For more detail, please refer to TP 02-02 (next section), which describes this study.

Summary

Since the July 2001 Status Report (Milestone RI020), Sandia has continued to perform experimental work to characterize the hydration-carbonation rates of Premier Chemicals MgO, and to determine the probable hydration-carbonation pathway MgO will take under repository conditions.

Initial inundated hydration experiments have concluded. Brucite was the only hydrated phase present in three of the solutions; in GWB, a second hydrated phase (sorel cement) formed. In most solutions, hydration appears to be readily modeled as a diffusion-limited reaction. Hydration ceased in samples immersed in DI water at 90°C after ~85% of the material converted to brucite. Non-reactive silicates and aluminates probably make up the remaining 10-15%. Since November 2001, a new set of inundated hydration experiments has been initiated to extend the curves for ERDA-6 and GWB.

Samples in GWB are difficult to quantify. Due to the high magnesium content in solution, amorphous sorel cement (identified by SEM) forms until the excess Mg is depleted and brucite becomes the stable phase. The hydrated phase contains a different amount of stochiometric water compared to brucite, making it difficult to determine, from data obtained by weight loss on ignition, the actual degree of MgO hydration that has occurred.

The ratio of MgO to the volume of GWB affects the amount of each hydration product formed. A previous experiment suggests the greater the volume of brine in the sample, the greater the fraction of sorel cement relative to brucite. Results from a second experiment, using 250 ml of brine, were compared to those from an inundated hydration experiment run under the same conditions using 100 ml of brine. As expected, the samples with 250 ml of brine never consumed the excess Mg in the system. This

Information Only

suggests that the system with a greater volume of brine had a larger quantity of sorel cement relative to brucite compared to the results from the other experiment.

Humid hydration experiments used four different relative humidities — 35%, 50%, 75%, and 95% - at four different temperatures between 25°-80°C. At higher temperatures and humidities, the MgO is readily converting to brucite. At 80°C, the higher humidity samples have converted to over 80% brucite after only four weeks. To date, enough data have been collected at the higher humidities to suggest that the system can be modeled as a diffusion-limited reaction.

It is expected that the carbonation experiments running under atmospheric P_{CO2} will take months or years for significant conversion to occur. Currently, GWB samples show less than 1% carbonation, whereas ERDA-6 has greater than 1%. Carbonates have not been identified using the XRD. The SEM has identified only Ca-bearing carbonates. However, conversion calculations imply other carbonate-bearing minerals (probably Mg carbonates) must be present in addition to the Ca-carbonates.

Experiments with 5% CO_2 will be started immediately. The matrix will differ from the current experiment by the addition of Fisher MgO, and pre-hydrated Fisher and Premier MgO.

The cemented cake experiments use three different thicknesses of MgO in two brines (GWB and ERDA-6) at temperatures between 25°C and 90°C. Samples are not agitated. The study examines whether the formation of a cemented cake of hydration products will affect the rate at which H_2O can diffuse into the sample and hydrate the remaining MgO. Results indicate that in all scenarios thickness is not a factor affecting rate of hydration, the exception being data from GWB at 25°C. Plots comparing agitated and unagitated MgO hydration show that it is hydrating at different rates in ERDA-6, but not in GWB.

Sampling of ISA experiments has concluded. Samples are currently being stored until the GC-MS becomes available for sample analysis.

Finally, Sandia will initiate a study of the possible formation of MgO colloids (See TP 02-02 in the next section).

Information Only

References

Glaus, M. A., Van Loon, L. R., Achatz, S., Chodura, A., and Fischer, K., 1999: "Degradation of cellulosic materials under the alkaline conditions of a cementitious repository for low and intermediate level radioactive waste Part I: Identification of degradation products," *Analytica Chimica Acta*, 398, 111-122.

Greenfield, B. F., Moreton, A. D., Spindler, M. W., Williams, S. J., and Woodwark, D. R., 1992: "The effects of the degradation of organic materials in the near field of a radioactive waste repository," *Material Research Society Symposium Proc.*, 257, 299-305.

Oversby, V.M., 2000: *Plutonium Chemistry Under Conditions Relevant for WIPP Performance Assessment, Review of Experimental Results and Recommendations for Future Work*, EEG-77, 47 p.

Papenguth, H.W, Krumhansl, J.L., Bynum, R.V., Nowak, E.J., Wang, Y., Kelly, J.W., and Linarez-Royce, N.J., 1997: *Chemical Conditions Model: Results of the MgO Backfill Efficacy Investigation*. Draft Report issued to the WIPP Conceptual Models Peer-Review Panel, April 23, 1997 (Prepared for the 3rd Supplementary Meeting of the Conceptual Models Peer Review Panel, held on April 25, 1997.) (Copy on file in the Sandia WIPP Central Files, Sandia National Laboratories, Albuquerque, NM.)

Papenguth, H.W, Krumhansl, J.L., Bynum, R.V., Wang, Y., Kelly, J.W., Anderson, H.L., and Nowak, E.J., (1999) "Status of Research on Magnesium Oxide Packfill," in Bennett, D.G., Papanguth, H.W., Chu, M.S.Y., Galson, D.A., Duerden, S.L., and Matthews, M.L. (editors), *International Workshop on the Uses of Backfill in Nuclear Waste Repositories*, Carlsbad, New Mexico, USA, May, 1998. Bristol, United Kingdom, Environment Agency, R&D Technical Report P178, p. 3-43 to 3-63.

Sandia National Laboratories Technical Baseline Reports—Repository Investigations, RI010. Report to the DOE, dated January 31, 2001.

Sandia National Laboratories Technical Baseline Reports—Repository Investigations, RI020. Report to the DOE, dated July 31, 2001.

Wang, Y., Bryan, C., and Wall, N., (2001). *Experimental Study of WIPP MgO Backfill at Sandia National Laboratories Carlsbad Facility*, TP 00-07 Rev. 1.

Wilson, C., Porter, D., Gibbons, J., Oswald, E., Sjoblom, G., and Caporuscio, F., (1997): *Conceptual Models Third Supplementary Peer Review Report*, U.S. EPA Air Docket A93-02, II-G-22, April 1997.

Zhang, P., Hardesty, J., and Papenguth, H., 2001: "Report of Hydration Experiments Conducted at SNL-ABQ," 10 p. in *Sandia National Laboratories Technical Baseline Reports—Repository Investigations, RI010*. Report to the DOE, dated January 31, 2001.

Information Only

Information Only

IMPORTANT NOTICE: The current official version of this document is available via the Sandia National Laboratories NWMP On-line Documents web site. A printed copy of this document may not be the version currently in effect.

Sandia National Laboratories
Waste Isolation Pilot Plant (WIPP)
Test Plan, TP 02-02

Generation of Colloids from the WIPP Backfill

Revision 0

Task 1.3.5.4.3.1

Effective Date: 01/24/02

Prepared by:

Nathalie A. Wall (6822)

Sandia National Laboratories
Carlsbad, NM

WIPP:1.3.5.4.3.1:TD:QA:DPRP1:NF;Test plan for Generation of Colloids from the WIPP Backfill, TP02-02

2002 Sandia Corporation

Information Only

135

1.0 Approval Page

Author:	*Original signed by Nathalie A. Wall* Nathalie A. Wall (6822)	*1/20/02* Date
Technical Reviewer:	*Original signed by L.H. Brush* Larry H. Brush (6822)	*1/22/02* Date
Management Reviewer	*Original signed by F.D. Hansen* Francis D. Hansen (6822)	*1/22/02* Date
QA Reviewer	*Original signed by Jonathan G. Miller* Jonathan G. Miller (6820)	*01/22/02* Date

Information Only

2.0 Table of Contents

3.0 List of Acronyms

ξ	zeta potential
AFM	atomic force microscope
κ	Debye-Hückel parameter
DLVO theory	after the four scientists Deryaguin, Landau, Verwey and Overbeek
I	ionic strength
IEP	isoelectric point
PZC	point of zero charge
SEM	scanning electron microscope
T	temperature
V_T	total potential energy of interaction
WIPP	Waste Isolation Pilot Plant

4.0 Revision History

This is the first version of this test plan. Subsequent revisions will be made in accordance with the Sandia National Laboratories Nuclear Waste Management Program Procedures: NP 20-1 Test Plans, NP 6-1 Document Review Process and NP 6-2 Document Control Process.

Information Only

5.0 Purpose & Scope

The results of this study will be used to determine whether the WIPP backfill "Premier Chemicals MgO", which is being used in the WIPP to mitigate the effect of microbial CO_2 generation on actinide mobility in a post-closure repository environment, will generate colloids, whether these colloids will be stable in WIPP conditions and whether these colloids will affect the WIPP compliance.

6.0 Background

6.1 Generalities

A colloidal phase is an intermediate state between a true solution, containing dissolved entities of ionic or molecular dimensions, and suspended particles sufficiently large to settle by gravity. The size range of colloids is considered to be from 1 nm to 1 µm (Figure 1).

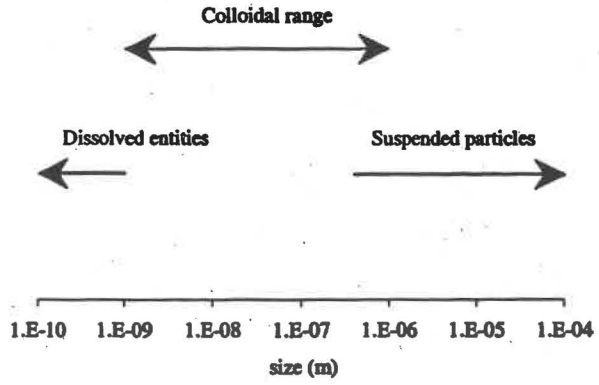

Figure 1: Size ranges of aqueous particles. (Adapted from Gaffney et al. 1996)

Colloids can be generated by dispersion or condensation. In the dispersion methods, a sample of bulk material is broken down to colloidal dimensions by some mechanical process (e.g. grinding), or ultrasonication (very high frequency sound waves, ≈ 20 kHz) in a liquid-in-liquid dispersion. The condensation methods include dissolution and reprecipitation, condensation from vapor through formation of a mist or fog from a supersaturated vapor, or chemical reactions, including reduction, oxidation or decomposition.

Colloids may be important to WIPP performance assessment because they have very large surface areas, may be mobile in aqueous solutions, and under favorable conditions colloids can adsorb metal ions.

Information Only

6.2 Colloidal coagulation / stability (Hunter 1993)

Colloids would affect actinide mobility only if they remain as stable suspended entities; coagulated colloids are not mobile. Therefore, it is important to understand the processes leading to stable colloids versus coagulated entities.

The DLVO theory (named after the four scientists Deryaguin, Landau, Verwey and Overbeek) explains the colloidal stability in terms of forces: a repulsive one due to formation of a double layer, and an attractive one due to van der Waals interactions. Colloids can possess high negative charges at their surface; as a result, ions present in the system are attracted in a compact layer adjacent to the colloid (i.e. the Stern layer), with a gradually decreasing concentration with increased distance from the colloid surface, resulting in a diffuse double layer. When double layered systems interact with each other, due to random Brownian motion, the sum of the interactions taking place in the near surroundings of the colloid creates a total potential energy of interaction V_T (sum of interactions and repulsions) which defines an energy barrier. The stability of a system depends on the energy barrier height and thickness. If the potential energy barrier is higher than the thermal energy of the colloidal particles, coagulation is hindered but, as the potential energy barrier approaches the thermal energy level, coagulation is increasingly favored. Although the DLVO theory is known to be incomplete (Manciu and Ruckensein, 2001), it has the advantage of simplicity and offers a reasonable approach for obtaining quantitative results.

V_T depends on many parameters that will eventually affect the stability/coagulation of the colloidal population: the temperature T, the charge z of the ion present in the double layer, the double layer thickness $1/\kappa$ (κ is the Debye-Hückel parameter and is directly proportional to the square root of the ionic strength I). For example, an increasing coagulation can result from increasing ionic strength of the system or an increasing charge density of the neighboring ions.

The colloidal stability will also depend on the degree of ionization of the colloidal surface, which itself is a function of the pH. The electrical potential between the bulk solution and the colloid is called zeta potential (ξ); this potential indicates the stability of the colloidal system: the greater ξ (positive or negative), the greater the colloidal stability. The isoelectric point (IEP) or point of zero charge (PZC) represents the value of pH at which the colloid has a zero net charge ($\xi = 0$). For hydroxo complexes $M^{z+}(OH)_n^{z-n}$, the PZC represents the pH resulting in an electrically equivalent concentrations of positive and negative complexes. Outside its PZC region, the colloid surface is charged. PZC values for magnesium oxide and hydroxide were reported by Parks (see Table 1).

Information Only

Material	PZC
MgO	12.4 ± 0.3
$Mg(OH)_2$	≈ 12

Table 1: PZC of Mg oxide and hydroxide (from Parks 1965).

In the case of the WIPP, charged colloids would coagulate due to the high ionic strength of the brine. But if colloids presenting a neutral charge were generated, these colloids could be stable. The pH of the brines in equilibrium with the backfill have been calculated (US EPA 1998). The pH of Salado brine in equilibrium with brucite and hydromagnesite [$Mg_5(CO_3)_4(OH)_2{\cdot}4H_2O$], or hydromagnesite [$Mg_4(CO_3)_3(OH)_2{\cdot}3H_2O$], or nesquehonite [$MgCO_3{\cdot}3H_2O$], or brucite [$MgCO_3$] is 8.69; the pH of Castile brine in equilibrium with brucite and either hydromagnesite [$Mg_5(CO_3)_4(OH)_2{\cdot}4H_2O$], or hydromagnesite [$Mg_4(CO_3)_3(OH)_2{\cdot}3H_2O$] is 9.24; the pH of Castile brine in equilibrium with brucite and nesquehonite [$MgCO_3{\cdot}3H_2O$] is 9.18; the pH of Castile brine in equilibrium with brucite and magnesite [$MgCO_3$] is 9.23. Under these pH conditions, Mg speciation calculations (Figure 2) show that the majority of Mg species exist as neutral species.

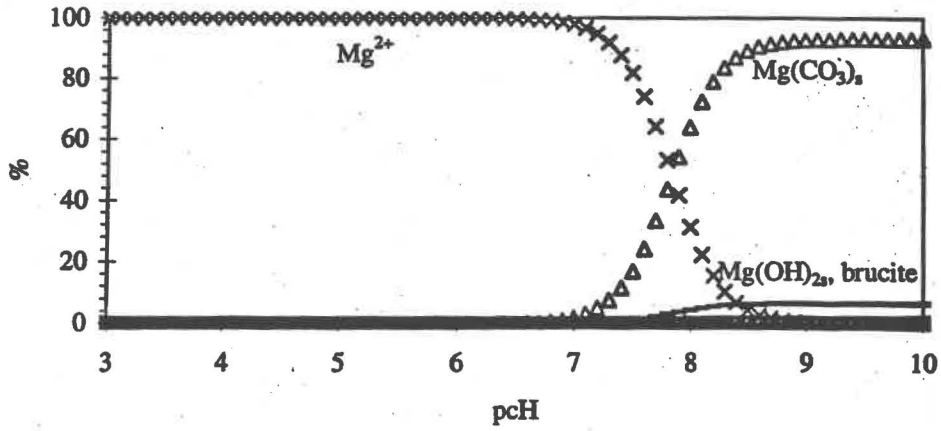

Figure 2: Mg Speciation, P_{CO_2} 10^{-5} atm. Calculated from Smith et al. 1998.

Dr. Bernhard Kienzler, from Forschungszentrum Karlsruhe in Germany, has communicated to the author of this document unpublished results regarding the finding of stable colloids originating from brucite. Dr. Kienzler stated: "Literature concerning existence, stability and mobility of colloids in highly concentrated salt solutions is rarely available. In our institute we did some work, however, it is not yet published. In German salt domes Mg bearing salts are available to a large extent,

Information Only

resulting in highly concentrated brines (Q-brine: ~4 molal $MgCl_2$). The brines have a high buffer capacity with respect to pH. In the presence of cement, pH is buffered by precipitation of brucite ($Mg(OH)_2$ or various magnesium oxychloride hydrates. These phases are not crystalline and show a slow flocculation. We consider the possibility that colloidal phases may be formed even in highly concentrated solutions." (Kienzler, 2001).

7.0 Experiments

7.1.1 Experimental processes

As stated above, literature concerning the colloidal stability in concentrated brine is not readily available. Moreover, Dr. Kienzler has also mentioned that the colloids observed were slow to form (months) and very small at first (consequently difficult to observe). For these reasons, several techniques will be used for our experiments.

Samples of pure MgO (Fisher chemicals) and WIPP backfill (Premier Chemicals MgO) will be separately inundated for various periods of time in different solutions (de-ionized water, NaCl, and a variety of synthetic WIPP brines). The Premier Chemicals MgO contains impurities such as forsterite [Mg_2SiO_4], monticellite [$MgCaSiO_4$] and portlandite [CaO]. Techniques such as filtration, ultrafiltration, centrifugation and/or ultracentrifugation will be used to separate the colloidal suspension from the solids. To detect colloids, instruments such as SEM and AFM will be used. To evaluate the stability of the colloids, the zeta potential ξ will be determined for the different systems considered, using a zeta potential sizer.

Parameters to be controlled include the ionic strength, pH, temperature, presence of secondary ions (Ca^{2+}, ...). At first, the experiments will be performed under atmospheric conditions of $CO_{2(g)}$. In a later stage of the program, the effect of $CO_{2(g)}$ will be studied.

7.1.2 Data Processing and Mathematical Models

If data processing is necessary, it may be done by hand calculation with the aid of an electronic calculator, or with a standard spreadsheet program, such as Microsoft Excel. The experimental results and the calculations generated from these results will be reviewed by technical peers.

7.1.3 Sample Handling and Control Requirements

Standard procedures for sample identification, handling, storage, shipping, archiving and disposition have been described in Sandia National Laboratories Nuclear Waste Management Program Procedure NP 13-1. Sample handling will be performed under the guidance of NP 13-1.

Samples will be labeled with unique identification numbers, date, and a reference to specific laboratory notebook page(s). Solutions will be handled and stored in accordance with documented procedures.

Information Only

7.1.4 Sample Disposal

Solutions will be disposed of in accordance with standard operating procedures in place at the Sandia National Laboratories Carlsbad laboratory.

7.1.5 Data Identification and Use

Data that are amenable to written recording will be inscribed by hand in appropriate laboratory notebooks. Such information includes, but is not limited to:

- reagent and solution preparation procedures and results
- sample preparation procedures
- sample composition and conditions e.g. pH, reagent volume, reagent concentration, temperature
- sample handling
- sample analysis procedures and results

7.1.6 Data Transfer and Reduction Controls

Typical data transfer is from instrumental output to laboratory notebook and from laboratory notebook to a spreadsheet program, if applicable. Printed copies of instrumental output (e.g. photo) will be permanently attached to the laboratory notebook within the section dedicated to the pertinent experiment.

7.1.7 Identification, Segregation, Disposal of Erroneous Data

Data suspected to be erroneous will be tested by comparison to replicate samples or replicate experiments. Statistical justification for rejection of erroneous data will be provided within the laboratory notebook.

7.1.8 Equipment testing

The equipment used for these experiments will be tested in accordance with the Sandia National Laboratories Nuclear Waste Management Program Procedure NP 12-1, Control of Measuring and Test Equipment.

8.0 Training and Other Standard Procedures

All personnel participating in the work described in this Test Plan will be trained and qualified for the assigned tasks. This requirement will be implemented in accordance with NWMP procedure NP 2-1, "Qualification and Training." Evidence of qualification and training will be documented with Form NP 2-1-1 *Qualification and Training*. Additionally, the following NWMP Procedures and Project Specific Procedures are applicable:

SOP-C001: "Standard Operating Procedure for Activities in the SNL/Carlsbad Laboratory Facility."
SP 13-1 "Chain of Custody
NP 6-1 "Document Review Process"
NP 13-1 "Sample Control"
NP 12-1 "Control of Measuring and Test Equipment"
NP 20-2 "Scientific Notebooks"

Information Only

NP 2-1 "Qualification and Training
NP 17-1 "Records"

9.0 Health & Safety

The health and safety requirements relevant to the tasks for work in this test plan are described in SOP-C001

10.0 Permitting/Licensing

There are no special licenses or permitting requirements for the work described in this test plan.

11.0 References

1. DOE (US Department of Energy), "Title 40 CFR Part 191 Compliance Certification Application for the Waste Isolation Pilot Plant", DOE/CAO-1996-2184, Vol. 1-21. Carlsbad, NM: US Department of Energy, Carlsbad Area Office. 1996.
2. Gaffney J.S., Marley N.A., Clark S.B. Humic and Fulvic Acids and Organic Colloidal Materials in the Environment. In *Humic and Fulvic Acids. Isolation, Structure, and Environmental Role*. Gaffney, Marley and Clark Eds. ACS, Washington, DC. 1996, 2-16.
3. Hunter R.J. In *Introduction to Modern Colloid Science*, Oxford Science publications. 1993.
4. Kienzler B. Personal communication. July 2001.
5. Manciu M. and Ruckensein E. Role of the hydration Force in the Stability of Colloids at High Ionic Strengths. *Langmuir*, 2001, 17, 7061-7070.
6. Parks G.A. The Isolelectric Points of Solid Oxides, Solid Hydroxides, and Aqueous Hydroxo Complex Systems. *Chemical Reviews*, 1965, 177-197.
7. Smith, R. M., Martell A. E., Motekaitis, R. J.: NIST Critically selected stability constants of metals complexes database, Version 5.0. User's Guide. U.S. Department of Commerce. Technology Administration, National Institute of Standards and Technology, Standard Reference Data Program, Gaithersburg, MD 1998.
8. US Environmental Protection Agency. Technical support document for 194:23 – Models and computer codes. Washington DC. May 1998.

Information Only

Information Only

3.3 Cementitious Materials

Experimental Work to Develop a Model for Cement/Brine Interactions[1]

Charles R. Bryan
Sandia National Laboratories, MS 1395
4100 National Parks Highway
Carlsbad, NM USA 88220

Abstract

Sandia National Laboratories/Carlsbad is currently performing research to develop a model for cement/brine interactions to be used in performance assessment (PA) of the Waste Isolation Pilot Plant (WIPP). Modeling cement degradation in WIPP-relevant brines is critical for predicting the long-term integrity of cement borehole plugs, an area of uncertainty in conceptual models used for WIPP PA. Assumed degradation rates have a first order influence on PA conceptual models by controlling brine flow into and out of the repository in human intrusion scenarios, directly affecting such PA parameters as the source term for the Culebra Dolomite, gas generation rates, and spallings releases. In addition, cementitious waste forms are a significant fraction of the waste inventory, and cement-brine reactions may affect repository chemistry and actinide solubility. Dissolution of cement components could result in high-pH microenvironments, while calcium released during cement degradation will serve as an additional sink (with MgO) for carbon dioxide.

Information for developing a model for cement/brine reactions and borehole plug failure rates is being gathered from two sources. The first consists of laboratory experiments with cement and brine, being run to develop an equilibrium thermodynamic model. They include gibbsite ($Al(OH)_3$) solubility experiments to determine Pitzer parameters for Al under conditions relevant to the WIPP, and batch experiments with crushed, hydrated cement to determine the equilibrium mineral assemblages that form at varying cement/brine ratios. Applying this model to borehole plug degradation rates requires obtaining additional data on the effects of non-equilibrium processes (diffusion, mineral precipitation, etc.). Batch experiments with cement wafers and cement core-column (flow-through) experiments are being run for this purpose.

The second source of information on borehole plug degradation is sampling of downhole cement samples and casing corrosion products during borehole plugging and abandonment (P&A), borehole recompletion, and general borehole maintenance at the WIPP site. Casing corrosion is of importance because it represents a second, possibly much faster,

[1] This work is covered by BOE #1.3.5.4.3 and WBS #1.3.5.4.3.2

Information Only

mode of borehole plug failure. This opportunistic sampling allows recovery of samples that have been exposed to WIPP brines for up to 20 years—a much longer time scale than that available for laboratory experiments. Several wells were sampled in FY00 and FY01, but only casing corrosion products were collected and analyzed—no opportunity for cement retrieval occurred.

Introduction and Objectives

An understanding of cement/brine interactions is important in evaluating the future performance of the WIPP repository. In 1996, the National Academy of Science (NAS) stated that the only credible scenarios resulting in release of radionuclides from the WIPP repository are those involving human intrusion, such as drilling for potash or oil (NAS/NRC Peer Review, 1996). Calculated releases during and after intrusion are dependent upon the predicted integrity of cement borehole plugs, which directly control brine flow into and out of the repository, determining the Culebra source term and indirectly affecting other important parameters such as gas generation rates and spallings releases. In addition, cementitious waste forms are a significant fraction of the waste inventory, and cement-brine reactions will affect repository chemistry. Dissolution of cement components could result in high-pH microenvironments, while calcium released during cement degradation will serve as an additional sink (with MgO) for carbon dioxide released by microbial degradation of organic components in the waste.

A primary goal of the cementitious materials work at Carlsbad is to develop a model for the degradation and failure of cement borehole plugs. In order to do this, it is necessary to develop a thermodynamic model for cement/brine interactions, which can also be used to evaluate the potential effects of cement on repository chemistry.

The degradation of borehole plugs is being examined both by laboratory investigations and by opportunistic sampling of downhole cement and casing corrosion products during plugging and abandonment (P&A), recompletion, and general maintenance of water monitoring wells in and around the WIPP site. The test plans for these activities are, respectively, TP 00-06 "Experimental Work to Develop a Model for Cement Borehole Plug Degradation at the WIPP Site," and TP 00-02 "Collection and Analysis of Downhole Cement and Steel Samples During Borehole Plugging and Abandonment."

Laboratory work on cement/brine interactions has recently begun. Experiments currently being carried out include those aimed at developing an equilibrium thermodynamic model and those for evaluating the mechanisms and kinetics of cement degradation in WIPP brines. Experiments are being run to determine Pitzer interaction parameters for silicon and aluminum, two of the dominant constituents in cement. While data for Si and Al are available at low and moderate pH, no data exist for the high pH values typical of cement. A second set of experiments is determining the equilibrium mineral assemblages present in cement/WIPP brine (Castile and Salado) systems; the compositional data for the brines and solids in these experiments will also be used to validate the thermodynamic model, once it is developed. Cement degradation rate experiments consist of two types: batch experiments with cement wafers, sampled periodically to evaluate rates of cement degradation and of diffusion of brine components into the

Information Only

cement; and column (flow-through) experiments, for evaluating the kinetics of cement degradation in a system in which the cement is continually being exposed to fresh brine. Mineral precipitation (gypsum, brucite, ettringite, and carbonate minerals are likely precipitates) is likely to be a dominant factor in the column experiments, and may either decrease the reaction rate by forming mineral coatings and plugging porosity, or speed plug failure, if expansive minerals form and degrade cement integrity by causing flaking or fracturing.

The field sampling program consists of collecting downhole cement and casing corrosion samples from materials brought out of the hole—generally casing, tubing, or corrosion products dredged from the bottom of the hole—during borehole plugging and abandonment, recompletion, or general maintenance. Future sampling may consist of drilling bottom-hole cement plugs, or coring the casing and casing cement using a side-core sampler. Casing corrosion samples are collected in addition to cement because borehole plugs may lose integrity due to casing failure as well as by cement degradation. These samples offer information on long-term (>20 years, in some cases) products of cement/brine reactions, of steel corrosion pathways in WIPP relevant brines, and of failure modes for cement borehole plugs. Several wells were sampled in FY00 and FY01, but only casing corrosion products were collected and analyzed—opportunities for cement retrieval are rare, and have not yet occurred. The borehole sampling effort is currently being maintained at a very low level—the M&O plugging and abandonment program was not funded in FY01.

Laboratory experiments to develop a model for cement degradation and borehole plug failure.

Laboratory work on cementitious materials has recently begun. The primary objective of this research is to develop a model for cement/brine interactions, which will be used to estimate cement borehole plug lifetimes and to evaluate the effect of cementitious wastes on repository chemistry. A great deal of thermodynamic data are available on cement and alteration phases, and thermodynamic models for cement degradation in dilute solutions have been formulated. The information needed to expand those existing models to cover WIPP conditions, and to develop a model for borehole plug failure rates, can be summarized as follows:

1. Parameters for a Pitzer model for the activities of aqueous species in the brines. Pitzer parameters for the dominant species present in WIPP brines are summarized in Harvie et al. (1984) and Pitzer (1987). Some solubility data and Pitzer interaction coefficients are available for Si and Al in concentrated electrolytes at low to intermediate pH and in some cases, at high pH (Marshall, 1980; Chen and Marshall, 1981; Gasteiger, et al., 1992; Palmer and Wesolowski, 1991; Wesolowski, 1992; Wesolowski and Palmer, 1992, 1994; Felmy et al., 1994a,b; Azaroual et al., 1997; Richter et al., 2000). However, a complete data set of the necessary Pitzer parameters is not available for Si and Al at pH values and brine compositions relevant to the WIPP or to cement pore fluids (pH 9-13).

Information Only

2. Identification of the initial hydrated cement phases, cement alteration phases, and alteration pathways. The phases that are present in hydrated cement are well known, and can be calculated modally from the initial composition of the cement blend (Atkins et al., 1992a; Macphee et al., 1989). Degradation of both salt-free and salt-saturated cement in different electrolytes has been widely studied (Atkinson and Hearne, 1990; Bonen, 1992; Bonen and Cohen, 1992; Havlica and Sahu, 1992; Krumhansl 1993, 1995; Krumhansl and Lambert, 1992; Lambert et al., 1992; Wakeley et al., 1992, 1994; Poole et al., 1994; Neall, 1994, 1996; Bonen, 1996; Pfingsten and Shiotsuki, 1998), and possible alteration phases that are likely to form have been identified. Although some studies have been done with synthetic WIPP brines, the results varied from study to study and were in some cases inconsistent, possibly due to differences in experimental conditions (some experiments were run at elevated temperatures). New experiments will be run at ambient temperatures, more similar to conditions expected in the WIPP, and will include Castile brine, an electrolyte of primary importance to this study which has not previously been examined.
3. Once the important phases have been identified, thermodynamic data must be compiled, and an equilibrium thermodynamic model will be generated. Thermodynamic data are available for cement phases, alteration phases, and naturally-occurring mineral analogs (Goto et al., 1979; Gartner and Jennings, 1987; Glasser et al., 1987; Atkinson et al, 1989; Atkins et al., 1991a, 1991b, 1992b; Damidot and Glasser, 1992, 1993; Taylor, 1992; Xie and Beaudoin, 1992). Where possible, data for the actual cement phases will be used, as mineral analogs are commonly more crystalline than the cement phases, and are not compositionally identical. Finally, the model will be compared to existing thermodynamic models for cement degradation (Berner, 1987, 1988, 1990; Atkins et al., 1992a; Bennett, et al., 1992; Neall, 1994, 1996; Krumhansl, 1995; Pfingsten and Shiotsuki, 1998).
4. A complete equilibrium thermodynamic model for brine/cement interactions is still insufficient for describing cement plug degradation, as it is not an equilibrium process. Reaction kinetics may inhibit formation of specific phases; coatings may form on cement/brine interfaces or precipitated phases may reduce porosity and permeability, inhibiting further reaction; or expansive alteration phases may fracture the cement, forming "fast paths" for brine flow through the cement plug. Batch experiments with hydrated cement wafers and column experiments with cement cores are being performed to evaluate the impact of these non-equilibrium processes. Finally, a more comprehensive degradation model, incorporating these non-equilibrium processes, will be implemented.

Laboratory experiments to determine the necessary information are being run concurrently and are described in the following sections.

Cement Preparation

In order to determine the appropriate type of cement to be used in the plug degradation experiments, 52 borehole plugging logs for wells in the Delaware Basin were examined. Where the type of cement was specified (slightly more than half of the cases), either Type

Information Only

C or Type H oilfield cement was used. Both cement types are sulfate-resistant and chemically similar—the major difference between the two is that Type H is coarser-ground and hence hydrates and hardens more slowly. Thus, Type H was commonly used in the deeper holes (greater than ~7000 feet), to prevent premature solidification. Aggregate was not added, but 2% by weight $CaCl_2$ (3 cases) or KCl (1 case) was occasionally added as an accelerator.

As there is little chemical difference between Type C and Type H cement, it was decided to use only type C for the borehole plug degradation studies. Lone Star Industries, Inc., an oilfield cement company that services the Delaware Basin, was contacted and 25 kg of dry Type C cement was obtained. The cement was mixed with water using standard oilfield ratios as obtained from Schlumberger/Dolwell; dry cement was mixed with 44 wt% DI water (27 wt% is sufficient for complete hydration). Salt-saturated cement was also produced, by adding NaCl equivalent to 37 wt% of the water present (both salt-free and salt-saturated cement is used in Delaware Basin borehole plugs, depending upon the formations intersected). After curing for two weeks, a fraction of each was crushed to <150 μm for use in batch equilibration experiments. The remainder of the solidified, hydrated cement was either sliced into wafers (25 mm x 25 mm x 3 mm) for the wafer experiments, or cored with a 25 mm diameter diamond coring bit for use in column flow-through experiments.

Cementitious waste forms in the repository will be dominantly ordinary Portland cement (opc). As this material is not sulfate-resistant and will not be salt-saturated, it is likely to react more rapidly with WIPP brines than the Type C oilfield cement. Thus, samples of this material will also be obtained and used in powdered cement and wafer batch experiments.

Following crushing, samples of all hydrated cement are being analyzed by X-ray Diffraction (XRD) and scanning electron microscope (SEM) to determine initial mineralogy and texture.

Brines
Two WIPP-relevant brines are being used in the cement work. These are GW and ERDA-6 brines, which are synthetic Salado and Castile brines, respectively.

Lab experiments
Experiments that are currently underway or planned for the coming year are listed in Table 1, along with the information to be derived from each, and the current status.

Al solubility experiments are being run to determine Pitzer interaction parameters for aluminum and silicon, two of the dominant constituents in cement. Our experiments deal primarily with aluminum, as other workers (Andrew Felmy at Pacific Northwest National Laboratories, funded from non-WIPP sources) are currently determining Pitzer parameters for silicon. Pitzer parameters are derived from Al solubility data at varying

Information Only

Table 1. Experimental matrix for research on cement/brine interactions.

Experiment	Information gained	Status
Al/Si solubility experiments	Pitzer parameters for Al and Si in WIPP-relevant brines	In progress (7/01)
Crushed cement reaction rate experiment	The proper time interval for equilibrium batch experiments.	In progress (1/02)
Crushed cement/ brine equilibration experiments.	Equilibrium mineral assemblages/ brine compositions at varying brine/cement ratios.	In progress (12/01)
Crushed cement leaching experiments.	A"mixing tank" type experiment to determine the brine volume necessary for complete degradation of the cement. Will also be used to validate the eventual thermodynamic model.	In progress (1/02)
Wafer experiments	Effects of non-equilibrium processes (e.g., precipitation of mineral coatings, fracturing caused by expansive alteration products).	In progress (1/02)
Column experiments.	Effects of non-equilibrium processes in a flow-through system (e.g., plugging of pores by mineral precipitates, fracturing due to mineral growth).	Will start soon (2/02)

hydrogen ion concentration (pC_H) in simple binary electrolytes representing the major components in WIPP brine (e.g., $CaCl_2$, $MgCl_2$, and $NaSO_4$). Experimentally, the solubility of gibbsite ($Al(OH)_3$) is measured in batch systems over a range of pH values, while the solid phase present is identified by XRD. To calculate the pC_H in the solutions, each electrolyte is titrated with acid or base, and a correction factor for the measured pH is determined by plotting the observed hydrogen ion concentration ($[H^+]_{observed}$) against the actual concentration, known from the amount of acid or base added ($[H^+]_{added}$). Titration and Al solubility results for one electrolyte of interest, $CaCl_2$, are shown in Figure 1.

Experiments with crushed, hydrated cement (<150μm) are aimed primarily at determining the equilibrium mineral assemblages present in cement/WIPP brine (Castile and Salado) systems. In addition, compositional data for the brines and solids in these experiments will be used to validate the thermodynamic model eventually developed. Three experiments are currently underway. In the reaction rate experiment, cement was added to GW and Castile brines, and samples of the brine are being collected repeatedly over several months. By monitoring the change in brine composition, the time required to reach equilibrium will be determined. Another experiment will be run at 60°C to determine if accelerating the reaction through heating results in a different equilibrium mineral assemblage. In the equilibration experiment, cement and brine were mixed in varying ratios, and once equilibrium has been reached (after the time interval determined by the rate experiment), solid and liquid phases will be sampled and analyzed chemically and mineralogically. In these mixed batch systems, the small size of the cement grains and the continuous agitation should preclude formation of mineral coatings, and an equilibrium assemblage of alteration minerals should form. In the leaching experiment, brine and cement are being continually mixed and allowed to equilibrate, and the electrolyte is periodically centrifuged off, and fresh brine added. The composition of the

Information Only

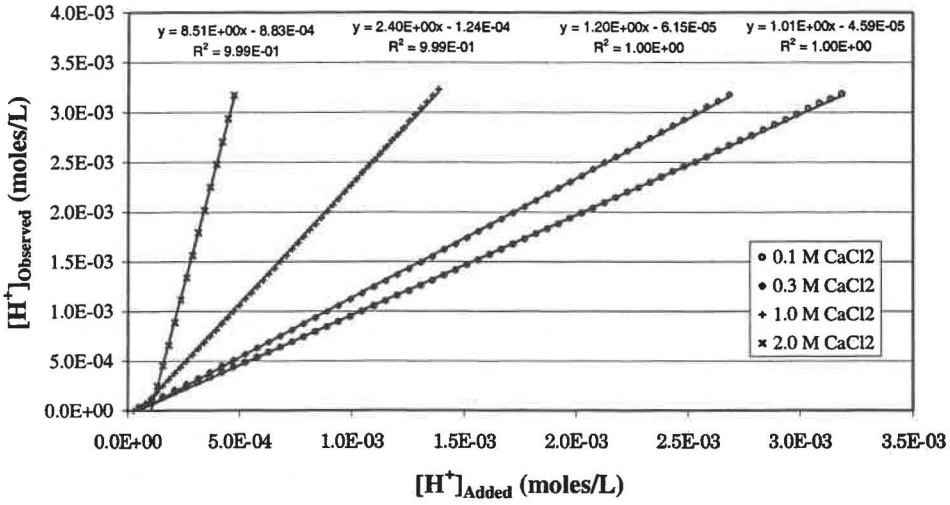

a.

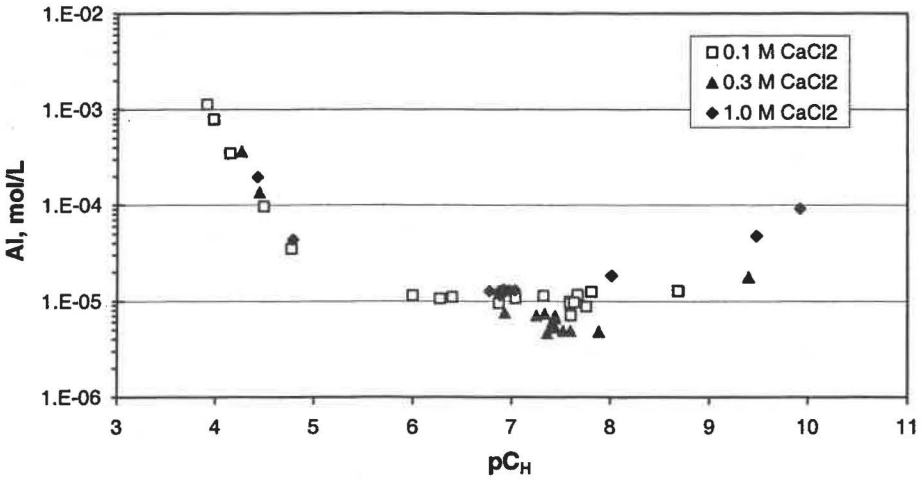

b.

Figure 1. Solubility of $Al(OH_3)$ (gibbsite) in $CaCl_2$ electrolytes. a) Titration data for 0.1 M, 0.3 M. 1.0 M, and 2.0 M $CaCl_2$ solutions. The slopes of the lines represent the factor necessary to correct pH to pC_H. b) $Al(OH)_3$ (gibbsite) solubility data for $CaCl_2$ electrolytes at varying pC_H.

Information Only

brine and the solid phase are monitored at each step. This equilibrium "mixing tank" experiment will provide information on cement degradation rates based upon equilibrium conditions—that is, based on a mass balance of cement and brine reactants.

The degradation rate experiments consist of two types: batch experiments with cement wafers, and core-column (flow-through) experiments. In the wafer experiments, 3 mm thick wafers of cement were placed in 200 ml of GW and ERDA-6 brines, and will be sampled periodically and analyzed by SEM to observe the mineral coatings that form and possible effects these may have on the alteration mineral assemblage that forms in the underlying cement. Formation of low-porosity mineral coatings may significantly deplete cement pore waters in some aqueous species, resulting in formation of different alteration products than those observed in the crushed cement batch systems.

The core-column experiments will evaluate the kinetics of cement degradation in a system in which the cement is continually being exposed to fresh brine. Brines will be pumped through whole and synthetically fractured cement cores, and the effluent will be collected and analyzed. Eventually, the cores will be removed from the holders, sectioned, and characterized texturally and petrographically by optical microscopy and SEM imaging. Some material will be crushed and analyzed by XRD to determine the alteration phases present, or digested and chemically analyzed to determine the chemical changes associated with alteration. These experiments will provide information on the effects of non-equilibrium processes, such as diffusion and mineral precipitation (gypsum, brucite, ettringite, and carbonate minerals are likely precipitates) on cement permeability and degradation.

Sampling During Well Maintenance and Abandonment

In FY00 and FY01, samples were taken from several monitoring wells at the WIPP site. No opportunities for cement recovery occurred—cement recovery is generally limited to cases where a poor cement/casing bond requires that the casing be pulled from the hole prior to pouring a cement plug. Samples of casing corrosion were collected from several wells, but only from depths above the Salado Formation. In the Compliance Certification Application (CCA), borehole plugs at these depths are assumed to fail rapidly (CCA, Appendix MASS, DOE, 1996), so casing corrosion is of relatively little interest. Unfortunately, corrosion samples from depths below the repository, where casing corrosion models are critical to estimating the borehole plug lifetimes, have not yet become available.

The casing corrosion samples from above the Salado were densely cemented and orange-black, and strongly magnetic. Sample mineralogy and texture was determined by XRD analysis and SEM examination. Sample mineralogy was surprisingly similar in all cases (XRD patterns for 5 samples are shown in Figure 2), consisting mostly of magnetite (Fe_3O_4), goethite (FeOOH), and lepidocrocite ($FeO(OH_{1-x},Cl_x)$). Examination by SEM shows that the samples consist dominantly of dense layers, presumably formed parallel to the steel casing surface, of finely crystalline mixed magnetite, goethite, and lepidocrocite (Figure 3a). Lens-like vugs occur between the layers, and contain more coarsely

Information Only

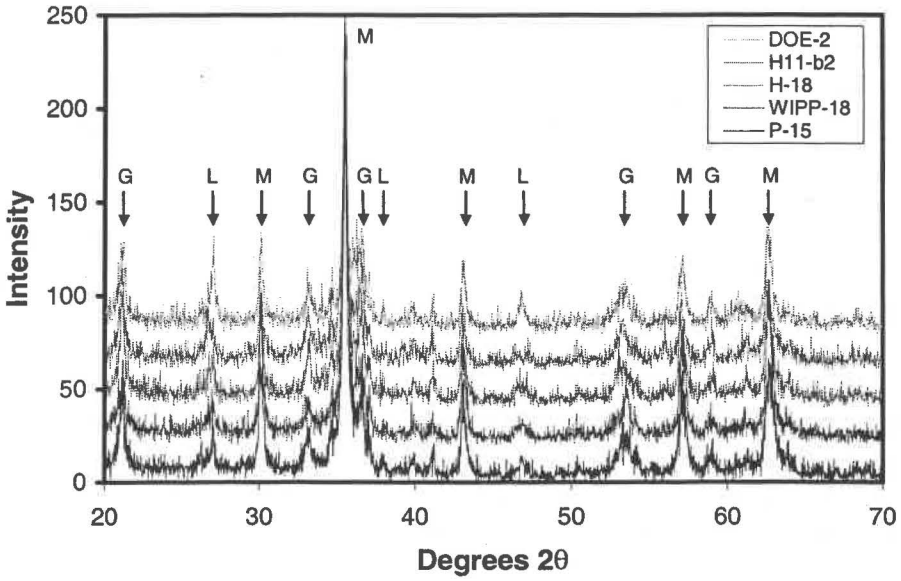

Figure 2. XRD patterns for casing scale, collected from several boreholes at supra-Salado depths. Patterns are identical, and indicate that the material contains magnetite (M), goethite (G), and lepidocrocite (L). Peak heights are not indicative of mineral abundance.

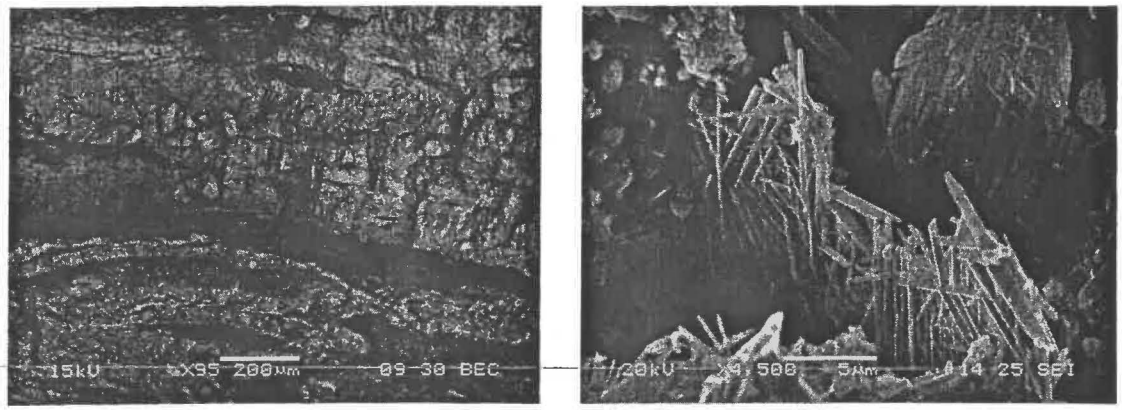

a) b)

Figure 3. SEM images of casing scale: a) low magnification image, showing the overall layered structure; b) goethite lining a lens-like vug, pseudomorphing a coarsely-bladed precursor mineral.

Information Only

153

crystalline goethite, present as plate-like clusters apparently pseudomorphing a coarsely bladed precursor mineral (Figure 3b).

The concentration of iron in the ferrous state was determined by wet chemistry, and used to quantify the amount of magnetite present in each sample. Results are given in Table 2. The similarity in mineralogy and in magnetite content of the samples suggests that the corrosion pathway for all samples was similar. This pathway probably involves formation of a precursor mineral, possibly pyroaurite ("green rust"), a mixed ferrous/ferric oxide that can contain significant amounts of chlorine. Decomposition of this mineral into magnetite, goethite and lepidocrocite could yield the mineralogy and replacement textures seen in the samples.

The corrosion pathway observed in these samples, collected from the oxidizing or at most mildly reducing groundwater above the Salado, is unlikely to apply to casing corrosion below the repository, where highly reducing conditions are expected. However, the presence of a ferrous iron-containing phase, magnetite, in the reaction products suggests that the model for casing corrosion at depth advanced in the CCA, in which goethite is the end product, is probably not realistic. The corrosion pathway is of importance because it determines the rate of hydrogen gas production, and it was proposed in the CCA that corrosion-generated hydrogen gas would inhibit casing corrosion and failure.

Another important parameter in performance assessment is the permeability of boreholes after plug failure. In the CCA, the boreholes were assumed to be filled from top to bottom with corrosion products that flaked off the casing walls, and that this material was texturally and hydraulically similar to fine sand. To test this, an effort was made during P&A sampling to collect samples of the bottom sediments prior to scraping and cleaning holes for plugging. Only holes that were cased from top to bottom were considered candidates for bottom hole sampling--in uncased holes, geologic materials that cave or

Table 2. The magnetite content of several WIPP casing corrosion samples.

Borehole #	Sample Description	% Magnetite (Fe_2O_3)
H2-b2	Casing scale, recovered after scraping well (average of 5 samples).	25.19
DOE-2	Casing scale, scraped from 0'-150'.	15.12
DOE-2	Casing scale, scraped from 650'-750'.	19.34
WIPP-18	Casing scale, scraped from 650'-750'.	18.59
H-18	Casing scale, recovered after scraping well (average of 2 samples).	19.58
H11-b2	Casing scale, recovered after scraping well.	18.31
P-15	Casing scale, recovered after scraping well.	25.23
P-15	Casing scale recovered as sludge from the bottom of the hole.	16.23

Information Only

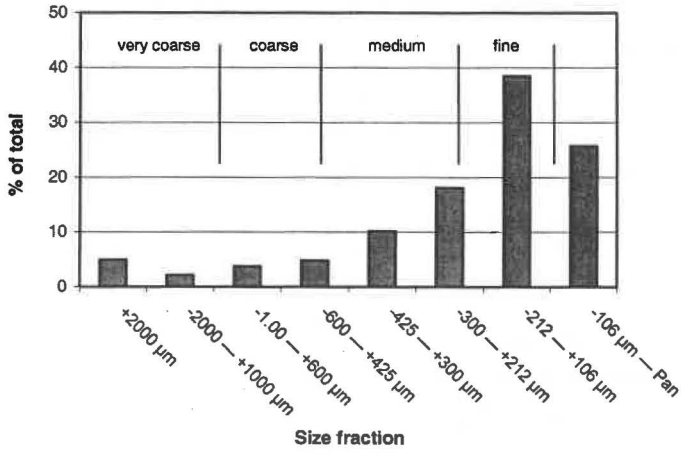

Figure 4. Size distribution for casing scale recovered from the bottom of Hole P-15. This material flaked off of casing walls naturally—it was not scraped. Sand size fractions are listed across the top of the figure. The material is dominantly fine-grained sand.

spall from the walls dominate the bottom hole sediments. Only one sampling opportunity for bottom-hole sediments, borehole P-15, occurred. The collected material was sieved, and the results of the size analysis are shown in Figure 4. Although the material contains rare coarse (>1 mm) fragments of scale, and some finer, silt-sized material, the majority of the sample is indeed fine sand. The sample volume was too small to actually measure porosity and permeability, but this data does offer support for the CCA assumption of "fine sand" in the borehole.

Although the results of the plugging and abandonment sampling program are of interest, it is apparent that collection of downhole cement and of casing corrosion samples from repository depths and greater is necessary for this program to significantly modify the current CCA models for borehole plug degradation. Such opportunities will be taken, if they arise.

References

Atkins, M., Bennett, D.G., Dawes, A.C., Glasser, F.P., Kindness, A., and Read, D., 1992a: "A Thermodynamic Model for Blended Cements," *Cement and Concrete Research*, 22 (2-3), 497-502.

Atkins, M., Glasser, F.P., and Kindness, A., 1992b: "Cement Hydrate Phases; Solubility at 25 °C," *Cement and Concrete Research*, 22 (3), 241-246.

Atkins, M., Glasser, F.P., and Kindness, A., 1991a: "Phase Relations and Solubility Modelling in the CaO-SiO_2-Al_2O_3-MgO-SO_3-H_2O System: for Application to Blended Cements," *Cement and Concrete Research*, 22 (3), 241-246.

Information Only

Atkins, M., Macphee, D., Kindness, A., and Glasser, F.P., 1991b: "Solubility Properties of Ternary and Quaternary Compounds in the $CaO-Al_2O_3-SO_3-H_2O$ System," *Cement and Concrete Research*, 21(6), 991-998.

Atkinson, A., and Hearne, J.A., 1990: "Mechanistic Model for the Durability of Concrete Barriers Exposed to Sulphate-bearing Groundwaters," *Mat. Res. Soc. Symp. Proc.,* 176, 149-156.

Atkinson, A., Hearne, J.A., and Knights, C.F., 1989: *Aqueous Chemistry and Thermodynamic Modelling of CaO-SiO2-H2O Gels at 80°C*, DOE Report # DOE/HMIP/RR/91/045., 37 pp.

Azaroual, M., Fouillac, C., and Matray, J.M., 1997: "Solubility of Silica Polymorphs in Electrolyte Solutions, I. Activity Coefficient of Aqueous Silica from 25 °C to 250 °C, Pitzer's Parameterization," *Chemical Geology*, 140, 155-165.

Bennett, D.G., Read, D., Atkins, M., and Glasser, F.P., 1992: "A thermodynamic model for blended cements II: Cement hydrated phases; Thermodynamic Values and Modelling Studies," *J. Nuclear Materials*, 190, 315-325.

Berner, U.R., 1987: "Modelling Porewater Chemistry in Hydrated Portland Cement," *Mat. Res. Soc. Symp. Proc.*, 84, 319-330.

Berner, U.R., 1988: "Modelling the Incongruent Dissolution of Hydrated Cement Minerals," *Radiochim. Acta*, 44/45, 387-393.

Berner, U., 1990: *A Thermodynamic Description of the Evolution of Pore Water Chemistry and Uranium Speciation During the Degradation of Cement*, Technical Report 90-12, Paul Scherrer, Villigen, Switzerland.

Bonen, D., 1992: "Composition and Appearance of Magnesium Silicate Hydrate and its Relation to Deterioration of Cement-Based Materials," *J. Am. Ceram. Soc.*, 75, 2904-2906.

Bonen D., and Cohen, M.D., 1992: "Magnesium Sulfate Attack on Portland Cement Paste II. Chemical and Mineralogical Analysis," *Cement and Concrete Research*, 22, 707-718.

Bonen, D., 1996: "Petrographic Analyses of Concrete and Grout Recovered from the Waste Isolation Pilot Plant," The Technological Institute, Northwestern University, Interim Report to SNL dated January 15, 1996, 9 pp.

Chen, C.A., and Marshall, W.L., 1981: "Amorphous Silica Solubilities IV. Behavior I Pure Water and Aqueous Sodium Chloride, Sodium Sulfate, Magnesium Chloride, and Magnesium Sulfate Solutions up to 350 °C," *Geochim. Cosmochim. Acta*, 46, 279-287.

Damidot, D., and Glasser, F.P., 1992: "Thermodynamic Investigation of the $CaO-Al_2O_3-CaSO_4-H_2O$ System at 50°C and 85°C," *Cement and Concrete Research*, 22, 1179-1191.

Damidot, D., and Glasser, F.P., 1993: "Thermodynamic Investigation of the $CaO-Al_2O_3-CaSO_4-H_2O$ System at 25°C and the Influence of Na_2O," *Cement and Concrete Research*, 23, 221-238.

Department of Energy, 1996: *Title 40 CFR Part 191: Compliance Certification Application for the Waste Isolation Pilot Plant, Appendix MASS Supplemental Information on Modeling Assumptions*, Department of Energy/Carlsbad Area Office, Carlsbad, NM.

Felmy, A.R., Schroeder, C.C., and Mason, M.J., 1994a: *A Solubility Model for Amorphous Silica in Concentrated Electrolytes*, DOE Report # PNL-SA-25345.

Information Only

Felmy, A.R., Rustad, J.R., Mason, de la Bretonne, R., 1994b: *A Chemical Model for the Major Electrolyte Components of the Hanford Waste Tanks: the Binary Electrolytes in the System: Na-NO_3-NO_2-SO_4-CO3-F-PO_4-OH-Al$(OH)_4$-H_2O*, DOE Report # PNL-SA-23952.

Gartner, E.M., and Jennings, H.M., 1987: "Thermodynamics of Calcium Silicate Hydrates and Their Solutions," *J. Am. Ceram. Soc.*, 70 (10), 743-749.

Gasteiger, H.A., Frederick, W.J., and Streisel, R.C., 1992: "Solubility of Aluminosilicates in Alkaline Solutions and a Thermodynamic Equilibrium Model," *Ind. Eng. Chem. Res.*, 31, 1183-1190.

Glasser, F.P., Lachowski, E.E., MacPhee, D.E., 1987: "Compositional Model for Calcium Silicate Hydrate (C-S-H) Gels, their Solubilities and Free Energies of Formation," *J. Am. Ceram. Soc.*, v. 70, #7, 481-485.

Goto, S., Tsunetani, M., and Kondo, R., 1979: "Free Energy of Formation of $3CaO{\cdot}Al_2O_3{\cdot}CaCl_2{\cdot}12H_2O$ in Connection with Durability of Hardened Cement Immersed in Sea Water," *Ann. Chim. Fr.*, 4, 425-429.

Harvie, C.E., Moller, N., and Weare, J.H., 1984: "The Prediction of Mineral Solubilities in Natural Waters: The Na-K-Mg-Ca-H-Cl-SO_4-OH-HCO_3-H_2O System to High Ionic Strengths at 25 °C," *Geochim. Cosmochim. Acta*, 44, 981-997.

Havlica, J., and Sahu, S., 1992: "Mechanism of Ettringite and Monosulfate Formation," *Cement and Concrete Research*, 22 (4), 671-677.

Krumhansl, J.L., 1993: "The Accelerated Testing of Cement in Brines" *Proc. Am. Ceramic Soc., Cement-Based Materials*, April 19-22, 1993, Cincinnati, OH, 153-154.

Krumhansl, J.L., 1995: *Brine-Concrete Interactions and their Implications for WIPP Seal Performance*, unpublished SNL letter report, dated Oct. 25, 1995.

Krumhansl J.L., and Lambert, S.J., 1992: "Degradation of Portland Cements Exposed to Evaporite Brine at Hydrothermal Temperatures," *Mat. Res. Soc. Symp. Proc.*, 245, 123-128.

Lambert, S.J., Nowak, E.J., Wakeley, L.D., and Poole, T.S., 1992: "Interactions between Concrete and Brine at the Waste Isolation Pilot Plant (WIPP) Site, New Mexico," in *Advanced Cementitious Systems: Mechanisms and Properties, Materials, Research Society Symposium Proceedings*, 245, 111-122.

Marshall, W.L., 1980: "Amorphous Silica Solubilities — I. Behavior in Aqueous Sodium Nitrate Solutions; 25-300°C, 0-6 molal*," *Geochim Cosmochim Acta*, 44, 907-913.

Macphee, D.E., Atkins, M, and Glasser, F.P., 1989: "Phase Development and Pore Solution Chemistry in Ageing Blast Furnace Slag-Portland Cement Blends," in *Scientific Basis for Nuclear Waste Management XII*, MRS Proc. 127, 475-480.

NAS/NRC, 1996: *The Waste Isolation Pilot Plant: A Potential Solution for the Disposal of Transuranic Waste*, National Academy Press, Washington D.C., 1996.

Neall, F.B., 1994: *Modelling of the Near-Field Chemistry of the SMA Repository at the Wellenberg Site: Application of the Extended Cement Degradation Model*, Paul Scherrer Institute Paper # 94-03, 85 pp.

Information Only

Neall, F.B., 1996: *Modelling the Long-Term Chemical Evolution of the Near-Field of a Cementitious Repository Using SEQDISSOLVE – Model, Assumptions, and Results*, Paul Scherrer Institute Paper # TM 44-95-08, 41 pp.

Palmer, D.A., and Wesolowski, D.J., 1991: "Aluminum Speciation and Equilibria in Aqueous Solution: II. The Solubility of gibbsite in Acidic Sodium Chloride Solutions from 30-70 °C," *Geochim. Cosmochim. Acta*, 56, 1093-1111.

Pfingsten, W., and Shiotsuki, M., 1998: "Modelling a Cement Degradation Experiment by a Hydraulic Transport and Chemical Equilibrium Coupled Code," *Mat. Res. Soc. Symp. Proc.*, 506, 805-812.

Pitzer, K.S., 1987: "A Thermodynamic Model for Aqueous Solutions of Liquid-like Density," in *Thermodynamic Modeling of Geological Materials: Minerals, Fluids, and Melts*, I.S.E. Carmichael and H.P. Eugster (eds), Min. Soc. Am. Reviews in Mineralogy, 17, 97-142.

Poole, T.S., Wakeley, L.D., and Young, C.L., 1994: *Individual and Combined Effects of Chloride, Sulfate, and Magnesium Ions on Hydrated Portland Cement Pastes*, SAND93-7040 (Contractor Report; Army Waterways Experiment Station, Vicksburg, Miss.), 50 pp.

Richter, U., Brand, P., Bohmhammel, K., and Könnecke, T., 2000: "Thermodynamic Investigations of Aqueous Solutions of Aluminium Chloride," *Jour. Chem. Thermodynamics*, 32, 145-154.

Taylor, H.F.W., 1992: "Tobermorite, Jennite, and Cement Gel," *Zeitschrift für Kristallographie*, 202, 41-50.

Wakeley, L.D., Poole, T.S., and Burkes, J.P., 1992: *Deteriorated Concrete from Liner of WIPP Waste Shaft*, Technical Report SL-92-14, Army Waterways Experiment Station, Vicksburg, Miss., 90 pp.

Wakeley, L.D., Poole, T.S., and Burkes, J.P., 1994: *Durability of Concrete Materials in High-Magnesium Brine*, SAND93-7073, (Contractor Report; Army Waterways Experiment Station, Vicksburg, Miss.), 52 pp.

Wesolowski, D.J., 1992: "Aluminum Speciation and Equilibria in Aqueous Solution: I. The Solubility of Gibbsite in the System Na-K-Cl-OH-Al$(OH)_4$ from 0 to 100 °C," *Geochim. Cosmochim. Acta*, 56, 1065-1091.

Wesolowski, D.J., and Palmer, D.A., 1992: "Experimental Studies of Aluminum Solubility and Speciation in Brines," in *Water-Rock Interaction*, Kharaka and Maes (eds), Balkema, Rotterdam.

Wesolowski, D.J., and Palmer, D.A, 1994: "Aluminum Speciation and Equilibria in Aqueous Solution: V. Gibbsite Solubility at 50 °C and pH 3-9 in 0.1 Molal NaCl Solutions (a General Model for Aluminum Speciation; Analytical Methods," *Geochim. Cosmochim. Acta*, 58 (14), 2947-2969.

Xie, P., and Beaudoin, J.J., 1992: "Mechanism of Sulphate Expansion. I. Thermodynamic Principle of Crystallization Pressure," *Cement and Concrete Research*, 22 (4), 631-640.

Information Only

Information Only

3.4 Panel Closures[1]

Physical Barriers Studies involving the Panel Closure Systems (PCS) are reported in this section. This work addresses WBS element 1.3.5.4.3.2, which comprises both the re-evaluation of the PCS and studies of cementitious materials. The term "Engineered Barriers" in the context of repository investigations includes MgO hydration, carbonation and colloids, cementitious materials research, and panel closure systems. In order of maturity of investigations, the MgO work in Carlsbad is now well underway, cementitious materials laboratory studies in Carlsbad are initiating and panel closure evaluations have been re-directed as recently as January 7, 2002.

The CBFO has identified new panel closure considerations to be evaluated by Sandia. A summary of the expected path forward will be given. Over this recent reporting period, effort was lent to address an array of issues pertaining to PCS. A short review of the PCS issues and material delivered to the CBFO this reporting period is given here.

First, a condition of the EPA certification requires use of the Option D panel closure system. The compliance submittal panel closure system was designed by the M&O for operational RCRA considerations. The WIPP project's perception at the time of the CCA was that the panel closures were constructed only for operational and RCRA considerations, and not for long-term performance.

Second, the construction specifications contained several sections that could be improved. Construction enhancements pertaining to Option D were compiled and submitted to the EPA (April 17, 2001). Subsequently, this submittal was withdrawn by CBFO on September 4, 2001.

Third, a performance calculation is necessary to establish a technical baseline. This will incorporate parameters from the EPA PAVT calculations. In addition, the Technical Baseline Migration (TBM) will provide detail of the baseline calculations with an Option D panel closure configuration. These calculations will be conducted under guidelines of an Analysis Plan, which is being drafted at this time. The PCS team has contributed parameters and parameter justification to this Analysis plan.

Fourth, subsequent to the TBM evaluation, sensitivity calculations regarding the PCS will be executed. It is possible that an alternative to the Option D would provide a more optimal panel closure system for both long-term performance and RCRA operational considerations.

During this reporting period, numerous discussions were held between the CBFO, WTS and Sandia regarding panel closure issues. As of this report Sandia's contribution to the path forward (based on redirection by CBFO on 01/07/02) looks like this:

[1] This work is covered by BOE #1.3.5.4.3 and WBS #1.3.5.4.3.2

Information Only

Sandia will perform calculations to migrate the baseline to the Option D Panel Closure System using a refined mesh for BRAGFLO and parameter distributions for the DRZ and the panel closure concrete. Two main purposes emerge from this analysis:

1. It provides a technical baseline migration which includes PAVT parameters and
2. Results will be used for evaluation of proposed changes.

Subsequently, this information will be compared to a PA sensitivity analysis, where properties of the PCS and DRZ are varied to represent other possible configurations of the PCS. A technical report will summarize these results and will provide a basis for recommendations for specific design changes to the panel closure system. The schedule calls for these calculations to begin in February 2002 and completed by the next Milestone Report (July 31, 2002).

One of the panel closure options considered during this reporting period involved the use of temporary panel closures that allowed gas monitoring. The gases could include RCRA volatile organic compounds (VOC) and gases pertinent to PA. Sandia prepared a draft assessment of the use of microsensor technology for this purpose. The monitoring memorandum is included here.

Information Only

Sandia National Laboratories
Operated for the U.S. Department of Energy by
Sandia Corporation

4100 National Parks Highway
Carlsbad, NM 88220

Phone: (505) 234-0030
Fax; (505) 234-0061
Internet: ywang@sandia.gov

date: August 20, 2001

to: Frank D. Hansen (Dept. 6822)

from: Yifeng Wang (Dept. 6823)

subject: Air Monitoring in a Temporarily Closed WIPP Waste Panel with Microsensor Technology – A Preliminary Feasibility Study

Introduction

To response the suggestion of the National Academy of Sciences (NAS) on monitoring gas generation in a closed waste panel in the Waste Isolation Pilot Plant (WIPP), the Department of Energy (DOE) Carlsbad Field Office (CBFO) is currently evaluating the possibility of using microsensor technology for such monitoring. This memorandum summarizes the results of our preliminary study on the availability of microsensor technology and the feasibility of using such technology for NAS proposed waste panel monitoring. Robert C. Hughes (Dept. 1744), Clifford K. Ho (Dept. 6115), Donald E. Wall (Dept. 6821), David Guerin (6820), and James W. Garner (Dept. 6821) partly contributed the information summarized below. This study intends to provide information only for a programmatic decision. The further work, if it is decided to go forward, will follow Sandia National Laboratories WIPP Quality Assurance Procedures.

Compounds to Be Monitored and Related Chemical Processes

The chemical compounds to be monitored are listed in Table 1. The gases of H_2, CO_2, CH_4, N_2, and H_2S are generated from either of three chemical processes: metal corrosion, microbial degradation of organic materials, and radiolysis. It is assumed in the WIPP Compliance Certification Application (CCA) that the contribution of radiolysis to gas generation will be negligible relative to the other two processes. It is also assumed that any CO_2 generated in a disposal room will be instantaneously removed by MgO reactions. Additionally, it is expected that atmospheric O_2 initially present in the repository will be consumed quickly by both metal corrosion and microbial degradation, thus creating a reducing environment in a disposal room. The partial pressure of H_2O vapor in a closed waste panel could be an important parameter for microbial reactions and other chemical processes. The water vapor pressure is expected to be significantly lower than that buffered by a WIPP brine, due to the hydration of MgO backfill. In short, the in-situ monitoring of H_2, CO_2, CH_4, N_2, H_2S, O_2, and H_2O in a closed waste panel will provide valuable information on gas generation and other chemical processes in the actual repository environment and thus will be important for further demonstrating the robustness of WIPP long-term performance.

Currently, nine volatile organic compounds (VOCs) are required to be quantified in waste characterization. Room-based concentration limits of these compounds are listed in

Information Only

Table 2. The in-situ monitoring of these VOCs in a closed panel will provide useful information for establishment of a credible argument for relaxing the existing waste characterization requirements for headspace gas sampling and analysis. We suggest that as a first step the air monitoring in a closed panel be focused on one or two representative VOCs (e.g. carbon tetrachloride) due to the current limitation of microsensor for differentiation of multiple VOCs,. As the technology advances, more VOCs will be included.

Table 1. Availability of microsensor technology for air monitoring

Compound	Related Chemical Process	Availability of Microsensor Technology	Chance for success
H_2	Generated from metal corrosion and, to a less extent, from radiolysis	Commercially available; developed by Sandia National Laboratories and licensed to DCH	Very high; long-term stability yet to be tested.
CO_2	Generated from microbial degradation; presumably consumed by MgO	Commercially available	Very high; long-term stability yet to be tested.
CH_4	Generated from microbial degradation and, to a less extent, from radiolysis	Commercially available	Very high; long-term stability yet to be tested.
N_2	Generated from microbial degradation	Commercially available	Due to its high initial concentration in the air, N_2 generated from microbial degradation might be difficult to detect.
H_2S	Generated from microbial degradation	Commercially available	Very high; long-term stability yet to be tested.
H_2O	Controlled by brine inflow and MgO hydration	Commercially available	Very high; long-term stability yet to be tested.
O_2	Initially present in the air; consumed by both metal corrosion and microbial degradation	Commercially available	Very high; long-term stability yet to be tested.
Volatile organic compounds (VOCs)	Evolved from wastes	Available for representative VOCs; Sandia National Laboratories has developed chemiresistor sensors	Very high; long-term stability and sensitivity yet to be tested.

Availability of Microsensor Technology

As shown in Table 1, microsensor technologies are commercially available for the first seven chemical compounds listed in the table. The ranges of concentration changes of these compounds in a closed panel are listed in Table 2. These ranges are estimated from the CCA gas generation model using maximum gas generation rates (Helton et al., 1998, fig. 7.3.1). Since the detection limits of most commercially available microsensors can be as low as 10 ppmv, as shown in Table 2, the concentration changes of the relevant compounds in a closed panel can be easily detected by microsensors even in the first couple of years after apnel closure, if the gas generation predicted in the CCA is realized. Therefore, the in-situ air monitoring in a closed panel will provide very useful information for testing the gas generation model used in the CCA.

Information Only

Table 2. Concentration limit of gaseous compounds in a closed waste panel estimated from the CCA gas generation model. The maximum gas generation rates were used in the estimation. The detection limits of commercially available microsensors can be down to 10 ppmv.

Compound	Concentration (ppmv)		
	Initial	1 Year after[1]	5 Years after
H_2	0.51	12,000	120,000
CO_2	360	~0	~0
CH_4	0	200,000	2000,000
N_2	780,840	6,000	60,000
H_2S	0	4,000	40,000
O_2	209,460	~0	~0
H_2O	~70% RH	Significantly low	Significantly low

[1]Anoxic steel corrosion and anaerobic biodegradation will be inhibited in the first half of year by the initial presence of atmospheric O_2.

Certain chemiresistor sensors developed at Sandia National Laboratories are available for detecting VOCs such as carbon tetrachloride and tetrachloroethane. As shown in Table 3, the chemiresistor sensors combined with a pre-concentrator are capable of detecting all nine monitored VOCs. A major limitation of the existing microsensors is the difficulty with differentiating coexisting multiple (>3) compounds. It is expected, however, that this limitation will be significantly improved in the next few years. Sandia National Laboratories are funding a Laboratory Directed Research & Development (LDRD) project in FY02 through FY04. One of the objectives of this LDRD project is to optimize the ability of microsensors for the differentiation of individual VOCs in transuranic wastes. The optimized VOC sensors can be incorporated in WIPP underground air monitoring as needed.

Table 3. Room-based concentration limits for nine volatile organic compounds and detection limits of VOC microsensors.

Volatile Organic Compound	Room-Based Concentration Limit (ppmv)	Typical Headspace Concentration in waste stream[1] (ppmv)	Detection limit of microsensor[2] (ppmv)	Detection limit of microsensor with pre-concentrator[3] (ppmv)
Carbon tetrachloride	9,625	0.1 – 1,230 For solidified organics: >3,340	120	1
Chlorobenzene	13,000	0 - 260	10	< 1
Chloroform	9,930	0 - 280	210	2
1,1-Dichloroethane	5,490	0 - 240	240	2
1,2-Dichloroethane	2,400	0 - 230	110	1
Methylene chloride	100,000	0.3 - 2550	460	5
1,1,2,2-Tetrachloroethane	2,960	0.2 - 230	10	< 1
Toluene	11,000	0.4 - 360	30	< 1
1,1,1-Trichloroethane	33,700	8 - 6590	130	1

[1]Ranges of mean concentrations in individual waste streams tested at Idaho National Engineering and Environmental Laboratory (INEEL) and Rocky Flats Environmental Technology Site (RFETS) (Connolly et al., 1998).

[2]Detection limits of VOC microsensors are usually about 0.1% of VOC vapor pressures. The vapor pressures of VOCs are taken from *http://cis.sandia.gov/cgi-bin/mdlsearch/ohslang.pl*. The actual detection limits of VOC sensors need to be tested.

[3]Use of a pre-concentrator could reduce the detection limits by a factor of ~100.

Information Only

In-situ air monitoring in a closed waste panel requires microsensors to be durable and long-term stable in WIPP repository environments, in order to avoid frequent maintenance and calibration. All these sensors used for the monitoring will be tested for their long-term stabilities.

Possible Configuration and Duration

Conceptually, microsensors can be emplaced in two ways: (1) Once microsensors are emplaced, the panel will be sealed, and the sensors can be accessible only by signal transmission wires. (2) Small pipe tubes are placed in a panel seal, through which microsensors can be placed and retrieved. Depending on the long-term stability of microsensors, the second option may be more preferable. It will be necessary to emplace multiple sensors at various locations due to the possibility of gas stratification in the disposal room. All these sensors will be connected to one centralized data acquisition system.

As shown in Table 2, the optimal duration for the proposed monitoring is about 5 years. Over that time period, sufficient gas composition changes will be induced due to both steel corrosion and microbial degradation.

Cost Analysis and Plan

The cost of a microsensor system has been estimated. The commercial sensors would probably cost \$2 K - 15 K per package that includes a specific type of gas sensors and a compact data acquisition system. (Microsensors themselves are cheap, probably less than \$1 K each; but the manufactures usually prefer not to sell them separately.) Since the multiple types of sensors will be needed for multiple gaseous compounds, the largest expense would be sensor integration/packaging, software development, data fusion, and testing, which ranges probably from \$100 K to \$150 K. Therefore, a complete microsensor system for the intended air monitoring, which will include multiple gas sensors and a centralized data acquisition system, could cost \$200 K. Note that once a system is set up, the cost for adding additional sensors is minimal.

Use of microsensors for air monitoring is very preferable as compared with Gas Chromatography-Mass Spectrometer (GC-MS) gas sampling and analysis. A GC-MS analysis for VOCs could cost \$100 to \$300 per sample. Assuming that we need to take 10 samples each time and sampling 100 times per year, the cost for analysis alone would be \$100 - 300 K/year, besides the cost for sampling. However, once a microsensor system is setup, the cost for the subsequent years will be minimal. In addition to cost saving, the microsensors will provide real-time, continuous, and in-situ measurements. In contrast, with GC-MS analysis, taking a representative air volume over a long pipe tube in a closed panel could pose a significant sampling problem. Furthermore, a GC-MS is not set up for detecting WIPP Performance Assessment-related gases: H_2, CO_2, CH_4, N_2, H_2S, H_2O, and O_2. A GC-MS could be used to detect CO_2 and H_2S, but it requires a special setup, which could double the cost for sample analysis.

Information Only

Schedule and Plan:

Year 1:

- Long-term stability and sensitivity test of microsensors
- Integration of sensor system
- Conceptual design

Year 2:

- Field implementation
- Data acquisition

Budget:

Labor (2 FTEs): $500 K
Equipment: $200 K
Total for Year 1: $700 K Total for Year 2: $ 700 K

References

Connolly M. J., Djordjevic S. M., Liekhus K. J., Loehr C. A., and Spangler L. R.,1998. "Position for Determining Gas Phase Volatile Organic Compound Concentrations in Transuranic Waste Containers." Idaho National Engineering and Environmental Laboratory, INEEL-95/0109.

Helton J. C., Bean J. E., Berglund J. W., Davis J., Economy K., Garner J. W., Johnson J. D., Mackinnon R. J., Miller J., O'Brien D. G., Ramsey J. L., Schreiber, J. D., Shinta A., Smith L. N., Stoelzel D. M., Stockman C., and Vaughn P., 1998. "Uncertainty and Sensitivity Analysis Results Obtained in the 1996 Performance Assessment for the waste Isolation Pilot Plant." Sandia National Laboratories, SAND98-0365.

Distribution:

MS 1395 P. S. Shoemaker (6820)
MS 1395 D. Guerin (6820)
MS 1395 M. K. Knowles (6821)
MS 1395 D. E. Wall (6821)
MS 1395 F. D. Hansen (6822)
MS 1395 L. H. Brush (6822)
MS 1395 D. S. Kessel (6823)
MS 1395 Y. Wang (6823)

Information Only

Information Only

4.0 Rock Mechanics

4.1 An Overview of DRZ Studies in the WIPP Repository[1]

Terry L. MacDonald
Sandia National Laboratories, MS 1395
4100 National Parks Highway
Carlsbad, NM USA 88220

Abstract

This report briefly describes the Disturbed Rock Zone (DRZ) repository studies conducted in the Waste Isolation Pilot Plant (WIPP) repository during the current reporting period. Tests associated with these studies were performed in accordance with the Sandia National Laboratories (SNL) National Waste Management Program (NWMP) Test Plan TP 99-04, *Disturbed Rock Zone Characterization Test Plan* (DRZ Test Plan). DRZ repository studies have been limited to activities associated with ultrasonic velocity tests in the Air Intake Shaft (AIS) and near the Q Room.

Introduction

Considerable experimental data and operational evidence supports the existence of a DRZ in the WIPP repository. In the Department of Energy/Carlsbad Field Office's (DOE/CBFO) Compliance Certification Application (CCA), these data provided the basis for the modeling of the DRZ around both the waste storage panels and the vertical shafts. However, considerable uncertainty remains concerning the transient behavior of the DRZ, its role in brine inflow, and the likely heterogeneous distribution of its permeability. To reduce this uncertainty, the DRZ Test Plan was written to complement, not duplicate, the historical database used in the previous modeling of the DRZ. DRZ repository studies to include:

- Ultrasonic velocity tests near the Q Room
- Data analysis and maintenance of the ultrasonic velocity test arrays in the AIS
- Completion of ultrasonic velocity tests borehole mechanics documentation and technical papers.

The strategy to be implemented in FY2002 is still being negotiated with the CBFO. The scope of work for FY2002 will likely include evaluation of deep boreholes (up to 100 feet), development of a mine-by test plan, and preparation of a comprehensive document on the DRZ (with implications to WIPP PA). These topics will be updated both in the biannual progress reports and as separate milestone deliverables.

This report briefly describes DRZ repository studies performed during the current reporting period, and studies planned for the future. Current DRZ repository study reports, pertaining to the Q Alcove ultrasonic velocity tests, are provided in greater detail in Sections 4.2 and 4.3 of this technical baseline report

Current DRZ Repository Studies

Additional ultrasonic velocity tests conducted by David Holcomb (6117) and Bob Hardy (6117) near the Q Room were the main DRZ repository studies accomplished during the current

[1] This work is covered by BOE #1.3.5.4.4 and WBS #1.3.5.4.4.1

Information Only

reporting period. Specifically, these tests were conducted in 4-in diameter boreholes located at two DRZ test locations:

1) Location 1 (in the S-90 Drift/Q Room Access Drift)
2) Q Alcove southeast (SE) corner.

The boreholes at Location 1 are perpendicular to the drift wall, while the boreholes in the Q Alcove are parallel to a plane that bisects the SE corner ("into" the alcove corner). New P-wave ultrasonic velocity transceivers were used to obtain complementary cross-hole, and same-hole data to compare with data collected previously at these test locations. The analysis of the most current ultrasonic velocity data compares favorably with the previously collected data. These data show a decrease in the ultrasonic velocity near the drift/alcove surface, which correlates to the DRZ near the surface. These data also indicate that the effect of the DRZ may extend further into the host rock than previously assumed. Analysis of the Q Alcove data indicates the geometry of the SE corner has an effect on the depth and direction of the DRZ in this region of the host rock. In particular, the DRZ near the alcove corner is less extensive than the DRZ that develops at Location 1. The results of the Q Alcove ultrasonic velocity tests were compiled into an abstract for the NARMS-TAC 2002 EDZ Workshop to be held in Toronto in July 2002 (Section 4.2) and into an October 2001 DOE/CBFO level-4 milestone report (Section 4.3).

Access for the ultrasonic velocity test equipment to study the DRZ in the WIPP repository required the drilling of 4-in diameter boreholes at Location 1 and in the Q Alcove SE corner. Upon the completion of the boreholes, detailed borehole survey data and diametric data were recorded and provided to Dave Holcomb and Bob Hardy to complete the analysis of the ultrasonic velocity test measurements. This information was recorded on forms and submitted to the SNL/CB Records Center for archiving. Cores were extracted and preserved during the drilling of the boreholes. Some of theses cores were used during DRZ observational core studies (Section 4.4). A detailed core log was generated for each core section recovered. Copies of these core logs were submitted to the SNL/CB Records Center for archiving.

The three AIS ultrasonic velocity tests arrays, first installed in 1989, continue to monitor the DRZ in the AIS. These arrays require periodic downloading of the data by Westinghouse TRU Solutions (WTS). An electronic copy of the data is sent to Bob Hardy for analysis. These ultrasonic velocity arrays also require periodic maintenance. During this current reporting period, a corroded connection in a junction box for the array at AIS Level 1575 (ft) was repaired, and the array was brought back on line. The Level 1575 array had been out of service for two years before the repair was completed.

Future DRZ Repository Studies

Additional DRZ repository studies outlined in the DRZ Test Plan, along with several new studies, were scheduled to commence in FY 2002. The new studies, designed to complement data collected during the ultrasonic velocity tests in the WIPP repository, received concurrence from cognizant DOE/CBFO, SNL/CB, and WTS personnel. These activities will be discussed with CBFO counterparts and initiated if SNL/CB budget is available.

The DRZ Test Plan outlined the implementation of two feasibility studies to evaluate the effect of the DRZ on moisture content (pore water saturation) and porosity of the host rock in the WIPP repository. Neutron probe testing and gamma ray densitometry/tomography were the testing methods recommended by the test plan to measure moisture content and porosity, respectively. A neutron moisture probe and gamma ray densiometer have been purchased and are awaiting setup and evaluation.

Information Only

Hydrological tests are planned for implementation in boreholes drilled at Location 1 and the Q Alcove SE corner. The hydrological tests, as planned, would study the effect of the DRZ on the permeability of the host rock. Data from the hydrological tests would be correlated to results of the ultrasonic velocity tests and to DRZ observational studies (Section 3.3) associated with these locations. A test plan/test plan addendum to the DRZ Test Plan will be written for the hydrological tests.

A mine-by experiment near the WIPP repository Panel 3, utilizing several ultrasonic velocity test arrays embedded in the host rock, received concurrence from cognizant DOE/CBFO, SNL/CB, and WTS personnel. The purpose of the mine-by experiment is to study the formation and growth of the DRZ during and after the mining of an opening in the WIPP repository. The information gathered from this study will complement data from a previous mine-by experiment. Additional tests (i.e., hydrological tests) can be incorporated into the mine-by experiment, as funding allows. A test plan will be written for the mine-by experiment.

Results from the recently completed ultrasonic velocity tests at Location 1 and in the Q Alcove SE corner indicate that the depth of the DRZ may extend farther into the host rock than previously assumed. Cognizant DOE/CBFO, SNL/CB, and WTS personnel recommend deepening the 4-in boreholes planned for DRZ Location 2 (next to Location 1) to 100 ft to study the depth of the DRZ into the host rock. These boreholes will undergo ultrasonic velocity testing, and their cores will undergo DRZ observational studies (Section 4.4). These boreholes will also determine the depth and alignment that 4-in boreholes can be drilled in the WIPP repository using current drilling equipment and will serve as a validation of drilling techniques for the mine-by experiment planned near Panel 3.

References

Knowles, M.K., 2001, *Disturbed Rock Zone (DRZ) Characterization Test Plan*, SNL National Waste Management Program (NWMP) Test Plan TP 99-04, Revision 1, effective date 3/28/01, 35 p.

MacDonald, T. L., 2001, *DRZ Characterization Test Plan (DCTP) Activities Monthly Status Memorandum*, for DRZ Characterization Test Plan (TP 99-04) Activities, 6 status reports from July 2001 through December 2001.

Information Only

Information Only

4.2 DRZ Ultrasonic Velocities (NARMS Abstract)[1]

Submitted for consideration for the July 2002 NARMS EDZ Workshop

David J. Holcomb, Robert Hardy and Terry MacDonald

Sandia National Laboratories
PO Box 5800, MS0751
Albuquerque, NM 87185-0751
djholco@sandia.gov, (phone 505.844.2157), (fax 505.844.7354)

(DOE/CBFO review and approval, and SNL/CB managerial, QA, and technical reviews, completed Oct.16, 2001.)

Using Ultrasonic Waves to Assess the Disturbed Rock Zone (DRZ) in an Alcove Corner Excavated in Salt at the WIPP (Waste Isolation Pilot Plant)

There is a continuing need to understand the spatial and temporal development of the disturbed rock zone (DRZ) around openings at the Waste Isolation Pilot Plant (WIPP). Possible leakage paths around seals, performance assessment models, and safety issues are affected by the DRZ. An alcove constructed about 12 years ago provides an opportunity to conduct geophysical investigations of the damage that has developed in the salt for a complex three-dimensional configuration. Specifically, an interior room corner is used to study the damage caused by stress fields unique to the corners of rectangular openings in salt formations. The mature DRZ is the macroscopic manifestation of grain-scale and larger cracks that form as a result of the shear stress around the newly created opening, and as a result of creep-related deformation over a period of years. As part of a suite of measurements designed to study the hydrological and mechanical properties of the salt in the alcove corner, twelve, 10-cm diameter ultrasonic transducer emplacement holes were drilled in the alcove corner rib to a depth of about 7.5 m. Elastic wave velocity and attenuation in the salt are a function of the density of cracks, as is the permeability. The design of the borehole array and the transducer assemblies allows the measurement of elastic wave velocities and amplitudes (for attenuation studies) along vertical and horizontal paths tangential to the alcove corner and, within the same hole, at a 45° angle to the rib. Orthogonal paths are necessary to detect the anisotropy of the cracking in the DRZ.

Transducer positions were carefully surveyed, allowing absolute velocity measurements. One set of measurements was completed at roughly 30-cm intervals in 12 boreholes to a depth of 6 m, vertical, horizontal and perpendicular to the alcove corner axis, giving a complete and redundant data set. This set of measurements included 17 cross-hole paths and 12 axial paths. A second set of measurements was repeated in 5 of the boreholes at roughly 15 cm intervals for the first shallowest 2 m, and at 30 cm intervals for an additional 4 m. These measurements were made along paths through the salt near the back, floor and center of the alcove corner, to detect the effect of the varying stress state on the development of the DRZ in these locations.

The data can be used to delineate the DRZ as a function of depth from the alcove corner and as a function of the varying stress state around a rectangular alcove corner cross-section. The

[1] This work is covered by BOE #1.3.5.4.4 and WBS #1.3.5.4.4.1

Information Only

paper will report results from the acquired data sets. Results will be related to the damage, due to microcracking, required to produce the observed changes. The results are expected to be useful to other studies of the long-term deformation characteristics of salt. The significance of the results lies in the length of time the DRZ has had to develop (approximately 12 years), the geometrical complexity of the alcove corner, which will allow a more rigorous test of models than is possible in simpler geometries, and the hydrological measurements to be made in conjunction with the velocity and attenuation measurements. Understanding the time-dependent changes in damage, and thus permeability, as the DRZ develops is important because these changes strongly affect the sealing of underground openings at the WIPP.

Information Only

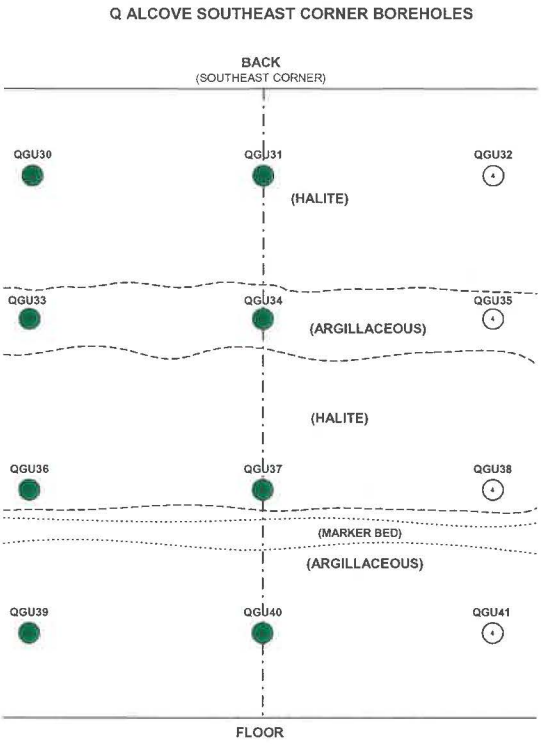

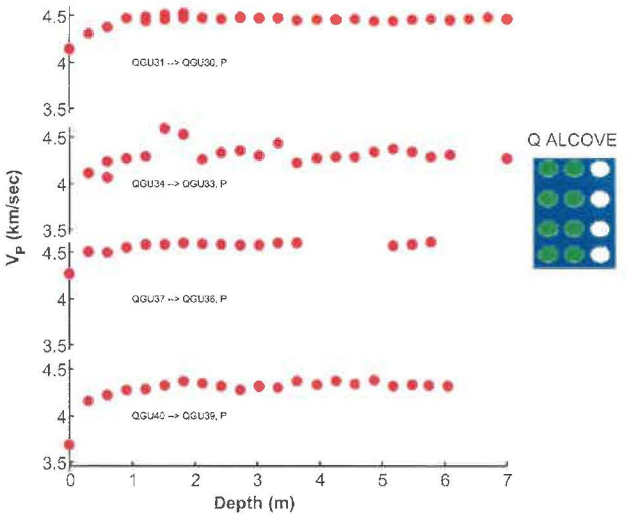

Top Left: A typical ultrasonic wave test setup in the Q Alcove SE corner for studying the DRZ. *Top Right:* The array of boreholes in the Q Alcove SE corner used for studying the DRZ using ultrasonic waves. *Bottom Center:* Velocities from several sets of cross-hole measurements, in the holes indicated by the filled green circles, are plotted as a function of distance from the rib face. The complexity of the DRZ at this location reflects the 3-D geometry. Near the back and floor (top and bottom traces), a DRZ extends in approximately 1.5 m. At the intermediate levels there is little or no DRZ evident in the data, except possibly at the shallowest depths.

Information Only

Information Only

4.3 DRZ Ultrasonic Velocities[1]

(SNL/CB managerial, QA, and technical reviews completed Nov. 16, 2001.)

Sandia National Laboratories
Operated for the U.S. Department of Energy by
Sandia Corporation

Albuquerque, New Mexico 87185-

date: October 24, 2001

to: Frank Hansen

from: David Holcomb and Robert Hardy, Org. 06117, MS 0715, Terry MacDonald, Org. 6822, MS 1395

subject: Using Ultrasonic Waves to Assess the Disturbed Rock Zone (DRZ) in the Q Room Alcove, WBS 1.3.5.4.4.1

Introduction:

There is a need to understand the spatial and temporal development of the disturbed rock zone (DRZ) around openings at the Waste Isolation Pilot Plant (WIPP). Possible leakage paths around seals, effects on closure rates and safety issues related to deterioration of the salt mechanical properties are issues affected by the DRZ. An alcove constructed about 12 years ago provided an opportunity to conduct geophysical investigations of the damage that has developed in the salt for a complex three-dimensional (3-D) configuration. Specifically, an interior room corner was used to study the damage caused by the complex stress fields existing near the corners of rectangular openings in salt formations. The mature DRZ found in such a location is the macroscopic manifestation of grain-scale and larger cracks that form as a result of the instantaneous shear stress induced around a newly created opening, and as a result of creep-related damage over a period of years. Velocity and attenuation of elastic waves in the salt are a function of the density of cracks, as is the permeability.

As part of a suite of measurements designed to study the hydrological and mechanical properties of the salt in the alcove corner, twelve, 10-cm diameter ultrasonic transducer emplacement holes were drilled in the alcove corner rib to a depth of about 6 meters. The design of the borehole array and the transducer assemblies allows the measurement of elastic wave velocities along vertical and horizontal paths parallel to the walls intersecting at the alcove corner and, within the same hole, at a 45^{O} angle to the rib. Orthogonal paths are necessary to detect the anisotropy of the cracking in the DRZ.

[1] This work is covered by BOE #1.3.5.4.4 and WBS #1.3.5.4.4.1

Information Only

Previous work at the WIPP, (Munson et al., 1995, Holcomb, 1999, Hardy and Holcomb, 2000, and Holcomb and Hardy, 2001) delineated the DRZ as a function of depth from the drift wall and as a function of the varying stress-state around the approximately rectangular drift cross section. Using results published by Brodsky (1995), changes in velocity can be related to the damage, due to microcracking, required to produce the observed changes. Holcomb and Hardy (2001) discussed the results of measurements conducted in the near-by Q Room Access Drift, which is geometrically simpler than the current study area because the drift's length results in a plane stress-state around the drift. Cross-hole and same-hole velocity measurements gave a consistent picture of the DRZ around the Q Room Access Drift. The DRZ was well developed at mid-height on the rib, extending in 2 m and possibly as much as 4 meters. Near the back and floor, the DRZ was shallower (1 meter or less) or not detectable. Compressional mode (P) waves in same-hole measurements are most sensitive to the DRZ because of favorable orientation of particle motion perpendicular to the cracking. Changes in compressional velocity, V_P, as large as 22% were observed for P waves propagating perpendicular to the drift axis at room mid-height. Using results from Brodsky (1995 Figure 4-2), these changes would correspond to the velocity changes observed in salt loaded close to failure in triaxial compression.

It is expected that the current results will be useful to other studies of the long-term deformation characteristics of salt. The data delineate the DRZ as a function of depth from the alcove corner and as a function of the varying stress-state around a rectangular alcove corner cross-section. The significance of the results lies in the length of time the DRZ has had to develop (approximately 12 years), the geometrical complexity of the alcove corner, which will allow a more rigorous test of models than is possible in simpler geometries, and the hydrological measurements to be made in conjunction with the velocity and attenuation measurements. Understanding the time-dependent changes in damage, and thus permeability, as the DRZ develops is important because these changes strongly affect the sealing of underground openings at the WIPP.

Approach:

Open cracks and loosened grain boundaries decrease elastic moduli and therefore, elastic wave velocities. The effect on elastic wave velocities is strongest for cracks oriented perpendicular to the particle motion induced by the wave. Thus, the physical extent of the disturbed zone can be determined by propagating elastic waves through successive portions of the formation until an undisturbed zone is reached, as indicated by a constant velocity with increasing depth from the rib. In this case, the cracking responsible for the disturbed zone is expected to vary as a function of distance from the walls of the Q Room Alcove and to depend on the position of the measurement path relative to the back, floor and corner.

Measurements were made in holes cored parallel to a line bisecting the corner angle, along horizontal and vertical paths lying in vertical planes parallel to the corner walls. Transducer positions were surveyed to an accuracy of $\pm$ 1 mm, allowing absolute velocity measurements. One set of measurements was completed at approximately 30-cm intervals in 12 boreholes to a depth of about 6 m, along cross-hole vertical and horizontal paths parallel to the corners of the alcove and same-hole paths, necessarily at 45^{O} angles to the room walls. This set of measurements included 17 cross-hole paths and 12 same-hole paths. A second set of measurements was repeated in five of the boreholes at approximately 15-cm intervals for the first shallowest 2 m, and at 30-cm intervals for an additional 4 meters.

Information Only

The cross-hole measurement paths were nominally one-meter long, while the same-hole measurements all had the same fixed path length of 33 centimeters. Figure 1 shows the arrangement and naming scheme for the measurement holes, QGU30, QGU31, … QGU41. Travel time measurements were made using the technique commonly used for laboratory determinations of sound speed in rock; a sound pulse was applied to the rock at a known time and place and, after traveling through the rock, was received by a transducer at a known distance. The travel time and distance combine to give the average velocity over that path.

Lithology and Hole Layout

Twelve holes were cored (see Figure 1) to sample the lithologies exposed in the alcove corner and the stress-state as it varied near the corner. Two rows of holes, 1 and 3 counting from the top, were in halite, while rows 2 and 4 were in argillaceous salt. Each hole was 10.16 cm (4 inches) in diameter, 6+ m deep and as close to horizontal as possible. Great effort and care was taken by the surveying and drilling crews to align the holes parallel and horizontal, resulting in hole-to-hole separations that varied by less than 10 cm over the 6 m depth, indicating very good control on the starting angle and carefully controlled drilling. Hole locations were chosen that sampled the map units present (labeled halite and argillaceous in Fig. 1), and also the expected variation in damage around the corner.

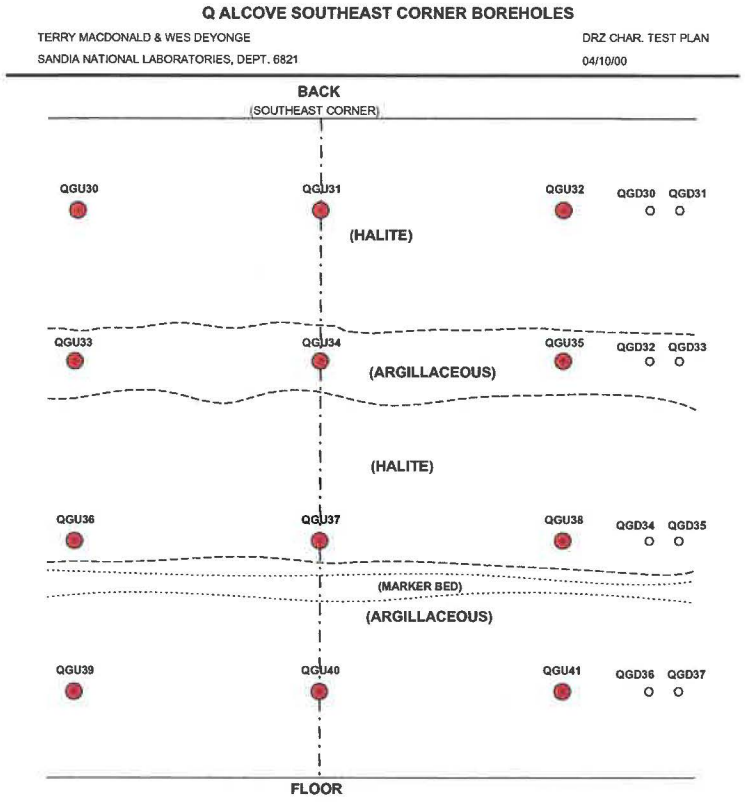

Figure 1: Layout of holes for the Q alcove, with holes used for ultrasound measurements indicated in red. Other holes indicated are for the associated hydrological studies.

Information Only

Measurement System:

Piezoelectric transducers were used as both the transmitter and receivers of the ultrasonic elastic waves. In the current work, only compressional mode transducers were used, although in certain configurations, a shear mode can be generated. A 300 kHz, PZT-5A piezoelectric disk was the basic element; four of these were used, two as transmitters and two as receivers. Each disk was mounted inside of a housing that could be pressed against the side of the 4-inch boreholes using air pressure. Suitably curved faces on the aluminum housing increased the area of contact when the housing was extended by pressurization to, typically, 60 psi. To further, and very substantially, increase the energy transmission across the housing-rock interface, a couplant was extruded between the housing face and the rock. Corn syrup was used for this work; it is inexpensive, cleans up easily and provides good coupling for both compressional and shear elastic waves.

Two transducer housings were coupled together (Figure 2) to form the tool inserted into the borehole. Each transducer was electrically independent, meaning that either could be driven and/or act as a receiver. One advantage of this approach is the ability to make two measurements at one tool position; repositioning the tool occupied about half the measurement time, so cutting the number of repositionings in half accelerated the measurement pace. An additional capability is gained by placing two transducers in one hole; one transducer can be driven as a transmitter while the other acts as a receiver. In this way, measurements can be made along paths normal to the rib face and orthogonal to the cross-hole measurements. As the orientation of the damage is expected to be anisotropic, it adds information to be able to measure the effects of damage along orthogonal paths. In particular, it is expected that the cracking planes will be preferentially parallel or sub-parallel to the rib, resulting in the largest changes in velocity along paths normal to the rib.

In addition to measurements of compressional mode (P) velocity, this technique allows the generation and propagation of shear (S) waves through the material parallel to the hole axis. A similar technique is discussed by Maxwell et al., (1998). Although it is common to talk about P and S mode transducers, it is a misnomer. All PZT-5 ceramic transducers expand and contract along the axis parallel to the direction of polarization when an electrical field is applied, and generate an electrical field when an impinging mechanical disturbance causes strain along the axis of polarization. A disk of PZT-5, none as a P mode transducer, is polarized parallel to the axis of the disk; application of an electrical field results in the disk getting thicker or thinner, according to the sense of the electrical field. When coupled mechanically to the surrounding medium, as discussed above, the rapid change in shape causes a wave to propagate into the rock, much as if a tiny hammer had struck the side of the hole. In the direction parallel to the disk axis, the result is a wave where the particle motion is parallel to the propagation direction - a P wave, analogous to a sound wave in air. However, at right angles to the disk axis, a disturbance propagates also, with the particle motion still parallel to the disk axis, but the propagation direction is now orthogonal. This is a shear wave, characterized by particle motion perpendicular to the direction of propagation, and has no analogue in fluids such as air. Thus, a ``P`` transducer can in fact generate and detect S waves and this was done using the pair of transducers in a single hole.

Once positioned and pressurized, a 100-volt square pulse, with a rise time of about 200 ns, excited the chosen transducer. The resulting wave was detected by the chosen receiver,

Information Only

path length was possible, so the path had to be determined indirectly by determining the 3-D position of each transducer as a function of depth in the hole.

A survey was carried out by Westinghouse True Solutions (WTS) to locate the centerline of each of the measurement holes to an accuracy of 1 millimeter. A repeated survey showed that this accuracy was attained, and surpassed.

Data Analysis

Calculating the velocity was a several step process involving coordinate determination, corrections for various offsets and choosing the arrival time for the P or S wave at the receiver. Coordinates were determined by parameterizing the North, East and vertical coordinates (N, E, Z) of the surveyed centerline of each hole as a function of depth into the hole. Three, second order-fits for N, E, and Z, as functions of depth, were determined and found to reproduce the surveyed coordinates within the required precision. For each measurement set, the measured depth of emplacement for the transducer was used in the second-order fits to calculate the coordinates of the transducer in space. Offsets were applied to account for the actual position of the transducer against the wall, instead of the centerline of the hole. Knowing the coordinates of the transmitter and receiver, the path length could be calculated. Non-systematic errors are estimated to make the uncertainty in cross-hole path length less than 3 millimeters. Same- hole measurements used the fixed 0.33-m separation of the transducer heads (see Figure 2), eliminating path length as a systematic error.

Determining the travel time requires knowing the difference between the time of the initiating electrical pulse applied to the transmitter and the time of arrival of the P or S wave at the receiver. Pulse time, which is easily determined from the recorded rapidly rising square wave to an accuracy limited only by the typical sample interval of 50 or 100 ns, contributed a negligible amount to uncertainty in velocity. It is much more difficult to fix the arrival time of the wave at the receiver. The waveform is an emergent sinusoid, not a square wave pulse, whose unsharp beginning is additionally obscured by electrical noise in the highly amplified signal. S waves, which travel slower and arrive later than P waves, are additionally confounded by the coda of the P wave that extends into the S-wave signal.

Although signal quality was improved by signal averaging, the determination of arrival times could still be difficult especially for measurement paths that passed close to the surface where damage was greatest, resulting in high attenuation of the signal. Typically, the first arrival is small in amplitude, making it easy to miss the first cycle or more in a highly attenuated signal. This would result in unacceptable errors in the travel time and velocity. Visual comparison of the signals in a given data set can be used to minimize the risk of missing first arrivals. Low pass filtering was also used on some data sets to equalize the frequency content of the signals, easing comparison of the filtered traces.

An interactive Matlab program has been developed that allows the signals from a given data set to be plotted, and offset so that the arrival times are aligned. When arrival times are correctly chosen, the similarity of the signals is usually obvious. The program allows the arrival times to be adjusted interactively until the signal-to-signal correlation is good. For the measurement paths at some distance from the free surface, the actual arrival time is easily determined, allowing these signals to be used as a guide for choosing the arrival time for the less distinct signals from paths near the free surface. Typically, one clear arrival is used as a

Information Only

amplified by 60 dB and recorded on a digital oscilloscope to 16-bit precision, at a sampling rate of 10 or 20 MHz. Each data set, consisting of the recorded driving pulse and received pulse, was transferred to computer storage for later analysis. To enhance signal quality, 100 signals were averaged at each position. For cross-hole measurements, only P waves were recorded, with measurements made at approximately one foot intervals from the full depth of the holes to the surface, or as close as possible. Positioning was done by measuring the tool depth relative to surveyed marks on reference plates affixed as a collar at the hole's entrance. Calculating velocities requires an accurate knowledge of the transmitter and receiver positions.

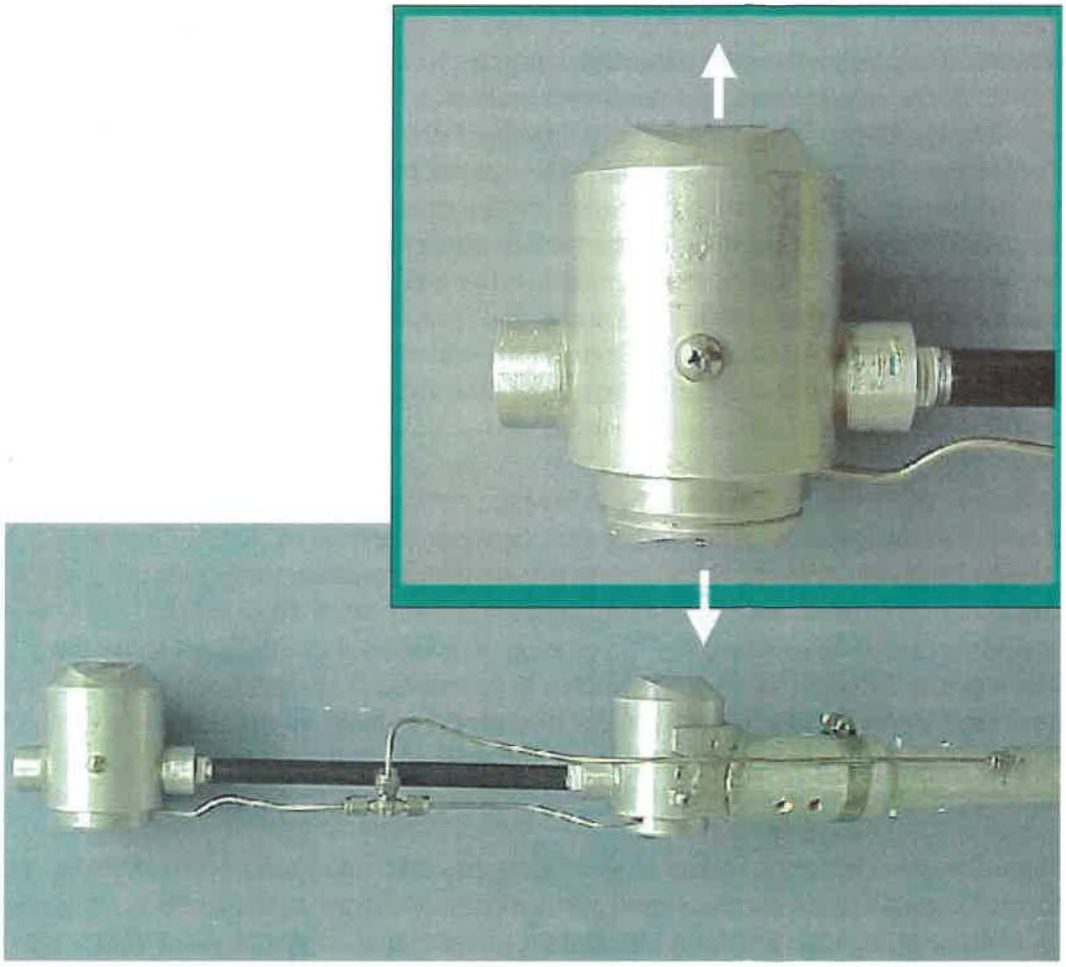

Figure 2: Transducer assembly showing two air-actuated clamping heads. Enlarged photograph is a close-up of one of the heads with the direction of motion during clamping indicated by arrows.

Surveying

The goal was to determine wave speeds with an accuracy of 0.5% or better. Path lengths ranged from about 1 m for the cross-hole measurements to a fixed 0.33 m for the same-hole measurements. The wave speed for P waves in salt is approximately 4500 m/s for undisturbed salt. Thus travel times were expected to be in the range of 200 to 70 microseconds. To maintain the desired accuracy, the path length had to be known to substantially better than 0.5%, or 5 mm for the cross-hole paths. No direct measurement of

Information Only

reference and all the other signals are adjusted to correlate well with that reference. This builds in a systematic error corresponding to the error in picking the reference signal, but reduces the scatter between measurements, making it much easier to see trends in the velocity with depth. The systematic error is determined by the error in picking the arrival time of the reference, which for the cross-hole P waves is less than 200 ns, a negligible amount. Same-hole P waves are much lower amplitude because of the unfavorable geometry of the transmitter and receiver. As a result, the errors are larger, and the effect more significant due to the shorter path lengths. The systematic error is close to 1% for these paths, but of course, that is a constant error for all measurements. Trends are not obscured as a result.

Shear waves travel slower than P waves and there is always energy emitted as P waves. Thus, the S wave arrival must be detected while the P wave is still influencing the transducer. Typically a large, fairly sharp sinusoid emerging from the P wave coda is taken as the S wave arrival. The technique of comparing waveforms is essential to get consistent results for S waves as determining the actual arrival time is usually difficult. A reference signal with the sharpest S arrival is chosen and a particular peak within the signal is used to align the other signals. Inevitably, this introduces a systematic error of 1 or 2% in the S velocity, but the trends are unaffected as the error applies to all the referenced signals.

Results and Discussion

Measurements were made for all cross-hole possibilities, resulting in nine sets of measurements for vertical paths and eight horizontal paths in planes parallel to the corner walls. Twelve same-hole measurement sets were completed. All of the data plots follow the same format, consisting of a title giving the location data and the wave type, P or S, and the data plotted as the measured velocity plotted at the depth of the transmitter. A typical title would be

QGU31 → QGU30, P

for a compressional wave measurement set, with the wave propagating between holes QGU30 and QGU31 (see Figure 3). To ease comparison of various paths, data are plotted in sets corresponding to logical subsets, such as all horizontal paths on the left-hand wall. An icon in each data plot shows the subset being plotted; using filled green circles to indicate the source of the data. For the current, work all data are from the Q Room Alcove.

Horizontal Paths

The P wave velocity, V_P, was measured at 30-cm intervals for the eight possible horizontal paths. Figure 3 summarizes measurements made in the left-hand wall with four plots arranged in the same way as the physical arrangement of the holes in the rib. The icon at the right of the plots shows, using filled green circles, the eight holes where the four plotted data sets were measured. Beginning at the top of Figure 3, V_P is plotted as a function of depth for the horizontal path between the top left and top center holes nearest the back (Figure 1), and similarly for the next three hole pairs in descending order down the page and rib wall. Results for the horizontal paths in the right hand wall are shown in an identical arrangement

Information Only

in Figure 4. Overall, the compressional velocity was observed to be 4.4 km/sec ± 0.1 km/sec for all four levels at depths greater than about 1 m from the rib. A variation of less than ± 2% indicates several things. First, the surveying and corrections for non-parallelism of the holes has been correctly handled. Even with the excellent control on drilling the holes, the runout between any given pair of holes frequently exceeded 10% of the hole spacing. If not corrected for, the cross-hole velocities would show a significant trend with depth, and indeed, several errors in the analysis were revealed by such trends. Second, small velocity differences were observed between the two halite layers and the two argillaceous layers, indicating little difference in the elastic moduli, despite the visual differences. There is a difference between halite, where V_P = 4.5 km/sec and the argillaceous units where V_P at depth is closer to 4.4 km/second.

Results for QGU31 --> QGU30 (Figure 3, first plot) show how constant the velocity can be at depth. At depths greater than about 1 m, variations from the mean are less than 0.5%, which is getting close to the attainable accuracy. Similarly, constant velocities were observed in the other paths through halite (QGU37 --> QGU36, Figure 3, QGU31 --> QGU32 and QGU37 --> QGU38, Figure 4). In contrast, V_P along paths in the argillaceous layers varied by several percent even at depths beyond the DRZ. (QGU34--> QGU33 and QGU40 --> QGU39, Figure 3, QGU34 --> QGU35 and QGU40 --> QGU41, Figure 4). This variation was particularly noticeable for the measurements made in the thin argillaceous layer (Holes QGU33, QGU34 and QGU35). Given the constancy observed in the halite layers, it is reasonable to argue that the variations of V_P with depth observed in the argillaceous layers are real. In the access drift, Powers (2000, p 6) describes significant variations in lithofacies for the core in the argillaceous layers and speculates that the differences may be of such magnitude as to influence the elastic wave velocity. This observation is believed to be the case in this study. Further work will be required to correlate the velocity results with the core logging.

All four data sets for the horizontal cross-hole V_P measurements made in halite layers indicate a constant velocity as the measurement depth approaches 6 meters. Two data sets show clear evidence of a disturbed zone extending in about one meter – QGU31--> QGU30 (Figure 3) and QGU37-->QGU38 (Figure 4). At the surface, V_P is 4.1 km/s, 10% below the value observed at depth. A smooth increase in velocity was observed over the first meter. Little or no evidence for a DRZ was found in the other two measurements in halite -- QGU37--> QGU36 (Figure 3) and QGU31-->QGU32 (Figure 4). Only at the shallowest depth, where signal quality is lowest, was there any evidence for velocity reduction.

Because of the symmetrical arrangement of the hole pairs around the corner, it would be expected that a similar pattern of DRZ development would be observed in the left and right walls if the assumption is made that the stress distribution near the corner is unaffected by the layout of the room and the Q-entry drift. Conversely, if stresses on either side of the corner are significantly different, then a distinct asymmetry should be observed that 3-D modeling could relate to the geometry of the room and its surrounding. Symmetry was not observed for the paths in halite. There was a well-developed DRZ in the upper left corner (QGU31-->QGU30) but not in the upper right corner (QGU31-->QGU32). Lower down, the second set of hole pairs in halite did exhibit a more symmetric DRZ, with a slightly clearer development seen in QGU37-->QGU38 than in the matching pair on the left side of the corner, QGU37-->QGU38.

Information Only

Large variations in velocity occurred for paths in the upper argillaceous layer (QGU34 -->QGU33 and QGU-->QGU35), making it difficult to discern a DRZ. Certainly, there is no obvious pattern of low velocity near the surface that could be interpreted as evidence for a DRZ. Measurements on both paths in the lower argillaceous layer QGU40--> QGU39 (Figure 3) and QGU40-->QGU41 (Figure 4) do show a DRZ, with a very low value of V_P near the surface, extending in about one meter. The DRZ appears to be symmetrically developed about the corner axis in the lower argillaceous layer.

Previous work (Holcomb and Hardy, 2001), in the access drift leading into the Q Room Alcove, showed a much simpler pattern of DRZ development and a more extensive damaged zone. In the access drift, where the geometry is essentially two-dimensional (2-D), the DRZ was observed to be best developed at mid-height of the drift and to extend in as much as two meters. The complexity observed in the current work reflects the influence of the 3-D geometry on the stress-state and subsequent development of the DRZ.

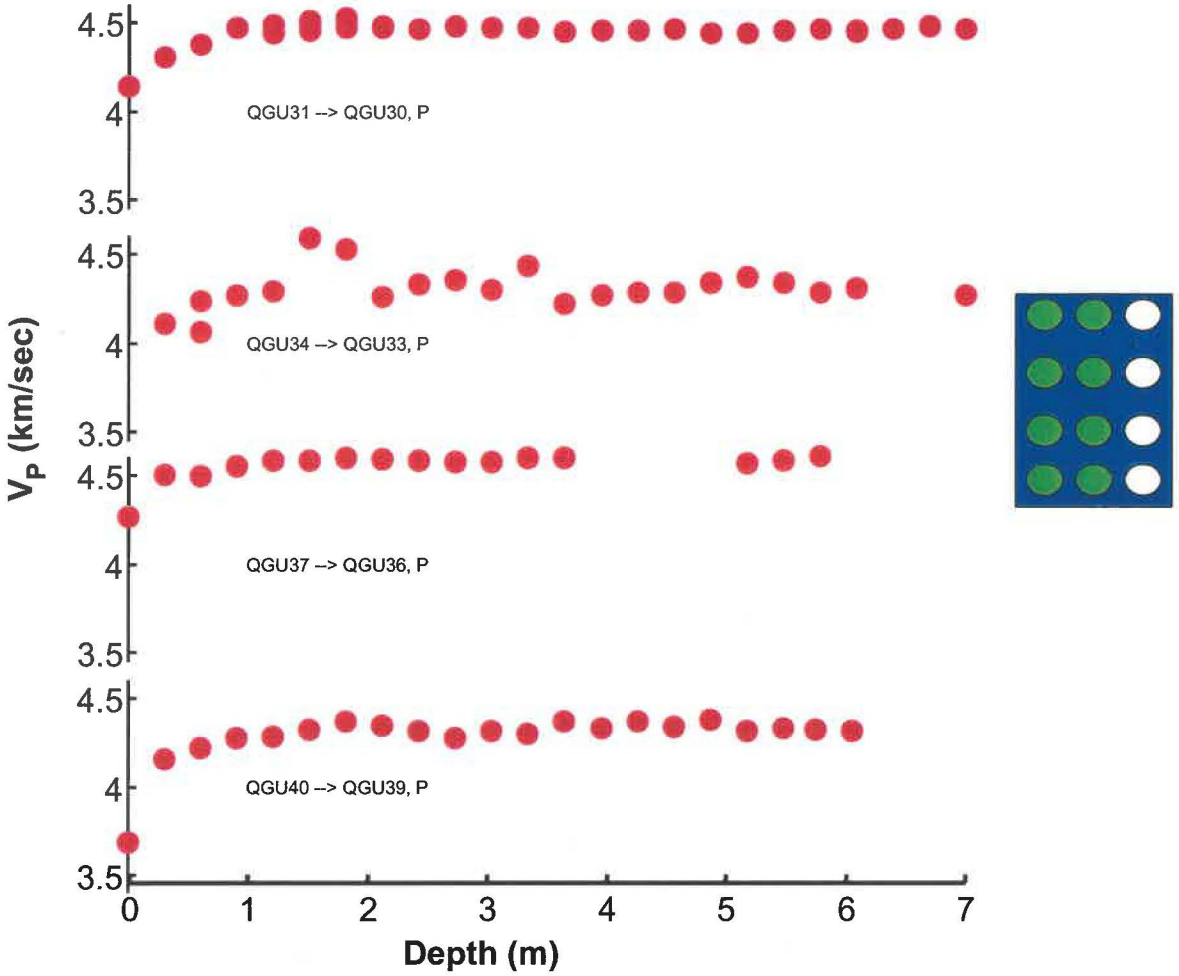

Figure 3: V_P for the four sets of horizontal cross-hole paths parallel to the left-hand wall of the alcove corner. The center column holes were drilled into the intersection of the corner walls.

Information Only

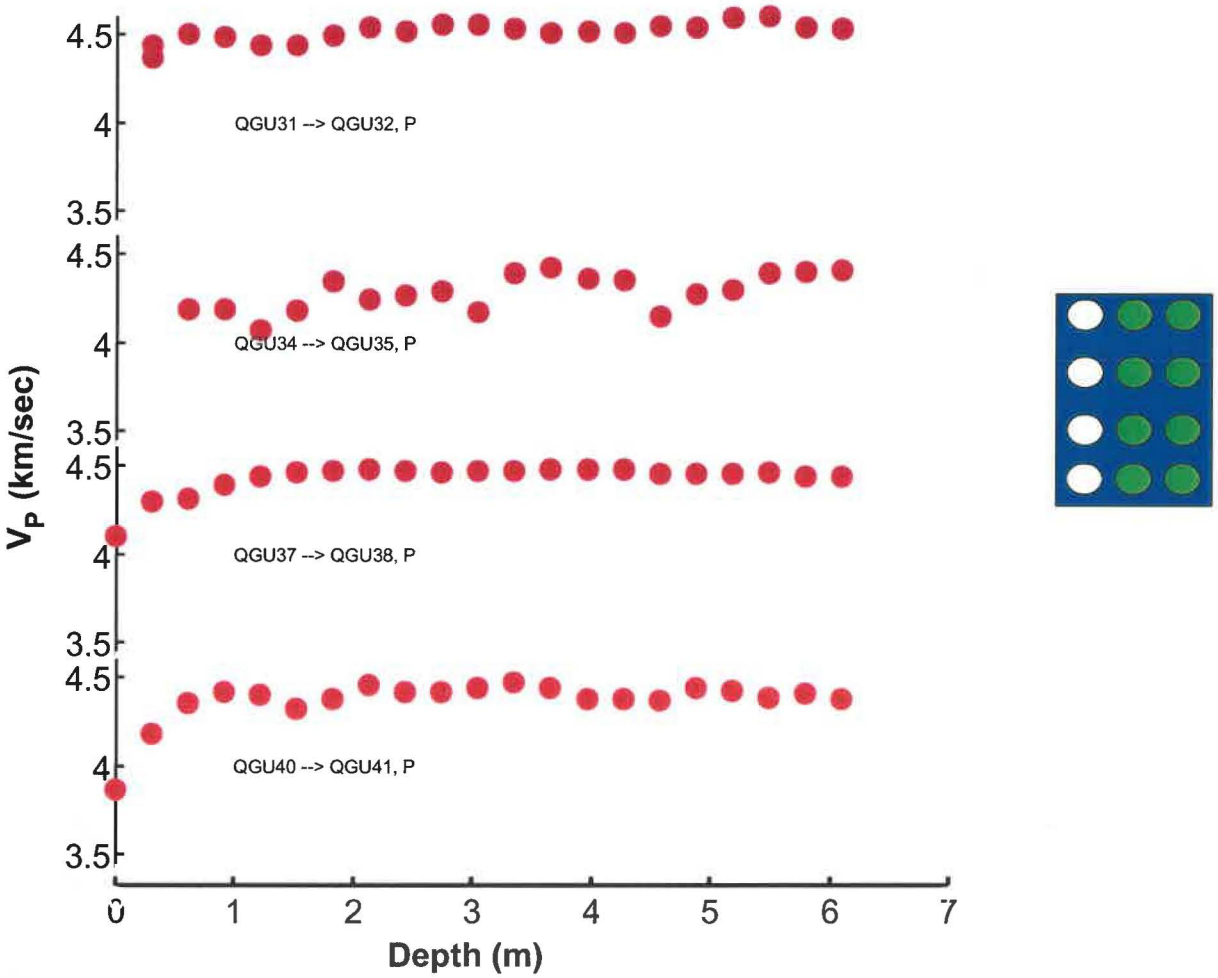

Figure 4: V_P for the four sets of horizontal cross-hole paths parallel to the right-hand wall of the alcove corner. The center column holes were drilled into the intersection of the corner walls.

Vertical Paths

Nine sets of vertical cross-hole paths were used to measure V_P, one set of three paths each in the left and right walls and one set of three in the walls' intersection. Results for the paths in the walls will be discussed together and contrasted with the observed velocities in the intersection.

Figure 5 contains the results of measurements made along vertical paths in the left wall, showing V_P to a depth of seven meters. All three sets of data indicate a shallow DRZ, extending to a depth of no more than 1 m and more reliably to about 0.5 meters. Velocity decreased the most in the center hole pair (QGU33-->QGU36) where V_P was lowered by about 9% from the far field value of 4.4 km/sec to 4 km/sec at the surface. Only the outermost 0.5 m shows a clear DRZ. In the upper and lower hole pair, QGU33-->QGU30 and QGU36-->QGU39, the evidence for a DRZ is slight; a small decrease in V_P appears to exist in the outermost 0.3 m, particularly near the top of the room between QGU33 and QGU30.

Information Only

As discussed earlier, the symmetry of the vertical paths about the corner can be used to examine the symmetry of the stress state and the influence of nearby openings such as the Q Access Drift. A symmetric stress state would be expected if the local geometry dominates, leading to the expectation that the pattern of velocities should be identical for the paths in the left and right walls. As indicated by the results shown in Figure 5 and Figure 6, this was closer the case than was observed for the horizontal paths discussed earlier. Partly this is true because there is less evidence of damage for measurements made along the vertical paths, as compared to the horizontal paths. Between QGU35 and QGU32, (top plot, Figure 6), considerable variation in V_P was observed, at three distinct points near 0, 1.5 and 6.3 m depth. These appear to be real, as indicated by the duplication of the values at adjacent points, but are rather large to be due to lithology fluctuations. Localized macro-cracking may explain the results at shallow depths but seems unlikely at 6.3 meters. Examination and filtering showed that the anomalous velocity values were associated with signals that, when compared to the signals observed at adjacent points, appeared to have had the high frequency components removed during their passage through the salt. Distributed damage typically acts as a high frequency filter, providing credibility to the possibility that real damage is being observed, especially given the duplication at adjacent measurement points. At this time, there is no better explanation for the anomalous results, particularly the low values of V_P observed near 6.3 meters. The data give clear evidence of a DRZ in the region between QGU38 and QGU41 (bottom plot, Figure 6) where the decrease in V_P extends in almost a meter.

Compared to the horizontal paths discussed earlier, damage measured along vertical paths is less extensive, reaching shallower depths and producing smaller changes in V_P. The general pattern of damage is similar and slightly asymmetric, with greatest damage observed in the upper portion of the left wall and the lower portion of the right wall.

A very different picture of damage was observed in the third set of vertical paths that lay in the plane bisecting the room corner (Figure 7). To the limits of measurement accuracy, no DRZ was observed, even at the shallowest depths. This is a novel observation and unlike anything observed at other locations in the WIPP. This is also the only measurement of V_P made into a room corner at WIPP, although the geometry is related to the arrangement in the Air Intake Shaft (AIS) (Holcomb, 1999, Hardy and Holcomb, 2000), where measurements are being made in the wall of a 24-foot diameter shaft. Only a shallow DRZ has been observed in the AIS. Given the length of time the Q Room Alcove has been open, to find no DRZ is a surprising result.

Damage along the entire measurement path contributes to the decrease in velocity that is a signature of the DRZ. Thus, the constant V_P observed in the alcove corner along vertical paths indicates that no point from ceiling to floor has experienced significant damage in the form of cracks that could decrease the speed of a compressional wave propagating vertically. Cracks oriented perpendicular to the direction of propagation are most effective in decreasing V_P; in this case, horizontal cracks would be most effective. Thus, it appears that little or no horizontal cracking has occurred near the bisecting plane of the corner, at any depth, even 12 years after excavation. A meter away, the stress-state is sufficiently different that V_P in the vertical direction is decreased, indicating some horizontal, or at least non-vertical, cracking did occur.

Information Only

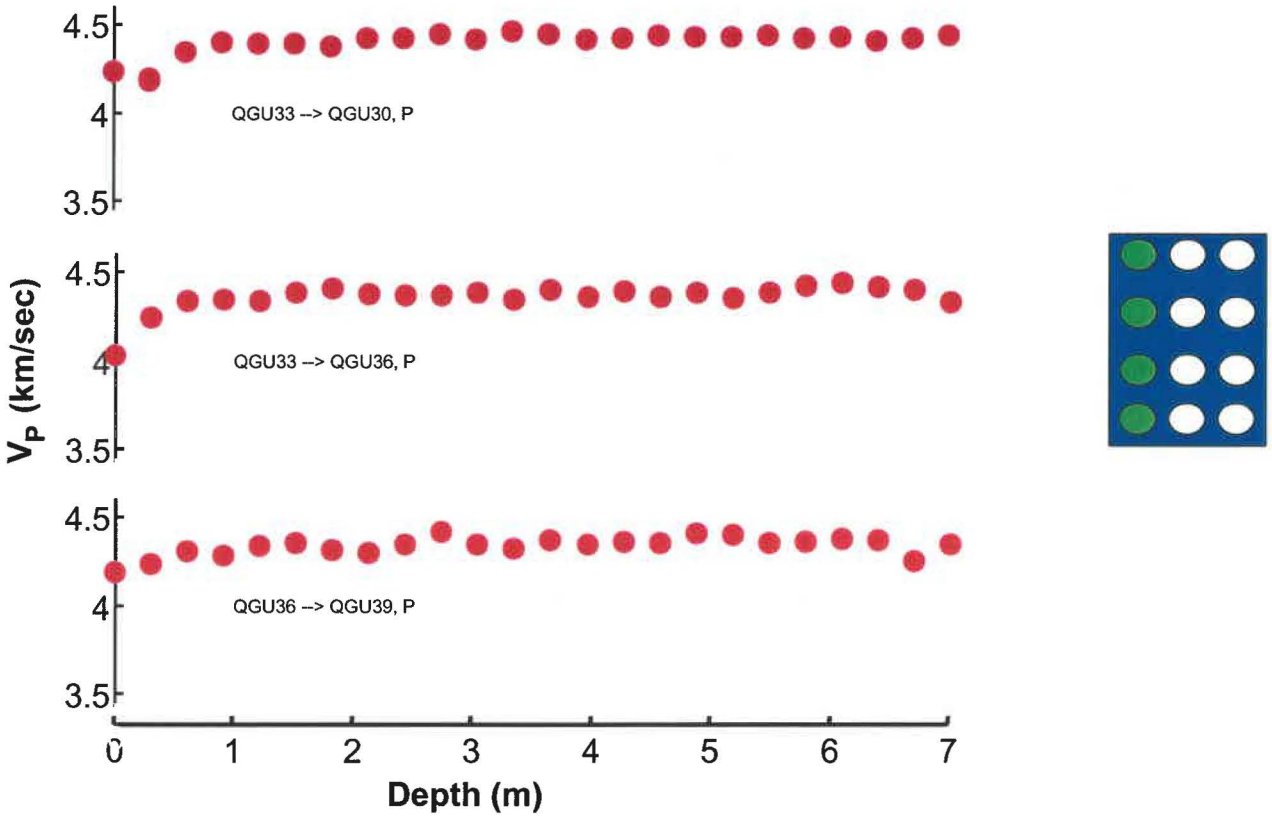

Figure 5: **V_P for the three sets of vertical cross-hole paths in the left-hand wall of the alcove corner.**

Information Only

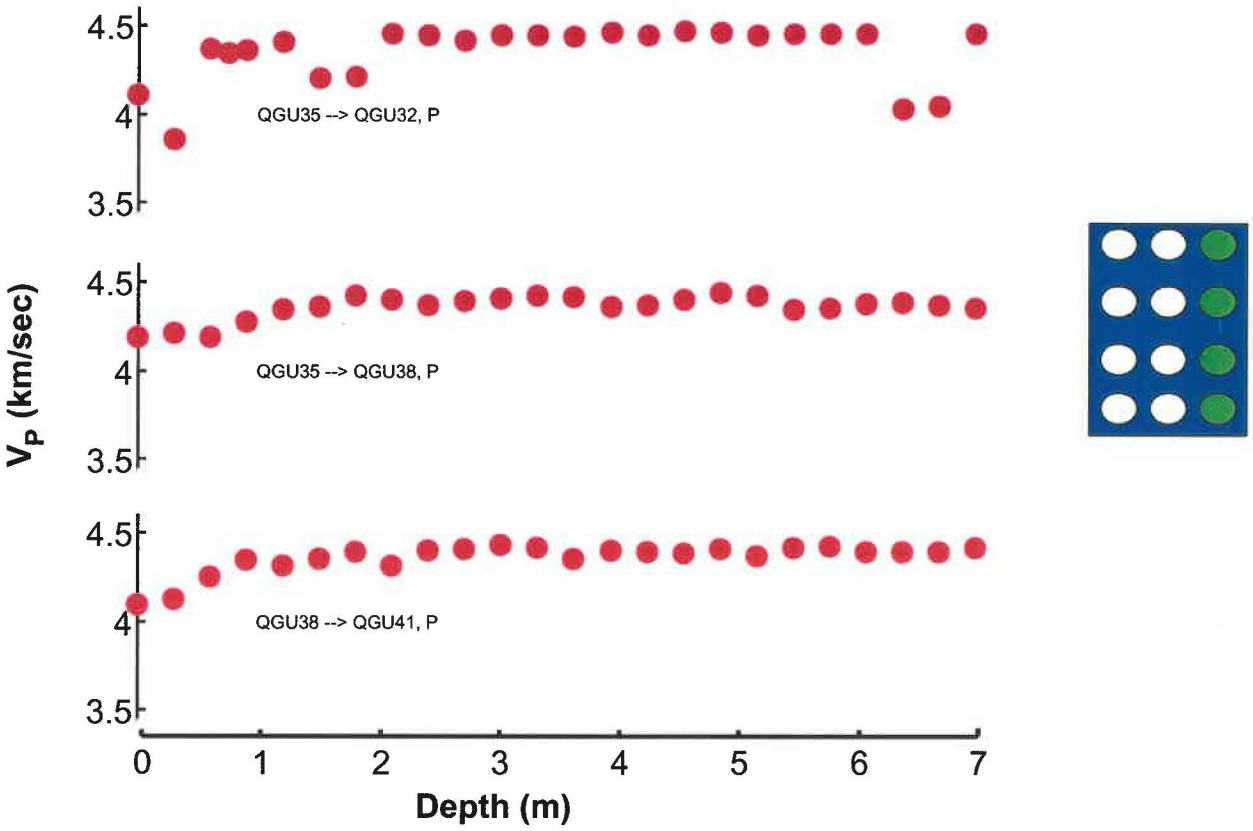

Figure 6: **V_P for the three vertical sets of cross-hole paths in the right-hand wall of the alcove corner.**

Information Only

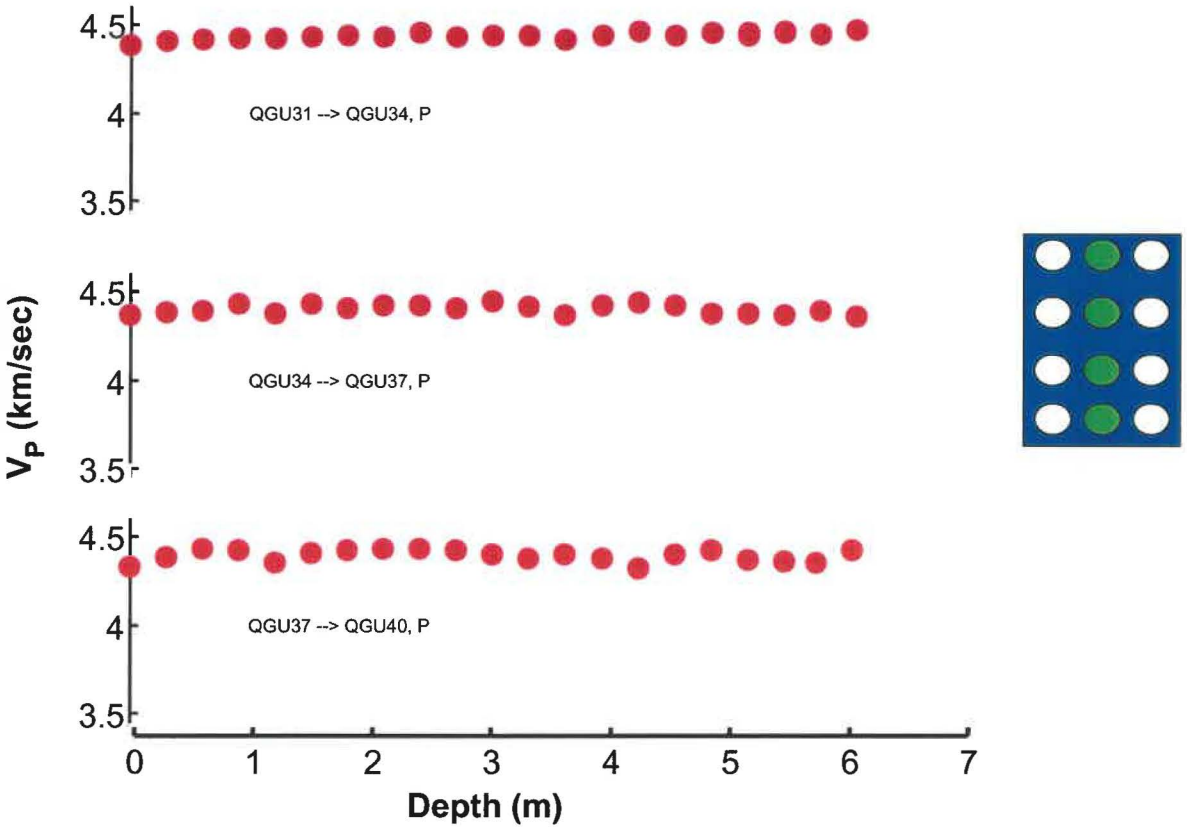

Figure 7: V_P for the three sets of vertical cross-hole paths in the alcove corner. The center column holes were drilled into the intersection of the corner walls.

Same-hole Paths

Same-hole paths, where the transmitter and receiver are in the same hole offer a number of advantages:
maximum sensitivity of V_P to the expected orientation of cracks, fixed path length to eliminate surveying as a source of error, and the ability to measure both P and S waves with one set of transducers. To offset these advantages there is the poor quality of the P wave signal due to the geometry of the transducer arrangement and the lower sensitivity of V_S. In this arrangement, the shear wave is propagating perpendicular to the expected crack orientation, but the particle motion is parallel to the plane of the cracking, thus reducing the effect of the DRZ on the velocity of the shear wave.

Because of the shallowness of the DRZ and to check the absence of a DRZ in the corner, a more extensive series of measurements was carried out in some of the holes. Measurements were made every 0.15 m for the first 2 meters. The same general pattern of damage seen in the cross-hole measurements was observed in these same-hole measurements. Two sets of data are particularly effective in showing the strong variation in damage near the corner; V_P measured along the axis of QGU36 and QGU37 is plotted in Figure 8. A DRZ is clear in

Information Only

QGU36, located about a meter to the left of the corner, but only a hint of a DRZ is observed in QGU37, drilled directly into the corner. V_P decreased from 4.4 to 3.8 km/s, with the decrease beginning at about 1.5 m, indicating that there was substantial damage at this location. Just a meter to the right, in QGU37, there is little or no evidence of damage. There is a slight decrease of V_P through the shallowest 0.3 m, but it is not obviously due to damage. The fluctuations observed deeper in QGU37 are of the same size. In any case, the DRZ is clearly much less well developed here, than in the same horizon only a meter away. A short distance from the corner, the DRZ is similar to that observed in the access drift (Holcomb and Hardy, 2001). Clearly the difference is due to the dependence of the stress-state on proximity to the corner.

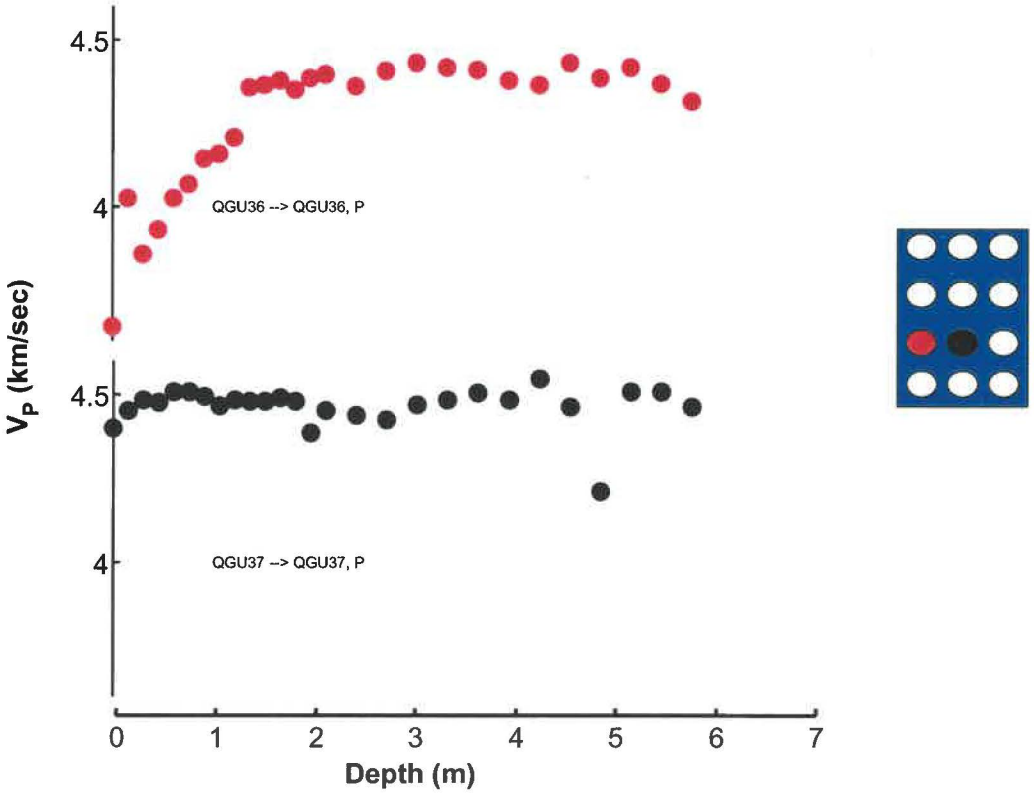

Figure 8: Same-hole measurements for adjacent holes, one in the left-hand wall (red) and in the corner (black).

Comparison of Laboratory and In Situ Results

Previous laboratory work (Brodsky, 1995) determined the changes in V_P under axisymmetric stress conditions. However, the in-situ stress-state is fundamentally non-axisymmetric with the minimum compressive stress approaching zero along the normal to the surfaces of openings. Parallel to the surfaces, stress concentrations vary, depending on the shape of the opening and its orientation. For a long drift, stress parallel to the drift is essentially the same as the far field lithostatic stress, which is about 15 MPa. The vertical stress concentration factor is approximately two, leading to a vertical stress of 30 MPa, although higher values can be attained initially near corners. Damage due to cracking is driven by both instantaneous processes and time-dependent creep, both of which produce more damage at

Information Only

higher stress differences. An experiment was carried out to help separate the instantaneous and time-dependent contributions to damage.

Using a true-triaxial test frame, WIPP salt was subjected to a stress path designed to simulate the instantaneous (short-term) stress path experienced by salt near a drift as it was mined. In the following discussion, a numbered coordinate system will be used to refer to the axes along which stresses and strains were measured, using subscripts to denote the proper axis. Thus, the stress or strain measured along the one (1) axis would be σ_1 or ε_1. By the usual convention for geomechanics, the maximum compressive stress is applied along the one (1) axis, intermediate stress is parallel to the two (2) axis and the minimum compressive stress is parallel to the three (3) axis. During this test, the maximum compressive stress, σ_1, was increased from 15 to 30 MPa, the intermediate stress, σ_2, was held constant at 15 MPa, and the minimum compressive stress, σ_3, decreased from 15 to 0 MPa. This condition approximated the in-situ stress during mine-by and allowed the effect of the instantaneous damage on V_P to be determined. Figure 9 summarizes the experiment, showing the sample and the stress-strain data from the test. Samples were approximately 5 cm by 5 cm in cross section and 12 cm long. After jacketing with copper foil, strain gages and LVDT gages were mounted to measure the three principal strains. PZT transducers mounted on the sample or in the platens were used to measure V_P at intervals during the test. Stresses were servo-controlled so that σ_1 and σ_3 changed in equal but opposite increments, while σ_2 was held constant. The intermediate stress was slightly above the goal of 15 MPa for experimental reasons. Strain in the one direction, corresponding to maximum compressive stress, was the control variable, increasing at a fixed rate during the test.

Figure 9 includes a plot of strains versus σ_1, with compression to the right; strain parallel to the maximum compressive stress is plotted as a black line, strain parallel to the intermediate stress is plotted as a green line, and in the minimum compressive stress direction, strain is indicated by the red line. Yielding occurred after σ_1 surpassed 22 MPa, followed by more-slowly increasing stress, until the test was halted after σ_3 reached 0 MPa. At that point, all stresses were returned to the initial values. Dilatational strain, assumed to be due to opening of cracks as the salt was damaged, can be seen in ε_{33}, which began increasing rapidly when σ_1 exceeded the yield stress. In contrast to both ε_{11} and ε_{33}, ε_{22} remained unchanged.

Velocities, measured along the stress axes, are plotted in Figure 10 superimposed on the stress history using the same color-coding as for the strains in Figure 9. Solid lines show the stress history as a function of time, beginning near hydrostatic stress-state and evolving to the final stress of (30, 17, 0) MPa, before the stress was returned to the starting values. Colored dots are used to plot the normalized values of V_P during the course of the test (right-hand scale). Parallel to σ_1 and σ_2, the maximum and intermediate compressive stresses, V_P was essentially constant as shown by the black and green dots, respectively. Although initially constant, V_{P3} began to decrease when the yield stress was exceeded and decreased throughout the test, reaching a final value about 3.5% below the starting value.

Strains and velocities are telling a consistent story of anisotropic damage under stresses similar to those expected instantaneously during a mine-by. Compressive strain along the one (1) axis (maximum compressive stress) would close, not open cracks, leading to little change in V_P along the axis parallel to σ_1. Along the two (2) axis, parallel to σ_2, little strain was observed at any time during the test. Again, this is consistent with no cracks opening

Information Only

and no change in V_{P2}. Dilatational strain was only observed in the three (3) direction, parallel to the minimum compressive stress, and this is the direction where a decrease in V_{P3} was measured. The primary strain contribution of cracks opening in the three (3) direction would be to cause the magnitude of ε_{33} to increase more rapidly than would be observed for the Poisson contribution in the more-or-less elastic, low-stress, portion of the test. Increased dilatational strain is assumed to be the result of cracks opening under the shear stress being applied and newly opened cracks cause V_P to decrease for waves propagating in the direction of the opening cracks. The primary strain contribution of cracks opening in the three (3) direction would be to cause the magnitude of ε_{33} to increase more rapidly than would be observed for the Poisson contribution in the more-or-less elastic, low-stress, portion of the test.

Instantaneous damage under stresses similar to what would be encountered near a drift, or other opening being mined, only changed V_P in the direction of the minimum compressive stress and then by only 3.5 percent. As the previous discussion and earlier work in the Q Access Drift (Holcomb and Hardy, 2001) showed, much larger changes were observed in-situ. Figure 11 compares the in-situ results (in red) with the laboratory experiment discussed above (in black). In-situ, V_P was found to be change by up to 7% in the vertical and horizontal directions, parallel to the drift, and 20% perpendicular to the drift. Equivalent results for the instantaneous effects of applying appropriate stresses in the laboratory were 0% change in the horizontal and vertical directions and 3.5% in the minimum stress direction, which is equivalent to perpendicular to the drift. The prominent difference is a measure of the impact of time-dependent deformation on the production of damage in-situ.

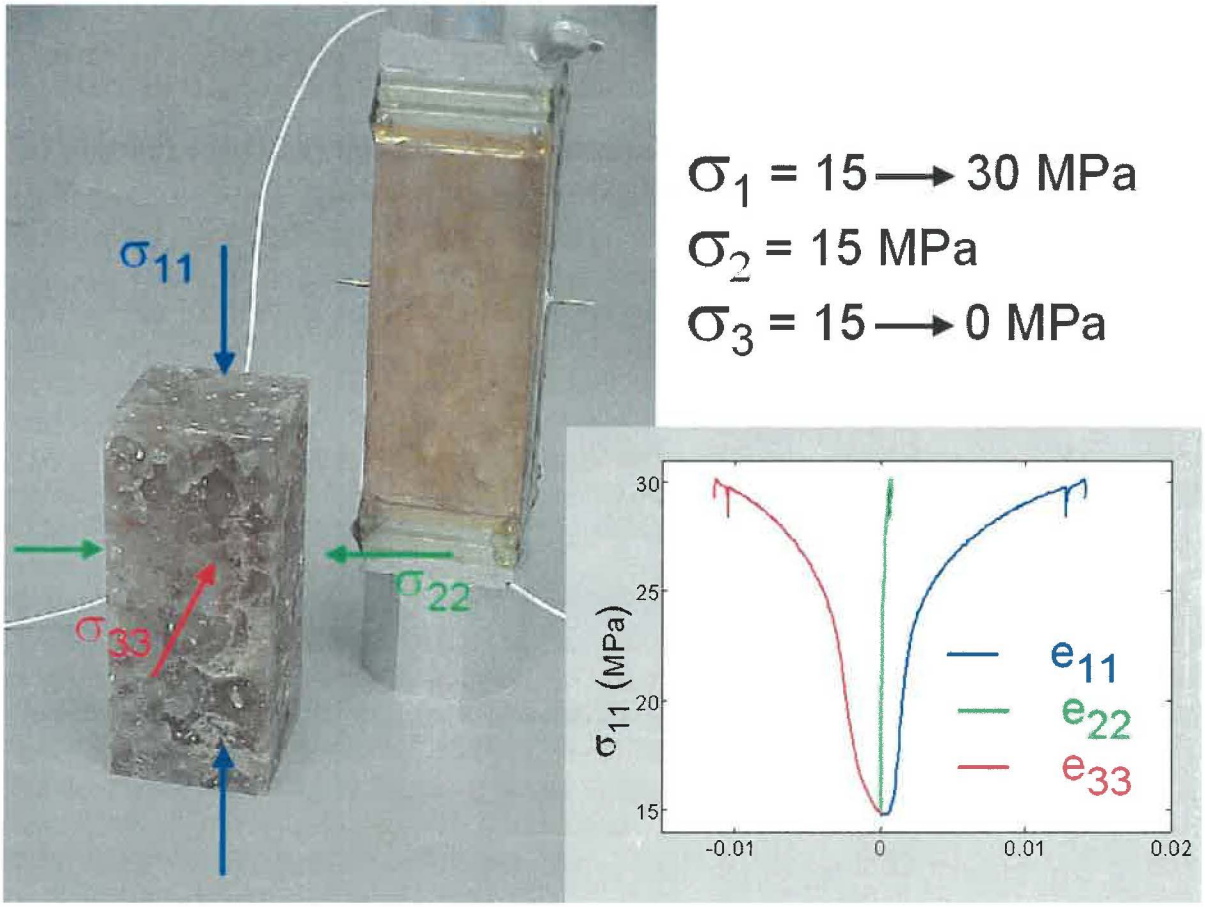

Information Only

Figure 9: **Photograph of sample, unjacketed and ready for testing, with stress-strain data for a test simulating results of a mine-by.**

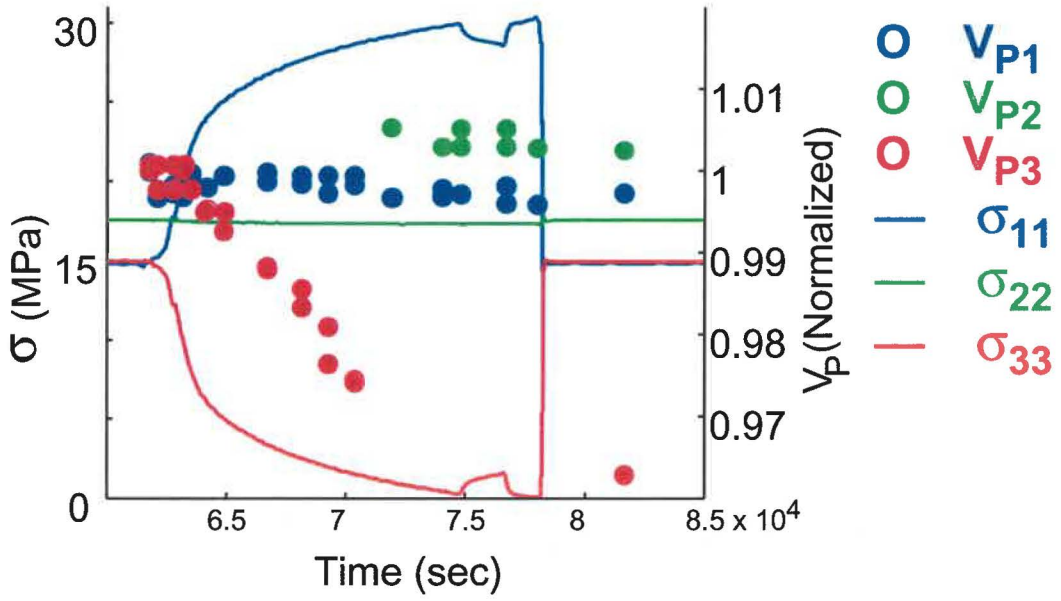

Figure 10: **Stress history (solid lines) and normalized V_P (dots, right axis) as a function of time for the mine-by simulation experiment.**

Information Only

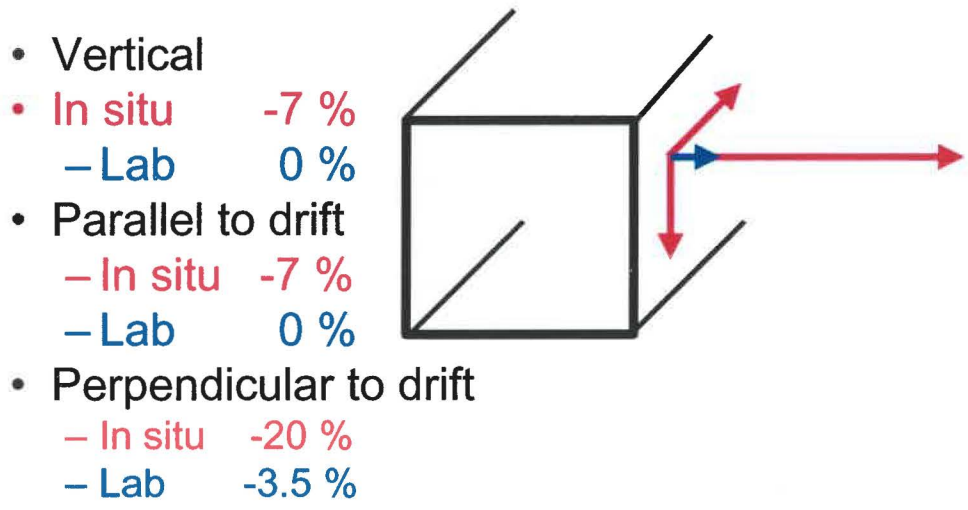

Figure 11: Summary of velocity changes observed in the simulated mine-by experiment compared to the results observed in situ. Sketch indicates orientation and magnitude, relative to a drift.

Summary:

Previous work had examined the DRZ in simple geometries, typically a room wall or a long drift. The current work is an extensive look at what happens in the corner of a room, an area intentionally chosen for its complexity. As expected, the pattern of damage was found to be more complex than in the simpler geometries previously studied. Two features were unexpected: damage did not extend in as far as in the previous studies, and along the bisecting axis of the corner, no DRZ was observed.

First, the similarities will be summarized. Near the floor and ceiling the DRZ was less pronounced than in similar zones closer to the mid-height of the room. Damage was clearly anisotropic, with the maximum decrease in V_P being observed in directions closer to perpendicular to the walls. This fits with the assumption that the DRZ is the result of cracks opening in the direction of minimum compressive stress. The decreases in V_P were similar to those observed before, but the spatial variation of DRZ development was very different.

.

In previous work, velocity measurements typically indicate a DRZ extending in about 2 meters. An exception to that rule was found in the AIS (Hardy and Holcomb, 2000) where the DRZ only extends 0.5 to 1 meters. In the current work the DRZ, when found at all, only extended in about 1 meter and there were many areas that did not appear to be damaged. Of greatest interest are the results from the cross-hole, vertical path and the same-hole measurements made in holes drilled into the bisecting axis of the corner. No DRZ was

Information Only

observed here, even for the same-hole measurements, which are most sensitive to damage in the expected orientation. Same-hole measurements made in a hole only a meter away from that hole where no DRZ was observed found a well-developed DRZ. The complete absence of discernable damage, even after 12 years, indicates the effectiveness of a rounded interior corner in suppressing damage.

This observation suggests a possibility for constructing seals that would avoid the effects of the DRZ on permeability. If a slot with a rounded end were mined into the wall of an existing drift to a depth of about 3 meters, then the slot would extend past the DRZ induced by the drift, reaching relatively undisturbed, low-permeability salt. The results of the current work suggest that there would be a zone, approximately along the axis of the slot, where no or limited damage would occur, either immediately or for years. Thus, leaks past the seal through a DRZ could potentially be eliminated since the DRZ may not form to begin with. Given the complexity of the geometry studied in the current work, it is clear that a more systematic investigation would be required to substantiate this possibility. In particular, the details of the influence of curvature and width of the slot on extent of the DRZ would need to be studied to see if the absence of a DRZ is reproducible and predictable.

A comparison of laboratory and in-situ results show that plastic creep is producing more crack damage than was produced by the instantaneous effect of applying shear stresses equivalent to the 3-D stress expected in-situ.

References

Brodsky, N.S., *Thermomechanical damage recovery parameters for rock salt from the Waste Isolation Pilot Plant, Sandia National Laboratories Report, SAND93-7111, 1995*

Hardy, R.D. and D.J. Holcomb, *Assessing the disturbed rock zone (DRZ) around a 655 meter vertical shaft in salt using ultrasonic waves, An Update,* Proc. 4th North American Rock Mechanics Symposium, 2000

Holcomb, D.J. and R.D. Hardy, *Assessing the disturbed rock zone (DRZ) at the WIPP (Waste Isolation Pilot Plant) in salt using ultrasonic waves*, Proc. 38th U.S. Rock Mechanics Symposium, 2001, pp. 489-496, Ed. Elsworth, D., J.P. Tinucci and K.A. Heasley, Balkema.

Holcomb, D.J., *Assessing the Disturbed Rock Zone (DRZ) around a 655 meter vertical shaft in salt using ultrasonic waves*, Proc. 37th U.S. Rock Mechanics Symposium, 1999

Maxwell, S.C., R.P. Young and R.S. Read, *A Micro-velocity Tool to Assess the Excavation Damaged Zone, Int. J. Rock. Mech. Min. Sci., 35, pp. 235-247, 1998*

Munson, D.E., D.J. Holcomb, K.L. DeVries, N.S. Brodsky, and K.S. Chan, *Correlation of theoretical calculations and experimental measurements of damage around a shaft in salt, pp. 491-496, Proc. 35th U.S. Symp. On Rock Mechanics, 1995*

Powers, D.W., *Core Descriptions from Location 1, S90 Drift, for DRZ Test Program, April 2000, Contractor's report*

Information Only

Information Only

4.4 DRZ Core Studies[1]

A snap-shot of the DRZ core studies is summarized in Table 4.4.1. Our observational work in the Carlsbad laboratory includes quantifying fracture porosity, free dislocation density, mineralogy and moisture. In addition to WIPP cores, we are evaluating similar properties of DRZ cores from sites in Germany. The German information will be compared to WIPP data and discussed with researchers involved in the BAMBUS II consortium research. A published paper on the completed portions of this work was provided in the previous (07/31/01) milestone report.

Table 1: Laboratory DRZ Core Evaluations

Repository Core	Fracture Analysis	Free Dislocations	Mineralogy	Moisture Content
Asse Mine DJ-V ALOHA II [lined drift]	**C**	**C**	**C**	**C**
Asse Mine HD-V ALOHA II [unlined drift]	**C**	**C**	**C**	**C**
WIPP Mine Run QGU14	**C**	**C**	**C**	**C**
WIPP Mine Run QGU36	**C**	**AIP**	**N/A**	**N/A**
WIPP Mine Run QGU39	**AIP**	**AIP**	**N/A**	**N/A**
German TSDE Core #1	**TBD**	**TBD**	**TBD**	**TBD**
German TSDE Core #1	**TBD**	**TBD**	**TBD**	**TBD**

Legend

C: Analysis Completed

AIP: Analysis In-Progress

N/A: Analysis Will Not Be Performed

TBD: Analysis Will Be Performed When Core is Procured from BAMBUS II Collaborators

[1] This work is covered by BOE #1.3.5.4.4 and WBS #1.3.5.4.4.2

Information Only